Initial retention of the bacterium Escherichia coli on silicone elastomers : the effects of stiffness and topography

Viktoriia Drebezghova

Initial retention of the bacterium *Escherichia coli* on silicone elastomers: the effects of stiffness and topography

DISSERTATION

to obtain the degree of doctor at the Université de Pau et des Pays de l'Adour,
to be publicly defended on December 17, 2021

by **Viktoriia DREBEZGHOVA**

Jury composition

Pr. Lydie Ploux	INSERM – BIOMAT (Strasbourg, France)	*Rapporteur*
Pr. Frédéric Restagno	UPS – LPS (Paris, France)	*Rapporteur*
Pr. G. Julius Vancso	UT – MESA+ (Enschede, The Netherlands)	*Committee member*
Pr. Régis Grimaud	UPPA – IPREM (Pau, France)	*Committee member*
Pr. Corinne Nardin	UPPA – IPREM (Pau, France)	*Supervisor*
Pr. Frédéric Léonardi	UPPA – IPREM (Pau, France)	*Co-supervisor*

Acknowledgement

First of all, I would like to express my gratitude to Dr. Lydie Ploux (INSERM - BIOMAT, Strasbourg) and Dr. Frederic Restagno (Université Paris-Saclay, Paris) for agreeing to be the rapporteurs of this dissertation. I am deeply honored they have accepted to evaluate my work. Further, I would like to thank my committee members Pr. G. Julius Vancso (University of Twente, The Netherlands) and Pr. Régis Grimaud (Université de Pau et des Pays de l'Adour) for agreeing to participate to my dissertation defense and for the thoughtful comments and recommendations on this dissertation they have given me in the course of my PhD studies.

From the bottom of my heart, I would like to thank my supervisor Pr. Corinne Nardin, who has supported me throughout this research project, for her patience, motivation, enthusiasm, immense knowledge, and her personal support in my academic career. Her guidance helped me in all the time of research and writing of the thesis. I could not have imagined having a better supervisor for my PhD study.

I would also like to express my gratitude to Pr. G. Julius Vancso, Dr. Hubert Gojzewski, and Pr. Corinne Nardin for our collaborative working, which yielded two scientific papers. I am honored to participate this research team.

I would like to thank my co-supervisor Pr. Frédéric Léonardi for his substantial contribution to the analysis of the material bulk properties, to which I devoted the first year of my PhD study. I particularly appreciate his readiness to propose a solution or idea and to help with some advice. I would also like to thank Pr. Ahmed Allal, who found the financial support for my research project, for his enthusiasm and participation.

I am very grateful to Pr. Régis Grimaud and Florence Hakil, who trained me to work in the world of microbiology, for their participation in the microbiological studies, on which I spent two years of my research.

I would like to say special thanks to Mickael Le Bechec, who helped me on numerous occasions with ideas. He also greatly helped me with the equipment required for my experimental studies which were called into question because of the work restriction during the COVID-19 pandemic.

I am extremely grateful to Pr. Ross Brown and Sylvie Blanc for working together on fluorescence imaging, Virginie Pellerin, Christine Lartigau-Dagron, Bernard Berkowitz, Anthony Laffore for training me in SEM imaging, IRTF, DSC, TGA, and DMA techniques.

It is impossible to overestimate the contribution in this thesis work of Benoit Caubet, who had been working with me as an internship student under my supervision for 6 months. I would like to thank him for the excellent teamwork experience and original ideas. I would also like to say thank Marwan Puaud, who also had been an internship student under my supervision. Although our common experimental work was over-complicated because of the restriction due to the pandemic, he has shown high motivation and enthusiasm.

I would like to express my gratitude to the MESA+ team for the warm welcome and a great time spent together during my 4-months stay within the University of Twente in the Netherlands.

I am extremely grateful to the members of the team I have been a part for four years, for their goodwill, support, willingness to help and give some advice, and, finally, for sharing a lot of good moments together.

I would like to thank for funding my PhD study by the project POCTEFA HEALTH LSR 2017-146 (Région Nouvelle Aquitaine 1R10103-00013013) and E2S UPPA (Energy and Environment Solutions).

Last but not the least, I would like to thank my family and friends that I made within the laboratory for their patience, encouragement, and support during the years of my PhD project.

Résumé (*français*)

La contamination bactérienne est de nos jours un problème crucial en milieu cliniques et dans plusieurs secteurs industriels. La prévention de l'adhésion initiale des bactéries aux surfaces représente une approche efficace afin d'empêcher la croissance de biofilms bactériens dans lesquels celles-ci sont plus résistantes aux antibiotiques et aux conditions environnementales. Parmi les différentes stratégies possibles de développement de surfaces antibactériennes nous nous sommes focalisés sur le développement de surfaces résistantes à l'adhésion bactérienne selon une approche préventive qui consiste à moduler les propriétés intrinsèques des matériaux. Le but principal de ma thèse, conduite dans le cadre du projet transfrontalier Interreg V-A Espagne-France-Andorre (POCTEFA) Health-Liquid Silicone Rubbers (Health-LSR) et subventionné par la région Nouvelle-Aquitaine, est d'étudier la réponse bactérienne aux propriétés physiques des élastomères en silicone telles que la dureté et la topographie de surface pour des applications biomédicales.

Pour les surfaces « modèles », nous avons sélectionné le poly(dimethylsiloxane) (PDMS) Sylgard 184, le silicone commercial le plus étudié. La structure en réseau tridimensionnel du PDMS réticulé à l'échelle nanométrique a été visualisée et analysée par microscopie à force atomique (AFM) haute résolution. En utilisant une souche d'*Escherichia coli*, nous avons établi la corrélation entre le degré de réticulation et donc la dureté du PDMS et la rétention bactérienne. Nous avons également démontré l'effet des chaînes libres de PDMS sur la rétention bactérienne même si la nature de cet effet reste difficile à mettre en évidence directement. Toutefois, l'effet de l'extraction de chaînes libres sur plusieurs propriétés physico-chimiques (composition chimique, nano-topographie, la densité de réticulation) a été étudié, et son influence potentielle sur la rétention bactérienne analysé.

Dans le cadre du projet « POCTEFA Health-LSR », nous avons étudié plus particulièrement la rétention bactérienne sur le silicone liquide (LSR). C'est un produit commercial constitué principalement de chaînes de PDMS et de charges en silice en différentes proportions afin de moduler les propriétés mécaniques du LSR. Dans un premier temps nous avons caractérisé le comportement thermique et mécanique du LSR. Nous avons également mis en évidence « l'effet lotus » des surfaces LSR texturées par moulage à chaud. Suite aux tests microbiologiques effectués sur le LSR, les surfaces texturées ne permettent pas de réduire la rétention bactérienne malgré ses propriétés superhydrophobes. Au contraire, elles sont plus favorables à la rétention bactérienne que

les surface « lisses », car la taille caractéristique des structures et une transition de l'état de mouillage Cassie-Baxter à l'état Wenzel augmente la surface d'encrage disponible pour les bactéries.

Mot clés : *PDMS Sylgard 184, Silicone liquide LSR, dureté, topographie, superhydrophobe, Escherichia coli*

Abstract (*English*)

Bacterial contamination is nowadays a crucial issue in a wide range of industrial and clinical settings. Preventing initial bacterial adhesion to material surfaces represents an effective approach for avoiding biofilm growth in which bacteria become much more resistant to antibiotics and environmental stresses. Among different possible strategies of antibacterial surfaces development, we were especially interested in the development of materials resistant to initial bacterial adhesion due to their intrinsic properties. The main objective of this thesis, conducted in the frame of both the Project Interreg V-A Espagne-France-Andorre (POCTEFA) Health-Liquid Silicone Rubbers (Health-LSR) "POCTEFA Health-LSR" further granted by the Nouvelle Aquitaine Research Council, was to investigate the bacterial response to physical properties of silicone elastomers such as stiffness and surface topography for biomedical applications.

As model surface, we selected poly(dimethylsiloxane) (PDMS) Sylgard 184 commercial silicone, the characteristics of which are the most reported in the literature. The network structure of the cross-linked PDMS was visualized and analyzed by high resolution atomic force microscopy (AFM) at the nanometer scale. Using *Escherichia coli* strains, we established the correlation between the cross-linking degree and thus the stiffness of PDMS and bacterial retention. We also shown the effect of uncross-linked free, PDMS chains on bacterial retention. However, even if this effect is not intuitive at a first glance, we characterized the physico-chemical properties (chemical composition, nano-topography, cross-link density) of the material to assess the potential role of the free chains on bacterial retention.

In the frame of the project "POCTEFA Health-LSR", we investigated the bacterial retention on Liquid Silicone Rubbers (LSR). It is a commercial product mainly composed of PDMS chains and silica fillers in different ratios to vary the mechanical properties of LSR. In the first stage, we characterized the thermal and mechanical behavior of the elastomers under investigation. We also textured by hot molding LSR surfaces that reveal the "lotus-leaf" effect. According to microbiological tests achieved on those, the textured LSR surfaces do not allow for any reduction of bacterial retention regardless their superhydrophobic properties. Rather, they are more favorable to bacterial retention than "smooth" surfaces, given that anchor surface available to bacteria is considerably increased due to the texture characteristic size associated with a Cassie-Baxter to Wenzel wetting state transition.

Key words : *PDMS Sylgard 184, Liquid Silicone Rubbers (LSR), stiffness, topography, superhydrophobic, Escherichia coli*

List of abbreviations

AFM – Atomic Force Microscopy
c-di-GMP – Cyclic diguanylate monophosphate
CFU – Colony forming units
DLVO theory – Derjaguin-Landau-Verwey-Overbeek theory
DMA – Dynamic mechanical analyses
DMT theory – Derjaguin, Muller, and Toporov theory
DSC – Differential scanning calorimetry
DTG curve – Derivative thermogravimetry curve
EPS – Extracellular polymeric substances
FTIR – Fourier transform infrared spectroscopy
FWHM – Full width at half maximum
G' – Storage modulus, real part of the complex shear modulus
G'' – Loss modulus, imaginary part of the complex shear modulus
GFP – Green fluorescent protein
HCRs – High consistency rubbers
HTV silicone rubbers – High temperature vulcanizing silicone rubbers
JKR model – Johnson, Kendall, and Roberts model
LB – Lysogeny broth
LPS – Lipopolysaccharides
LSRs – Liquid Silicone Rubbers
LVR – Linear viscoelastic region
MCP – Methyl-accepting chemotaxis protein
OM micrograph – Optical microscopy micrograph
OP – Optical profilometry
PBS – Phosphate buffered saline
PCM – Plate count method
PDMS – Poly(dimethylsiloxane)
PEG – Poly(ethylene glycol)
PF-QNM – Peak force quantitative nanomechanical mapping
PMMA – Poly(methyl methacrylate)
PS – Polystyrene
Pt - Platinum
QS – Quorum sensing

RMS surface roughness – Root mean square surface roughness

RTV silicone rubbers – Room temperature vulcanizing silicone rubbers

SEM – Scanning electron microscopy

SEs – Secondary electrons

SH foil – Superhydrophobic foil

TGA – Thermogravimetric analysis

WCA – Water contact angle

XDLVO theory – Extended DLVO theory

XPS – X-ray photoelectron spectroscopy

Table of contents

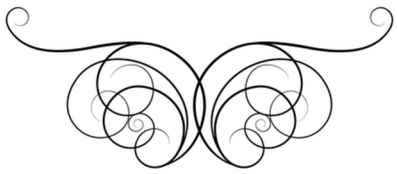

General introduction

Controlling the contamination of materials by pathogenic microorganisms is crucial nowadays in a wide range of industries (e.g., agri-food, biomedical sectors) and clinical settings. Materials in liquid environments are exposed to numerous microorganisms (bacteria, yeasts, etc.), including potentially pathogenic species, and to macromolecules such as proteins, which can adsorb / adhere to a surface and colonize it. They pose a danger to human health, especially for vulnerable patients in health-care facilities [1]. Health-care associated, nosocomial infections are mostly associated with such species as *Escherichia coli*, *Staphylococcus aureus*, *Pseudomonas aeruginosa*.

In combination to antibiotic resistance of bacteria, which is becoming an imminent public health concern, researches across the world focus on the development of different antibacterial approaches. One of the most known and extensively investigated approach consists in the use of metal or metal-oxide based nanoparticles. The antibacterial mechanisms of specific nanoparticles such as silver [2,3], zinc [4–6], copper [5], iron [7,8] and gold [9,10], and their modes of action are known and discussed in an overwhelming number of studies (reviewed in [11–13]). Their antibacterial activity is related to the local disruption of the bacterial cell membrane that slows down bacterial growth, without being of toxicity to the surrounding tissue.

Another antifouling approach consists in functionalizing a surface with polymer chains that inhibit bacterial adhesion. For instance, numerous studies have attempted to fabricate substrates functionalized with poly(ethylene glycol) (PEG) brushes since PEG

chains exert large steric repulsion forces, which may impede the approach of bacteria towards the surface [14–16]. There is also a growing interest in developing stimuli-responsive polymers that respond to environmental changes such as pH, temperature, etc. These promote the release of dead bacteria upon an environmental change. The particular interest in these smart materials stems from the fact that traditional antifouling surfaces accumulate dead bacteria, thereby providing nutrients for other microorganisms, which renders the antifouling coating ineffective on the long term. For instance, the stimuli-responsive system comprising pH-responsive cross-linked poly(2-vinyl pyridine) (P2VP) films of 10–20 nm thickness and poly(ethylene oxide) (PEO) grafted to the P2VP surface and within the P2VP network can enable a 4-fold increase in longevity of antifouling, since a pH change activates the rearrangement of PEO chains (reviewed by Zhang *et al*. [17]).

If comparison to the numerous studies which aim at the modification of the surface chemistry in order to provide them with antibacterial properties, there are only humble beginnings in the topic that we address in this thesis. The effects of intrinsic physico-chemical properties of material surfaces on bacterial response, and particularly of the effects of mechanical properties and surface topography, constitute however a topic of fundamental importance, since it enables to comprehend the mechanisms through which bacteria adhere to the surface.

In this study, we thus investigated the response of the bacterium *Escherichia coli* to, first, the mechanical properties of poly(dimethylsiloxane)-based (PDMS) elastomers of various stiffnesses, and, secondly, to the elastomer surfaces exhibiting superhydrophobic properties by mimicking the "lotus leaf effect". PDMS-based elastomers, chosen as substrates for microbiological assays, are widely used in the biomedical industry – from contact lenses to medical devices – because of their biocompatibility and biomechanical behavior, comparable to that of biological tissues. They exhibit excellent thermal stability, mechanical resistance, chemical inertness, and absence of cytotoxicity.

These research activities have found their practical implementation within the frame of the European project POCTEFA Health-LSR. This project aims at the development of a cross-border pole of liquid silicone rubbers (LSRs), which involves the partners from different activity sectors within the Euroregion:

- Universidad de Navarra (CUN)
- Asociación de la Industria Navarra (AIN)

- Chambre de Commerce et d'Industrie Bayonne Pays Basque (CCI de Bayonne)
- Université de Pau et des Pays de l'Adour (UPPA),
- Centre Hospitalier Universitaire de Toulouse (CHU de Toulouse).

The Health-LSR project aims at creating LSR prototypes of devices that can be used in the medical sector with the final objective of their commercialization. Therefore, they must satisfy microbiological standards for surface hygiene. Our contribution in this project, discussed in detail in **Chapter II** and **III** of this thesis, consists in, first of all, thorough analyses of bulk properties of a series of LSRs grades from Wacker Chemie A. G. (Munich, Germany) that covers a stiffness range from 5 to 80 Shore A. Secondly, we investigated the effects of surface texturing, which provides to the LSR surfaces superhydrophobic character, on bacterial retention. Finally, we established the correlation between the LSR stiffness and topography and the bacterial retention on its surface.

Chapter I of this thesis gives the literature review, mainly divided into two sections – the bacterial adhesion behavior and the essential characteristics of silicone elastomers, the materials of interest. In the first section, we first provide the description of the structure of bacterial cells and their interaction with abiotic surfaces. Then, we review the existing studies on the dependence of bacterial adhesion behavior on physico-chemical properties of the substrate (hydrophobicity, charge, roughness, topography, stiffness). In the second section, we review the essential characteristics of silicone elastomers that we address in our study, particularly the PDMS chain properties and the specificities of the silicone elastomer network.

In **Chapter II**, we discuss the results of analyses of bulk properties of the series of LSR grades under investigation. We start by identifying the chemical composition of the commercial grades of LSRs, including the silica content and the cross-linking agent content in different ratios to vary their mechanical properties. Then, we analyze the cross-linking behavior of the LSRs, and, finally, we provide the analysis of static and dynamic mechanical properties of different silicone rubber grades.

In **Chapter III**, we begin by providing the analysis of surface properties of the cross-linked LSR samples (surface energy, hydrophobicity). Then, we proceed to the characterization of the topography of both textured and flat-like LSR surfaces, measured by means of electron microscopy (SEM), optical profilometry (OP) and by the sessile drop technique. In the further course of the chapter, we describe the results of microbiological

assays performed by epifluorescence microscopy imaging and by the plate count method, and provide the interpretation of the observed correlations between the number of bacteria retained on the LSR surfaces and the LSR stiffness and topography.

The contents of **Chapter IV** and **V** is dedicated to, first, the characterization of the PDMS surface properties which determine bacterial retention (chemical composition, stiffness, and surface topography), and, secondly, to subsequent investigations of the effects of PDMS stiffness on initial bacterial retention, using model PDMS surfaces. As model surface, we selected a PDMS grade Sylgard 184, whose surface characteristics can be perfectly controlled. The stiffness is varied by adjusting only one parameter, the cross-linking density.

In **Chapter IV**, we provide a systematic study of the elastomer mesh structure at the nanometer length scale, visualized by peak force tapping atomic force microscopy. This AFM imaging mode can provide superior resolution, when compared to the traditional tapping mode, and can yield nanographs with molecular scale details. The results of this study were recently published in *Macromol. Chem. Phys*. 2020, 2000170.

Finally, in **Chapter V** we establish the correlation between the initial bacterial retention and the PDMS substrate stiffness. We also investigated the effect of uncross-linked, free PDMS chains on bacterial retention. Finally, we provide the physical interpretation of the revealed correlations.

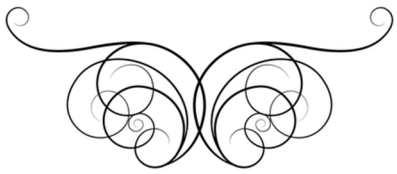

Chapter I

State of the art

1. Bacterial adhesion

1.1. A bacterial cell: Generalities

Bacteria are prokaryotic (i.e., cells without nuclei) unicellular microorganisms naturally present in our environment, suspended in more or less complex fluids. Compared to eukaryotic cells, bacteria exhibit a relatively small size. Typical bacteria diameters vary between 0.5 and 2 μm [1]. They are ubiquitous (present everywhere) and able to inhabit many different types of environments: from soil to food, from human body to industrial settings.

The bacterial world displays a wide diversity which can be classified by different criteria such as:

- Cell morphologies: cocci (spherical), bacilli (rod-shaped) and spirilla (spiral-shaped).
- Chemical and physical properties of cell walls.
- Presence of cell surface appendages (flagella, pili, curli, exposed proteins) that enable bacteria swimming motility and play an important role in attachment on surfaces.
- Bacterial oxygen need: aerobic or anaerobic [2]
- Nutritional types: phototrophs (use light energy), heterotrophs (oxidize organic compounds), lithotrophs (oxidize inorganic compounds), autotrophs (use CO_2), etc.

Intracellular structure. Despite the large variety of bacteria, they all share similar features in their cellular structure and composition. The intracellular structure of bacteria consists of a **nucleoid** (usually a single, circular chromosome) and **ribosomes** (sites of protein synthesis) suspended in the cytoplasm (**Fig. 1a**). In addition to the chromosome, bacterial cells often contain **plasmids** – small circular DNA molecules that are physically separated from the nucleoid and can replicate independently. In contrast to the bacterial chromosome containing all the essential genetic information for cell nutrition, development and reproduction, plasmids are usually very small and contain only additional genes encoding some extra functions, e. g. antibiotic resistance.

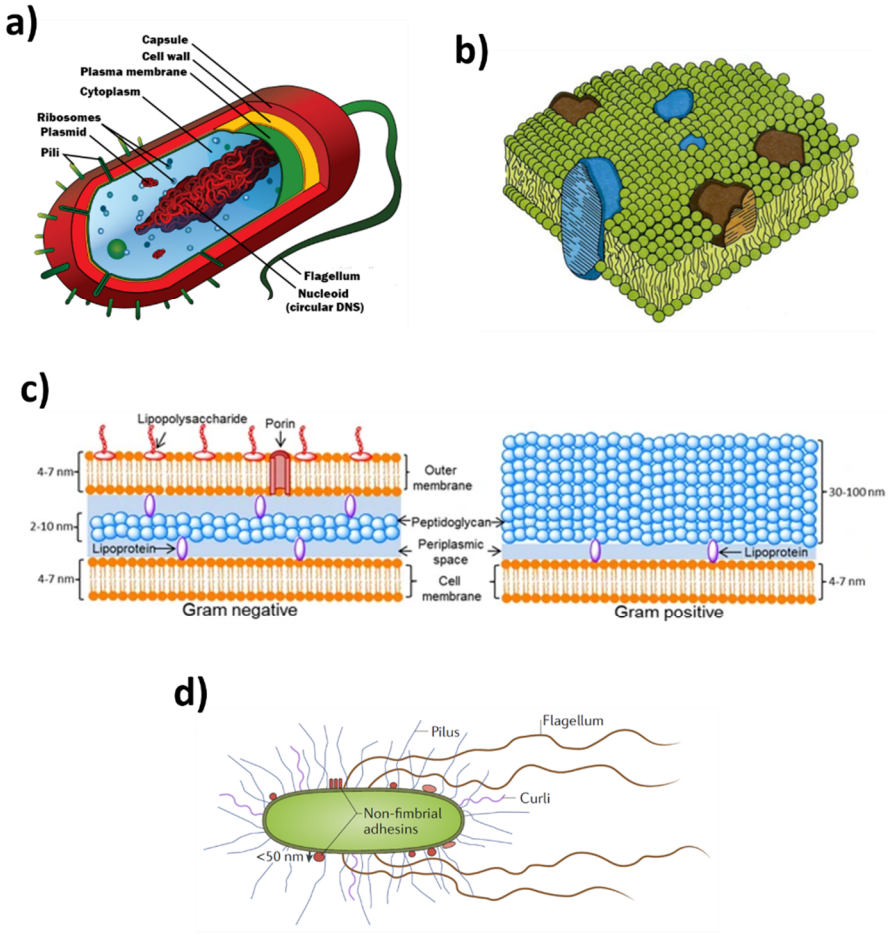

Figure 1.1. (a) Structural components of a Gram-positive bacterium cell [3]; (b) Bacterial plasma membrane with embedded proteins [4]; (c) Cell wall structure of Gram-negative (left) and Gram-positive (right) bacteria [5]; (d) Heterogenous bacterial cell surface [6].

Extracellular structure. The extracellular structure of bacteria involves the cell envelope and surface appendages of bacteria. The cell envelope of any bacterium comprises two essential parts: the plasma membrane and the cell wall (**Fig. 1a**). The bacterial **cell wall** is a rigid polymer, known as peptidoglycan, that consists of highly cross-linked polysaccharide chains and is essential for bacteria to maintain their shape and protect them from osmotic shocks [7]. The **plasma membrane** is composed of a lipid-bilayer of 4–7 nm in thickness, which varies depending on humidity and temperature [8] (**Fig. 1b**). The lipid-bilayer is made up of two layers of phospholipid molecules. In fact, the phospholipids are amphiphilic molecules with a polar hydrophilic "head" and two non-polar hydrophobic tails. In aqueous environments, they structure themselves in such a way that they form a lipid bilayer, hence constituting the plasma membrane. Blue and brown incorporations illustrated in **Fig. 1b** represent membrane proteins. The main function of the plasma membrane is to prevent bacteria from shrinking or swelling in

response to variations in osmotic pressure caused by different fluid environments. The **bacterial capsule** illustrated in **Fig. 1a** is found among many bacteria and is usually composed of a polysaccharide layer that lies outside the cell envelope.

There are two main types of bacterial cell envelope that classify bacteria into Gram-positive and Gram-negative ones (**Fig. 1c**). The cell envelope of Gram-negative bacteria consists of a thin cell wall composed of a single layer of peptidoglycan (2-10 nm), sandwiched between two plasma membranes. The outer membrane contains lipopolysaccharides (LPS) on its outer surface and channels such as porins to facilitate membrane transport (the diffusion of molecules across a membrane with the assistance of membrane transport proteins) [5] (**Fig. 1c**, left). The cell envelope of Gram-positive bacteria consists of a single plasma membrane surrounded by a cell wall composed of a much thicker layer of peptidoglycan (30–100 nm) (**Fig. 1c**, right). The cell wall is usually complexed with teichoic acids exposed on its surface (anionic linear polymers comprising either glycerol or ribitol phosphates as indispensable components of the main chain).

The bacterial cell surface is highly heterogeneous and contains various appendages such as exposed proteins, non-fibrillar adhesins, fimbriae, pili, flagella, etc. (**Fig. 1d**) Extracellular appendages, characteristic of many bacteria, are involved in host recognition and attachment.

Fimbriae and pili are filamentous structures typically of a few nanometers in diameter, made up of fibrillin and pilin proteins, respectively, that extend from the cell surface. Francius *et al*. [9] reported pili and fimbriae total lengths of about ~10-100 µm and ~1-10 µm, respectively. While fimbriae are found in both Gram-negative and Gram-positive bacteria and are expressed by the bacterial chromosome machinery, pili are only found in Gram-negative cells and are expressed by plasmid genes. Fimbriae and pili play an important role in initial adhesion of a bacterium. Pili are often involved in the transition from reversible to irreversible bacterial adhesion. [10] The majority of pili are able to create nonspecific links with various substrates through yet unidentified mechanism.

Flagella are long (typically of 20 nm diameter), helical filaments made of flagellin proteins, that are composed of three main substructures: the motor that uses the proton motive force to generate the torque, the basal body and hook that anchor the flagellum filament to the cell membrane and transmit the motor torque and the flagellar filament. [6] Flagella enabling bacteria swimming motility play a crucial role in initial bacterial attachment. Indeed, bacteria harbouring a flagellum (or flagella) are able to swim towards a surface in response to environmental cues (chemical signals, light, temperature, oxygen,

etc.) [6], [11]. Moreover, the flagellum plays an important role in initial bacterial adhesion through anchoring on the surface and functioning as an adhesin. [12] On rough surfaces, flagella are able to reach into crevices, relatively small for a bacterium cell, and thus initiate bacterial adhesion. [13]

Reproduction. Bacteria reproduce through asexual reproduction, usually by binary fission. This process, in which a single bacterial cell, called a mother cell, produces two new identical daughter cells, involves duplication of the DNA, synthesis of new cell envelopes, separation of the two chromosomes, septum formation, and cell division.

Bacteria of interest. In this study, we have focused on one bacterium *Escherichia coli*. Historically, *E. coli* has been frequently used in microbiology because *E. coli* cells are easily cultured with simple nutritional requirements, can reproduce very fast and can be separated from their natural habitats. As early as the 1940s, its use in many foundational studies on bacterial physiology and genetics established *E. coli* as the bacterial model organism [14]. As a result, *E. coli* is the first organism which has been investigated for various aspects of life such as the genetic code, transcription, translation, and replication. Nowadays, *E. coli* is the most studied organism and apparently the most studied bacterium cell.

Escherichia coli is of interest for our research because this bacterium is frequently associated with nosocomial infections (infections acquired in hospitals) in the medical field. According the French National Institute of Health and Medical Research [15], three bacteria are the cause of half of the cases of hospital-acquired infections: *Escherichia coli* (26 %) that is commonly found in the intestines of people and warm-blooded organisms; *Staphylococcus aureus* (16 %), frequently found in the upper respiratory tract (the nose and throat mucous membranes) and on the skin of about 15 to 30 % of individuals; *Pseudomonas aeruginosa* (8.4 %) that is commonly found in soil and water and known for its ubiquity and particular dangerousness for vulnerable patients, especially those with cystic fibrosis or hospitalized in intensive care units because of lung infections caused by the bacterium. Moreover, the majority of *E. coli* strains are harmless (nonpathogenic) that enable investigations in a low Safety Level laboratory.

Escherichia coli is a Gram-negative, rod-shaped bacterium, sized of about 0.5 µm in diameter and 1-3 µm in length varying according to growth conditions. This bacterium belongs to the anaerobic heterotrophic organism class. As mentioned above, *E. coli* does reproduce very fast and is able to divide every 20 minutes in laboratory conditions (at 37 °C in a nutrient-rich medium). Its extracellular architecture involves various appendages,

such as short rigid adhesins (~10 nm long), long flexible Type 1 fimbriae and pili, and flagella located all over the cell surface. These proteinaceous organelles dispersed on the *E. coli* surface enable directional swimming motion of a bacterium and promote its adhesion onto a surface, as described above.

There are different strains of the same bacterium *Escherichia coli*, e. g. K12, O157:H7, etc. In this study, we used the DH5α *Escherichia coli* derivative, genetically engineered to produce a green fluorescent protein (GFP), very useful for fluorescence microscopy assays, as well as a protein that confers its resistance to Chloramphenicol.

1.2. Bacterial adhesion and biofilm formation

In this part we will focus on the mechanisms of bacterial adhesion, a crucial step of bacterial colonization of surfaces. It is a common knowledge that in the natural habitats bacteria prefer to reproduce on any available surface rather than in the liquid phase [16]. Bacteria naturally accumulate on a wide variety of biotic and abiotic surfaces exposed to liquid environments, where they form sessile communities, referred to as "biofilm". In 1995, Costerton *et al*. [34] defined a bacterial biofilm as "a matrix-enclosed bacterial population adherent to each other and/or to surfaces or interfaces". Bacterial biofilms are ubiquitous and can be observed on any surface in natural, industrial, and medical settings as diverse as river rocks, ship hulls, water pipes, food-processing surfaces, contact lenses, all variety of biomedical implants, etc.

The transition from a planktonic lifestyle in which bacteria float in liquid bulk as single cells to a sessile state where they function as communities occurs in a few stages, common for all bacterial species (**Fig. 1.2**):

- Bacterial transport to the surface
- Reversible adhesion
- Irreversible adhesion
- Microcolonies formation
- Biofilm maturation and detachment

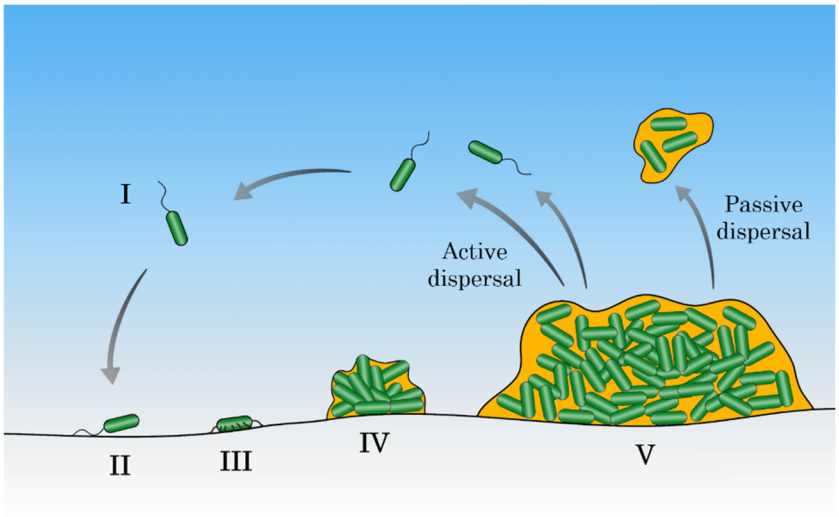

Figure 1.2. Illustration of biofilm formation mechanisms (I – transport of a planktonic bacterial cell to the surface, II – reversible adhesion, III – irreversible adhesion, IV – microcolonies formation, V – biofilm maturation and detachment).

On the transitional pathway of a single bacterium to a sessile lifestyle in communities, the bacterial adhesion is an essential, highly complex step which cannot be overlooked.

1.2.1. Bacteria transport to the surface

Free-floating in aqueous environments, bacterial cells can be brought close to the surface by passive transport such as Brownian motion, gravitational forces, transport by fluid flow, etc. Apart from passive transport, bacteria that exhibit flagellar motility are able to swim directly towards the surface. This directional swimming of a bacterium in response to environmental cues is referred to as "taxis". Bacteria can respond to chemicals, light, oxygen, temperature, etc. [18]. When this movement occurs in response to a chemical gradient, it is referred to as chemotaxis [19]. Chemotaxis is mediated through transmembrane proteins embedded in the cell membrane (so-called, methyl-accepting chemotaxis proteins MCPs). If they detect beneficial substances like carbon compounds, bacteria will go towards it, propelled by flagellum(a) rotating counterclockwise.

It is noteworthy to mention that in liquid environments, molecules present in the bulk flow (organic and inorganic) adsorb on surfaces, forming the so-called "conditioning film". The composition of conditioning films varies greatly depending on the kind of environment the surface is exposed to. Molecules/biomolecules accumulated on the surface could be of a very different nature:

- those from the surrounding medium: proteins (e.g. serum albumins, globulins, fibrinogens) and saccharides from blood [20], proteins and polysaccharides from urine [21], [22], etc.;
- those secreted by bacterial cells floating in the bulk liquid and/or readily adhered to the surface: polysaccharides, proteins, cell debris [23], [24].

Accordingly, conditioning of the surface leads to higher concentration of nutrients at the surface compared with the bulk liquid, thereby enables movement of bacteria directly towards the surface via flagellar-mediated chemotaxis.

Apart from that, conditioning films necessarily affect the physicochemical properties of surfaces, thereby altering bacterial affinity to a surface. Recently, Talluri *et al*. [24] highlighted the net effect of conditioning films on the surface hydrophilicity/hydrophobicity of photobioreactor materials. Conditioning films can also act as shielding of surface charges that consequently alter bacteria-surface interactions (reviewed in Song *et al*. [25]).

1.2.2. Reversible adhesion

Once a bacterium is in close contact with a surface (usually <1 nm) [26], *in the first instance* its fate depends on the sum of attractive and repulsive forces occurring between the bacterium and the surface. These forces typically include nonspecific interactions between the cell wall and the surface, such as electrostatic, Van der Waals, hydrophobic interactions, and steric hindrance.

In a study published in 1971, the bacterium-surface interaction was for the first time explained using the Derjaguin–Landau–Verwey–Overbeek (DLVO) theory [27]. The classical DLVO theory, commonly used to describe the stability of colloidal particles, takes into account only van der Waals and electrostatic forces (**Fig. 1.3a**). Later, van Oss *et al*. [28] adopted the extended DLVO (XDLVO) theory that takes into account both Van der Waals (F_{VdW}) and electrostatic interactions (F_{el}), as well as short-range hydrophobic interactions (F_H).

$$F_{total}^{XDLVO} = F_{VdW} + F_{el} + F_H$$

According to the DLVO theory, Van der Waals interaction between a bacterium and a surface is usually attractive, whereas electrostatic interactions between bacteria and inert surfaces are, as a general rule, repulsive, because bacterial cells and inert surfaces in aqueous solutions are negatively charged (**Fig. 1.3b**) [12], [29], [30]. Hydrophobic

interactions, for their part, can be attractive or repulsive depending on the environment, bacterium, and surface chemistries (see part 1.3.1 “Effect of surface charge and energy”).

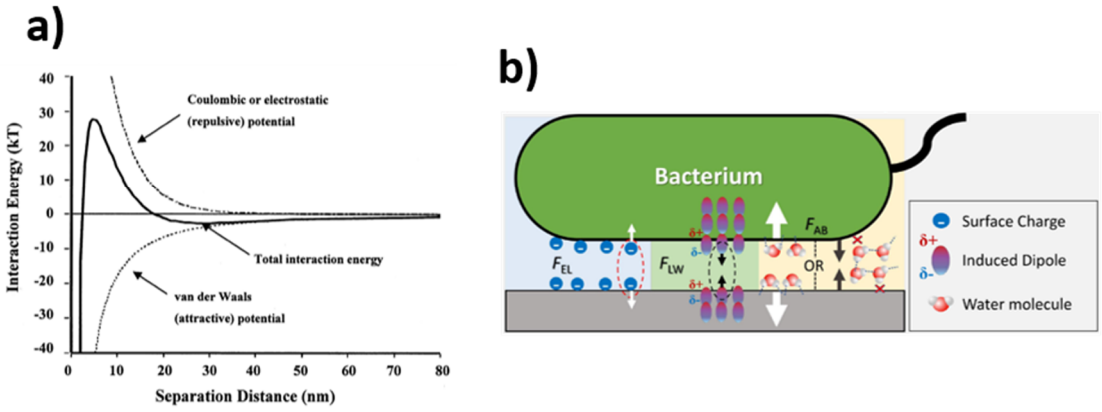

Figure 1.3. (a) Schematic illustration of the factors that influence initial bacterial attachment to a surface (electrostatic interaction F_{EL}, Van der Waals interaction F_{LW} and hydrophobic interaction F_{AB}). Reprinted from Y. Cheng *et al*., *Frontiers in Microbiology* 10, 191 (2019) [31]; (b) Schematic plot of the energy of interaction between a colloidal particle and a surface as a function of separation distance based on the classical DLVO theory. Reprinted from J. H. Adair *et al*., Surface and Colloid Chemistry, 8996-9006 (2001) [49]

However, this oversimplified theoretical approach does not take into account the heterogenous character of the bacterial cell surface. The colloidal theory used in microbiology consider a bacterium cell as a rigid spherical particle exhibiting homogeneously dispersed negative charge and completely ignores the presence of various structures exposed on a bacterium surface (non-fimbrial proteins, lipopolysaccharides, fimbriae, pili, flagella, etc.).

Bacteria typically use extracellular appendages, such as flagella or pili, to overcome repulsive barriers. Bellon-Fontaine *et al*. [33] attempted to predict the adhesion of *Leuconostoc mesenteroides* and *Streptococcus thermophilus* on various solid substrata with different thermodynamic approaches and suggested that positively charged appendages present on a bacterial cell surface facilitate adhesion by localized attractive electrostatic forces despite the thermodynamic predictions. In some bacteria, such as *Escherichia coli* and *Pseudomonas aeruginosa*, initial surface contact is mediated by flagella and pili, which leads to polar adhesion [6]. Bacteria can also use flagella to explore the local surface topography and to attach to surfaces inaccessible to the cell body [13] (see part 1.3.2 “Effect of substrate roughness and topography”).

It is noteworthy to mention that bacterial surface can adapt to changes in pH, ionic strength, osmolarity and even to the presence of other surfaces [12]. As an example, Gram-negative *Pseudomonas aeruginosa* has an ability to respond to environmental influences by modifying the relative proportion of two LPS molecules exposed on its outer surface, the first LPS molecule is electroneutral at physiological pH and hydrophobic and the second one is negatively charged at physiological pH and relatively hydrophilic [34].

In addition to the foregoing, this theory does consider a surface as perfectly smooth and homogenous, which is pretty complex to achieve in practice. Moreover, surfaces exposed to liquid are conditioned with molecules originating from the surrounding medium and from cell lysis.

1.2.3. Irreversible adhesion

After a short time (around 1 minute [35]), loosely bound bacteria involve various short-range interactions (covalent and hydrogen bonds, hydrophobic interactions) to strengthen the adhesion to the surface. This step is usually matched by repositioning of the bacterium cell on the surface. For example, *E. coli* and *P. aeruginosa* operate a transition from initial polar adhesion mentioned above to permanent adhesion by repositioning the cell body to a longitudinal position which enables stronger bonds with the surface [6].

Bacterial appendages play the vital role in irreversible adhesion and further biofilm formation. For example, pili are involved in consolidating the bonds with surfaces, spreading along surfaces and intercellular interaction. In the case of *E. coli*, type I pili are essential for initial adhesion and type IV pili facilitate the spreading along a surface via twitching motility [9], [36].

Such appendages as flagella, type IV pili act not only as adhesins but also as **mechanosensors** [37], [38]. The sensing and subsequent respond to mechanical cues by bacteria through the cell envelope or extracellular appendages when contacting a surface is referred to as **surface mechanosensing.** Using as an example a flagellum, once a bacterium is closely bound to a surface, the restriction of flagellar rotation motility triggers the synthesis of polysaccharides and, potentially, an increase in cyclic dimeric GMP (c-di-GMP) intracellular levels, which control the transition from a free-living to a sessile lifestyle. The above mentioned polysaccharides improve anchoring of bacterial cells to a surface [38], [39].

At the conclusion of the second stage, adhesion becomes irreversible in the absence of physical or chemical intervention, and the organism is attached firmly to the surface like a cocoon on a leaf [26]. Bacteria can also stick to each other forming aggregates on a surface and involving "quorum sensing (QS)," in which individual cells can sense the status quo of the surrounding microbial community and subsequently adopt strategies for metabolism and survival [31].

1.2.4. Microcolony formation and biofilm maturation

When conditions are favorable for growth, irreversibly attached cells form multicellular microcolonies, which then develop into a mature biofilm. The extracellular matrix environing bacteria in biofilms is mainly composed of water and extracellular polymeric substances (EPS) produced by bacteria: polysaccharides, DNA and proteins (reviewed in Di Martino *et al*. [39]). Bacterial cells lying deep within the biofilm have more difficult access to nutrients from the outside environment [16]. When the biofilm matures, limited nutrient availability or decreased oxygen levels can trigger the release of cells from the biofilm to the bulk liquid environment. This phenomenon is referred to as active dispersion.

Bacteria gain certain advantages from living in biofilms. They are far more resistant to environmental stresses (heat, shear stress) and antimicrobial agents. In several cases, the concentrations of antibiotics required to achieve bactericidal effect on biofilm inhabitants can be 1000 times higher than for planktonic bacteria, depending on the species-drug combination (reviewed in Costerton *et al*. [40], [41], Dunne *et al*. [26]). The resistance of biofilms to antibacterial agents may cause many issues in different application fields [16], [41].

To conclude this part, we would like to emphasize the usefulness of preventing approach consisting in inhibition of attachment rather than elimination of developed biofilm colonies far more resistant to environmental factors.

1.3. Effects of material properties on bacterial adhesion

The bacterial adhesion process is dictated by a number of factors, including cell surface properties, substrate properties, environmental conditions, etc. In this part we provide a literature review of studies investigating the influence of substrate material properties such as surface energy, charge, roughness, topography, and mechanical properties on bacterial adhesion and biofilm formation.

1.3.1. Effects of surface charge and energy

After more than four decades of studies on bacterial response to substrate surface properties, the surface energy and charge has been recognized as key surface properties that impact the bacterium–surface interaction [58–61].

a. Effects of surface energy

The surface energy of a solid is closely related to its wettability. Since every system tends to a state of minimum free energy, solid surfaces form an interface with a liquid in ways that reduce the free energy of a system. The degree of wettability varies from water-repelling or hydrophobic, usually for low-energy surfaces, to hydrophilic (high-energy surfaces) at which water wets easily a surface. The wettability of a surface can be quantified by measuring the contact angle value between a liquid droplet and the solid surface itself (**Fig. 1.4**). For a perfectly smooth and chemically homogeneous solid surface, the contact angle of a liquid θ is given by the Young-Dupre equation:

$$\cos\theta = (\gamma_{SV} - \gamma_{SL})/\gamma_{LV}$$

where, γ_{SV}, γ_{SL}, and γ_{LV} are the interfacial surface tensions of the solid – vapor, solid – liquid, and liquid – vapor interfaces, respectively.

Generally, if the water contact angle value WCA < 90° the surface is considered hydrophilic and when WCA approaches zero the surface becomes superhydrophilic. In contrast, if WCA > 90° the solid surface is hydrophobic, and it becomes superhydrophobic when WCA is greater than 150° and the droplet is rolling off.

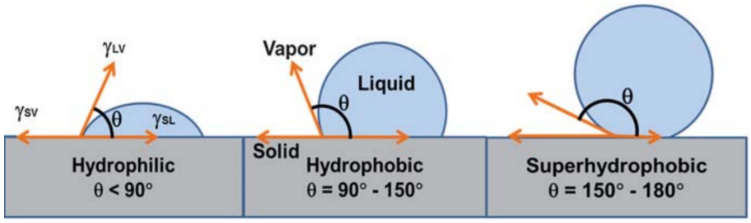

Figure 1.4. Schematic views of hydrophilic, hydrophobic and superhydrophobic surfaces. Reprinted from N. Nuraje *et al., J. Mater. Chem. A* 1, 1929–1946 (2013) [62]

Bacterial adhesion depends on both bacterial cell surface and substrate hydrophobicity/hydrophilicity. It is well known that in an aqueous medium adhesion between hydrophobic surfaces which can enter in close contact to reduce the water-surface contact area is favorable [60]. It is therefore expected that hydrophobic bacterial

cell surfaces exhibit a greater propensity for adhesion to hydrophobic surfaces than hydrophilic bacterial cell surfaces. Indeed, in a study conducted by Grivet *et al*. [63], the polished metal surfaces, which are hydrophobic, were more favorable to adhesion of the bacterial strains (*Streptococcus mutans*, *Streptococcus oralis*, and *Streptococcus sanguinis*), which are characterized by a hydrophobic cell surface.

Liu *et al*. [64] investigated the adhesion of the *E. coli* bacterium on Ni–P–PTFE coatings of various surface energies and found that the number of cells attached to the surfaces decreased with decreasing the substrate surface energy or with increasing total interaction energy. The substrates of surface energy between 21 and 26 mN m^{-1} revealed excellent antimicrobial properties. The total interaction energy was determined using the extended DLVO theory. In the calculation, the measurements of the surface energy of the substrates and *E. coli* strain were used. However, the authors highlighted an important influence of the environing liquid to the total interaction energy (pH, temperature, ionization).

Pereni *at al*. [65] tested the retention of the *P. aeruginosa* bacterium on five types of coating with various surface energies and also found a decrease of the number of adhered bacteria with decreasing substrate surface energy. The minimum level of *P. aeruginosa* cells retention was found for a surface energy ranged 20 and 27 mN/m, which is in good agreement with the study mentioned above [64].

Another study [66] reported that bacterial adhesion increases with decreasing the difference in surface free energy between the bacterium and the substrate. The maximum level of adhesion is observed when the substrate surface energy is close to the bacterium cell surface energy. The microbiological assays were performed on two model substrate surfaces, i.e., clean glass and silanized glass surfaces, using three rod-shaped Gram-negative bacteria (*Pseudomonas putida*, *Salmonella typhimurium*, *Escherichia coli*) and two Gram-positive cocci (*Staphylococcus epidermidis*, *Enterococcus faecalis*). These findings confirm the outcomes of the above-mentioned studies [63–65].

It is important to note that during the bacterial adhesion, the physicochemical surface properties of substrates can be modified by extracellular polymeric substances produced by bacteria. Indeed, several studies [40,67] showed a significative loss in hydrophobicity following surface conditioning with bacterial debris.

b. Effects of surface charge

Since most bacterial cells are negatively charged *in a neutral medium*, it is expected that they adhere preferentially to positively charged materials (attractive electrostatic forces). Indeed, a study conducted by Rose *et al*. [68] evidenced that *P. aeruginosa* cells have a greater propensity for adhesion to surfaces carrying a high number of cationic charges. Kang *et al*. [69] assessed the adhesion of *Porphyromonas gingivalis* and *Fusobacterium nucleatum* on Ca-ion-implanted and Mg-ion-implanted Ti surfaces, carrying a positive net charge, and found that the Ca- and Mg-ion implanted surfaces are more favorable to bacterial adhesion than the non-implanted surfaces. The authors also made an assumption that non-specific electrostatic force affected by positively charged ions might be the predominant factor in adhesion.

Song *et al*. [42] pertinently remarked in their review that controlling bacterial adhesion with surface charge may not work in static conditions since the dead cells can potentially represent a shield reducing the surface charge, and thereby facilitating the adhesion of bacterial cells in a next layer.

1.3.2. Effects of surface roughness and topography

a. Effects of surface roughness

Effects of surface roughness and topography on bacterial adhesion and viability have received much attention over the last two decades. There is no more doubt that once a bacterium does reach the surface, the surface topography starts to play a crucial role in bacterial attachment and biofilm maturation along with surface chemistry, charge, hydrophobicity, environmental conditions such as pH, temperature, shear flow etc. [25], [43]– [47]

For a long time, rough surfaces have been considered to be more favorable to bacterial adhesion and biofilm formation than smoother ones. The first reason was simply that an increase in surface roughness involves an increase of the contact area between the substrate surface and bacterial cells. Furthermore, smooth surfaces were believed to reveal a repellent environment to bacteria because of the presence of external hydrodynamic forces. Indeed, depressions on the roughened surfaces in which bacteria are protected from external hydrodynamic shear would provide more favorable sites for bacterial adhesion. It is therefore not surprising that in designing equipment for various applications with which hygiene risks to the consumer could occur, “hygienic surfaces”

and “smooth surfaces” were used synonymously. According to sanitary standards, surfaces with a mean roughness (S_a) value of less than 0.8 μm, defined as an average deviation of height values from the mean plane, are assumed to be hygienic [48].

For example, Taylor *et al*. [49] investigated the effect of the surface roughness of poly(methyl methacrylate) (PMMA) abraded with silicon carbide papers of different grades on the adhesion of *Pseudomonas aeruginosa* and *Staphylococcus epidermidis* and reported that bacterial cells attached preferentially to rough surfaces. In this study, an increase from 40 nm to 7.89 μm of the mean roughness (R_a) measured on a 0.8 x 0.8 mm^2 areas caused an increase in bacterial attachment with a maximum at 1.24 μm. However, a non-linear correlation between roughness and bacterial adhesion remained unexplained.

A frequently cited study in dental biofilm research was performed in 1996 by Quirynen *et al*. [50] They explored the flora on four titanium abutments of different surface roughness after 3 months of intraoral exposure and concluded that although a decrease in surface roughness S_a inhibits bacterial adhesion, there is a threshold surface roughness of 0.2 μm below which the reduction in roughness had no effect on bacterial adhesion.

Nevertheless, a growing body of literature on the bacterial response to surface patterning at the nanometer scale, when surface topographic features are much smaller than bacteria characteristic sizes reports conflicting results. More recent studies reported that bacterial adhesion can be affected by changes in nanoscale surface topography [51]–[56]. Moreover, few studies evidence that, in contrary to conventional wisdom, nanopatterned surfaces may impede bacterial adhesion, in comparison to smooth ones. Mitik-Deneva *et al*. [51], [52] showed how the adhesion of Gram-negative bacterial species to a glass surface differing in shape, size and cell surface’s hydrophobicity is affected by the nanometer scale roughness. The authors assessed the adhesion of *Escherichia coli*, *Pseudomonas aeruginosa*, and *Staphylococcus aureus* on native and chemically etched glass surfaces with corresponding root mean square roughness (R_q) of 2.8 nm and 1.6 nm (measured on 5 x 5 μm^2 scanning area). They demonstrated that although bacteria revealed different patterns of attachment, all of the species exhibited a greater propensity for adhesion to the smooth surface. Furthermore, in a subsequent study, Mitik-Deneva *et al*. [53] investigated the response of five rod-shaped Gram-negative marine bacteria to the roughness of the above-mentioned glass surfaces and confirmed their previous findings.

Similar investigations on the effect of nanometer scale roughness have been conducted by Ivanova *et al*. [54]. Using magnetron-sputtered thin titanium films of varied thickness and, consequently [54], [55], differing in nanometer scale roughness, they reported that *Staphylococcus aureus* preferred molecularly smooth TiO_2 surface (R_q, 0.2 nm) to the "nano-rough" one (R_q, 0.7 nm), whereas *Pseudomonas aeruginosa* were not affected by the nanoscale roughness. Another study [56] has also shown a decrease in bacterial adhesion and viability on nanostructured surfaces, compared to smooth ones. The authors examined the amount of viable *Staphylococcus epidermidis* on smooth and nanostructured gold surfaces with corresponding root mean square roughness of 0.9 nm and 32 nm measured on 2 x 2 μm^2 scanning area.

Thus, there are contradictory results concerning the effects of surface roughness on bacterial adhesion that do not provide an insight into the interaction between roughened surfaces and bacterial cells. The most apparent weakness of the above-mentioned studies is the limited description of surface topography based on the average roughness (R_a), average deviation of height values from the mean plane, and the root mean square roughness (R_q), root mean square deviation from the mean plane, that do not provide an insight into the spatial distribution or shape of the surface features. For instance, the two profiles with completely different surface structures as presented in **Fig. 1.5** may have identical R_a and R_q values.

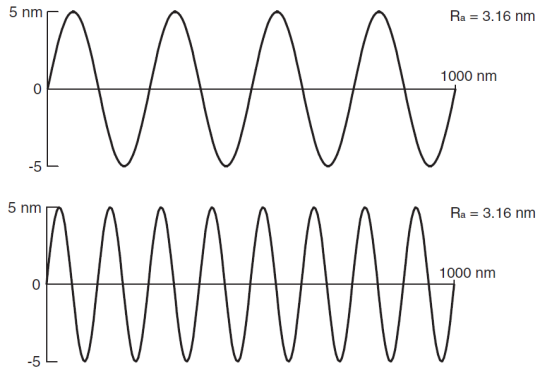

Figure 1.5. Example of two different surfaces with identical R_a values. Reprinted from R. J. Crawford *et al*., *Adv. Colloid Interface Sci.* 179–182, 142-149 (2012) [57]

However, the distribution of peaks and valleys is crucial for microbial adhesion and biofilm formation. To acquire a more detailed description of 3-dimensional surface topography, Crawford *et al*. [57] proposed a set of topographical parameters than includes:

- RMS surface roughness (root mean square deviation from the mean plane);
- Skewness S_{sk} (asymmetry of the height distribution);
- Summit density S_{ds} (number of summits per unit area on a surface);
- Developed area ratio S_{dr} (ratio of the surface area to the projected surface area);
- 10-point average roughness S_z (difference in height between the average of the five highest peaks and the five lowest valleys);
- Texture aspect ratio S_{tr} (ratio of the shortest repeating pattern to the longest repeating pattern on the surface);
- Bearing ratio t_p (ratio of the area a surface occupies in a single plane at a given height above the mean plane to the projected surface area)

Another spatial parameter that is not mentioned in this set is kurtosis S_{ku}. Surface kurtosis measures the sharpness of the surface height distribution and could be of interest to investigate bacterial adhesion depending on surface topographies.

To conclude on this point, it appears thus essential to use surfaces with defined features and chemistry to achieve a better understanding of how surface topography modulates bacterial attachment.

b. Effects of surface topography

Information in this section shall relate mainly to interaction between surface topographic features and bacterial cells. Several studies demonstrated that microtopography can significantly affect the binding energy between a surface and a bacterium, particularly when the size and shape of surface features tunes that of the bacterium.

Interesting results on the role of microtopography on spatial organization of bacterial cells have been reported by Medilanski *et al.* [58]. In this study, they investigated the response of four bacterial strains on the topography of stainless steel scratched with silicon carbide papers of different abrasive particle sizes. When the width of grooves corresponds to the width of rod-shaped bacterial cells (0.6 µm) but is less than their length (from 1.32 µm to 6.64 µm), bacteria fit in these grooves in the longitudinal orientation only (**Fig. 1.6a**). This study reported a minimum in bacterial adhesion on such a surface, compared to smooth and rougher ones, due to unfavorable interactions between the surface and bacteria oriented other than parallel to the grooves. Indeed, only a small fraction of a bacterium oriented other than parallel to the grooves gets in contact

with the solid surface. However, it is worth mentioning that adhesion of bacteria oriented parallel to the grooves of similar width is stronger than adhesion to flat surfaces, because of the increased contact area with the walls of the grooves.

Edward *et al*. [59] reported that the shape of surface topographic features is an important factor in total binding adhesion energy. Specifically, they demonstrated the strong impact of the cross-sectional shape of the groove on adhesion of a bacterium oriented parallel to the groove: "U"-shaped groove, more than "V"-shaped groove, increases the binding potential of the bacteria of the same or slightly smaller radius (**Fig. 1.6b**).

Furthermore, Whitehead *et al*. [60], [61] performed bacterial retention assays, using differently sized bacterial cells, on silicon wafer surfaces featured with pits with diameters and depths ranging from 0.2 to 2 μm and from 0.2 to 1 μm, respectively. The authors showed that the bacterial cells were preferentially retained on surface features of similar size than that of the cells.

This selective adhesion of bacterial cells was also demonstrated by Perera-Costa *et al*. [62], using three different bacterial strains, i. e., *Staphylococcus epidermidis*, *Bacillus subtilis* and *Escherichia coli*. In this study, microtopographic surface patterns were produced on polydimethylsiloxane (PDMS) surfaces by thermal imprinting using patterned silicon wafers. Results of bacterial adhesion assays carried out by the authors indicate that bacterial cells are able to differentiate upper and lower areas in spatially organized microtopographic surface patterns (**Fig. 1.6c**). This selective behavior of bacteria takes place markedly when the size and shape of the cells adjust to the dimensions of the topographical features.

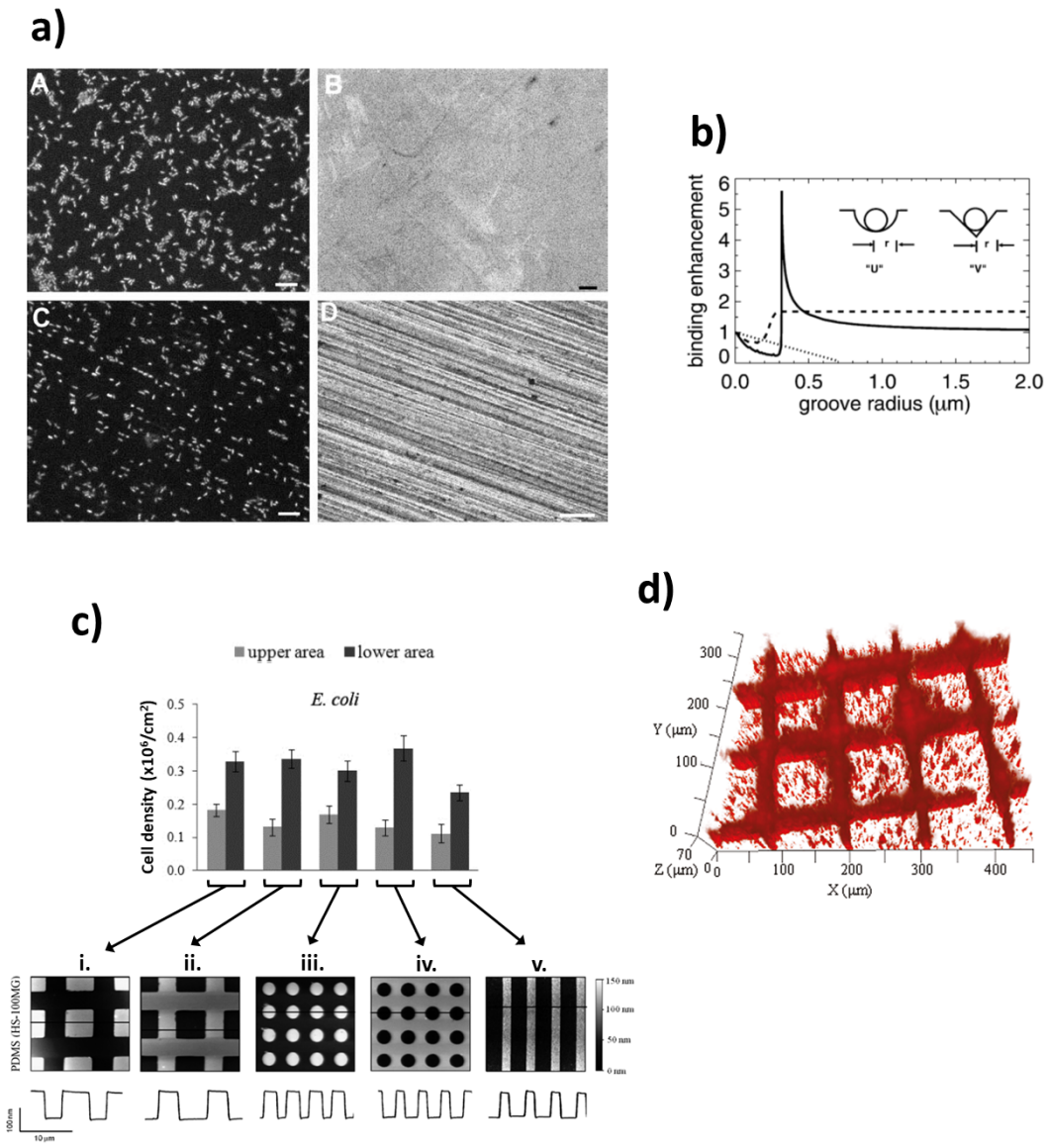

Figure 1.6. (a) Left column: epifluorescence micrographs of bacterial adhesion patterns on both smooth electropolished (A) and P1000-polished (C) steel surfaces. Right column: corresponding smooth (B) and P1000-polished (scratches of (0.7 ± 0.2) μm in width) (D) steel surfaces visualized by SEM. Scale bars 10 μm. Reprinted from E. Medilanski *et al.*, *Biofouling* 18, 3, 193-203 (2002); (b) The binding enhancement factor over a flat surface as a function of groove radius R for "U"-shaped and "V"-shaped grooves (solid and dashed, respectively). Reprinted from K. J. Edwards *et al.*, *Chemical Geology* 180, 19-32 (2001); (c) Bacterial adhesion to the upper (bright bars) and lower (dark bars) area of the featured PDMS surfaces. AFM height images (20 x 20 μm^2) of the PDMS surfaces containing topographical features of 115.6 nm in height/depth, respectively, are represented below the graph. Figure adapted from Figures 3 and 5 in Perera-Costa *et al.*, *Langmuir* 30, 4633–4641, 30 (2014); (d) Three-dimensional view of biofilm formation on a PDMS surface with 100 μm x 100 μm x 10 μm patterns and 20 μm spacing between them. Reprinted from S. Hou *et al.*, *Langmuir* 27, 6, 2686-2691 (2011).

In addition, several studies have confirmed that bacteria actively choose places to settle onto micropatterned surfaces. Perni *et al*. [63] investigated adhesion of *Escherichia coli* or *Staphylococcus epidermidis* on silicone surfaces exhibiting cones with diameters ranging from 20 to 40 µm spaced with distances of 4, 8 and 13 µm and found that bacterial cells were predominantly localized around the valley features and not on their tops. Hou *et al*. [91] assessed *Escherichia coli* biofilm formation on polydimethylsiloxane (PDMS) surfaces presenting 10 µm tall square-shape features differing in the dimension of the square patterns and in the distance between adjacent features. They revealed that preferential bacterial cells attachment and biofilm formation in the valleys between protruding features differing in their plateau dimension (top of the square features) is considerably larger than in the valleys (**Fig. 1.6d**).

c. Antibacterial surfaces inspired by nature

Superhydrophobic surfaces to reduce bacterial adhesion

Lotus leaves exhibiting excellent hydrophobicity (contact angle of over 150°) owing to their micro/nano structured surface combined with low surface energy draws scientists inspiration. The properties of the lotus leaves have been mimicked to develop antireflection and *self-cleaning* surfaces for several important applications [45], [65].

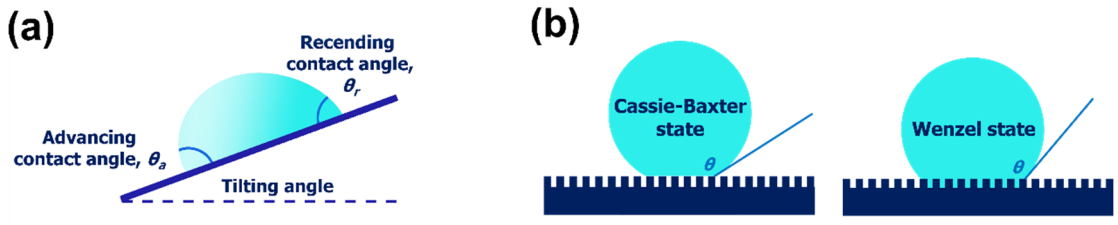

Figure 1.7. (a) Advancing and recending contact angles captured by tilting method. (b) A liquid droplet in the (left) Cassie-Baxter and (right) Wenzel wetting states on a superhydrophobic surface

Surfaces exhibiting water contact angle greater than 150° (**Fig. 1.4**), low contact angle hysteresis (difference between advancing and receding contact angles, **Fig. 1.7a**) and low tilting angle (a liquid drop rolls off the tilted surface easily) are usually referred to as superhydrophobic. The antibacterial effect of superhydrophobic surfaces is mainly due to a specific texture that favors the confinement of air cushions underneath a bouncing droplet, leading to the Cassie-Baxter's state. In the case of droplet configuration called Cassie-Baxter's state (sometimes Fakir's state) the actual liquid-solid contact area

is restricted to the summits of the textured surface (**Fig. 1.7b**). The apparent contact angle of a Cassie-Baxter droplet can be defined by the following equation:

$$\cos\theta_A = f_1 \cos\theta_1 - f_2$$

where θ_A is the apparent contact angle, f_1 is the fraction of solid material in contact with liquid, θ_1 is the contact angle of the smooth solid material and f_2 the fraction of air in contact with the liquid ($f_1 + f_2 = 1$). Therefore, a micro/nano textured surface shall enable to reduce available anchor points for bacterial attachment in the liquid medium and thus to prevent the bacterial contamination. In addition, superhydrophobicity can potentially ease the removal of bacteria due to the ultra-low contact angle hysteresis before biofilm formation on the surface takes place.

In contrast to the Cassie-Baxter state, in the Wenzel state [93], a liquid on the textured surface enters the grooves, resulting in higher surface wettability due to the increase in contact area:

$$\cos\theta_A = r \cos\theta$$

where θ_A is the apparent contact angle, θ is the fraction of solid material in contact with liquid, r is the ratio of the actual solid – liquid interface area to the projected surface area. The potential of transition from the metastable Cassie–Baxter state to the stable Wenzel state depends on the dimensions of topographic features; the thermodynamic parameters (temperature, pressure), the Laplace pressure inside a droplet (influenced by the mass of the droplet, surface feature geometries), the solid – liquid interface energy, etc. [94–96]

A thorough review on recent developments of superhydrophobic surfaces to prevent bacterial adhesion was performed by Zhang *et al*. [45]. The authors studied the most interesting research outcomes on this topic and found conflicting results among them. On the one hand, superhydrophobic surfaces with a Cassie-Baxter wetting mechanism (contact angle of over 160° and low tilt angle) have been shown to reduce bacterial adhesion compared to flat surfaces of the same material [66], [67]. For example, the decrease in bacterial adhesion has been observed in the case of the superhydrophobic silicone elastomer prepared *via* aerosol assisted deposition (AACVD) [66] and the superhydrophobic xerogel coating obtained from fluorinated silica colloids [67]. Recently, Hizal *et al*. [68] reported that *Staphylococcus aureus* and *Pseudomonas aeruginosa* adhesion is considerably reduced on nanopillared aluminum surfaces prepared by anodizing and post-etching processes further made hydrophobic by applying a Teflon coating (water contact angle $\theta_W = 162°$) (**Fig. 1.8a**). This preventive effect of the

superhydrophobic surface has been especially pronounced under flow conditions (average flow velocity of 1.33 cm/s).

On the other hand, several studies have shown that when the incubation time of bacteria goes beyond a few hours, bacteria are able to successfully colonize superhydrophobic surfaces. In a study conducted by Fadeeva *et al*. [69], *Staphylococcus aureus* cells exhibited the same adhesion on the laser ablated superhydrophobic titanium surfaces with contact angle of (166 ± 4)° after 18 hours than on the smooth Ti surface, whereas *Pseudomonas aeruginosa* cells did not attach to the structured surface (**Fig. 1.8b**). Sousa *et al*. [70] reported that both *Staphylococcus aureus* and *Pseudomonas aeruginosa* colonized the superhydrophobic poly(L-lactic acid) (PLLA) surface after 24 hours of incubation (water contact angle $\theta_W = 154°$) (**Fig. 1.8c**). Moreover, *P. aeruginosa* produced an extracellular matrix on the tested surface, indicating that this strain was able to form a biofilm on such a substratum.

A fascinating research study conducted by Friedlander *et al*. [71] has provided an understanding of bacterial response to substrates with regular surface topography as well as of the role of flagella in attachment. In this investigation, bacterial assays were performed on polydimethylsiloxane (PDMS) surfaces patterned with hexagonal features of 2.7 μm in height and 3 μm in diameter, separated by 440-nm trenches. Hence, the trenches width was smaller than the diameter of the investigated *Escherichia coli* strains (0.6 ± 0.1 μm). At the earliest incubation time point (2 h), both the wild-type *E. coli* and the *E. coli* mutant lacking flagella showed a preference for the smooth substrate. However, after 24 hours, a drastic increase in surface coverage by the wild-type *E. coli* cells was observed on the structured surface, in comparison to the smooth one. In addition, they observed the presence of a dense, fibrous network surrounding the adhered cells predominantly composed of flagellar filaments (**Fig. 1.8d**). In fact, during the attachment, bacterium flagella were able to insert between the surface features and attach within the submicron trenches. This behavior was accompanied by a Cassie–Baxter to a Wenzel wetting transition likely due to surface conditioning by bacteria resulting in complete wetting of the structured substrates. These results indicate that bacterial adhesion to patterned surfaces is far more nuanced than anticipated by simplistic models that consider bacteria as rigid rods or spheres and ignore the presence of extracellular appendages. As has been highlighted by the authors, flagella are involved in attachment and can enable bacteria to overcome unfavorable surface topographies.

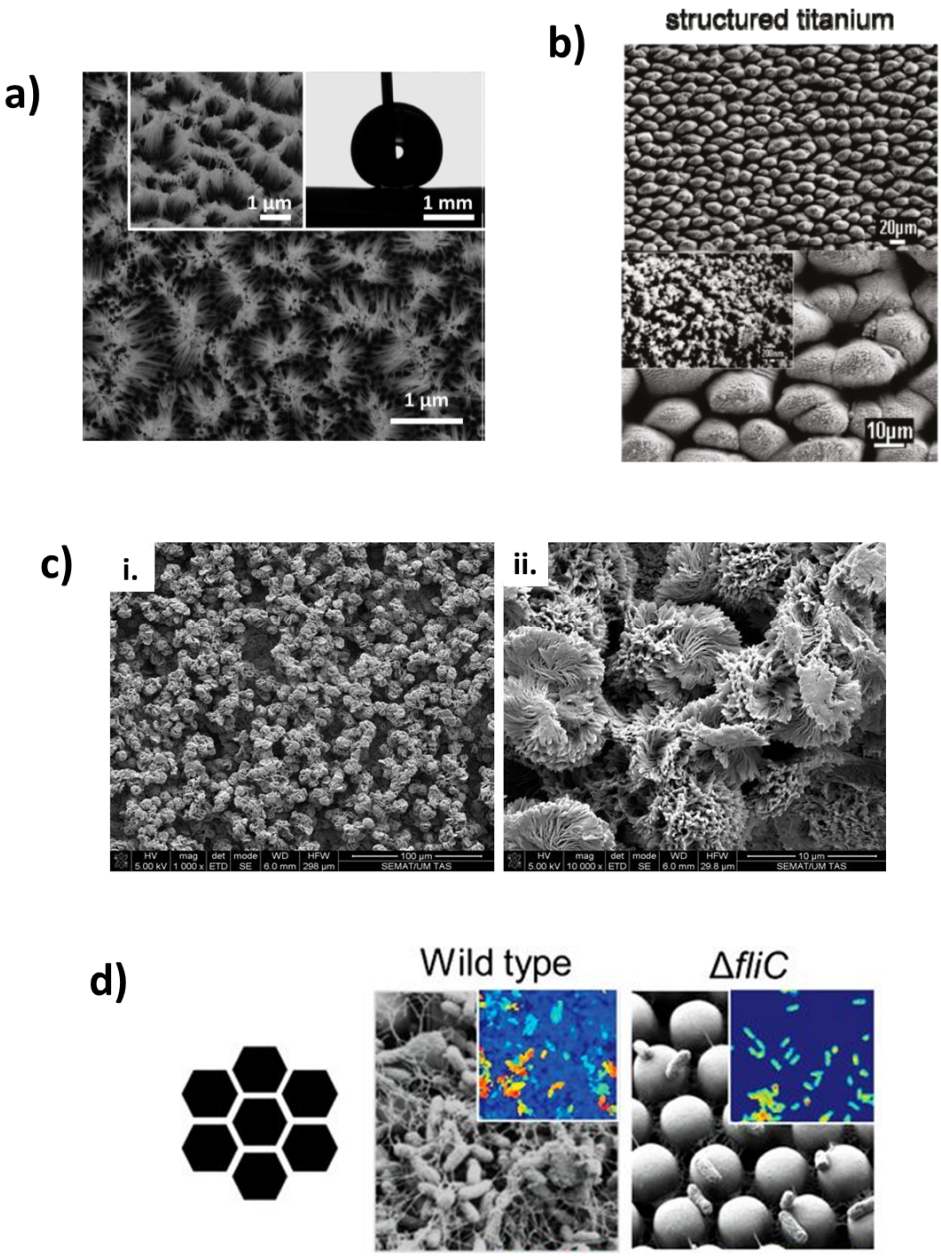

Figure 1.8. (a) SEM micrographs of Teflon-coated superhydrophobic nanopillared aluminum layer on aluminum substrate (contact angle $\theta_W = 162°$). Reprinted from F. Hizal *et al.*, *ACS Appl. Mater. Interfaces* 9, 12118-12129 (2017); (b) High-resolution SEM images of the structured titanium surface produced by femtosecond laser ablation (contact angle $\theta_W = 166°$). Reprinted from E. Fadeeva *et al.*, *Langmuir* 27, 3012-3019 (2011); (c) SEM images of the rough superhydrophobic PLLA surface. Scale bars 100 µm (i) and 10 µm (ii), respectively. Figure adapted from Figure 3 in C. Sousa *et al*. *AMB Expr* 1, n° 34 (2011); (d) Schematic top view of PDMS surfaces patterned with hexagonal features and SEM images of wild type and *ΔfliC E. coli* cells grown for 24 hours on the featured PDMS substrate. Reprinted from R. S. Friedlander *et al*., *Proceedings of the National Academy of Sciences* 110, 14, 5624-5629 (2013).

Notwithstanding a lack of consensus in these researches, there is a potential for using a superhydrophobic surface to reduce the initial bacterial adhesion, especially at early stages of incubation.

Bactericidal activity as an intrinsic property of nanostructured materials

Another approach to develop antibacterial surfaces draws its inspiration from insect wings which are able to remain clean by continuous cleansing through bactericidal action, rather than repelling bacterial cells. Ivanova *et al*. [103] discovered that cicada wings with nanopillar patterned surfaces can effectively kill adherent bacterial cells, such as Gram-negative *Branhamella catarrhalis*, *Escherichia coli* and *Pseudomonas fluorescens*, owing to their particular surface architecture.

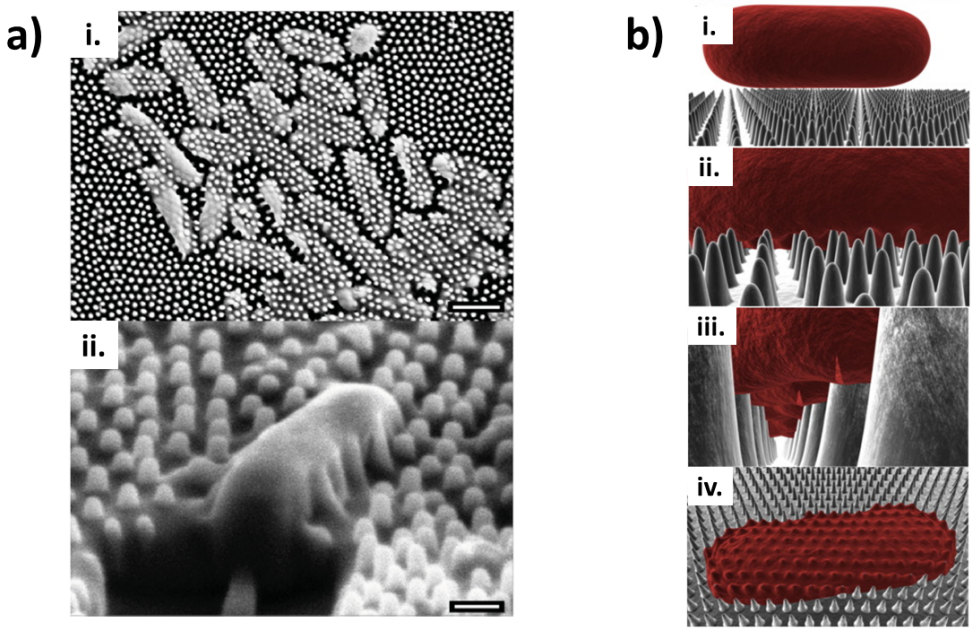

Figure 1.9. (a) *Pseudomonas aeruginosa* cells on the surface of a cicada wing. Cells are clearly penetrated by the nanopillar structures on the wing surface. Scale bar 1 μm. Reprinted from E. P. Ivanova *et al.*, *Small* 8, 16, 2489-2494 (2012); (b) Biophysical model of the interactions between cicada wing nanopillars and bacterial cells: A bacterial cell comes into contact (i) and adsorbs onto the nanopillars (ii), the outer layer begins to rupture in the regions between the pillars (iii) and collapses onto the surface (iv). Reprinted from S. Pogodin *et al.*, *Biophysical Journal* 104, 4, 835-840 (2013) [104].

In a follow up study [105], they discovered that dragonfly wings possessing nanopillars similar to those of cicada wings but of a random size, shape, and spatial distribution were able to kill not only bacterial cells such as Gram-negative *Pseudomonas*

aeruginosa, Gram-positive *Staphylococcus aureus* and *Bacillus subtilis*, but also *B. subtilis* spores. Subsequently, they produced nanopillar-patterned surfaces of black silicon by reactive ion etching, mimicking the topography of the dragonfly wings. The so prepared black silicon surfaces exhibiting nanopillars of 20 to 80 nm in diameter and of 500 nm in height with the spacing between them ranging from 200 to 1800 nm were found to kill *P. aeruginosa*, *S. aureus*, *B. subtilis* bacterial cells and *B. subtilis* spores with a high efficiency.

A systematic review performed by Modaresifar *et al*. [75]. studied the most relevant papers available on antibacterial effects of surfaces exhibiting high aspect ratio nanofeatures in the absence of bactericidal agents. Only a half of the papers provided a comprehensive discussion or presented a hypothesis on the killing mechanism of the nanopatterns. Most researchers agree on the role of mechanical deformation in general and on the rupture of the bacterial cell membrane on contact due to high local deformations and penetration of high aspect ratio nanofeatures.

However, it is still challenging to create nanofeatured surfaces on 3D-shaped devices effective in killing bacteria since the current patterning techniques are mostly only applicable to flat surfaces.

1.3.3. Effects of substrate mechanical properties

The cellular response to mechanical properties of substrates has been widely studied, but almost exclusively in mammalian cells [76]– [78]. Regarding bacterial cells, the effect of substrate stiffness is the least explored and only modest results are reported in the literature.

A pioneering study on bacterial response to the substrate stiffness was performed by Lichter *et al*. [79] They reported the positive correlation between the adhesion of *Staphylococcus epidermis* and the Young's modulus of polyelectrolyte multilayer ranging between 1 and 100 MPa. Furthermore, Kolewe *et al*. [80], [81] found a positive correlation between the adhesion of *Escherichia coli* and the Young's modulus of polyethylene glycol dimethacrylate (PEGDMA) ranging from 44.05 to 6489 kPa.

However, Saha *et al*. [82] reported the inverse correlation between the growth of *Escherichia coli* and the stiffness of photocross-linkable polyelectrolyte films. To investigate the influence of stiffness on bacterial growth, they used cross-linked (stiff, 150 kPa Young's modulus) and uncross-linked (soft, 30 kPa Young's modulus) polyelectrolyte films. Another strain *Lactococcus lactis* did not show any preference for stiffness.

In 2014 Song *et al.* [83] investigated the bacterial response to polydimethylsiloxane (PDMS) stiffness. PDMS samples with Young's modulus ranging from 0.1 to 2.6 MPa were prepared by adjusting the degree of cross-linking (the cross-linker concentration). The researchers found that initial adhesion and biofilm formation of Gram-negative *Escherichia Coli* and *Pseudomonas aeruginosa* strains were inversely correlated to the substrate stiffness, in contrast to previous studies (**Fig. 1.10a**). They suggested that this difference is due to the fact that the previous results [80]– [82] were obtianed on hydrophilic surfaces, whereas the PDMS surfaces used in this study are hydrophobic. The bacterial strains and Young's modulus ranges are also different.

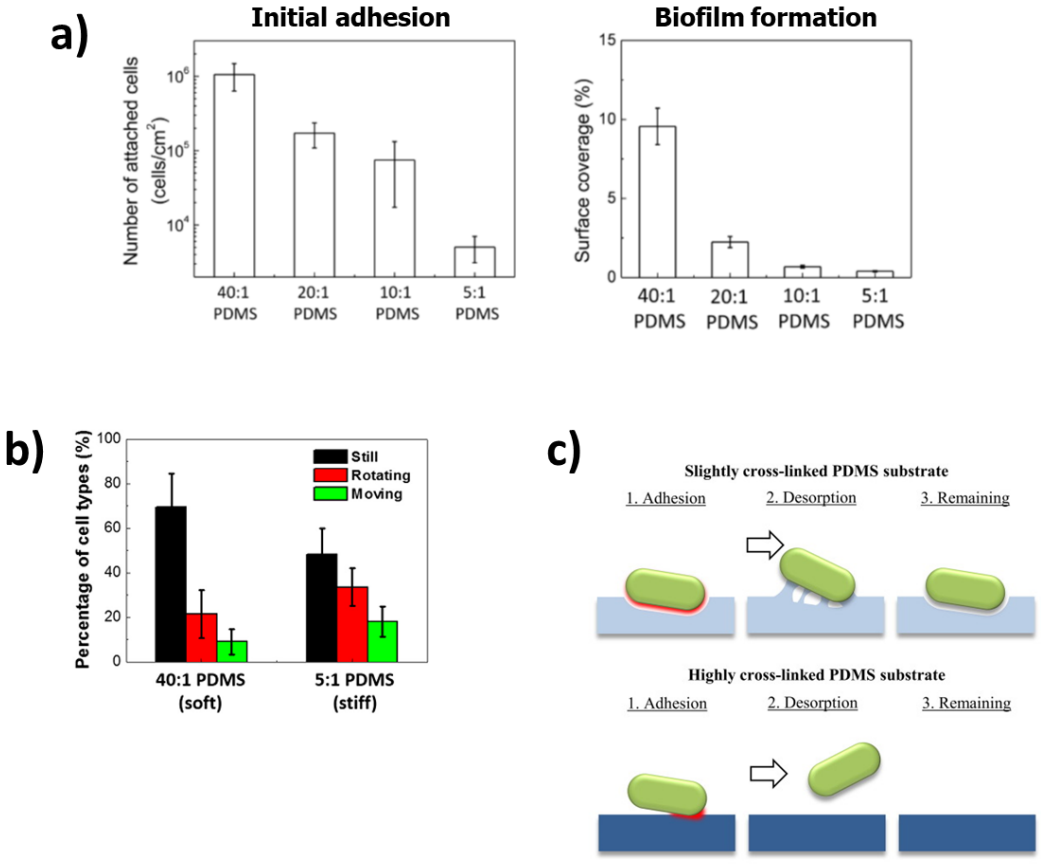

Figure 1.10. (a) Effect of PDMS stiffness on the attachment of *E. coli* cells (left) and on the growth of attached *E. coli* cells (right). Reprinted from F. Song et D. Ren, *Langmuir* 30, 34, 10354-10362 (2014); (b) Effect of material stiffness on the motility of attached *E. coli* cells. Reprinted from F. Song *et al.*, *ACS Applied Materials & Interfaces* 9, 27, 22176-22184 (2017); (c) Hypothetical model of the interaction between *E. coli* bacterium and different viscoelastic properties of PDMS substrates (1) before, (2) during and (3) after shear stress. Reprinted from J. D. P. Valentin *et al.*, *Journal of Colloid and Interface Science* 552, 247-257 (2019).

In a subsequent study, Song *et al*. [84] aimed at the understanding of the mechanisms by which bacteria sense mechanical properties of a surface. By comparing the movement of *Escherichia coli* cells attached on PDMS surfaces of varying stiffness, the bacteria attached on the stiff PDMS surface were found to be more motile than those on the soft ones (**Fig. 1.10b**). The authors made the assumption that during initial attachment *E. coli* can use extracellular appendages to sense the surface stiffness. If attachment is favorable (soft PDMS surfaces), the cells will reduce motility and start biofilm growth, otherwise, the cells will move more before settling or even leave the surface, as observed on stiff PDMS surfaces. In order to investigate the role of *Escherichia coli* flagellar motility on bacterial response to PDMS stiffness, they used its isogenic mutant with deletion of the *motB* gene required for the rotation of the flagellar. The nonmotile *ΔmotB* mutant exhibited defects in response to PDMS stiffness. They concluded that the *MotB* gene may not be an indispensable sensor of the surface stiffness but does facilitate mechanosensing.

In a following article published in 2019, Song *et al*. [85] reported that wild-type *Pseudomonas aeruginosa* cells adhered on the soft PDMS surface exhibited higher level of the intracellular cellular messenger, cyclic diguanylate monophosphate (c-di-GMP), which controls the switch from planktonic growth to biofilm formation, compared to those on the stiff PDMS surface. Additionally, *P. aeruginosa* mutants with inactivated *oprF* gene that have much higher level of intracellular c-di-GMP than the wild-type strain, exhibited defects in response to PDMS stiffness.

Straub at al. [86] also found a decrease in number of *P. aeruginosa* and *E. coli* cells attached on PDMS surfaces of increasing Young's modulus from 0.06 to 4.52 MPa. They wondered whether the observed adhesion behaviour of bacteria is caused by nonspecific physicochemical interactions, such as van der Waals, electrostatic, hydrophobic interactions, or by bacteria-specific mechanisms, such as specific interactions and surface mechanosensing of bacteria. To determine the main factor responsible for the bacterial preference to adhere to soft PDMS surfaces, they assessed the adhesion of abiotic carboxylated polystyrene (PS-COOH) microbeads (1 μm diameter) on the PDMS surfaces of varying stiffness. PS-COOH microbeads exhibited a similar adhesion pattern than *E. coli* and *P. aeruginosa*. Consequently, the researchers arrived at the conclusion that the initial stage of bacterial adhesion refers more to nonspecific physicochemical interactions, rather than to bacteria-specific interactions and surface mechanosensing.

Valentin *et al*. [87] have investigated the bacterial response on mechanical properties of a material from a different angle. The researchers correlated substrate viscosity and adhesion of *Escherichia coli* cells. PDMS samples used in this study belong to viscoelastic materials and exhibit both viscous and elastic characteristics. The mechanical properties of PDMS can vary from a viscous gel to an elastomer by adjusting the cross-linker concentration. They have proven that decreasing the cross-linker concentration leads to an increase in viscosity and stickiness of PDMS. *E. coli* cells were found to adhere preferentially on soft (more viscous) PDMS than on stiff (less viscous) one. Moreover, bacteria exhibited a stronger retention under fluid flow conditions on soft PDMS. These results are in good agreement with previous studies reported above. The authors made two potential hypotheses explaining the interaction between *E. coli* cells and the viscoelastic PDMS. First, highly deformable soft PDMS enables larger contact surface area between a bacterium and a substrate surface. Another hypothesis states that bacteria exhibited better retention under shear stress on the soft PDMS because the adhesion energy required to detach an object from the soft PDMS is much higher than that from the stiff one (**Fig. 1.10c**).

A study reported by Pan *et al*. [119] also found a decrease in number *E. coli* cells attached on PDMS surfaces of increasing Young's modulus from 0.06 to 4.52 MPa. They did show that *E. coli* fails to respond to the stiffness of PDMS substrates coated with a 2 nm highly cross-linked PDMS used to confer comparable surface chemistry to materials of differing stiffness. The authors suggested that uncoated PDMS of low Young's modulus contains free polymer chains and longer chain ends at the surface, leading to higher bacterial adhesion. In that case, PDMS chain ends and free PDMS chains can contribute to the nonspecific bacterial adhesion on the PDMS surfaces.

Arias *et al*. [120] systematically tuned the substrate topography and stiffness while keeping the surface free energy of PDMS substrates constant. The authors indeed used low energy singly charged inert ions to irradiate PDMS to achieve substrates of variable stiffness but exhibiting comparable surface free energy. However, this process resulted in the formation of a wavy (wrinkled) topography at the PDMS surface. The changing topography could limit bacterial surface attachment even in very compliant PDMS (Young's moduli of 0.02 and 0.2 MPa).

Collectively, above mentioned results indicate that the substrate stiffness is able to affect the behavior of bacterial cells. However, mechanisms by which bacteria sense the mechanical properties of a surface are still poorly understood. Understanding of the

complex interaction between a bacterium and a surface stiffness is nowadays an exciting challenge for scientists. The challenge is compounded by the need to control all the numerous factors that could undesirably influence the bacterial behavior, such as surface chemistry, charge, hydrophobicity, surface topography, environmental conditions etc.

2. Silicone elastomers

Silicones (or polysiloxanes) belonging to synthetic polymers are different from any of other polymers because of the presence of silicon atoms and Si-O bonds. They always includes a principal silicon-oxygen chain (the siloxane backbone) and an organic moiety bound to the silicon. The organic groups may be methyl, vinyl, phenyl, or other groups. The properties of silicones vary greatly depending on organic groups and a chemical structure, thereby providing a wide range of materials varying from liquid to hard plastics. The silicone materials can be classified according to their consistency as silicone fluids, silicone resins, and silicone elastomers.

In this part, we focus on silicone elastomers, used as substrates for further microbiological studies. These materials are of particular interest because, first of all , they are widely used in various biomedical applications [121,122], and secondly, they enable to rule out the role of hydration and surface charges on bacterial adhesion.

Elastomers are defined by their large deformability with essentially complete recoverability. In order to exhibit this type of elasticity, a material must meet three molecular requirements [123]:

- the material must consist of polymeric chains,
- the chains must have a high degree of flexibility and mobility,
- the chains must be joined into a network structure.

2.1. Poly(dimethylsiloxane) (PDMS) chain

Silicone elastomers are mainly composed of poly(dimethylsiloxane) PDMS chains characterized by a siloxane backbone and methyl side groups. **Fig. 1.11** displays a dimethylsiloxane unit $-[Si(CH_3)_2 - O]-$ with two methyl groups bound to a silicon atom.

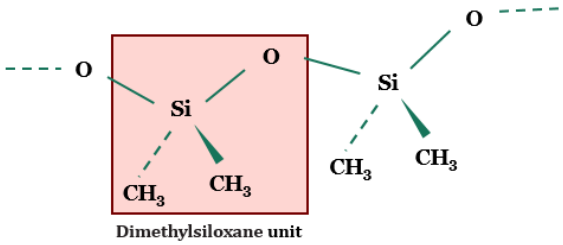

Figure 1.11. Dimethylsiloxane unit

The Si-O and Si-C bonds in the chain have an exceptionally high energy of 535 kJ/mol and 370 kJ/mol, respectively [124]. For comparison, C-C bonds have a bond energy of 305 kJ/mol. The strong Si-O bond provides to silicone elastomers an excellent thermal stability. In general, they can be heated in air to a temperature of about 200°C without major changes in their physicochemical properties.

Furthermore, the siloxane chain mobility and flexibility are very high. These properties are caused by the large Si-O-Si bond angle and the relatively high Si-O bond length (1.63 Å). The Si-O-Si, O-Si-O, and C-Si-C bond angles equal to142.5°, 109°, and 106°, respectively.[125] The enlarged Si-O-Si bond angle enables free rotation about the Si-O bond. Moreover, the organic moieties occupy a large effective volume, thus making the close packing of polymer chains impossible [126]. As a result, interactions between chains are reduced. The flexibility of PDMS can be expressed in terms of a low Glass transition temperature (about –125 °C for PDMS, compared to –64 °C the analogue hydrocarbon).

Another characteristic feature of PDMS is a low surface tension (about 21 mN/m), owing to hydrophobic organic moieties encasing the siloxane backbone. Nevertheless, polar Si-O bonds can interact with each other by dipole-dipole type interactions. The combination of polar Si-O bonds and non-polar organic side moieties provides a certain ambivalence to the siloxane chain, that is, siloxane chains exhibit both hydrophilic and hydrophobic character. Siloxane chains reorganize themselves so that Si-O bonds interact with a polar surface (for example, glass) through dipole-dipole type interactions, thereby reorienting their side organic groups away from the surface (**Fig. 1.12**). As a result, the tightly fixed siloxane chains make the covered surface highly apolar. PDMS can therefore be both water repellent and capable of wetting most surfaces (used as mold-release agent, anti-adherents for polar adhesives, etc.)

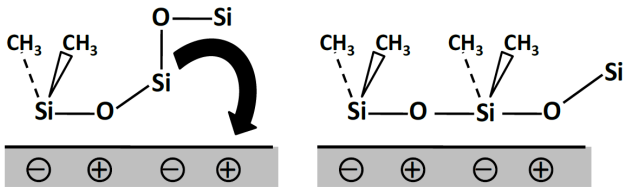

Figure 1.12. Dipole-dipole type interactions between a PDMS chain and a polar surface. Reprinted from F. Angot, Pierre and Marie Curie University - Paris VI (2016) [127]

2.2. Synthesis of the silicone elastomer matrix

An ideal elastomer network is based on irreversible covalent bonds between polymer chains such that elastic behavior is not transient in the presence of large strains or increased temperatures (thermoset elastomer). To form the silicone elastomer network consisting of covalently bound PDMS chains, there exist different cross-linking pathways [128]:

- Cross-linking with radicals
- Cross-linking by condensation
- Cross-linking by hydrosilylation

Cross-linking with radicals. Efficient cross-linking with radicals is only achieved in the presence of vinyl groups on the polymer chains [129]. The peroxide is added before processing as catalyst, and the peroxide's volatile residues are released as by-products of the reaction. Silicone rubbers processed through radical cross-linking reaction are often associated with the high temperature vulcanizing (HTV) silicone rubbers, since this reaction requires elevated temperatures.

Cross-linking by condensation. Silicone rubbers processed through this type of reaction are available as one-part and two-part systems. Cross-linking reaction for one-part system requires specific moisture conditions, releasing acetic acid as a by-product of this reaction. For the two-part system, organotin carboxylates are usually used as catalyst [130]. Alcohol is released as a by-product of the reaction, leading to slight shrinkage upon cross-linking (this reaction is also known as "alcoholysis"). The cross-linking by condensation is usually associated with the room temperature vulcanizing (RTV) silicone rubbers.

Hydrosilylation reaction. Silicone elastomers that cross-link by hydrosilylation reaction are generally available as two-part formulations. The part A (also referred to as "base") usually contains functional polymers – vinyl-termined PDMS – and a platinum (Pt)

catalyst. The part B (also known as "cross-linker") contains functional oligomers carrying Si-H groups used as cross-linking sites and some functional polymer in order to dilute the cross-linker prior to mixing the two A and B parts. Dilution is necessary since even a small drop of pure cross-linker added into the base can lead to immediate local cross-linking, resulting in dramatically inhomogeneous structures [131].

There exists a wide range of Pt catalysts and they differ in their reaction speeds and in which concentrations they are formulated. The Pt–divinyltetramethyldisiloxane complex, also known as Karstedt catalyst [132] is the most used in industrial applications to produce cross-linked polymers via hydrosilylation reaction (**Fig. 1.13**) [133]. Depending on the curing temperature and desired curing time, usually 10–30 ppm of Pt in the final elastomer formulation is used [131].

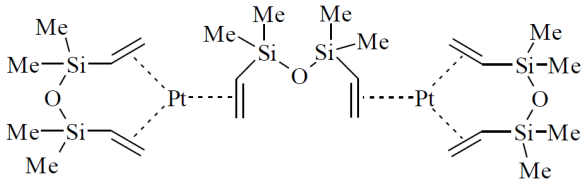

Figure 1.13. Karstedt catalyst

The formulation of the silicone elastomer network by hydrosilylation reaction is illustrated in **Fig. 1.14a**. PDMS chains cross-link through Pt-catalyzed reaction: the catalyst breaks the double bond of the vinyl group and then bonds to a Si-H bond of another chain, thereby forming the regular three-dimensional molecular network. Since Si-H groups at the chain ends are more reactive than those within the polymer chain of the cross-linker, the polymerization reaction takes place preferentially at the chain ends [134]. (**Fig. 1.14a**).

Fig. 1.14b illustrates a cross-linked PDMS network with the average length between cross-links, also known as mesh size ξ, on the order of 10 nm. A few physical chain entanglements and network defects such as freely dangling chains, i.e., chains linked only by one end to the network, and uncross-linked, free chains are also shown in the illustration.

The cross-link density is usually controlled by the molecular weight of the starting materials and the molar ratio of vinyl to hydride groups. Imbalanced stoichiometry (molar ratio of vinyl to hydride groups), which can be caused by side reactions and/or steric effects results in network defects: dangling chains, sol fraction (uncross-linked chains), loops, i.e., polymers reacting at both ends with the same cross-linker [131]. When the

formulation parts of the silicone elastomer are mixed in a non-stoichiometric ratio, it can lead to decrease in the effective number of elastic chains by increasing network defects.

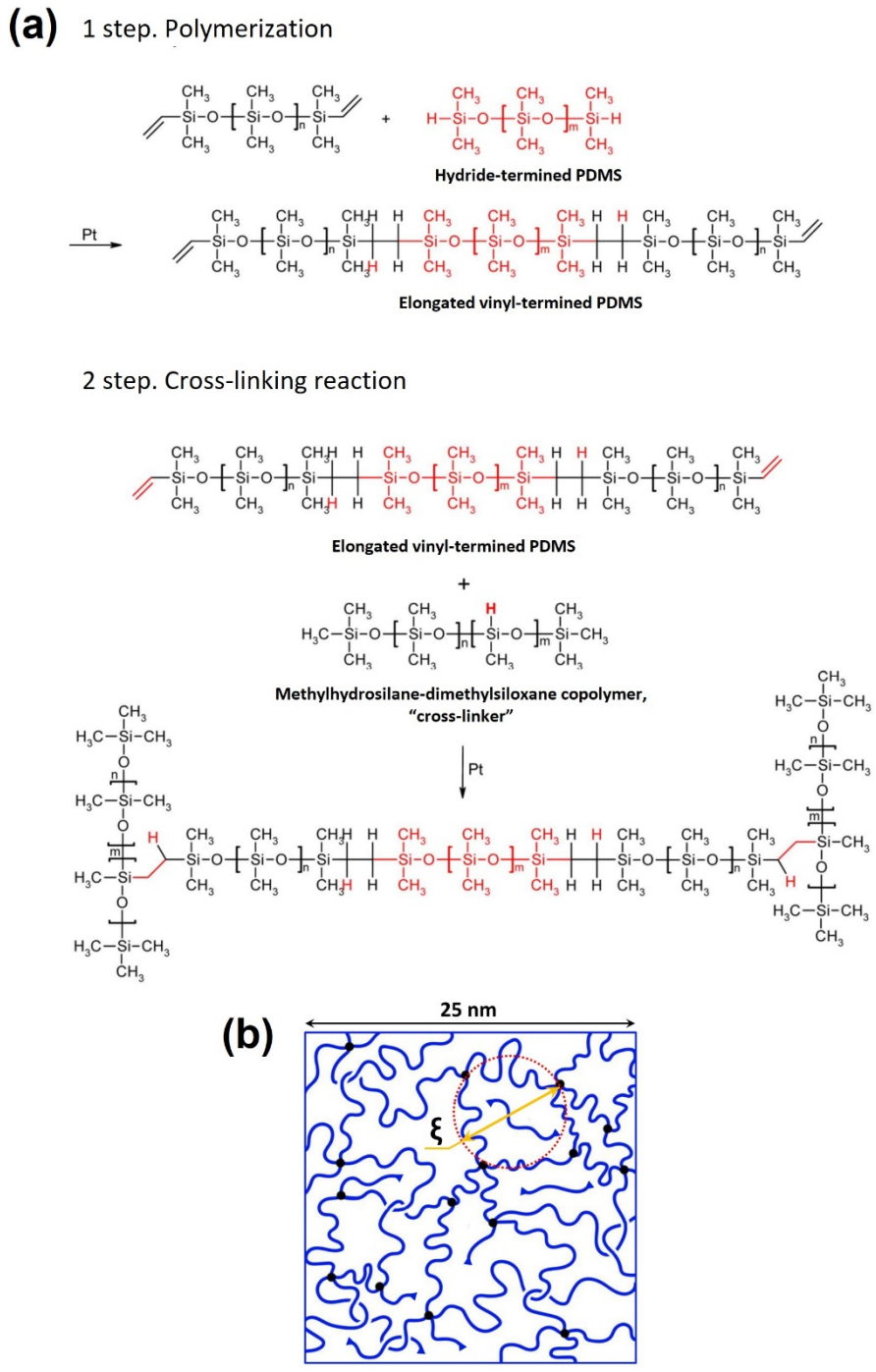

Figure 1.14. (a) Scheme of cross-linking of the silicone elastomer network by hydrosilylation reaction Reprinted from M. Mayer *et al.*, *PLoS ONE* 8, 10 (2013) [134]; (b) Illustration of a cross-linked PDMS structure with the average length between cross-links, ξ, on the order of 10 nm. Black dots represent chemical cross-links. Dangling chains and free chains are also shown. Reprinted from V. Drebezghova *et al.*, *Macromol. Chem. Phys*. 221, 17, 2000170 (2020) [135].

Pt-catalyzed hydrosilylation is the most common reaction for the formulation of thermoset silicones used for biomedical applications, primarily because hydrosilylation reaction implies that no volatile byproducts are formed during processing of elastomers [129]. Furthermore, molded pieces made with silicone using this cross-linking pathways are very accurate (no shrinkage upon curing).

In this dissertation, we address to two-part silicone elastomer systems, cross-linking via Pt-catalyzed hydrosilylation reaction. The first silicone elastomer system, referred to as liquid silicone rubber (LSR), consists of A and B parts made up of the same base – vinyl-termined PDMS and silica – that are supposed to be mixed in 1:1 ratio (stoichiometric ratio). Part A contains the platinum catalyst (mostly often Karstedt catalyst [133]) and part B contains an inhibitor preventing premature cross-linking of the polymer at ambient temperature and of the silane groups used as cross-linking agents. Commonly used inhibitors include electron-deficient alkenyl molecules, such as dimethyl maleate, dimethyl fumarate, etc. According to Delebecq *et al*. [137] the catalyst is inhibited by segregation in a phase in which the catalyst is solvated by the inhibitor. Cross-linking reaction is initiated when the temperature exceeds the boiling point of the inhibitor phase; once the inhibitor is volatilized, an elastomer network is formed. Therefore, LSRs are often mentioned as HTV rubbers.

The name "*liquid* silicone rubbers" is related to low viscosity of formulations prior to cross-linking, which can be easily injected into a mold cavity to manufacture a rubber piece. When compared to high consistency rubbers (HCRs), LSRs exhibit a low viscosity ranging between 35 and 2000 *Pa s* for our case, which is considerably lower than HCRs. The stiffness of the majority of commercial LSR grades ranged between 1 and 90 Shore A [138,139], is adjusted by varying cross-link density, silica filler content, and side groups.

The second silicone elastomer system that we used in this study is the commercial PDMS grade Sylgard 184, mentioned as RTV&HTV silicone rubbers by manufacturer, i.e., it can be cured both at elevated temperatures and under ambient conditions. As mentioned above in this section, the part A (base) contains functional vinyl-termined PDMS, the Pt catalyst (about 6.5 ppt according to Flowers *et al*. [140]), and some silica filler. The part B (cross-linker) contains functional oligomers carrying Si-H groups, some functional polymer to dilute the cross-linker, and a minor silica content. Parts A and B are supposed to be mixed in 10:1 ratio (stoichiometric ratio) prior to cross-linking. The stiffness of PDMS was adjusted by varying base: cross-linking ratio, i.e., the cross-link density. The PDMS grade Sylgard 184 was used as a model elastomer, whose composition

is known, and whose surface characteristics are relatively well investigated and can be perfectly controlled. The composition of Sylgard 184 is reported in **Annex IV** (see **Table S1**).

Reinforcing silica filler. Commercial grades generally contain 20–30 wt.% silica filler. The amorphous silica particles on the order of 10 nm in diameter[129] are added to the premix prior to cross-linking in order to reinforce the PDMS network and, consequently, improve mechanical properties of silicone elastomers. The hydroxyl groups (–OH) present on the surface of silica particles provide them specific chemical properties. The silanol groups (–Si–OH) cause specific interactions between the silica surface and PDMS chains. Taking into account the amphiphilic character of PDMS chains, they can enter in dipole-dipole interactions with the polar surface of silica filler introduced in the PDMS matrix. If these physical interactions are strong, the viscosity of the PDMS-silica blend will dramatically increase owing to the interaction nodes, strengthening cohesion within the material. To remedy this issue, manufacturers reduce the PDMS – silica interactions by modifying the surface of silica filler (e.g., hexamethyldisilane (HDMS)-modified silica, vinyl-modified silica [141])

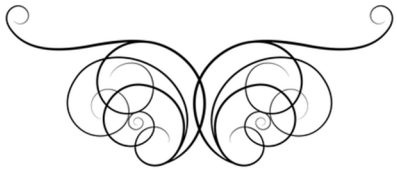

Chapter II

Bulk properties of liquid silicone rubbers (LSRs)

1. Introduction

To investigate the effects of either stiffness or topography on the initial retention of the *E. coli* bacterium, all the parameters which can alter bacterial adhesion behavior must be controlled. This chapter is devoted to the analyses of the bulk properties of the investigated LSRs. The chemical composition of commercial grades of LSRs, including the silica content and the cross-linking agent content, was investigated by thermogravimetric analyses and infrared spectroscopy. The cross-linking behavior of the LSRs was examined by means of both calorimetry and thermomechanical analyses. Finally, the mechanical properties of the cross-linked LSRs were examined by tensile tests and dynamic mechanical analyses.

2. Materials and methods

2.1. Preparation of samples

For the investigations described in this thesis, we used a series of liquid silicone rubbers (LSRs) "Elastosil® LR 3003" supplied by Wacker (Munich, Germany), which provides five LSR formulations of different stiffness.

The LSR "Elastosil® LR 3003" formulations (hereinafter referred to as "the LSR") of varied Shore A stiffness 5/30/40/60/80 are dedicated to automotive, technical and food contact applications. The available data on the properties of all the studied products is given in **Table 2.1**. We will henceforth use Shore A stiffness values as measured, which are in agreement with those given in **Table 2.1** (see details in the following sections).

Table 2.1. *Properties of analyzed LSR products (data given by the suppliers)*

Product		*Shore A Stiffness*	*Density, g/cm³*	*Elongation at break, %*	*Viscosity at 10 s^{-1}, Pa s*	*Viscosity at 0,9 s^{-1}, Pa s*
Elastosil® LR 3003	**05**	6	1,05	700	23	35
	30	31	1,09	620	150	190
	40	41	1,13	610	420	840
	60	60	1,13	340	420	1100
	80	79	1,16	210	710	2000

Standard commercial grades of LSRs consist of two components, A and B, made up of the same base, i.e., silica and a vinyl-terminated PDMS, that are supposed to be mixed in equal ratio [88]. Part A contains the platinum catalyst [Pt] and Part B contains an inhibitor preventing premature cross-linking of the polymer at ambient temperature and of the silane groups used as cross-linking agents. When parts A&B are mixed, the LSR cross-links by a hydrosilylation reaction, as described in Chapter I, part 2.2.

Since the two components A and B have the same density, we replaced the volumetric dosing (used in industry [89]) by the mass weighting in the laboratory. Mixed parts A&B appear in a more or less liquid state depending on the Shore A value. This pasty substance is clouded by the presence of tiny air bubbles trapped in the volume due to the high viscosity of the mixture that does not allow trapped air bubbles to escape during the blending. Once parts A&B are mixed, the pot life of the mixture is of about 3 days. LSR samples are molded in the heating press at 165 °C for 5 minutes according to the manufacturer's recommendation, and under 40 bars pressure to remove the air bubbles (**Fig. 2.1**). Then, the cured LSR sample, as recommended, is *post-cured* at 200 °C during 4 hours in order to remove reactive species remaining subsequent to curing.

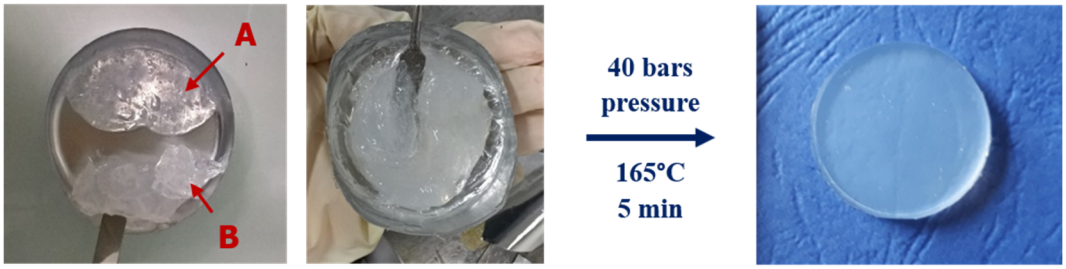

Figure 2.1. Compression molding process

2.2. Thermal analyses of the LSR

2.2.1. Differential scanning calorimetry (DSC)

Differential scanning calorimetry (DSC) relies on the measurement of a difference in the power, i.e., in the heat flow, required to maintain two cells at the same temperature as a function of temperature (**Fig. 2.2**). One cell contains a sample and the second one, called a "reference", contains the reference material (usually, vacuum). Differences in heat flow arise when a sample undergoes endothermic or exothermic processes such as phase transitions, chemical reactions, etc. Thus, DSC can be used to measure a number of

characteristic properties of a sample, including parameters such as glass transition, phase changes (melting, crystallization, vaporization), and cure kinetics.

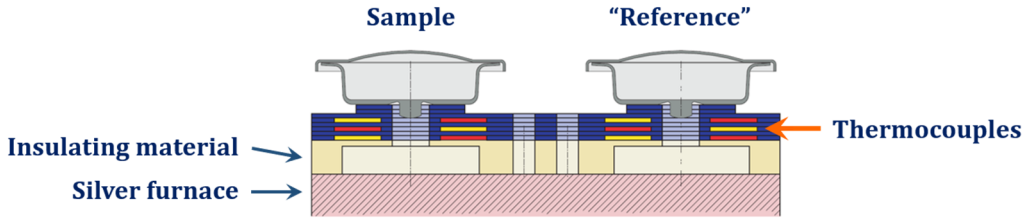

Figure 2.2. Scheme of the DSC functioning [90]

In this study, we used DSC to measure the cross-linking behavior of the LSR formulations. The cross-linking of LSR can be detected by DSC, due to the exothermic property of this reaction. The DSC measurements were conducted under nitrogen on a TA Instruments Q100 device (New Castle, DE, USA). For each measurement, the sample (i.e., the equal mixture of LSR parts A&B) was placed in a standard hermetic aluminum cell to be used with TA Instruments Q100.

For each sample, the temperature was stabilized at 40 °C, and then, brought up to 180 °C at a given heating rate. All the measurements were carried out at a heating rate of 10 °C/min, a good compromise between accuracy, resolution, sensitivity, and actual measurement time [91]. Since the shift of the exothermic peak of the reaction can be affected by the sample weight, a constant weight of 10 mg was used for each measurement. The set of measurements was done twice to assess the reproducibility of the data.

The result of a DSC experiment is a curve of heat flow versus temperature/time. Given a constant heating rate, temperature (°C) and time (s) are proportional. **Fig. 2.3** shows a curve obtained from a DSC measurement of the LSR sample of Shore A stiffness 42. We observe an exothermic peak at 111 °C corresponding to the cross-linking temperature.

The specific enthalpy of cross-linking, i.e., energy released by 1 g of a sample during the cross-linking (J/g), is calculated through the integration of the peak area. One might use heat flow (W/g) vs. time (s) curve $\Phi = f(t)$ for the integration of the peak area to obtain the specific enthalpy in J/g. If working with heat flow vs. temperature curve $\Phi = f(T)$, the integrated area must be divided by the heating rate in °C/s.

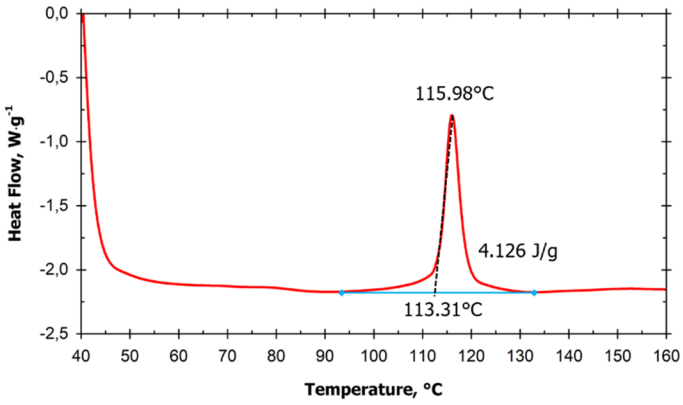

Figure 2.3. Heat flow as a function of temperature measured on the uncured LSR of Shore A stiffness 42 using DSC

2.2.2. Thermogravimetric analyses (TGA)

Thermogravimetric analyses (TGA) consist in measuring the mass loss of a sample with increasing temperature. In this study, we used the TGA techniques in order to investigate the thermal stability of the LSR formulations as well as to determine the final content of their residue at 900 °C.

For each LSR formulation, measurements were performed with each component of the uncross-linked material (part A and B) separately as well as with cross-linked LSR specimens. The TGA curves were obtained on a thermogravimetric analyzer Q50 (TA Instruments, New Castle, DE, USA). The experiments were carried out under a nitrogen flow, at a heating rate of 20 °C/min, in a temperature range from 40 to 1000 °C. Since the sample weight can affect the thermogravimetric curve because of the possible unevenness of the temperature throughout the sample, the initial sample mass value was kept at 10 – 13 mg. The set of measurements was done twice to ensure the reproducibility of the data.

2.3. Fourier transform infrared (FTIR) spectroscopy: LSR functional groups

To reveal the LSR functional groups, present in the commercial-grade LSR materials of interest, FTIR spectroscopy was performed with each component of the LSR formulations (A and B parts) as well as with the cross-linked LSR of varied Shore A stiffness (9, 34, 59, and 72). FTIR spectra were recorded on a Perkin-Elmer Spectrum One FTIR Spectrometer (Waltham, Massachusetts, USA).

The FTIR spectra of individually measured A and B parts of the LSR formulations were gathered in the transmission mode in the 650 – 4000 cm^{-1} spectrum range, with 4 cm^{-1} resolution. To this end, a thin layer of each LSR component (~100 µm) was spread

between two polyethylene films (10 µm in thickness) and then mounted into the sample chamber prior to measurement. The background spectrum of the polyethylene films was subtracted from those of the recorded FTIR spectra. The vibrational modes of the cross-linked LSR samples were measured in the Attenuated Total Reflection (ATR) mode in the same spectral range.

2.4. Mechanical properties of the LSR

2.4.1. Shore A stiffness measurements

The stiffness of both cured and post-cured LSR formulations was measured using a Shore A durometer. This technique consists in measurements of the depth of indentation in the material created by a given force on a standardized presser foot (**Fig. 2.4**). The experiment was carried out on LSR samples of 4 mm thickness. All the Shore A stiffness values of the LSR formulations reported in the disscussion part were measured using this protocol.

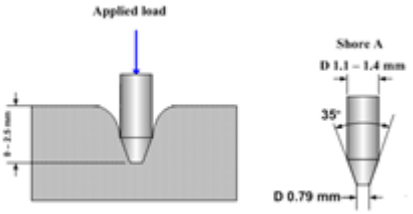

Figure 2.4. Shore A durometer indenter

2.4.2. Tensile tests: Young's modulus of the LSR

Tensile tests on investigated LSR formulations were performed by B. Caubet [145], Master 1 intern student supervised by F. Léonardi and the author. The main objective was to correlate the Young's modulus and Shore A values of the cross-linked LSR.

The primary objective was to use a clip-on extensometer mounted directly onto the specimen to measure small deformations and easily determine the Young's moduli of the LSR. It has been necessary to set up a system holding and fixing the extensometer to avoid the preliminary deformation of relatively soft LSR specimens under the weight of the extensometer. However, after several attempts, we had to measure the elastic modulus without using the extensometer because of the slipping between the extensometer attachment grips and the specimen during the stretching which makes the accurate stress measurement impossible.

Tensile tests were conducted on both cured (165 °C during 5 min) and post-cured (200 °C during 4 hours after the curing) LSR specimens of 120 × 10 × 4 mm dimensions, using the universal testing machine with a force sensor (10 kN) and 2 pneumatic grips (6 bars pressure). Young's modulus values were measured 5 times for each LSR formulation at a tensile test speed of 100 mm/min (**Fig. 2.5**).

Figure 2.5. Demonstration of the LSR specimens dedicated to tensile tests

2.4.3. Dynamic mechanical analyses (DMA): viscoelastic properties of the LSR

The viscoelastic behavior of the LSR formulations was evaluated by measuring the dynamic shear modulus of cross-linked LSR specimens. When a sinusoidal shear strain is applied to the specimen in the sine-wave form $\varepsilon = \varepsilon_0 \sin(\omega t)$, the stress is supposed to vary at the same frequency according to $\sigma = \sigma_0 \sin(\omega t + \delta)$. In perfectly elastic materials the stress and strain occur in phase. In perfectly viscous materials, there is a phase lag of 90° between stress and strain, strain is in phase with strain rate $\dot{\varepsilon}$. *Viscoelastic* materials, as their name suggests, combine both properties.

Viscoelastic materials are characterized by both elastic and viscous components related to the complex dynamic shear modulus and to each other through the phase angle δ by the following formula:

$$G^* = G' + iG'' \qquad \textbf{(2.1)}$$

$$\tan\delta = G''/G' \qquad \textbf{(2.2)}$$

where G' is the storage modulus, real part of the complex shear modulus characterizing the elastic behavior of materials, and G'' is the loss modulus, imaginary part of the complex shear modulus arising from the network defects (depends on the molar mass of dangling chains) and characterizing the viscous behavior of materials.

The viscoelastic behavior of the LSR formulations was analyzed using well-established experimental methodologies and equipment. This includes the parallel-plate rotational rheometry using *ex-situ* pre-prepared cylindrical samples and shear experiments by rectangular torsion rheometry.

a. DMA using the parallel-plate rotational rheometry

In the first stage, the viscoelastic properties of the cross-linked LSR formulations were evaluated in the parallel-plate geometry using the Anton Paar MCR 302 oscillatory rheometer (Les Ulis, France). The basic principle of an oscillatory rheometer consists in inducing a sinusoidal shear strain (stress) in the sample positioned between two plates and measuring the yield stress (strain) response. In a typical stress-controlled experiment, such as used in this study, a cylindrical sample is placed between two plates. While the bottom plate remains stationary, the top plate rotates, thereby imposing a time-dependent stress $\sigma(t) = \sigma_0 \sin(\omega t)$ on the sample (**Fig. 2.6a**). The time-dependent yield strain $\varepsilon(t)$ is simultaneously quantified. In the strain-controlled rheology, the torque or stress is the independent variable, and the strain is the dependent one.

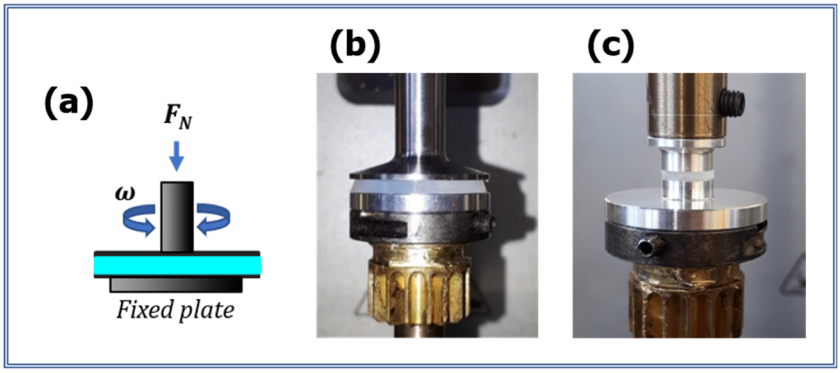

Figure 2.6. (a) A schematic representation of an oscillatory rheology setup, with a sample positioned between two parallel plates; (b) Cross-linked LSR sample of 25 mm in diameter and 2 mm in thickness placed between two plates prior to DMA measurements; (c) Cross-linked LSR sample of 8 mm in diameter and 1 mm in thickness placed between two plates prior to DMA measurements

Dynamic shear modulus measurements in the parallel-plate geometry were made using two different protocols. The first one, "standard" protocol, consists in measuring the storage and loss moduli of cylindrical LSR specimens prepared *ex situ* and positioned between the plates. The second protocol consists in measuring the storage and loss moduli of the LSR specimens prepared within the rheometer heating chamber (*in situ*).

This protocol, also called "control" protocol, ensures the measurements in "no-slip" conditions, when the sample is firmly fixed in the parallel-plate geometry.

Measurements leading to systematic errors

The primary objective was to perform "standard" dynamic measurements on *ex-situ* prepared LSR specimens of 25 mm in diameter and 2 mm in thickness at 1 N applied normal force (**Fig. 2.6b**). However, the selected geometry and the preload (normal force) cannot ensure the firm adhesion between a specimen and the plates. We detected the slippage at the specimen – plate interface leading to systematic errors of the experimental data.

To illustrate it, we compared the storage modulus values measured using this protocol (*ex-situ* prepared specimens, plates of 25 mm in diameter, 1 N applied normal force) to those measured using control *in situ* prepared specimens (described below). Storage moduli of both sets of samples (*ex situ* cured and *in situ* cured control samples) are represented as functions of Shore A stiffness in **Fig. S1** (**Annex I**).

As shown in **Fig. S1**, the storage moduli of *ex-situ* prepared LSR samples are one order of magnitude lower than those achieved in "no-slip" conditions. It is interesting to note that the measured storage moduli increased with Shore A stiffness until a threshold Shore A stiffness value at approximatively 42 was reached. For higher stiffnesses the storage moduli remained unchanged. Moreover, switching from the smooth plates to sand-blasted plates had no effect on the achieved values. These outcomes led us to the conclusion that the measurements following the "standard" protocol with the plates of 25 mm in diameter and the preload of 1N leads to a systematic deviation to lower storage modulus, especially in the case of stiffer LSR specimens.

Owing to this issue, the "standard" protocol was slightly modified, and the *ex-situ* prepared samples were examined using a smaller diameter geometry and higher static axial preload during the measurement.

"Standard" protocol of DMA in the parallel-plate geometry

First, we performed DMA measurements in the parallel-plate geometry with 8 mm diameter plates following the "standard" protocol. The cylindrical LSR samples of 8 mm in diameter and 1 mm in thickness of varied stiffness (9, 21, 34, 42, 59, and 72 Shore A) were prepared *ex-situ* (curing at 165 °C during 5 min).

In order to avoid the slippage at the specimen – plate interface, all the measurments were performed at a static axial preload (normal force) of 10 N. This preload value is a compromise that does improve the adhesion between the sample and the rotor plate, and at the same time causes minor deformation when squeezing the specimen. All the measurements were carried out at 30 °C.

The first step (stress sweep) consists in defining the linear viscoelastic region (LVR) in which the stress and the strain are proportional, and therefore both storage and loss moduli are independent on the applied shear stress. The stress sweep test was done for all the LSR specimens of varied stiffness in the 10 to 1000 Pa range at a constant frequency of 10 rad/s and at 30 °C.

As shown in the **Fig. S2** (**Annex I**), the storage (G') and (G'') moduli remain constant throughout a whole stress range, exhibiting a pronounced linear viscoelastic behavior in the probed stress interval.

In the following step, frequency sweep tests were done with all the LSR products in the 80 to 0.08 rad/s range with an applied shear stress of 50 Pa and at 30 °C. Storage and loss modulus master curves were measured 3 times for each LSR formulation.

"Control" DMA of LSR specimens in the parallel-plate geometry

To ensure the accuracy of the outcomes measured using the "standard" protocol, a series of LSR samples of varied Shore A stiffness (9, 21, 34, 42, 59, and 72) was examined following the "control" protocol. According to this experimental approach, LSR specimens were cured within the rheometer heating chamber (*in situ*) prior to DMA measurements thereby ensuring a firm adhesion between the specimen and plates.

For each measurement, the blended LSR components of a given stiffness was first degassed in a vacuum chamber for 1 hour in order to remove dissolved air bubbles from the material. Further, the pasty LSR blend was spread on the bottom plate using a spatula. Then the rotor plate was brought down toward the bottom plate squeezing the pasty LSR until the geometry reaches the predetermined top-bottom plates gap of 2 mm.

In a subsequent stage, the LSR squeezed between 18 mm diameter plates was cured in the heating chamber. The storage and loss moduli were measured as functions of temperature in the 30 to 170 °C range with a heating rate of 2 °C/min, a frequency of 1 rad/s and an applied shear stress of 50 Pa. During the curing, the static preload was kept at 0 N.

Finally, the *in situ* cured control specimens of 18 mm diameter and 2 mm thickness were examined in the 80 to 0.08 rad/s range with an applied shear stress of 50 Pa and at 30 °C. During the frequency sweep measurement, the static preload was kept at 0.5 N.

b. DMA on the cured LSR using the rectangular torsion rheometry

In addition to the measurements in the parallel-plate geometry, the cross-linked LSR samples of varied stiffness were examined in the rectangular torsion geometry. This method basically consists in applying a torsional deformation to a rectangular specimen gripped between clamps and measuring the torsion torque response (**Fig. 2.7a**). While the upper tool remains stationary, the lower tool rotates, thereby imposing a time-dependent torsional deformation on the specimen.

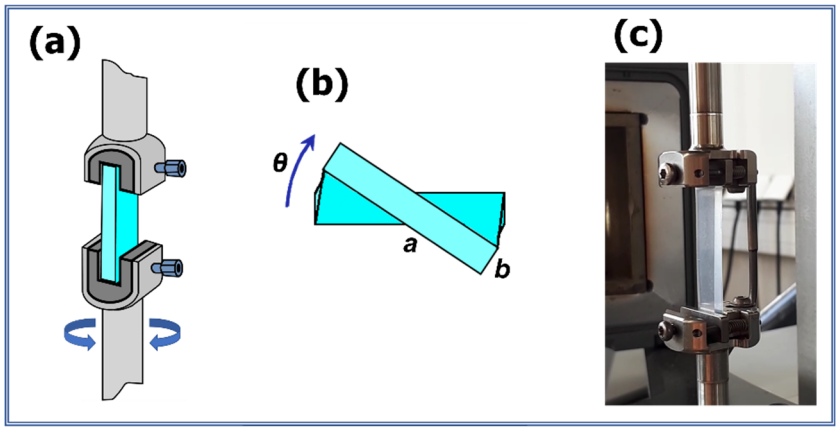

Figure 2.7. (a) A schematic representation of a rectangular torsion rheology setup, with a sample clamped between two grips; (b) Cross-section view of a thin-wall rectangular specimen under torsional loading (width a, thickness b); (c) Cross-linked LSR specimen of dimensions 40 × 10 × 2 mm clamped between two grips prior to DMA measurements.

The dynamic shear modulus was evaluated from the measured raw torsion torque values using the following equation based on the Saint-Venant torsion theory [146]:

$$G = \frac{TL}{J\theta} \qquad \textbf{(2.3)}$$

where G is the dynamic shear modulus, T is the internal torque, J is the polar inertia moment, θ is the maximum angle of twist, L is the specimen length.

In commercial rheometer softwares (e.g., TA Instruments) typically stress-strain relationship formula imply the adaptation of de Saint-Venant equation with a simple expression for J [147,148]:

$$J \cong \frac{ab^3}{3} \cdot \frac{1 - 0.378u^{-2}}{1 + 0.6u^{-1}} \qquad \textbf{(2.4)}$$

where a is the specimen width, b is the specimen thickness, and u is the width-to-thickness ratio (**Fig. 2.7b**). The Rheocompass software (Anton Paar) exploits another approximation for J [148,149]:

$$J \cong \frac{ab^3}{3}(1 - 0.63u^{-1} + 0.052u^{-5}) \qquad \textbf{(2.5)}$$

DMA measurements in the rectangular torsion geometry using ARES rheometer

The shear modulus measurements in the rectangular torsion geometry using the ARES rheometer (TA Instruments, New Castle, DE, USA) were performed by B. Caubet [92]. The LSR specimens of varied Shore A stiffness (9, 21, 34, 42, 59, and 72) in form of thin-wall rectangular bars (L = 40 mm, a = 10 mm, and b = 2 mm) were prepared *ex-situ* (curing at 165 °C during 5 min) and gripped between clamps prior to DMA testing.

To evaluate the LVR, the storage and loss moduli were measured at a constant frequency of 1 rad/s in the deformation range from 0.3 to 1 %. The temperature was set at 30 °C. Frequency sweep tests were subsequently done for all the LSR specimens in the 80 to 0.14 rad/s frequency range with an applied torsional deformation of 0.3 % (stiff samples) and 1 % (soft samples). These tests were performed twice for each LSR formulation.

As a control test, the rectangular LSR samples of dimensions 40 × 10 × 2 mm of identical Shore A stiffness range were examined in the rectangular torsion geometry using the Anton Paar MCR 302 rheometers (**Fig. 2.7c**). The LVR was evaluated in the 0.05 to 4 % deformation range at a constant frequency of 2 rad/s and at 30 °C (**Fig. S3**, **Annex I**). The storage and loss moduli of the LSR specimens were then measured in the 80 to 0.08 rad/s range with an applied torsional deformation of 0.1 % (stiff samples) and 0.3 % (soft samples). Master curve measurements were performed 3 times for each LSR formulation.

3. Results and discussion

3.1. Thermal analyses of the LSR

3.1.1. Differential scanning calorimetry (DSC)

The DSC analyses, as detailed in "Materials and methods", were performed on all the LSR formulations of varied Shore A stiffness (9, 34, 42, 59, 72). To avoid misleading of the reader, represented Shore A stiffness values were measured using a Shore A durometer (see part 2.4.1) and listed in **Table 2.4** reported below.

We noticed that the exothermic peak shifts to greater temperatures with increasing Shore A values (**Fig. 2.8**).

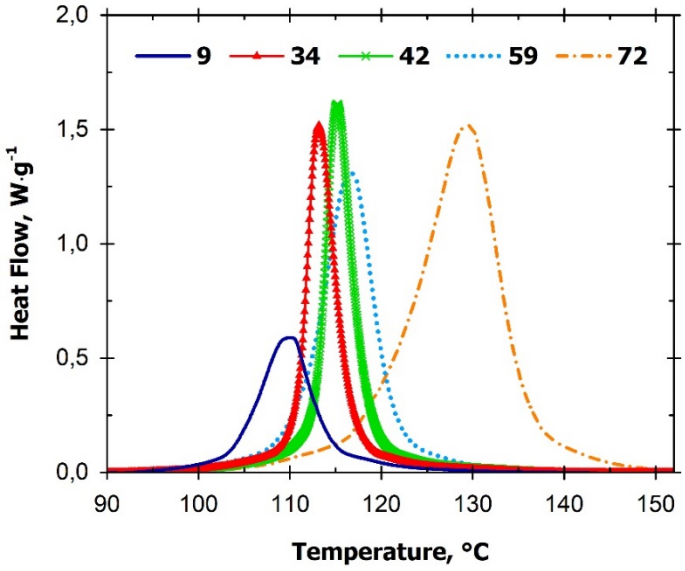

Figure 2.8. Cross-linking temperature of the LSR as a function of Shore A stiffness measured at a given heating rate of 10 °C/min

The LSR cross-linking temperature and the specific enthalpy of cross-linking are presented in **Fig. 2.9**, as functions of the Shore A stiffness. The higher the Shore A stiffness is, the more the cross-linking reaction shifts to a greater temperature. The specific enthalpy calculated through the integration of the cross-linking peak area increases with increasing Shore A values as well.

In addition, the measurement of the thermal changes can be used to deduce the progress of the cross-linking reaction, referred to as the "cross-linking degree α". The cross-linking degree as a function of temperature $\alpha(T)$ is obtained by integrating the heat

curve at each temperature step and by further normalization in relation to the total area under the heating curve Q_T [150]:

$$\alpha(T) = \frac{\int_{T_1}^{T} \left(\frac{dQ(T)}{dT}\right) dT}{Q_T} \qquad \textbf{(2.6)}$$

where T_1 is the starting temperature of the reaction.

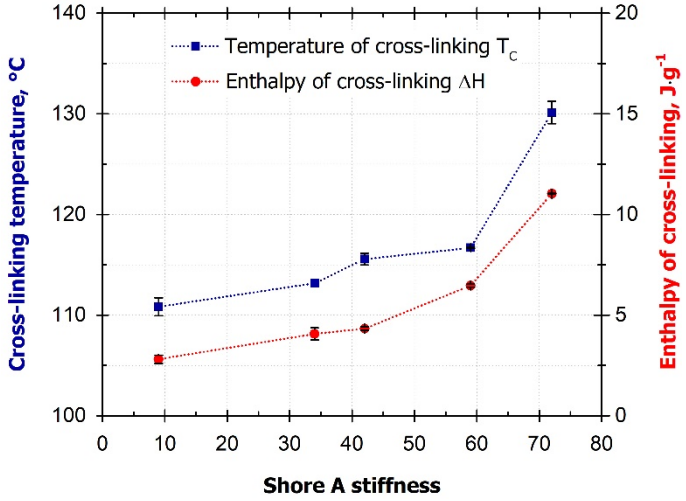

Figure 2.9. Cross-linking temperature and enthalpy of cross-linking of the LSR as a function of Shore A stiffness measured at a heating rate of 10 °C/min. Lines are only guides for the eyes.

Fig. 2.10 shows the cross-linking degree α of the LSR formulations of varied Shore A stiffness as a function of temperature. We can notice that not only the cross-linking reaction shifts to higher temperatures with Shore A stiffness, but also that the conversion rate for the LSR sample of the highest stiffness is slower. The time at which the LSR of Shore A stiffness 72 cross-links reaches 90 sec, whereas it is of about 60 sec for the other LSR formulations (values taken between the inflexion points of the curves, i.e., from 10 to 90 % of cross-linking degree α).

Certain assumptions on this issue can be considered. The cross-linking process can be affected by:

- The silica fillers in the LSR, used to enhance the material mechanical properties. The filler content inevitably alters the physicochemical properties of the elastomer, including kinetics of curing.
- The PDMS chains length: with this hypothesis, the chain length increases with the Shore A value. The PDMS chains composing the products of higher stiffness

are longer and less mobile, thus less prone to be involved in the initiation of the cross-linking process.

- Cross-linking agent concentration. As shown earlier, the silane content used as the cross-linking agent increases with the stiffness of the LSR formulations. In such a case, the increasing exothermicity can be explained by a positive relation between the number of cross-link sites and the enthalpy of cross-linking value.

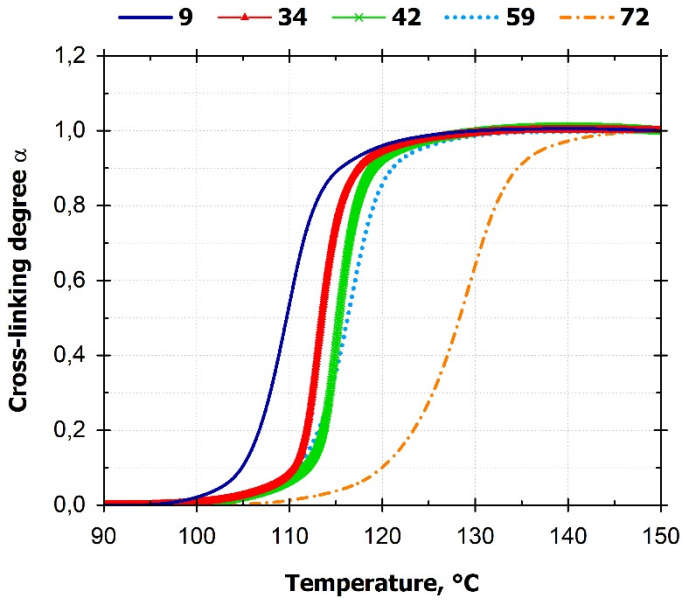

Figure 2.10. Cross-linking degree α of the LSR formulations of varied stiffness (9, 34, 42, 59, 72 Shore A stiffness) as a function of temperature based on the DSC measurements at a heating rate of 10 °C/min.

3.1.2. Thermogravimetric analyses (TGA) measurements

The silica fillers used in the LSR formulations to reinforce the cross-linked elastomer matrix inevitably alter the physicochemical properties of the elastomer. To determine more specifically the filler content in the LSRs under investigation, we performed TGA under nitrogen on each part separately. The degradation curves of parts A and B of two representative LSR formulations at low and high Shore A stiffness values are shown in **Fig. 2.11**.

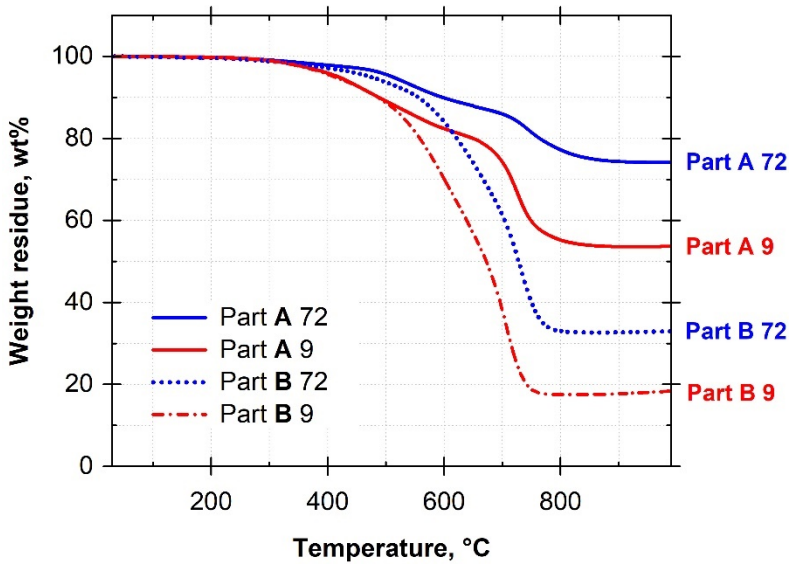

Figure 2.11. TGA thermograms of both components (parts A and B) of two representative LSR formulations of low and high Shore A stiffness (9 and 72, respectively) measured separately

From the **Fig. 2.11** it can be seen that for a given Shore A stiffness value, a considerably higher level of residue is produced with part A than with part B. The weight residue of all the LSR formulations are listed in **Table 2.2**.

Table 2.2. *Weight residue of the analyzed LSR formulations*

Shore A stiffness	*Part A, wt. %*	*Part B, wt. %*	*Cured LSR, wt. %*
9	54 ± 1	18 ± 2	71 ± 1
34	68 ± 2	25 ± 1	71 ± 4
42	68 ± 3	29 ± 3	77 ± 1
59	73 ± 1	33 ± 2	79 ± 2
72	74 ± 1	33 ± 2	78 ± 1

As was mentioned in the part "Materials and methods", standard commercial grades of LSRs consist of two components, composed of the same base, i.e., silica filler and a vinyl-terminated PDMS. Hence, we should look for the origin of a constant extra residue of 40 wt. % in part A, which contains the platinum catalyst.

Delebecq *et al.* [94]. performed an exhaustive study on the role of platinum and silica content on the degradation process and final residue content of vinyl-termined PDMS. They found that whereas the final weight residue corresponds to the silica content in the absence of platinum, vinyl terminated PDMS/silica/platinum combinations yield

high extra residue contents. By adding Pt (200 ppm) into PDMS filled with vinyl-modified silica, they could increase the extra residue up to 45 wt. %.

In the presence of platinum, PDMS chains generate cross-link points with the silica surface forming a layer of immobilized PDMS chains at the interface. Such joint immobilization leads to the ceramization of the chain fragments during degradation at high temperatures, and consequently to the final high extra residue content.

We also notice that, unlike part B, part A exhibits a two-step degradation process. To better illustrate the degradation process of part A, the corresponding derivative thermogravimetry (DTG) curves are plotted in **Fig. 2.12**.

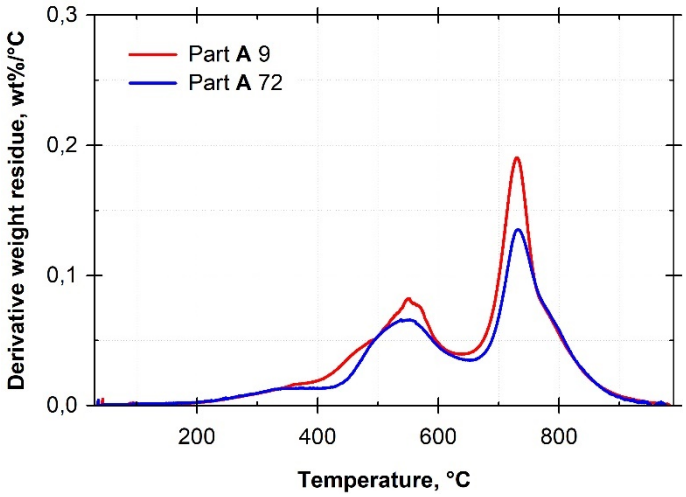

Figure 2.12. DTG curves of the part A of two representative LSR formulations of low and high Shore A stiffness (9 and 72, respectively)

According to Delebecq *et al.* [94], the combination of both silica and Pt in PDMS results in two well-separated DTG degradation peaks. The first degradation peak appears at temperatures ranging from 400 to 650 °C and, according to the TGA thermograms (**Fig 2.11**), is accompanied by a weight loss of 16 and 10 wt. % for Shore A stiffness 9 and 72, respectively. At this stage, the silicone phase undergoes a volatilization process of the highly mobile chains. The second degradation peak observed in the temperature range of 650 – 900 °C corresponds to a weight loss of 26 and 14 wt. % for Shore A stiffness 9 and 72, respectively. In this range of temperatures, the sample is no longer a polymer. The mechanism of degradation here consists in the removal of the highly constrained chains before ceramization takes place to generate a large final residue.

Summing up, the investigated LSR formulations are composed of a vinyl-modified silica filler content increasing from 18 to 33 wt. % with Shore A stiffness values. Along

with this, the part A of each formulation carries the platinum catalyst needed for hydrosilylation.

The cured LSR samples generate a slightly higher final residue than part A (see **Table 2.2**). As shown in the **Fig. S4** (**Annex I**), the TG and DTG curves of the cured LSR samples exhibit the same two-step degradation process than the respective parts A.

3.2. Fourier transform infrared (FTIR) spectroscopy: LSR functional groups

The spectra shown in **Fig. 2.13** provides information about the functional groups present in the part A (light blue) and the part B (dark blue) of the representative LSR formulation of 9 Shore A stiffness.

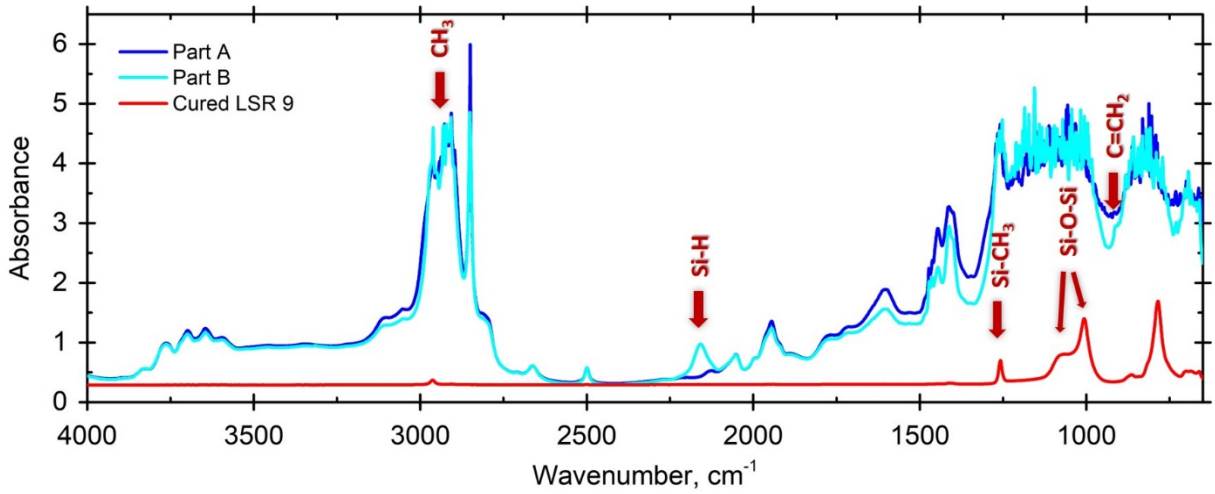

Figure 2.13. FTIR spectra of LSR components A and B (9 Shore A stiffness); FTIR spectrum of cross-linked LSR sample of the same Shore A stiffness in the transmission mode

The LSR parts exhibit a remarkably similar set of characteristic IR absorption bands listed in **Table 2.3**.

The absorption peak at 910 cm^{-1} associated with the vinyl functional group $C=CH_2$ *a priori* present in both LSR parts is barely visible on the spectra. We can assume that the representative band of the vinyl group overlaps with those of other groups present in the formulation.

Table 2.3. *IR absorption bands of parts A&B of an LSR formulation of 9 Shore A stiffness*

Peak n° (Fig. 3)	*Wavenumber, cm^{-1}*	*Description*	*Ref.*
1	2960	Asymmetrical CH_3 stretching in ≡Si–CH_3	[151]
2	2500	Overtone band of CH_3 deformation 1260 cm^{-1}	[152]
3	1945	Siloxane backbone stretching	[152]
4	1410	Symmetrical CH_3 stretching in ≡Si–CH_3	[151]
5	1260	Symmetrical CH_3 deformation in ≡Si–CH_3	[151]
6	1020–1090	Asymmetrical Si-O-Si stretching	[151,152]
7	910	Vinyl functional group C=CH_2	[153,154]

Despite all the similarities between the two LSR parts, the spectrum of the part B exhibits a peak at 2160 cm^{-1} that deserves particular attention. This band is assigned to the silane Si-H function used as the cross-linking agent in part B [152]. **Fig. 2.14** shows the absorption band resulting from the silane group for each LSR formulation.

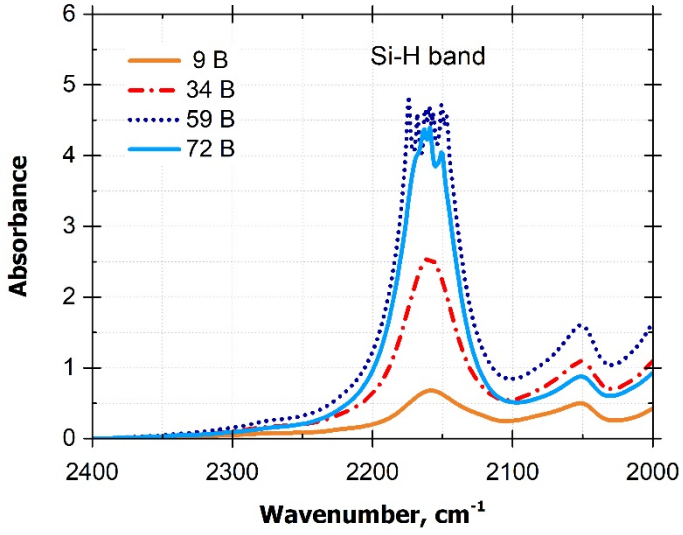

Figure 2.14. IR absorption band originating from Si-H group stretching used as the cross-linking agent measured for LSR formulations with varied stiffness (9, 34, 59, and 72 Shore A stiffness)

We notice from the **Fig. 2.14** that the absorbance intensity of the Si-H band grows with increasing Shore A stiffness value. The intensity of the Si-H band of the stiffest sample

is 8-fold higher than that of the softest one. According to the Beer-Lambert law, the absorbance is proportional to the concentration of the absorbing species. It can be therefore concluded that the cross-linking agent concentration increases with increasing Shore A stiffness value of the LSR formulations.

In a previous study reported by Delebecq *et al*. [137], it was shown that the stiffness adjustment of LSR formulations ranging from 20 to 50 Shore A was performed by playing on several parameters such as silica filler content, molecular weight between cross-links, and silica surface modifier. Considering the results described above, we can conclude that the mechanical properties of the LSR formulations under investigations were adjusted by playing on at least two parameters: cross-link density and silica filler content.

The FTIR-ATR data of cured LSR formulations (9, 34, 59, and 72 Shore A stiffness) are shown in **Fig. 2.15**. Cured LSR samples exhibit a series of characteristic IR bands, the origins of which are indicated in **Table 2.3**. The spectra are highly similar, apart from the small peak at 910 cm^{-1} that increases with increasing cross-linker concentration. This peak, as mentioned above, comes from the vinyl functional group $C=CH_2$. Concurrently, the absorption band at 2160 cm^{-1} associated with the cross-linking agent Si-H completely vanishes.

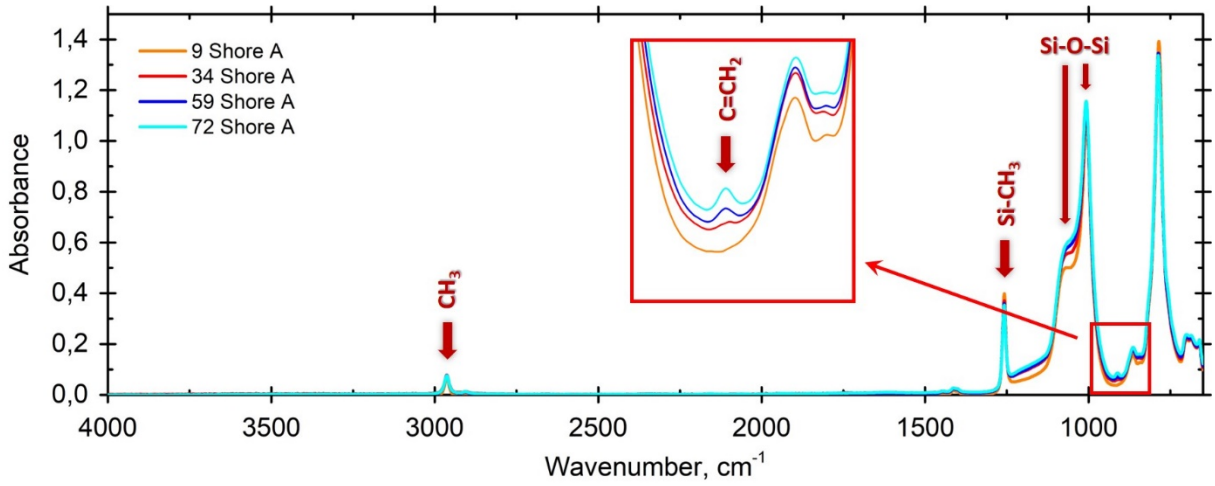

Figure 2.15. FTIR spectra of cross-linked LSR samples of different Shore A stiffness (9, 34, 59, 72) in the ATR mode

3.3. Mechanical properties of the LSR

3.3.1. Shore A stiffness measurements

The Shore A stiffness value for each LSR formulation was averaged from 12 measurements made on 3 LSR specimens from one set of samples (from one curing process). We can consider from the results given in the **Table 2.4** that, first of all, Shore A values are in good agreement with those provided by the supplier.

Table 2.4. *Comparison between Shore A stiffness values of cured and post-cured LSR*

Theoretical Shore A*	***Measured Shore A Cured LSR***	***Measured Shore A Post-cured LSR***	***Δ (Shore A)***
6	9.4 ± 0.3	9.1 ± 0.2	--
31	34.0 ± 0.4	32.3 ± 0.3	- 1.7
41	41.9 ± 0.3	41.0 ± 0.2	- 0.9
60	59.1 ± 0.2	61.1 ± 0.4	+ 2.0
79	71.9 ± 0.3	74.4 ± 0.3	+ 2.5

**Theoretical values given by the suppliers*

Since post-curing is supposed to ensure a complete reaction of species that have not reacted during curing, we expected an increase in Shore A values after post-curing. On the one hand, the changes in Shore A values after the post-curing seems to be of little significance. Moreover, in contrary to what was expected, the Shore A values of soft LSR decrease slightly after post-curing.

However, we observed a slight increase in the Shore A values of stiff LSR (60, 79) after post-curing, which is likely due to the presence of reactives remaining in the network after the first curing step. Since the only reaction during the cross-linking of the LSR which provides the strength to the elastomer is hydrosilylation, the reactive species possibly remaining in the unpost-cured LSR samples are vinyl $C{=}CH_2$ and silane Si-H groups.

3.3.2. Tensile tests: Young's modulus of the LSR

Stress-strain curves measured from the unpost-cured LSR samples of varied Shore A stiffness are shown below in **Fig. 2.16**. Stress-strain curves obtained from the post-cured LSR samples are represented in **Fig. S5** (see **Annex I**). It is noticeable that the tensile behavior of the LSR formulations with Shore A stiffness below 42 is typical of a rubber-like materials [155].

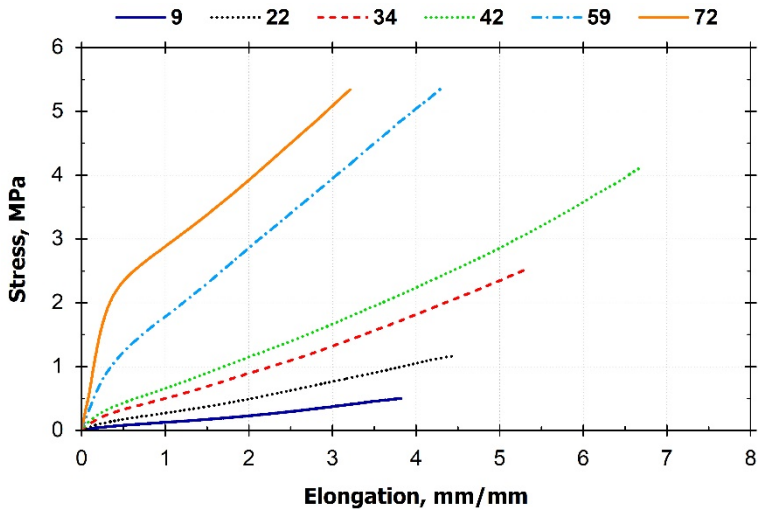

Figure 2.16. Stress-strain curves obtained from the post-cured LSR samples of varied Shore A stiffness

Fig 2.17 shows a representative stress-strain curve of the softest LSR sample (9 Shore A) with the fewest amount of silica filler.

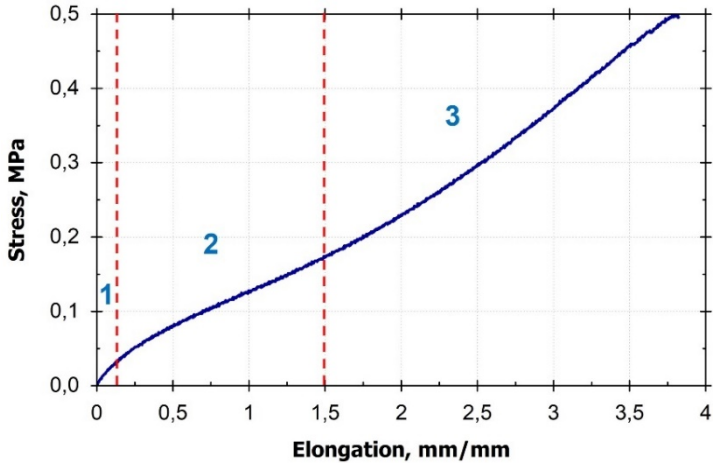

Figure 2.17. Representative stress-strain curve of the LSR sample with Shore A stiffness of 9

The first part 1 reveals a quasi-linear stress-strain curve evolution at small deformations (below 10 %) at which the elastomer displays a Hookean behavior. The relationship between stress and strain in this region can be described by the Hooke's law $\sigma = E\varepsilon$, where the coefficient of proportionality E is the Young's modulus. The second region starts from the first inflection point (at about 10 %) and can be associated with disentanglement of the chains which align according to the direction of the load. The third region, almost linear, starts from the second inflection point and represents the *strain hardening* of the material resulting from the chains alignment in the direction of the load which increases the strength of the material in the stretching direction.

Young's modulus values of both cured and post-cured LSR samples of varied Shore A stiffness were determined from the stress-strain curves at small deformations. **Fig. 2.18** presents the Young's modulus as a function of Shore A stiffness. We observe the exponential increase of Young's modulus with Shore A stiffness. The exponential correlation using equation (2.7) fits the experimental data with extremely good accuracy ($R^2 = 0.99$):

$$E = 0.17 \cdot \exp(0.05 \cdot Shore\ A) \qquad \textbf{(2.7)}$$

It is also apparent that unpost-cured and post-cured samples follow the same law, but both Shore A values and Young's modulus of post-cured samples are slightly higher.

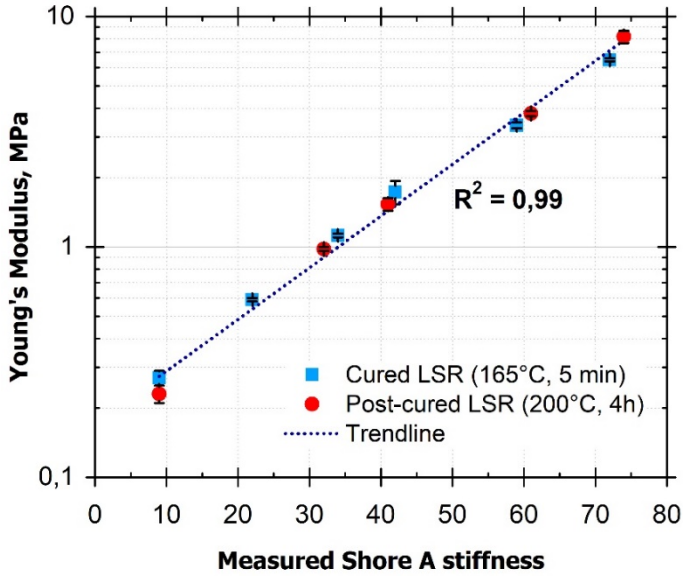

Figure 2.18. Young's modulus as a function of Shore A stiffness of Elastosil LSR formulations. Each data point is an average of 5 tensile tests

Young's modulus values of cross-linked LSR samples ranging from 0.3 to 6.5 MPa are listed in **Table 2.5**.

Fig. 2.19 represents the elongation-at-break values of both cured and post-cured LSR samples as functions of Shore A stiffness. We notice that both increase with Shore A stiffness until they reach a maximum at about 700-750 % at 42 Shore A stiffness then start to decrease to final 320 % and 210 % elongation-at-break for cured and post-cured LSR samples, respectively.

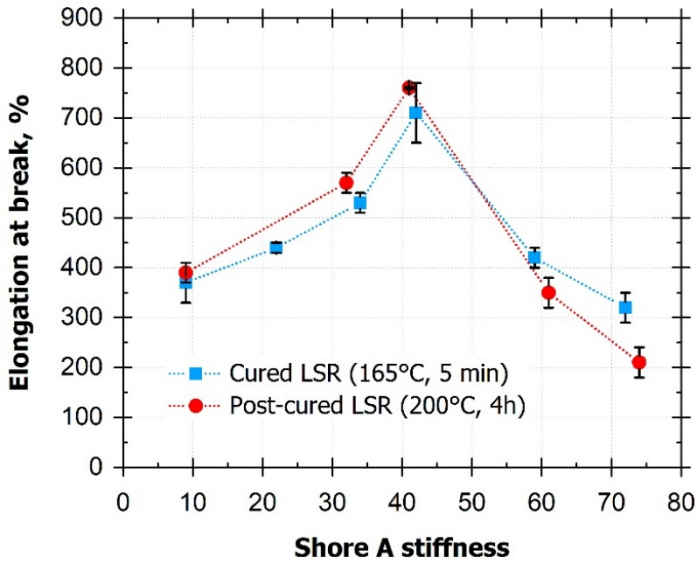

Figure 2.19. Elongation at break as a function of Shore A stiffness of Elastosil LSR formulations. Lines are only guides for the eye.

As we figured out earlier, Shore A stiffness of the LSR samples partially increases with increasing cross-linking agent concentration. Therefore, increasing of elongation-at-break in the first region of the curves can be explained by increasing cross-linking agent concentration closely related to the network junction density of the elastomers. At low cross-link density, the LSR samples exhibit a more pronounced viscous-like behavior since the number of elastic chains drops and the number of defects such as dangling and un-cross-linked chains grows. Hence, the bonds in the LSR samples at low stiffness start to break at lower tensile loading.

Conversely, when the cross-link density is too high, the elastomers lose in flexibility between the cross-link junctions and consequently exhibit fragile rubber-like behavior and break at low stress. The loss in flexibility can be also influenced by the silica content. The silica content in the stiff LSR samples is almost two-fold higher in comparison to the content in the softest ones.

3.3.3. Dynamic mechanical analyses (DMA): viscoelastic properties of the LSR

a. DMA using the parallel-plate rotational rheometry

"Standard" protocol of DMA in the parallel-plate geometry

Cylindrical LSR samples were examined by means of a stress-controlled parallel-plate rotational rheometer with 8 mm diameter plates using the "standard" protocol, as described in "Materials and methods". Storage and loss modulus master curves (G' and

G'' versus angular frequency) were measured with the prepared *ex-situ* LSR samples (curing at 165 °C for 5 min) of varied stiffness (9, 21, 34, 42, 59, 72 Shore A). A log-log plot of G' and G'' master curves of three representative LSR samples are shown in **Fig 2.19**.

Storage modulus values of the LSR samples taken at 1 rad/s are listed in **Table 2.5**.

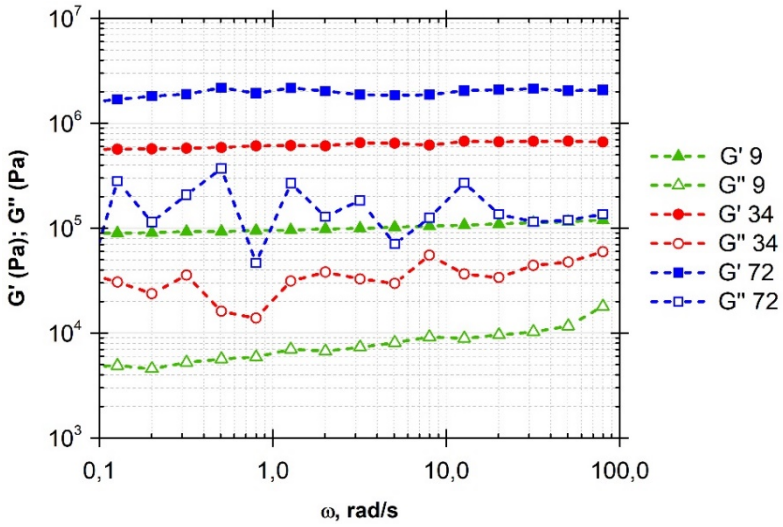

Figure 2.20. Representative storage G' and loss G'' modulus master curves of the *ex-situ* cured LSR samples with Shore A stiffness 9, 34, and 72. Measurements were performed in the parallel-plate geometry with plates of 8 mm in diameter at 10 N static preload.

"Control" DMA of LSR specimens in the parallel-plate geometry

For the control test, the LSR samples were cured within the rheometer (*in situ*) in order to provide an intimate contact with the plates, thereby establishing "no-slip" conditions for DMA testing. The temperature ramps were performed at a constant frequency of 1 rad/s and an applied shear stress of 50 Pa. Thermomechanical analysis (TMA) curves of two representative LSR formulations of Shore A stiffness 34 and 72 are represented in **Fig. 2.21a**. All the other curves are available in **Fig. S6**, **Annex I**.

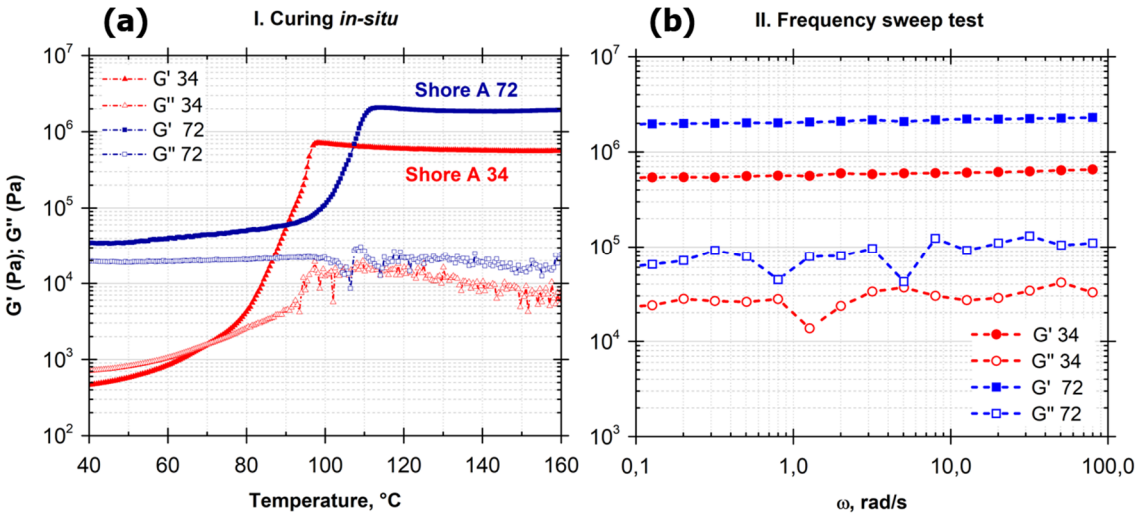

Figure 2.21. (a) Storage G' and loss G'' moduli evolution with temperature during the curing of two representative LSR formulations (34 and 72 Shore A stiffness); (b) G' and G'' master curves of the corresponding *in situ* cured LSR formulations measured at 30 °C

In addition, the cross-linking degree α of the LSR formulations wan be determined from thermomechanical curves using the following formula [150]:

$$\alpha(T) = \frac{G'(T) - G'_{min}}{G'_{max} - G'_{min}} \qquad \textbf{(2.8)}$$

Fig. 2.22 displays the cross-linking degree α(T) of the LSR formulations of varied Shore A stiffness as a function of temperature. Basically, the cross-linking degree evolution with temperature based on rheometric measurements showed a good agreement with α(T) measured by DSC (see **Fig. 2.10**). It can be clearly noticed that the cross-linking reaction shifts to higher temperatures with Shore A stiffness. Moreover, the cross-linking rate increases with Shore A stiffness. Given a heating rate of 2 °C/min, it was found that cross-linking of the LSR formulations takes from 3 (soft LSR) to 6 minutes (stiff LSR).

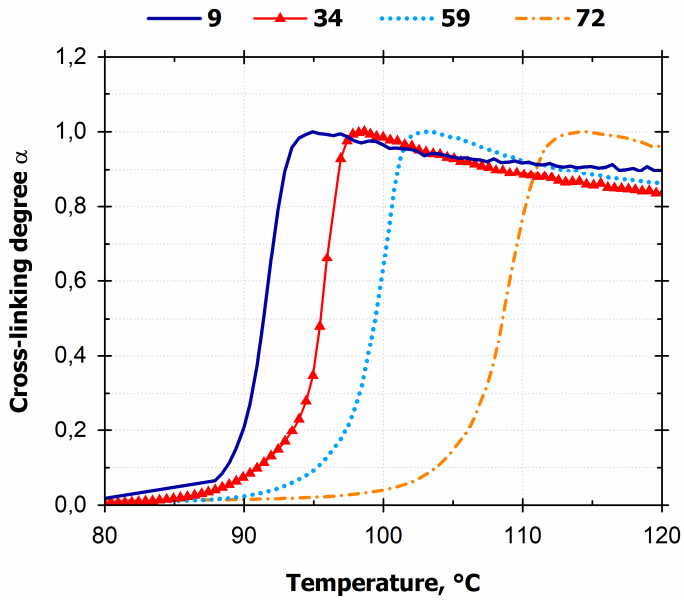

Figure 2.22. Cross-linking degree α of the LSR formulations of varied stiffness as a function of temperature as determined from the TMA measurements at a heating rate of 2 °C/min.

Following the initial step of *in situ* curing, the LSR specimens were subsequently tested by DMA in the 80 to 0.08 rad/s frequency range at 30 °C (**Fig. 2.21b**). **Fig. 2.23** compares the storage moduli of the LSR formulations of varied Shore A stiffness measured by the "standard" method (using *ex-situ* prepared specimens) and the "control" method (using *in situ* prepared specimens) at a frequency of 1 rad/s and at 30 °C.

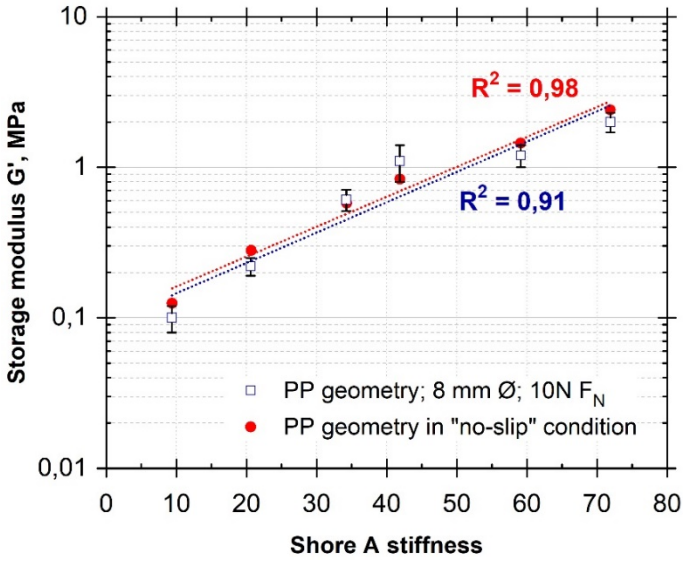

Figure 2.23. Storage modulus as a function of Shore A stiffness of Elastosil LSR formulations. Shear measurements performed in the parallel-plate mode. Each data point measured using the "standard" protocol (squares) represents an average of 3 tests

The exponential correlation fitting the experimental data measured using both the "standard" and "control" protocols are almost identical. They can be aligned to a common formula:

$$G' = 0.09 \cdot \exp(0.05 \cdot Shore\ A) \qquad \textbf{(2.9)}$$

From equation (2.7) and (2.9), the ratio of Young's modulus measured by tensile test, E, to shear modulus measured by DMA in the parallel-plate geometry tends to 2. The theoretical ratio of Young's modulus to shear modulus for ideal rubbers is equal to 3 [156]. These results are in a close agreement with each other, especially bearing in mind two different systems of measurement (in stretching and in shear).

The values in **Table 2.5** combine the elastic moduli of the cross-linked unpost-cured LSR samples of varied stiffness gathered using different approaches. Young's modulus values of the LSR samples were also estimated from DMA measurements using the theoretical relation for perfectly elastic materials between the Young's modulus, E, and the shear modulus $E = 3G$.

Table 2.5. *Comparison of elastic moduli of the cross-linked LSR samples measured using different approaches.* [a] *Young's modulus evaluated from DMA in the parallel-plate method using ex-situ prepared specimens.* [b] *Young's modulus evaluated from DMA in the parallel-plate method using in situ prepared specimens.* [c] *Young's modulus evaluated from tensile tests*

Shore A stiffness	G'_{std}, ***MPa***	G'_{ctrl}, ***MPa***	E_{std}, ***MPa*** [a]	E_{ctrl}, ***MPa*** [b]	E_{ts}, ***MPa*** [c]
9	(0.10 ± 0.02)	0.13	(0.30 ± 0.06)	0.4	(0.30 ± 0.02)
21	(0.20 ± 0.03)	0.3	(0.6 ± 0.1)	0.9	(0.60 ± 0.01)
34	(0.6 ± 0.1)	0.6	(1.8 ± 0.3)	1.8	(1.10 ± 0.02)
42	(1.1 ± 0.3)	0.8	(3.3 ± 0.9)	2.4	(1.7 ± 0.2)
59	(1.2 ± 0.2)	1.44	(3.6 ± 0.6)	4.3	(3.4 ± 0.1)
72	(2.0 ± 0.3)	2.4	(6.0 ± 0.9)	7.2	(6.5 ± 0.1)

b. DMA using the rectangular torsion rheometry

Fig. 2.24 displays the storage modulus values of LSR measured in the rectangular torsion geometry. The values obtained with the ARES and Anton Paar 302 rheometer are almost identical and differ from each other in the uncertainty limits. The storage modulus of the cross-linked LSR samples ranges from 0.3 to 4.8 MPa.

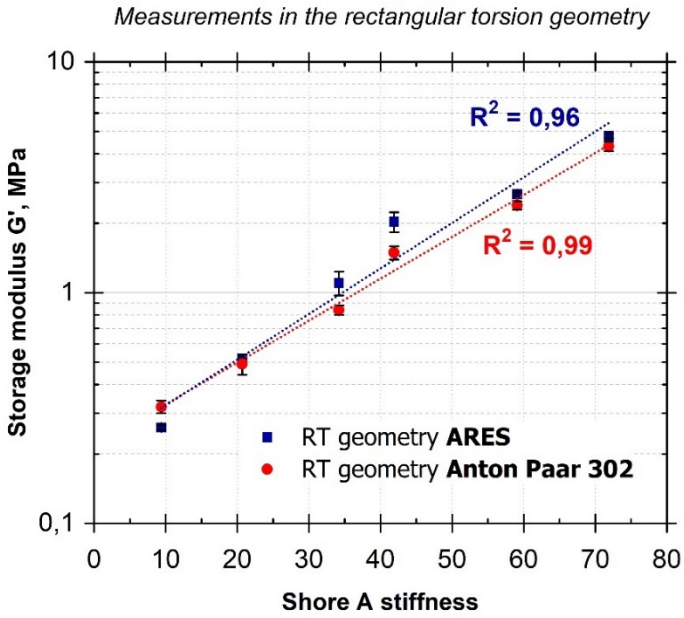

Figure 2.24. Storage modulus as a function of Shore A stiffness of Elastosil LSR formulations. Shear measurements performed in the rectangular torsion geometry. Each data point represents an average of 2 (by ARES rheometer) and 3 (by Anton Paar 302 rheometer) measurements

Compared to the moduli measured in the parallel-plate geometry, these values are considerably higher (from two to three times). Previously, Dessi *et al*. [157] reported an increase in shear modulus measured in torsion, resulting from extensional and compressional stresses occurring near the clamps. They also showed a clear dependence of the storage modulus on the length-to-width ratio ranging between 0.4 and 1.9.

A specimen subjected to a twisting moment exhibits two torsion components: primary torsion, generating in-plane (bar cross-section plane) shear stress distribution, and secondary torsion (sometimes, warping torsion), generating out-of-plane cross-section distortions along the axis of twist. As pointed by Dessi *et al*. [148], the secondary torsion is caused by the prevention of warping deformations at both ends of the specimen, due to the presence of clamps.

In most commercial rheometers, the shear modulus is evaluated from the measured raw torsion torque value using de Saint-Venant's equation. However, this equation does consider only the primary torsion component, i.e., the warping torsion effect, which leads to an overestimation of the shear modulus.

Chapter III

The effects of LSR surface texturing and mechanical properties on bacterial retention

1. Introduction

As described above (see part 1.4.2.c "Antibacterial surfaces inspired by nature", chapter I) the surface micro/nano texturing in combination with the low surface energy of materials leads to enhanced superhydrophobic properties.

The idea was to achieve a superhydrophobic LSR surface possessing a texture that favors the confinement of air cushions beneath a bouncing droplet, leading to the Cassie-Baxter's state (see **Fig. 1.4**, chapter I). In this state (sometimes named the Fakir's state) the true area of liquid-solid contact is restricted to the summits of the textured surface. Therefore, the surface texturing is expected to reduce the available anchor points for bacterial attachment in the liquid medium and thus to prevent bacterial contamination.

In this chapter, we begin by providing the comprehensive analysis of surface characteristics of the cured LSR samples such as surface energy and topography. The surface energy was determined on flat-like LSR samples through the Owens-Wendt method. The topography of both textured and flat-like LSR surfaces was investigated by means of electron microscopy (SEM), optical profilometry (OP) and by the sessile drop technique. In the further course of the chapter, we describe the effects of both the mechanical properties and the surface texturing of the LSR samples on bacterial retention which were examined. The *in vitro* retention assays of *Escherichia coli* cells were performed on both flat-like and textured LSR surfaces by epifluorescence microscopy imaging and by the plate count method.

2. Materials and methods

2.1. Preparation of LSR samples: transfer of a texture to the LSR surface

To assess the effect of LSR surface texturing on bacterial retention, both flat-like and textured LSR surfaces were obtained by hot molding.

2.1.1. Flat-like LSR surfaces

In order to obtain flat-like LSR surfaces, LSR specimens of 25 mm diameter and 2 mm thickness were processed by hot molding, i.e., in the heating press at 165 °C under 40 bars pressure for 5 minutes. Hard aluminum foils of 100 µm thickness, composed of at least 99.5 % of aluminum (pure alloy EN AW-1050A) were used as prints for both sides

of the LSR specimens. The foils exhibit a mean roughness R_a of about 0.2 µm, measured using a digital surface roughness tester.

Other surfaces, such as silicon wafers and glass slides exhibiting a mean roughness of about 1-2 nm, were tested as prints to obtain a perfectly flat LSR surface. However, since silicon wafers are brittle and fairly easy to break, only small pieces of silicon wafer (1×1 cm^2 area) can be used for molding to avoid a fracture of the silicon surface. Moreover, when using silicon wafers or glass slides as prints, the systematic appearance of fissures on cured LSR surfaces clearly indicates the cohesive fracture within the LSR material during the final demolding step. In most cases, cohesive fracture was observed with the soft LSR samples. This behavior is most likely due to the increase of energy required for interfacial rupture with the soft LSR samples. We suggest that the principal parameter leading to increased rupture energy is deformability of the soft LSR samples. On the one hand, increase of the rupture energy can be affected by energy dissipation through viscous forces. On the other hand, easily deformable samples establish a good contact with highly flat surfaces, thus increasing the molecular interaction at the sample – print interface and, consequently, the adhesion energy.

2.1.2. Textured LSR surfaces

Owing to low processing viscosity prior to cross-linking, LSR formulations enable the transfer of a pattern from a mold to the surface with great precision by molding. LSR surfaces of varied Shore A stiffness were textured by hot molding (heating press at 165 °C under 40 bars pressure for 5 minutes) using the foils with a superhydrophobic coating patented by Radchenko *et al*. [158] in 2016. The foils used as prints are coated with hydrophobic micro- and nanoparticles of sizes ranging from 5 nm to 35 µm, thus providing them superhydrophobicity. A scheme of the surface texturing process is shown in **Fig. 3.1**.

Textured LSR samples of varied Shore A stiffness (9, 21, 34, 59, 72) were produced using superhydrophobic foils (hereinafter SH foils).

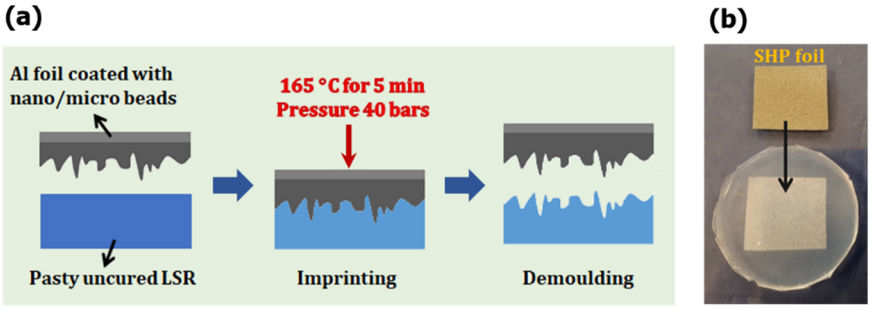

Figure 3.1. (a) Illustration of the LSR surface texturing by the hot molding process; (b) A representative LSR surface of 59 Shore A stiffness textured by hot molding

2.2. Surface characterization of the LSR

2.2.1. Determination of the surface free energy of the LSR by the Owens-Wendt method

The surface free energy of cross-linked LSR specimens was determined using the Owens and Wendt theory [159]. This theory was developed to take into account specific interactions between solid surfaces and liquids. Owens and Wendt divide the surface energy into two components – a dispersive component and a polar component. Since the dispersive component is theoretically related to Van der Waals interactions between a solid surface and a liquid, the polar component theoretically accounts for dipole-dipole interactions, hydrogen bonding, and other site-specific interactions with which a surface could engage in with a liquid. The theory combines the Good's [160] and Young-Dupre equations to extract:

$$\frac{\gamma_l(1+\cos\theta)}{2\sqrt{\gamma_l^d}} = \sqrt{\gamma_s^p}\cdot\sqrt{\frac{\gamma_l^p}{\gamma_l^d}} + \sqrt{\gamma_s^d} \qquad \textbf{(3.1)}$$

wherein γ_l is the overall surface tension of the wetting liquid, γ_l^p and γ_l^d are polar and dispersive components of the surface tension of the wetting liquid, respectively, γ_s^p and γ_s^d are the polar and dispersive components of the surface tension of the solid, respectively, and θ is the contact angle of a liquid on a solid. Equation (3.1) is a linear equation in the $y = ax + b$ form, in which:

$$y = \frac{\gamma_l(1+\cos\theta)}{2\sqrt{\gamma_l^d}}$$

$$x = \sqrt{\frac{\gamma_l^p}{\gamma_l^d}}$$

$$a = \sqrt{\gamma_s^p}$$

$$b = \sqrt{\gamma_s^d}$$

Therefore, the contact angle values of the probe liquids measured on a surface of interest and surface tension values of the probe liquids γ_l, γ_l^p, and γ_l^d provide the information necessary to plot x versus y. Once the values are plotted in this manner, the slope of the trendline a is used to calculate the polar component of the solid surface tension γ_s^p, and the intercept b is used to calculate the dispersive component of the solid surface tension γ_s^d. The surface tension of a solid material under study is calculated as a sum of polar and dispersive components $\gamma_s = \gamma_s^d + \gamma_s^p$.

For the LSR surface energy determination, three liquids with well-known surface tension values (**Table 3.1**), hexadecane, diiodomethane, and water, were used as probe liquids. The contact angle data of the probe liquids were obtained for each *flat-like* LSR sample using a homemade optical tensiometer. The measurements were carried out at a room temperature of 21 °C. A total of 10 droplets were analyzed per sample using the ImageJ software (version 1.53c).

Table 3.1. *Surface tension values of the probe liquids*

Probe liquid	γ_l, ***mN/m***	γ_l^d, ***mN/m***	γ_l^p, ***mN/m***	***x***
Hexadecane	27.1	27.1	0	0
Diiodomethane	50.8	48.5	2.3	0.22
Water	72.8	21.8	51	1.53

2.2.2. Wetting properties of the textured LSR

The wetting properties of the textured LSR surfaces of different stiffness (9, 21, 34, 59, 72 Shore A) were obtained via static contact angle measurements using a homemade optical tensiometer. The water droplets volume was of about 5-6 µL throughout all the contact angle measurements. A total of 10 droplets per sample were analyzed using the ImageJ software. All the contact angle measurements were done at a room temperature of 21 °C.

2.2.3. Characterization of the LSR surfaces by scanning electron microscopy (SEM)

The topographical features of the textured LSR surfaces were characterized by scanning electron microscopy (SEM). It is an important electron microscopy technique that enables to achieve high resolution images (on the order of nanometers) of a sample surface using the principle of electron-matter interactions.

Inelastic interactions between the primary electron beam directed to the specimen and the specimen surface result in emission of low-energy secondary electrons (SEs). Due to low energy of SEs, they can only escape from the near-surface regions of the sample (a few nanometers). Thus, a zone of SE emission is highly localized at the point of impact of the primary electron beam, which makes them beneficial for imaging the high-precision surface topography (**Fig. 3.2**). The SEs are collected by a secondary electron detector, and their impact is then transformed into electric signals. Scanning the electron beam (in a raster scan pattern) over the surface, it is possible to reproduce an image.

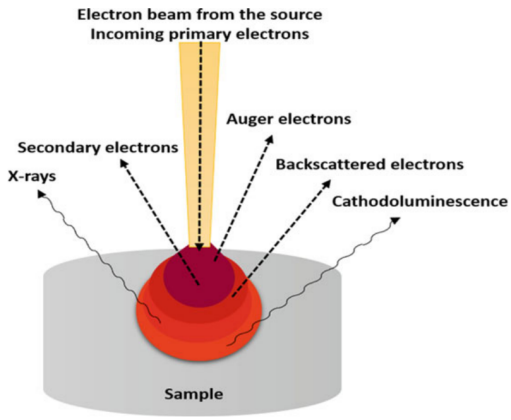

Figure 3.2. Scheme of interaction of the electron beam with the specimen surface. Reprinted from K. Akhtar *et al*., *Handbook of Materials Characterization,* Springer International Publishing, 113-145 (2018) [161]

The SEM micrographs were recorded with an SH-3000 scanning electron microscope (Hirox Europe, Lyon, France). Prior to mounting the LSR sample on a specimen holder, the samples were first metalized with gold at 30 mA emission intensity during 60 s. The resulting gold layer of about 10 nm in thickness serves to make elastomer surface electrically conductive. Each sample was subsequently fixed on a stub using a conductive carbon tape to enable it to withstand vacuum conditions. SEM images of the LSR surfaces of varied stiffness (9, 21, 34, 59, 72 Shore A) were captured at ×150 and ×500 magnification (809 × 608 μm^2 and 243 × 182 μm^2 scanned area, respectively).

2.2.4. Optical profilometry measurements

Both smooth and textured LSR surfaces were characterized by optical profilometry at the National school of engineers of Tarbes (ENIT). This technique allows to gather numerous information about the surface topography with nanometric vertical resolution. The LSR surface profiles were scanned using the Wyko NT1100 3D profiler (Veeco Instruments Inc., New York, USA), and topographical data were analysed using the Vision software (version 5.60).

For the LSR surface measurements, the vertical scanning interferometry technique was employed. White light passes through a beam splitter, which directs the light to the sample surface and a reference mirror (**Fig. 3.3a**). When the light reflected from these two surfaces recombines, a pattern of interference "fringes" forms. Maximum fringe contrast occurs at the best focus position. Thus, when the test surface is scanned vertically each point on the surface passes through focus (**Fig. 3.3b**). Frames of interface data imaged by a camera are captured and processed at intervals of about 40 nm during the scan.

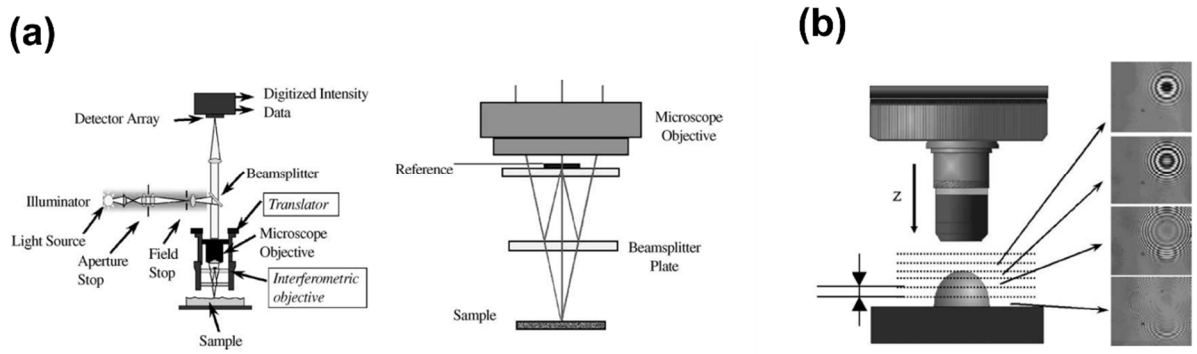

Figure 3.3. (a) Scheme of a vertical scanning interferometer; (b) While the objective scans along the vertical axis Z, the fringes develop as each area of the surface moves into focus. Reprinted from Devillez *et al*. *Wear* 256, 1-2, 56-65, (2004). [162]

To evaluate the LSR surface topography, we used characteristic parameters of surface topography such as mean surface roughness S_a, root mean square (rms) surface roughness S_q, skewness S_{sk}, kurtosis S_{ku}, and roughness factor r.

- Surface roughness S_a is a roughness parameter that expresses the difference in height of each point compared to the arithmetical mean of the surface.

$$S_a = \frac{1}{A}\iint_A |Z(x,y)|dxdy \qquad \textbf{(3.2)}$$

- Root mean square (rms) roughness S_q is a roughness parameter that gives the standard deviation of height.

$$S_q = \sqrt{\frac{1}{A}\iint_A Z^2(x,y)dxdy} \qquad \textbf{(3.3)}$$

- Surface skewness S_{sk} describes the asymmetry of the height distribution. Negative values of S_{sk} refer to a surface-porous sample; that is, the valleys dominate over the peak regimes. Respectively, the local summits dominate over the valleys when $S_{sk} > 0$.

$$S_{sk} = \frac{1}{{S_q}^3}\left[\frac{1}{A}\iint_A Z^3(x,y)dxdy\right] \qquad \textbf{(3.4)}$$

- Surface kurtosis S_{ku} measures the sharpness of the surface height distribution, equals 3.0 for a surface with a normal height distribution. Values smaller than 3.0 indicate a broad (heterogeneous) height distribution whereas values much higher than 3.0 refer to a surface with a sharper height distribution [163].

$$S_{ku} = \frac{1}{{S_q}^4}\left[\frac{1}{A}\iint_A Z^4(x,y)dxdy\right] \qquad \textbf{(3.5)}$$

- Roughness factor r is defined as the ratio of the real rough surface A_{real} area to the nominal surface area $A_{nominal}$. For perfectly smooth surfaces $r = 1$.

$$r = \frac{A_{real}}{A_{nominal}} \qquad \textbf{(3.6)}$$

2.3. Bacterial retention assays

2.3.1. Bacterial growth

The *Escherichia coli* strain used in this study is DH5α carrying the plasmid pSEVA337 which contains the green fluorescence protein (GFP) gene under the control of the constitutive Pem7 promoter. pSEVA337 carrying the resistance to chloramphenicol was obtained from the Standard European Architecture 3.0. [164]

A growth medium used for the cultivation of *E. coli* is lysogeny broth (LB), a nutrient-rich medium composed of 10 g/L of sodium chloride (NaCl), 10 g/L of tryptone and 5 g/L of yeast extract. The buffer solution used for bacterial retention assays is phosphate buffered saline (PBS), a water-based salt solution with pH ≈ 7.4 containing 8 g/L of NaCl, 0.2 g/L of potassium chloride (KCl), 1.42 g/L of disodium hydrogen phosphate (Na_2HPO_4) and 0.24 g/L of potassium dihydrogen phosphate (KH_2PO_4).

The *E. coli* strain *DH5α* was kindly provided by Prof. Régis Grimaud (Université de Pau et des Pays de l'Adour, France). LB and LB agar used for the preparation of agar plates were purchased from by Difco (Saint-Ferréol, France). PBS (10× concentrate), chloramphenicol (≥98%), and a nonionic detergent Tween20 (BioXtra) were supplied by Sigma-Aldrich (St-Quentin-Fallavier, France).

The *E. coli* strain was routinely grown at 37 °C in LB and LB agar supplemented with 34 μg/mL of chloramphenicol to maintain the plasmid. To illustrate the bacterial growth curve, the evolution of the optical density of the medium that was periodically sampled during the growth is shown in **Fig. 3.4**. All the optical density measurements were performed using an Eppendorf biophotometer (Marshall Scientific, Hampton, NH, USA). Using the exponential trendline formula, one can easily calculate that the bacterial population doubled every $(\ln 2/0.017)$ min, i.e., about every 40 min.

The bacterial cells were grown in LB medium under shaking at 37 °C up to the exponential phase of growth at optical density at 600 nm of 0.6. Cells were harvested by centrifugation at 5000 rpm for 10 min. The supernatant was removed, and bacteria were re-suspended in PBS to an optical density at 600 nm of 0.1 (≈ 10^7 cells/mL). A more detailed *E. Coli* growth protocol description is reported in the **Annex III**.

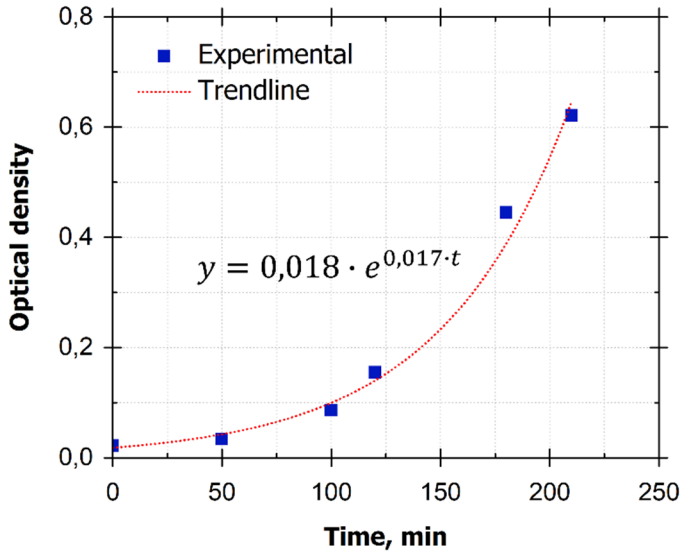

Figure 3.4. Representative bacterial growth curve. The beginning of the curve corresponds to the lag phase, characterized by no apparent cell division occurence

2.3.2. Bacterial retention assays using epifluorescence microscopy

The fluorescence spectrum of the bacterial suspension with ≈ 10^7 cells/mL was measured by means of a fluorescence spectrophotometer Edinburgh FLS920 equipped with the xenon lamp as an excitation source and a double monochromator which enables recording high-resolution spectra (1 nm resolution) (Edinburgh Instruments, Livingston, United Kingdom). The emission spectrum was recorded within the 490–650 nm scanning range at 480 nm excitation wavelength.

Bacterial retention on the flat-like LSR samples of varied Shore A stiffness (9, 34, 45, 59, and 72) was assessed using the epifluorescence microscopy. The cylindrical LSR samples of 22 mm in diameter and 2 mm in thickness were molded using an aluminum foil on both sides. Each sample was cleaned in an ultrasonic bath containing deionized water for 10 min, and subsequently put horizontally into a 50 mL sterile container.

The bacterial suspension with ≈ 10^7 cells/mL was poured in sterile containers containing clean LSR samples, 25 mL in volume for each one. After incubation at 37 °C for 1 hour (3 hours) without shaking, the LSR samples were gently washed by dipping in PBS three times (changed to clean PBS at each step). Then, a PBS droplet was deposited on surfaces under study, and glass coverslips were placed on top to obtain a monolayer of *E. coli*. In addition, attention was paid to put a coverslip on the top sides of the LSR samples, i.e., those which were in contact with the bacterial suspension during incubation (instead of the bottom of container).

The LSR samples were subsequently mounted between a glass slides and a coverslip and observed using an Axio Observer Z1 inverted fluorescence microscope (Zeiss, Jena, Germany) equipped with an oil immersion objective 63× NA 1.4. Green fluorescent protein-expressing cells were visualized using a BP 470/40 excitation filter, a FT 495 beam splitter, and a BP 525/50 emission filter. Images were acquired using a Zeiss Axiocam 506 mono camera monitored by the Zeiss Zen 2012 software.

2.3.3. Bacterial retention assays using the plate counting method

a. Enumeration of CFU

The plate count method (PCM) is based on the direct numeration of colonies formed on a nutrient agar by cultivating an aliquot from the initial sample or one of its serial dilutions (**Fig. 3.5**). It is worth noting that this method does not directly estimate a total number of microorganisms present in the sample. They are only estimations of the number of organisms able to multiply on a given medium, for a given duration to form a colony, also referred to as colonies forming units (CFU).

Usually, a number of colonies enumerated using the plate count method is underestimated in comparison to the total number of bacteria found in a sample [165,166]. Two or more bacteria can form a single colony if they form a cluster or if colonies merge to form a single one. Therefore, two or more bacteria can be enumerated as a single CFU. In addition, not all viable bacteria will form a colony within the cultivation duration, but they can recover with time and thus stay potentially pathogenic.

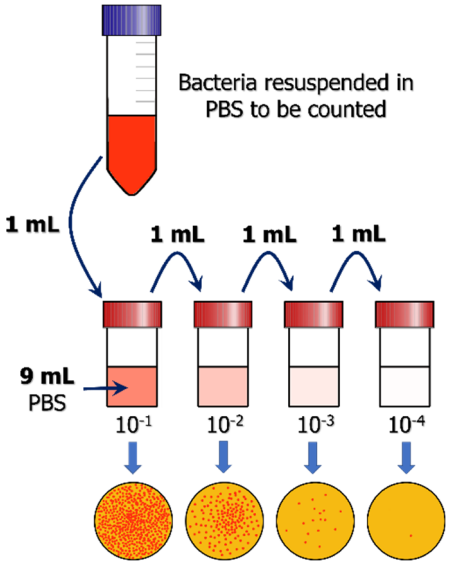

Figure 3.5. Scheme of the plate count procedure

Bacterial retention on both flat-like and textured LSR samples of varied Shore A stiffness (9, 34, 59, 72) was assessed using the plate count method. The cylindrical LSR samples of 22 mm in diameter and 2 mm in thickness were molded using an appropriate print on both sides. Each sample was cleaned in an ultrasonic bath containing deionized water for 10 min, and subsequently put into a sterile tube. All the sample from a series were oriented and positioned in exactly the same way to avoid the unequal bacteria sedimentation impact.

The bacterial suspension with approximatively 10^7 cells/mL was poured in sterile tubes containing clean LSR samples, 25 mL in volume for each tube. After incubation at 37 °C for 1 hour (3 hours) without shaking, the LSR samples were gently washed by dipping in PBS three times (changed to clean PBS at each step). Then, the adhered cells were detached from the LSR surfaces by shaking in 15 mL of PBS containing 0.01 vol. % of the Tween20 surfactant. Bacteria re-suspended in the surfactant-containing PBS were enumerated using the spread plate technique. 100 µL aliquots from a series of decimal dilutions of the surfactant-containing bacterial suspension were spread on agar plates using sterilized spreaders, as illustrated in **Fig. 3.5**. The agar plates were then incubated at 37 °C overnight to count colonies.

The CFU concentration in the bacterial suspension in which the LSR samples were incubated was also enumerated.

The number of CFU detached from the LSR surfaces was calculated as the weighted average from two successive dilutions, following the formula:

$$N = \frac{\sum N_{plate}}{(n_1 + 0.1 \cdot n_2) \times d \times V} \qquad \textbf{(3.7)}$$

where $\sum N_{plate}$ is a total number of CFU counted on all the plates selected for enumeration (at least one of them must contain > 15 CFU), V is a volume of aliquot applied to each agar plate (here 100 µL), n_1 is a number of selected plates from a first dilution (here 1), n_2 is a number of selected plates from a second dilution (here 2), d is a dilution factor of the first dilution selected for enumeration.

b. Assay reproducibility and bacterial cell survivability

The efficiency of bacterial detaching from LSR surfaces by rinsing in PBS containing the Tween20 surfactant was also probed by fluorescence microscopy. To do so, two LSR samples with Shore A stiffness 34 were incubated in the bacterial suspension

at 37 °C for 2 hours. One of the samples was gently washed in three PBS rinsing baths, then a PBS droplet was deposited on the sample and a coverslip was placed on top prior to epifluorescence imaging. The second sample also treated through three PBS rinsing baths, followed by shaking in PBS containing 0.01 vol. % of the surfactant for 20 sec, was subsequently imaged by epifluorescence microscopy. Following the shaking in PBS containing 0.01 vol. % of the detergent, bacterial cells completely disappeared from microscopy images (**Fig. 3.6**).

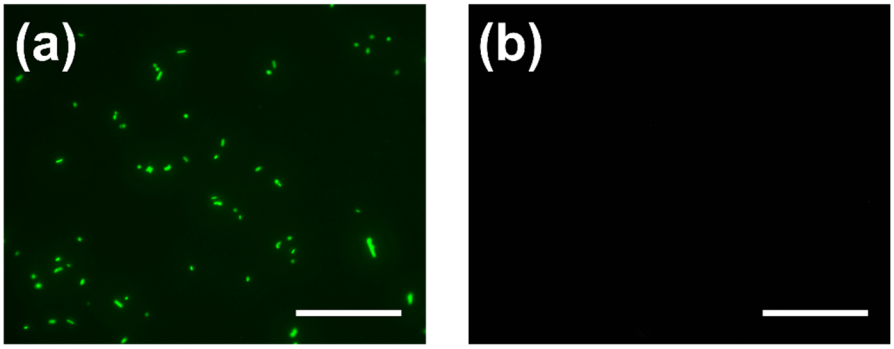

Figure 3.6. Representative images of *E. coli* cells retained on the LSR surface of Shore A stiffness 34 (a) only rinsed in three PBS baths and (b) rinsed in three PBS baths and shaken in PBS containing 0.01 % of the detergent for 20 sec. The scale bars represent 50 μm

To check that the Tween20 surfactant did not lyse bacterial cells during an assay, bacterial growth was initiated simultaneously in both LB containing 34 μg mL^{-1} of chloramphenicol and LB containing 34 μg mL^{-1} of chloramphenicol and 0.01 vol. % of the Tween20. Exponential growth curves of bacteria grown in both media, with and without the surfactant was monitored by measuring the optical density at 600 nm (**Fig. 3.7**). As can be noticed, the growth curves represented in **Fig. 3.7** are almost identical.

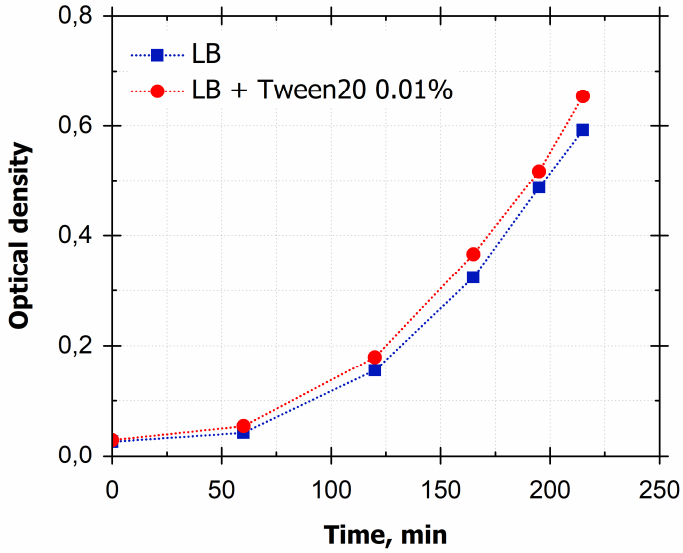

Figure 3.7. Bacterial growth curves of the inoculum suspended in LB medium (filled squares) and in LB medium containing 0.01 vol. % of Tween20 (filled circles). The beginning of the curve corresponds to the lag phase, characterized by no apparent cell division occurence.

3. Results and discussion

3.1. Surface characterization of the LSR

3.1.1. Surface free energy of the cross-linked LSR (Owens-Wendt method)

First of all, we measured static contact angles of the probe liquids (hexadecane, diiodomethane, and water) on the flat-like LSR surfaces of varied stiffness (9, 21, 34, 42, 59, 72 Shore A). **Fig. 3.8**. shows the contact angles of the probe liquids for each sample.

We noticed from **Fig. 3.8** that the contact angle of hexadecane (non-polar liquid) on the LSR surfaces increased with stiffness, while the contact angle of water (polar liquid) exhibited a slight decrease from 94° to 90° as the Shore A stiffness increased. Indeed, the Pearson correlation analysis indicates a positive correlation between the hexadecane contact angle and the stiffness of LSR formulations ($r = 0.72, p < 0.05$). By contrast, the water contact angle shows a modest negative correlation with the stiffness, the correlation coefficient $r = -0.40$ being statistically different from zero ($p < 0.05$).

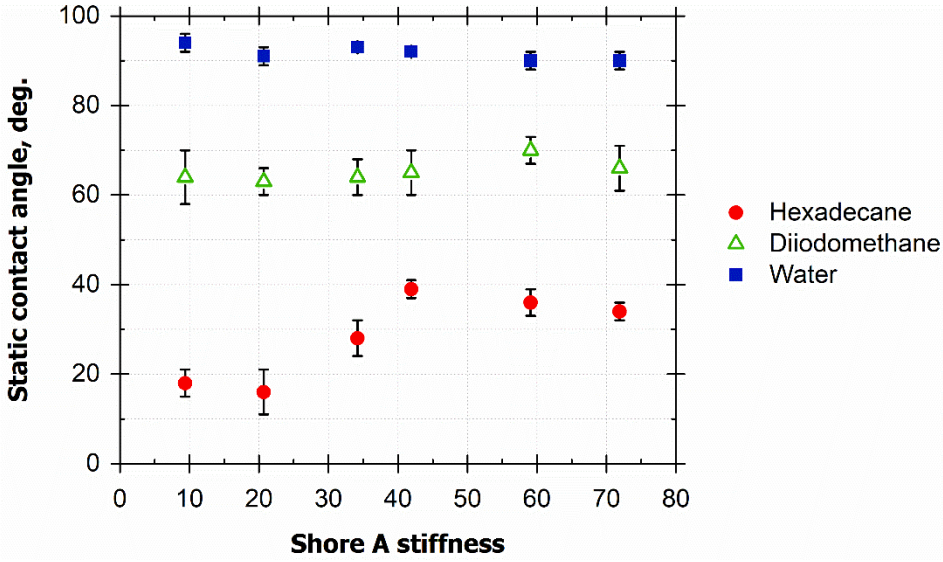

Figure 3.8. Static contact angles of hexadecane (filled circles), diiodomethane (unfilled triangles), and water (filled squares) on the flat-like LSR surfaces of varied stiffness. Averages of 10 droplets for each data point.

As mentioned in the part "**Materials and methods**", once we have the contact angles of the probe liquids on a given LSR surface, we are able to plot the contact angle data in the Owens-Wendt format (see equation (3.1)). First, we calculated x_i and y_i values for each probe liquid, and then we plotted a linear function $y = ax + b$ using the three points (x_i, y_i), each one corresponding to a probe liquid. The parameters of interest a and b, corresponding to the square root of the polar component γ_s^p and the dispersive component γ_s^d of a given LSR surface, respectively, are found by the method of least squares.

The surface energy values measured on the flat-like LSR surface of varied stiffness (9, 21, 34, 42, 59, 72 Shore A stiffness) are listed in **Table 3.2**.

Table 3.2. *Surface energy of the flat-like LSR samples (Owens-Wendt method)*

Shore A stiffness	γ_s^d, *mN m*$^{-1}$	γ_s^p, *mN m*$^{-1}$	γ_s, *mN m*$^{-1}$
9	25.1	2.1	(27 ± 3)
21	25.3	2.9	(28± 3)
34	24.0	2.6	(26.6 ± 0.2)
42	22.1	3.4	(26 ± 3)
59	21.0	4.4	(25 ± 4)
72	22.4	4.0	(26.4 ± 0.9)

The estimation of the confidence interval of the surface tension $\Delta\gamma_s$ is detailed in the **Annex II**. The Pearson correlation analysis strongly indicates no-correlation between the surface tension γ_s and the stiffness of the LSR formulations under study. However, we noticed that the polar component values γ_s^p of the stiff LSR surfaces was almost doubled compared to those of the soft ones ($r = 0.9, p < 0.05$).

Given the data obtained by TGA, we can suppose that the increase in the polar component γ_s^p with stiffness is related to the silica filler content in the LSR formulations. The content of silica filler increases almost twice with stiffness, from 18 wt.% for the softest sample to 33 wt. % for the stiffest one (see **Table 2.2**). Since polar materials are attracted to each other by dipole-dipole attractions, silica favors interaction with polar liquids, such as water. This principle is used, for example, in thin-layer chromatography (TLC) where silica gel serves as an adsorbent material [167]. Summarizing the above, the LSR formulations exhibit a low surface energy of 25 – 28 mN/m. Albeit the overall surface tension does not vary with stiffness, the elevated content of silica filler in the stiff LSR formulations can however enhance polar type interactions with liquids.

It is important to note that the Owens-Wendt equation assumes a perfectly flat homogenous surface. Therefore, achieved surface tension values must be taken with care, as most real surfaces are not perfect due to surface defects, chemical heterogeneity, etc. Specifically, the LSR surfaces used for determination of surface energy exhibit a significant roughness (see below) and are chemically inhomogeneous due to the presence of silica fillers. Nevertheless, the variation of the polar component with stiffness can still be retained.

3.1.2. Water contact angle measurements (WCA)

In order to evaluate the hydrophobicity of the textured LSR surfaces, the water contact angles of these surfaces were measured using the sessile drop method. **Fig. 3.9** compares the contact angle on two LSR surfaces of the same stiffness, the flat-like LSR surface printed with an aluminum foil and the textured LSR surface printed with an SH foil.

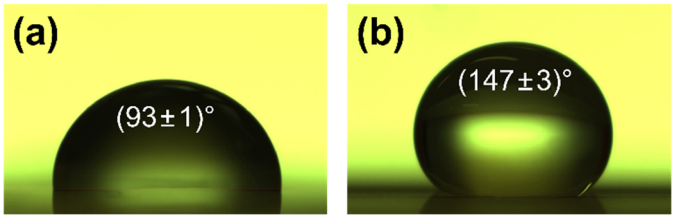

Figure 3.9. Water contact angle of the LSR surface of Shore A stiffness 34 printed with (a) an aluminum foil and (b) an SH foil.

As can be seen, the texturing significantly improves the water repellency of the LSR surfaces. The contact angles of the textured surfaces increase by 40 – 50° that makes them superhydrophobic. Apart from the static contact angle, the surface superhydrophobicity is also characterized by the low droplet retention on the surface. The tilting angle of the textured LSR wasn't determined, nevertheless, during the measurements water droplets rolled off the textured surfaces at a minor inclination. It was estimated to be tending to 0° due to the direct observations. That is, droplets deposited on the textured LSR sits upon surface asperities (Cassie-Baxter state), and tilt easily due to the reduced solid-liquid contact area.

Fig. 3.10 shows the positive correlation between the contact angle and the stiffness of the textured LSR samples ($r = 0.97, p < 0.05$, Pearson correlation analysis). The contact angle on the textured surfaces increased with stiffness and tends to reach that of the superhydrophobic foil.

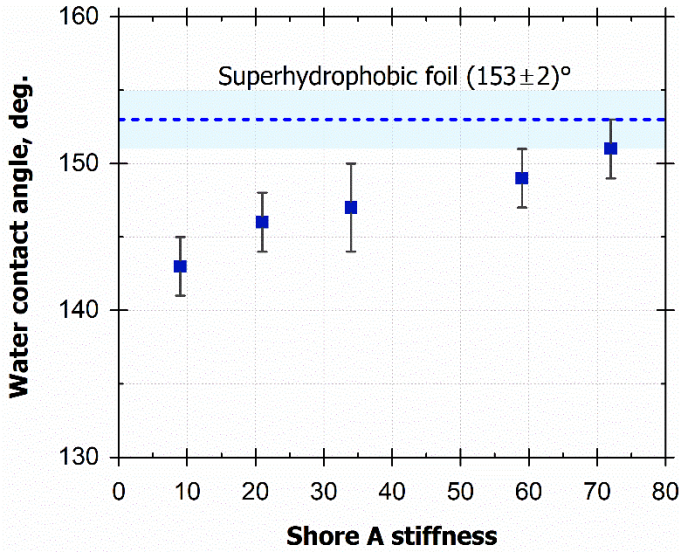

Figure 3.10. Water contact angle of the LSR surfaces textured with SH foils as a function of Shore A stiffness

If a droplet is in the Cassie–Baxter state, i.e., sits on top of asperities of a rough surface, thus trapping air cushions in cavities beneath the droplet, the appearing contact angle θ_{app} can be estimated as

$$\cos\theta_{app} = f\cos\theta - (1-f) \qquad \textbf{(3.8)}$$

where f is defined as the fractional area of the solid surface that is wetted by the liquid at the liquid – solid interface (solid – liquid contact area normalized by the projected area of the droplet base) (see **Fig. 1.7**, Chapter I). The fraction of the liquid – air interface is $(1-f)$, and θ is the contact angle on a flat surface of the same material.

The fraction f, derived from the Cassie–Baxter equation, was computed for each textured LSR surface:

$$f = \frac{1+\cos\theta_{app}}{1+\cos\theta} \qquad \textbf{(3.9)}$$

The contact angles and the fraction f of the textured LSR surfaces are summarized in **Table 3.3**. The fraction f, i.e., the surface area fraction wetted by water, decreases with stiffness by almost half.

To clarify the correlation between the contact angle on the textured surfaces and the stiffness, two factors need to be assessed:

- Ability of the LSR to transfer a surface pattern.
- Variation in surface energy with stiffness

Table 3.3. *Surface tension values of the probe liquids*

Shore A stiffness	$\boldsymbol{\theta_{app}}$	$\boldsymbol{f}$
9	(143 ± 2)°	0.22
21	(146 ± 2)°	0.17
34	(147 ± 3)°	0.17
59	(149 ± 2)°	0.14
72	(151 ± 2)°	0.13

As explained in the previous part, the higher content of silica fillers in the stiff LSR favors interaction with polar liquids, such as water. Thus, if the effect of stiffness on the water repellency observed in **Fig. 3.9** was caused by changes in surface energy, we would expect a decrease in contact angle with stiffness. However, the contact angle on the textured LSR was found to increase with stiffness from (143 ± 2)° to (151 ± 2)°. It

reaffirms that the increase of water repellency with stiffness is caused by the ability of the LSR to transfer a pattern, rather than surface energy.

To estimate the ability of LSR to transfer a surface texture, visualization of the textured LSR using scanning electron microscopy and thorough analysis of the topographic features of the textured LSR using optical profilometry were performed, as described below.

3.1.3. Characterization of the LSR surfaces by scanning electron microscopy (SEM)

SEM images of the textured LSR surfaces captured at ×500 magnification are shown in **Fig. 3.11a-e**. It can be seen from the images that the LSR samples under investigation exhibit randomly textured surfaces featured with pores with sizes ranging from a few up to several tens of micrometers that resulted from the surface pattern printing using the superhydrophobic foil. Indeed, the superhydrophobic foil imaged by SEM (**Fig. 3.11f**) exhibits topographical features in the form of spherical microbeads, in a size range similar to that of the porous features just mentioned.

SEM images of the textured LSR surfaces captured at ×150 magnification are less resolved regarding the small features, however, they provide a good representation of the texture that enables to achieve the Cassie-Baxter wetting state (see **Fig. S6**, **Annex III**).

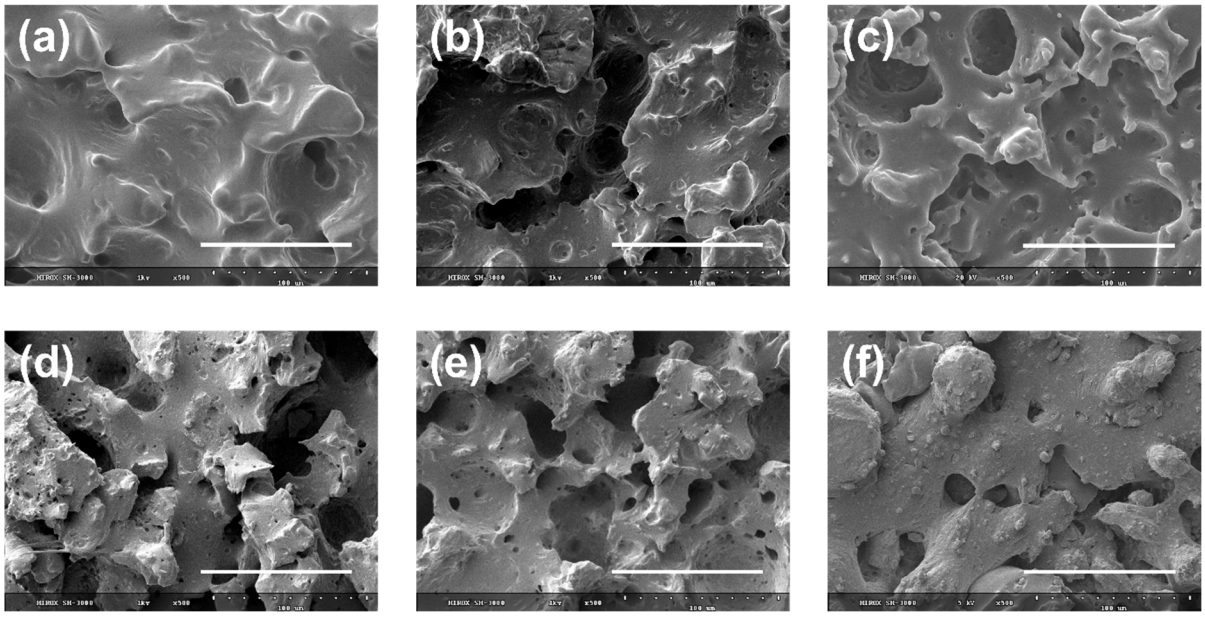

Figure 3.11. Representative SEM images of the textured LSR samples of varied Shore A stiffness: (a) 9, (b) 21, (c) 34, (d) 59, (e) 72. (f) SEM image of the superhydrophobic foil used as print surface. The scale bars represent 100 μm.

We noticed the appearance of tiny pores of a few micrometers (~1-10 µm) in the stiff LSR samples (**Fig. 3.11d,e**). Indeed, they become more and more pronounced with increasing stiffness value. Moreover, the smoothed features on the soft LSR samples become sharp-edged with increasing stiffness. Therefore, we came to the conclusion that the stiff LSR samples have a superior ability to transfer a surface pattern than the soft ones.

As mentioned in Chapter II, the LSR surfaces of low stiffness exhibit a more pronounced viscous-like behavior owing to the lower cross-link density and higher content of dangling and un-cross-linked chains. In addition, the PDMS chain mobility can be also influenced by the low silica content. The pores on the low-stiffness LSR surfaces (**Fig. 3.11a,b**) thus probably result from the high chain mobility that enables to adjust the surface features shape in ways that minimize the surface area, i.e., minimize the surface tension.

We can also assume that a further increase in stiffness would impair the ability of LSR to transfer of a surface pattern owing to the high processing viscosity prior to cross-linking.

Fig. 3.12 shows SEM images of the flat-like LSR surface of a Shore A stiffness 34 captured at ×150 and ×500 magnification. It can be noticed that the flat-like LSR samples exhibit groove-patterned surfaces reprinted from the aluminum foil. The topographical properties of the LSR surfaces are more detailed in the next part devoted to the measurements by optical profilometry.

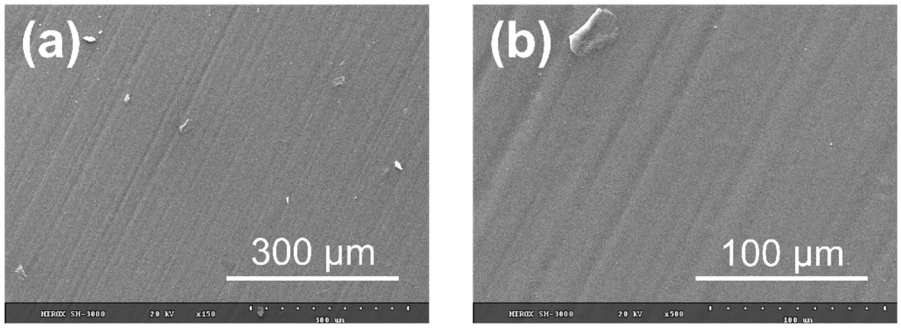

Figure 3.12. Representative SEM images of the flat-like LSR samples of Shore A stiffness 34 with a scale bar of (a) 300 µm and (b) 100 µm.

3.1.4. Topographic characteristics of the LSR surfaces

a. Flat-like LSR surfaces

The topography of the flat-like LSR surfaces of varied Shore A stiffness (9, 21, 34, 59, 72) was determined by scanning 1.2×0.9 mm^2 area spots on each sample. A representative image of the three-dimensional surface topography measured by optical profilometry is shown in **Fig. 3.13**. The flat-like LSR surfaces molded using aluminum foils are patterned with microscale grooves and ridges.

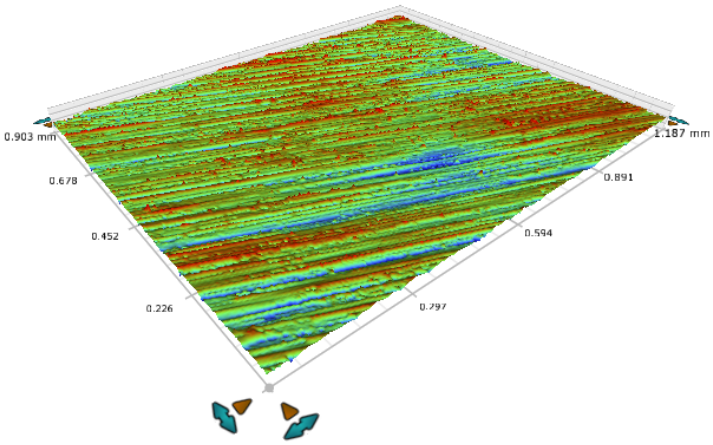

Figure 3.13. Topography of the flat-like LSR surface of Shore A stiffness 72 visualized by Vision software (mean roughness $S_a = 0.3\ \mu m$, rms roughness $S_q = 0.4\ \mu m$)

The values of topography parameters such as mean roughness S_a and rms roughness S_q are presented in **Table S1** (see **Annex II**). S_a and S_q are equal to 0.3 µm and 0.4 µm, respectively, for all the measured LSR surfaces of Shore A stiffness 9, 21, 34, 59, and 72.

However, the roughness parameters poorly describe the topography of a surface covered by ridges and grooves. To make a quantitative analysis of the topography of the flat-like LSR surfaces, the maximum height of ridges and the maximum depth of the grooves were measured, along with the width of the ridges and of the grooves, or more specifically their full width at half maximum (FWHM).

To do so, the height/depth and FWHM were measured from the profiles taken in a perpendicular orientation to the ridges/grooves (**Fig. 3.14a**). About 70 ridges and 70 grooves were considered and the values averaged for each sample (**Fig. 3.14b**).

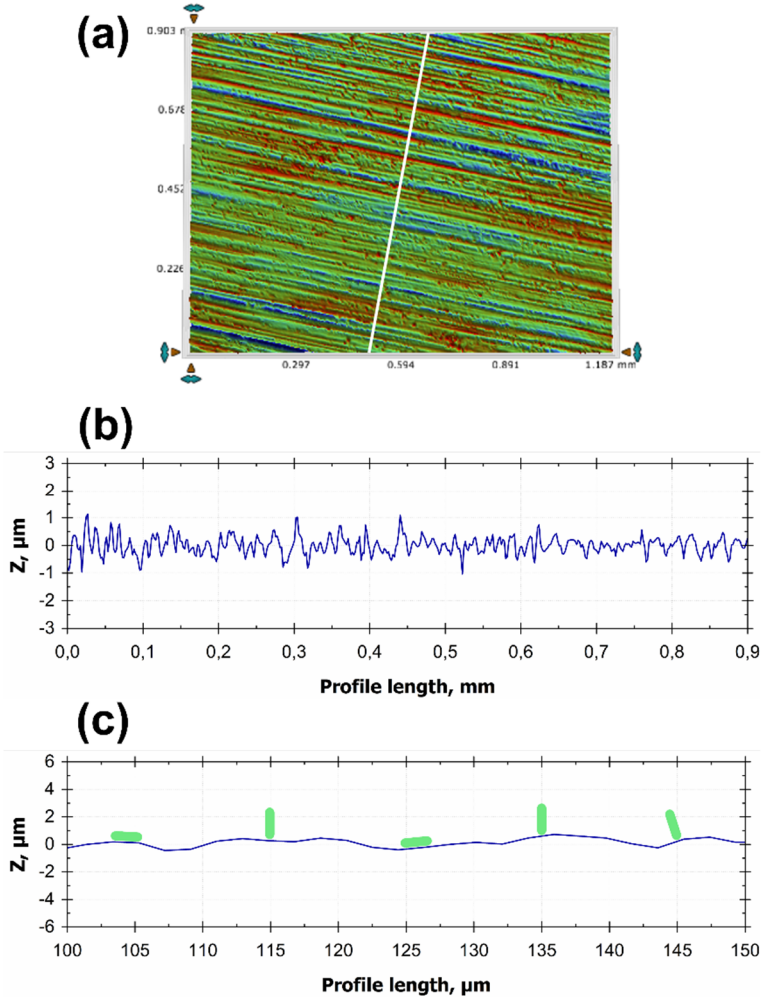

Figure 3.14. (a) Representation of the topography of the flat-like LSR surface of Shore A stiffness 59 at 1.2×0.9 mm² area. The white line indicates the position of the analyzed profile (b) Surface profile of the flat-like LSR taken in the perpendicular orientation to the grooves (profile length 900 µm). The *z*-axis is stretched by a factor of 36. (c) A part of the same profile represented at a real scale, to visualize the surface roughness (profile length 50 µm). Light-green pellets represent to-scale *E. coli* cells placed in arbitrary positions.

The height and width values of ridges and grooves from the flat-like LSR samples are gathered in **Table 3.4**.

The histograms in **Fig. 3.15** show the distributions of height and width values of about 70 ridges/grooves. The displayed distribution histograms were smoothened using 3-point moving averages. As can be noticed from **Table 3.4** and **Fig. 3.15**, the topographical characteristics of ridges and grooves do not significantly vary with stiffness. Moreover, the characteristics of the ridges are almost identical to those of grooves.

Table 3.4. *Height and width values of ridges/grooves of the flat-like LSR samples*

Shore A stiffness	**FWHM, µm**		**Height/depth, µm**	
	Ridges	*Grooves*	*Ridges*	*Grooves*
9	(4 ± 2)	(4 ± 2)	(0.3 ± 0.2)	(0.3 ± 0.2)
21	(4 ± 2)	(4 ± 2)	(0.4 ± 0.2)	(0.3 ± 0.2)
34	(4 ± 2)	(4 ± 2)	(0.4 ± 0.2)	(0.4 ± 0.3)
59	(4 ± 2)	(4 ± 2)	(0.4 ± 0.2)	(0.4 ± 0.2)
72	(4 ± 2)	(4 ± 2)	(0.4 ± 0.2)	(0.4 ± 0.2)

As discussed in Chapter I, bacteria oriented parallel to the grooves of similar width is stronger than adhesion to flat surfaces, because of the increased contact area with the walls of the grooves. The LSR surfaces molded using aluminum foils exhibit ridges and grooves with an average height/depth of 0.4 µm and an average FWHM of 3.2 – 3.8 µm. Given an average *E. coli* cell size of about 0.5 µm in diameter and 2 µm in length, we can assume that grooves on the LSR surfaces do not significantly alter potential adhesion of the bacteria. Indeed, a real-scale profile (**Fig. 3.14c**) illustrates the shallow and relatively broad grooves and the equally low and broad ridges in relation to the bacterial cell size. Bacteria can fit in the grooves in any orientation.

The roughness factor r, i.e., the ratio of the actual surface area to its projected area, of the flat-like LSR surfaces was found to be about 1.02 for each sample. That means that the real surface areas of the LSR samples are only 2 % higher than the nominal ones.

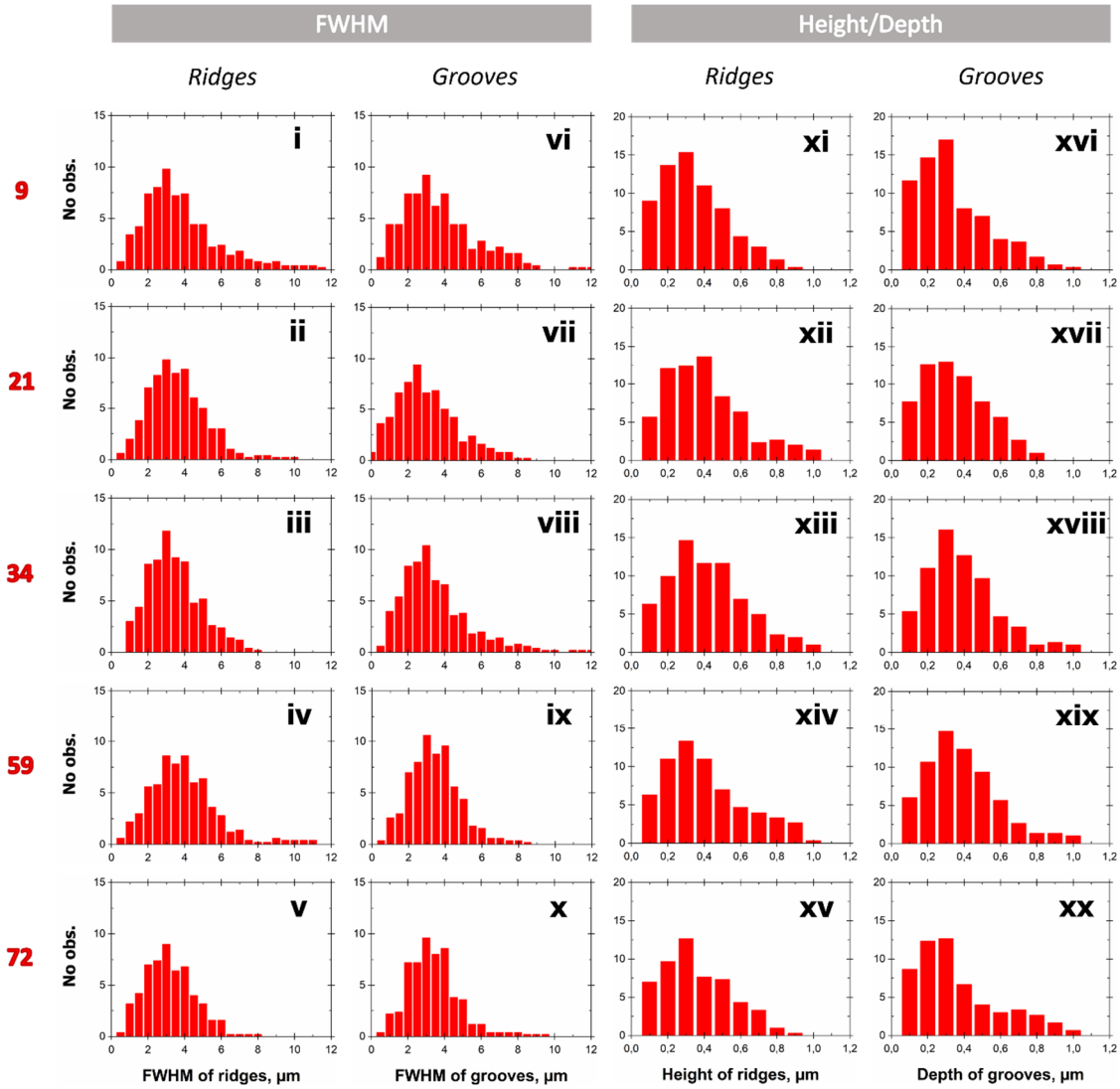

Figure 3.15. (i – v) FWHM distributions of ridges on flat-like LSR samples of Shore A stiffness (i) 9, (ii) 21, (iii) 34, (iv) 59, and (v) 72; (vi – x) FWHM distributions of grooves on flat-like LSR samples of Shore A stiffness (vi) 9, (vii) 21, (viii) 34, (ix) 59, and (x) 72; (xi – xv) Height distributions of ridges on flat-like LSR samples of Shore A stiffness (xi) 9, (xii) 21, (xiii) 34, (xiv) 59, and (xv) 72; (xvi – xx) Depth distributions of grooves on flat-like LSR samples of Shore A stiffness (xvi) 9, (xvii) 21, (xviii) 34, (xix) 59, and (xx) 72.

b. Textured LSR surfaces

The textured LSR topography of samples of varied Shore A stiffness (9, 21, 34, 59, and 72) was measured at 6 different spots of 1.2×0.9 mm^2. The topography of the SH foil was measured on 15 different spots across the whole foil surface which was subsequently cut into pieces and used for molding. A representative image of the three-dimensional surface topography as measured by optical profilometry is shown in **Fig. 3.16**. The LSR

samples molded using SH foils exhibit randomly textured surfaces featured with hills and valleys.

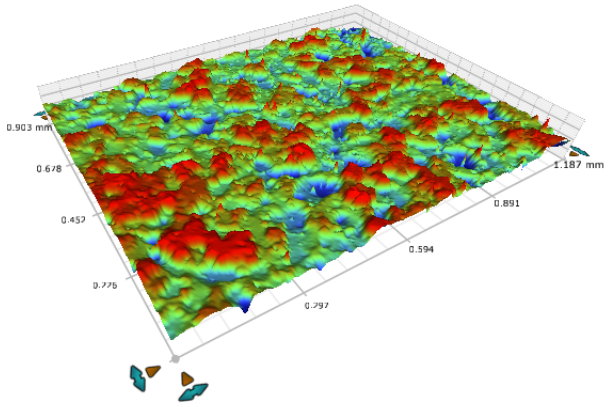

Figure 3.16. Topography of the textured LSR surface of 59 Shore A stiffness as reconstructed using the Vision software (mean roughness $S_a = 19.9\ \mu m$, rms roughness $S_q = 25.0\ \mu m$)

The values of topography parameters such as mean roughness S_a, rms roughness S_q, skewness S_{sk}, kurtosis S_{ku}, and roughness factor r are summarized in **Table 3.5**.

Table 3.5. *Surface topography parameters of the textured LSR samples of varied stiffness*

Shore A stiffness	S_a, **µm**	S_q, **µm**	S_{sk}	S_{ku}	r
9	(18.6 ± 0.5)	(23.8 ± 0.6)	(-0.1 ± 0.2)	(3.5 ± 0.4)	(2.5 ± 0.1)
21	(19.4 ± 0.8)	(24.7 ± 0.8)	(0.01 ± 0.04)	(3.4 ± 0.4)	(2.9 ± 0.01)
34	(20 ± 1)	(26 ± 2)	(0.2 ± 0.1)	(3.2 ± 0.3)	(2.6 ± 0.1)
59	(20.3 ± 0.4)	(25.4 ± 0.3)	(-0.2 ± 0.1)	(3.0 ± 0.1)	(3.2 ± 0.1)
72	(17 ± 2)	(22 ± 3)	(-0.03 ± 0.2)	(3.5 ± 0.3)	(2.5 ± 0.2)
SH foil	(18 ± 1)	(23 ± 2)	(0.07 ± 0.3)	(3.8 ± 0.3)	(3.2 ± 0.2)

The mean roughness and the rms roughness of the textured LSR surfaces range from 17 µm to 20 µm and from 22 µm to 26 µm, respectively. Interestingly, maximum S_a and S_q values of 20 µm and 26 µm occur at points corresponding to the medium stiff surfaces (34 and 59 Shore A stiffness). Although, maximum roughness values were expected for the SH foil surface used as print, the roughness values of the mentioned medium stiff surfaces are greater than those of the SH foil. The difference between the roughness values of the surfaces of Shore A stiffness 34 and 59 and those of the SH foil is statistically significative ($p < 0.05$, t-test). It can be tentatively explained by the heterogeneity of the superhydrophobic coating across the SH foil.

As an illustration of Gaussian-like surfaces, representative surface height distributions were plotted using the data collected from a spot area of 1.2×0.9 mm² for each sample. Surface height distributions of the textured LSR samples displayed in **Fig. 3.17** were fitted with unimodal Gaussian distribution functions. High coefficients of determination, R^2, tending to 1 indicate quite faithful fitting, i.e., the experimental data are well-modeled by a normal distribution. Skewness values ranging between -0.3 and 0.3 indicates fairly symmetrical distribution of heights for each textured LSR sample. Kurtosis values of the textured LSR surfaces are of 3, confirming the normal distribution of height.

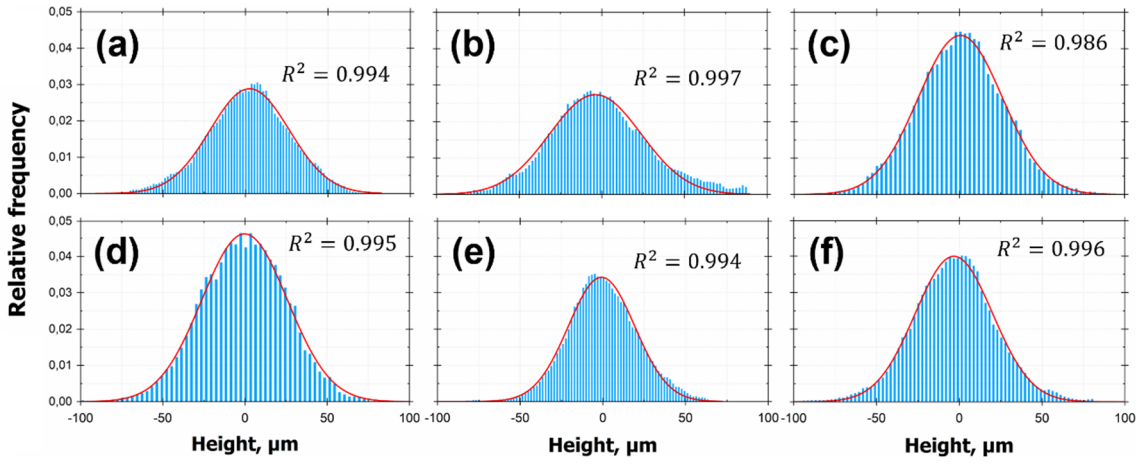

Figure 3.17. Representative surface height distributions of the textured LSR surface of Shore A stiffness (a) 9, (b) 21, (c) 34, (d) 59, (e) 72, and (f) of an SH foil. The distributions were fitted with Gaussians (red curves). The coefficient of determination for the fitting, R^2, is shown as well.

The roughness factor r of the textured LSR surfaces varies from 2.5 to 3.2. It means that the texturing of the LSR samples increased their surface areas by 150 – 220 %. The maximum r value of 3.2 occurring at a Shore A stiffness of 59 is identical to that of the SH foil. It is most likely due the high ability of the LSR of Shore A stiffness 59 to properly replicate the surface texture of the SH foil. The topographic parameters mentioned above, as well as the information gathered through scanning electron microscopy let us assume that there is a medium-stiff LSR formulation having the optimal mechanical properties which reveal a superior ability to transfer a surface pattern by molding. This LSR formulation of medium Shore A stiffness 59 has a Young's modulus of about 3.5-4.5 MPa, depending on the method used to measure the value (tensile test, DMA). The LSR of lower stiffness cannot exactly replicate asperities from the textured foil surface owing to the high polymer chain mobility which tends to minimize the surface area and smooths asperities out. The LSR of higher stiffness, in turn, fails to replicate a surface pattern owing to the high processing viscosity prior to cross-linking.

3.2. Bacterial retention on LSR surfaces

3.2.1. Bacterial retention assay using epifluorescence microscopy

The fluorescence emission spectrum of the *E. coli* strain under study is shown in **Fig. 3.18**. The maximum emission wavelength corresponds to 510 nm (green fluorescence).

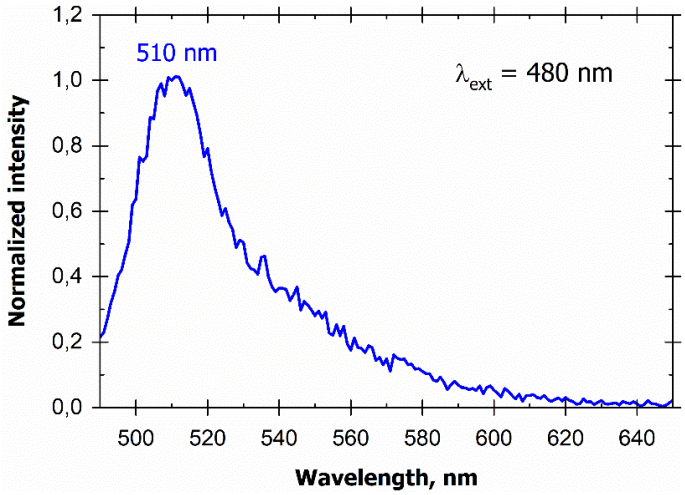

Figure 3.18. Emission spectrum of green-fluorescent *E. coli* with 480 nm excitation wavelength

Bacterial cells retained on the LSR surfaces were randomly imaged using epifluorescence microscopy at 10 spots of 200×160 μm^2 area for each sample. **Fig. 3.19** shows two representative images of bacteria retained on the LSR surface of Shore A 34 subsequent to 1 hour and 3 hours of incubation. The bacterial density, i.e., the number of visualized bacterial cells per area, retained on the flat-like LSR surfaces was calculated using the ImageJ software (version 1.53c).

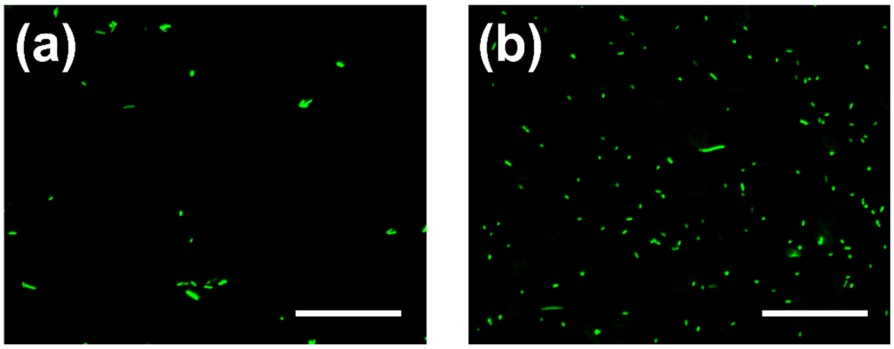

Figure 3.19. Representative images of *E. coli* DH5 cells retained on the LSR surface of Shore A stiffness 34 subsequent to (a) 1 hour and (b) 3 hours of incubation. The scale bars represent 50 μm

Epifluorescence microscopy assays were performed for a series of samples of various Shore A stiffness (9, 34, 45, 59, and 72). 4 assays were carried out for samples incubated for 1 hour, 7 assays were done for samples incubated for 3 hours. **Fig. 3.20** displays the data resulting from the microscopy assays.

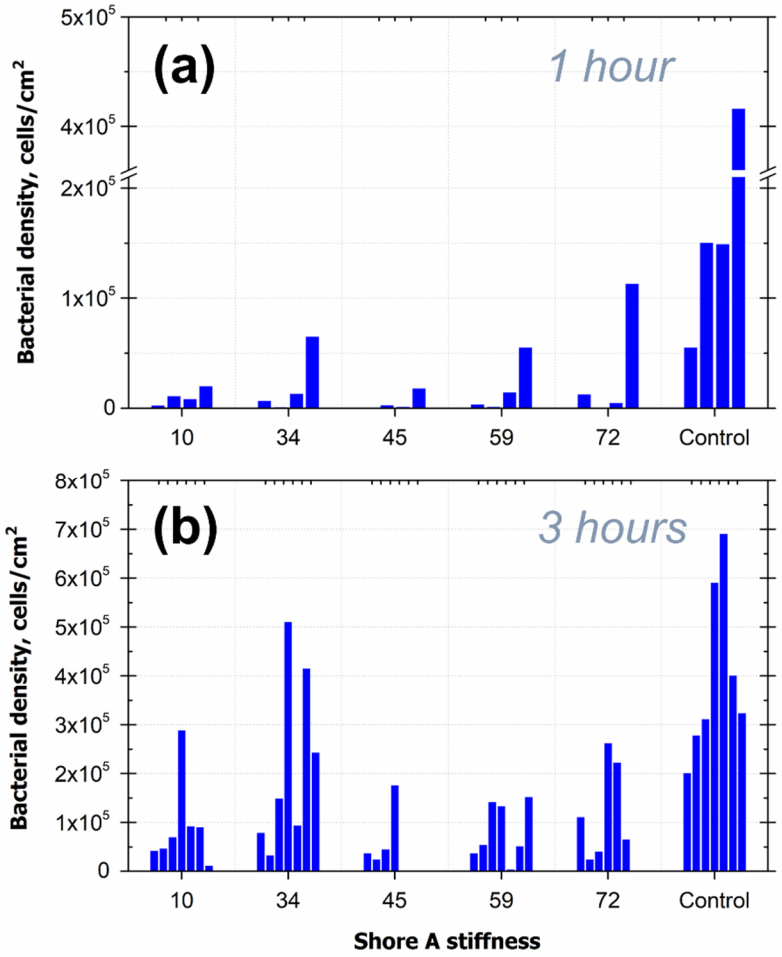

Figure 3.20. Bacterial density on the flat-like LSR surfaces of varied Shore A stiffness subsequent to (a) 1 hour and (b) 3 hours of incubation in a bacterial suspension containing ≈10^7 cells/mL. (a) Data gathered through 4 bacterial retention assays using epifluorescence microscopy, only 3 assays done with Shore A stiffness 45. (b) Experimental data gathered through 7 bacterial retention assays using epifluorescence microscopy, only 4 assays with Shore A stiffness 45.

It can be noticed from **Fig. 3.20** that the bacterial density measured by means of fluorescence microscopy varies enormously from one assay to another. The bacterial density on the control surfaces, i.e., microscope slides, varies from 2×10^5 to 7×10^5 cells/cm^2. We can also notice from **Fig. 3.20** that the bacterial density of the samples incubated for 3 hours increased compared to those incubated for 1 hour, by about one order of magnitude. To normalize the outcomes of each set of the measurements, the

bacterial density on the LSR surfaces was divided by the bacterial density on the control surface from a respective assay (**Fig. 3.21**).

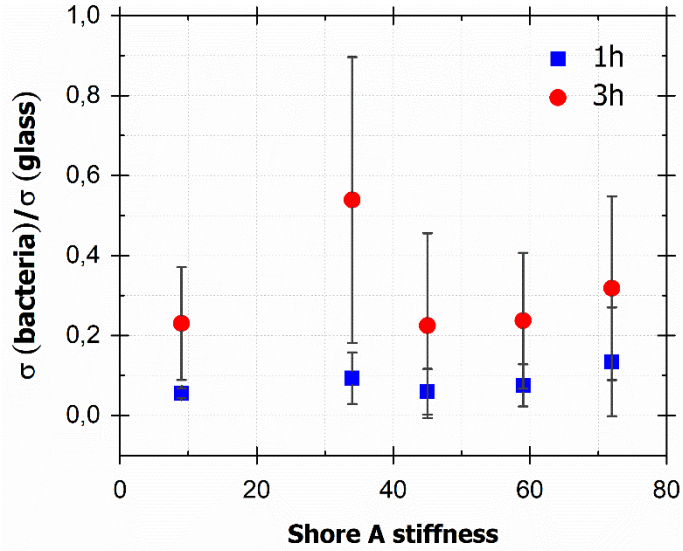

Figure 3.21. Bacterial density on the flat-like LSR samples of varied Shore A stiffness subsequent to 1 hour (filled squares) and 3 hours (filled circles) of incubation, divided by bacterial density on a glass slide from a respective bacterial retention assay. Each data point represents an average of 4 assays (filled squares) and 7 assays (filled circles).

Even when normalized (in this context, divided by bacterial density on the control surfaces), data points vary considerably, involving large error bars. As can be seen in **Fig. 3.21**, the normalized bacterial density for both 1 hour and 3 hours incubated samples varies within the experimental error.

Bacterial assays using epifluorescence microscopy revealed numerous disadvantages for this study. The prolonged exposition of bacteria to the light can cause photobleaching, a process whereby the GFP chromophore loses its ability to fluoresce effectively, leading to fading of the fluorescent signal. That is, bacteria exposed to the light stimulating their fluorescence gradually lose the brightness and finally become invisible by microscopy.

We compared the fluorescence of bacteria at the beginning of epifluorescence imaging and after 1 and 3 minutes of exposition to the UV light of the microscope. To do so, a droplet of the bacterial suspension was deposited on a glass slide and a glass coverslip was placed on top to obtain a monolayer of *E. coli*. Then, bacteria exposed to the UV light were imaged at one spot at different time points (**Fig. 3.22**).

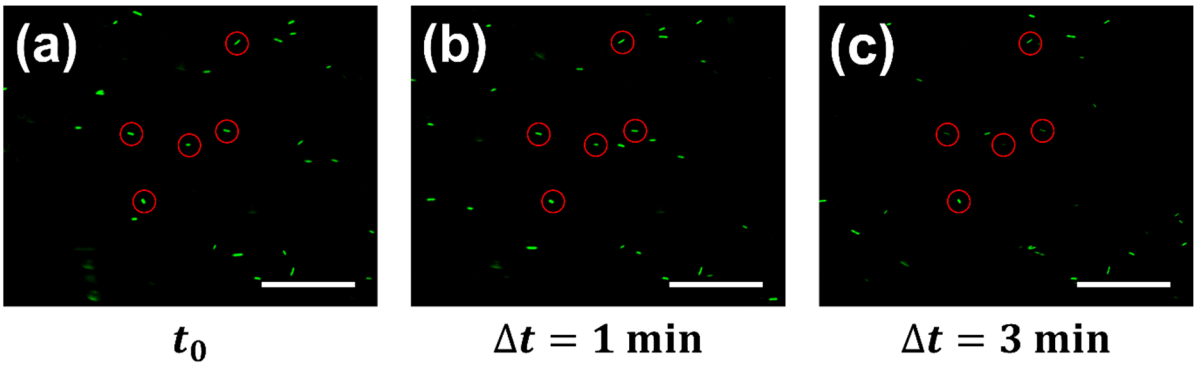

Figure 3.22. Representative images of *E. coli* DH5 cells (a) at the beginning of exposition to the UV light and subsequent to (b) 1 minute and (c) 3 minutes of exposition. The scale bars represent 50 μm

Fig. 3.22 illustrates the remarkable photobleaching of bacteria exposed to the UV light for 3 minutes, although the fluorescence of bacteria exposed to light for 1 minute is fairly stable, despite a little brightness loss. It should be noticed that a part of bacteria was moving from right to left across the image during the measurement, that is, some bacterial cells disappeared from the images by floating away. These issues could probably be resolved by means of confocal fluorescence microscopy, however only few assays using confocal microscopy were attempted in this study, with little success owing to an inappropriate microbial growth protocol used for these assays.

Another disadvantage, the depth of focus of the microscope is limited to a few hundred nanometers. When the flat-like LSR surface passes through focus, bacteria attached to this surface are in focus as well. However, it becomes an issue for the textured surfaces with roughness values of about 20 μm. To obtain an image showing all the bacteria retained on the textured LSR surface, numerous sequential images at each focal plane are required. With this method, sequential images are gathered by shifting the specimen at a fixed interval along the optical axis, and the 3D image stack is built (optical sectioning microscopy). However, this type of image is extremely long to achieve, and it is impossible to enumerate the attached bacterial owing to the rotating, moving, and floating movement of bacterial cells, which results in a blurred image.

To avoid photobleaching over the duration of fluorescence microscopy imaging and to exclude the issue of acquiring 3D images of textured substrates, we resorted to the plate count method, which requires the detachment of bacteria from the specimen surfaces for subsequent enumeration.

3.2.2. Bacterial retention assay using plate count method

Bacterial retention assays using the plate count method were performed with both flat-like and textured LSR samples of various Shore A stiffness (9, 34, 59, and 72). Six assays were carried out with each series of samples. For each assay, the concentration of *E. coli* CFU in the bacterial suspension was determined by CFU enumeration on agar plates. It was found that the samples were incubated in the bacterial suspension at a CFU concentration ranging between 1×10^7 and 2×10^7 CFU/mL from one assay to another.

Further, the number of CFU retained on the LSR surfaces was normalized to the CFU concentration in the bacterial suspension from a respective assay. Assuming the linear relationship between the bacterial suspension concentration and the number of cells adhered to the specimen surface and small variations of the bacterial suspension concentration (1 – 2, $\times10^7$ CFU/mL), the number of CFU was recalculated and the bacterial suspension concentration was of 1×10^7 for each assay.

Fig. 3.23 shows the number of *E. coli* CFU retained on the flat-like (textured) LSR surfaces subsequent to 1 hour (3 hours) of incubation, per area.

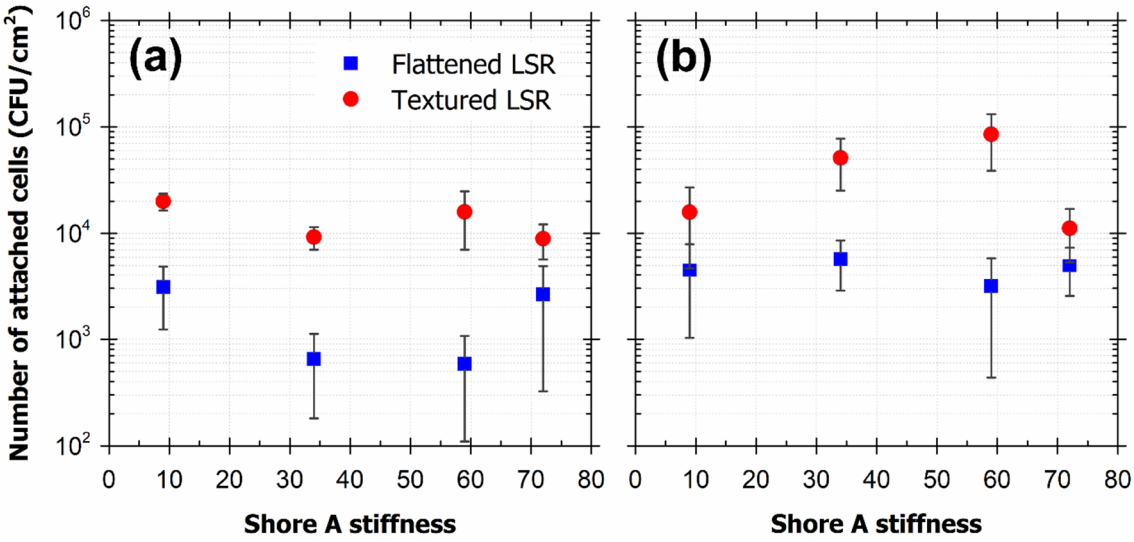

Figure 3.23. Bacterial retention versus Shore A stiffness on both flat-like (filled squares) and textured (filled circles) LSR surfaces subsequent to (a) 1 hour and (b) 3 hours of incubation. Each data point represents an average of 6 assays.

a. Effects of stiffness

To isolate the effects of stiffness from the effects of surface topography, we consider only the outcomes gathered from the flat-like surfaces. The bacterial retention

on the LSR surfaces incubated for 1 hour varies non-monotonically, exhibiting a minimum at medium stiffness values. Student's *t*-test ($p < 0.05$) revealed a significant difference between a data point corresponding the low-stiff surface of Young's modulus of 0.3 MPa and data points corresponding to medium-stiff surfaces with Young's moduli of 1.1 and 3.5 MPa, no significant difference was found between the other point combinations.

At that time, the number of bacteria retained on the LSR surfaces incubated for 3 hours fluctuates around 5×10^3 CFU/cm^2, the Pearson correlation analysis performed on these data indicates strong evidence for the null hypothesis (zero correlation). In addition, no significant difference was found between the data points using the Student's *t*-test.

In previous studies reported by Song *et al*. [114,115], it was found that initial adhesion and biofilm formation of *E. coli* cells were inversely correlated to the stiffness of PDMS elastomers. PDMS samples with Young's modulus ranging from 0.1 to 2.6 MPa were prepared by adjusting the degree of cross-linking. The authors claimed that the effects of the surface chemistry and roughness were negligible. A study reported by Valentin *et al*. [87] also found the inverse correlation between the adhesion of *E. coli* cells and the stiffness of PDMS substrates ranging from 0.02 to 0.6 MPa. The authors suggested that highly deformable soft PDMS reveals a larger contact surface area between a bacterium and a substrate surface. Pan *et al*. [119] also found a decrease in number *E. coli* cells attached on PDMS surfaces with increasing Young's modulus ranging from 0.06 to 4.52 MPa. They did show that *E. coli* fails to respond to the stiffness of PDMS substrates coated with a 2 nm highly cross-linked PDMS used to confer comparable surface chemistry to materials of differing stiffness. The authors suggested that uncoated PDMS of low Young's modulus contains free polymer chains and longer chain ends at the surface, leading to higher bacterial adhesion. They concluded that the PDMS chain ends and free PDMS chains can – on the one hand – work as "tentacles", and – on the other hand – contribute to the interfacial adhesion force to influence the nonspecific bacteria adhesion on different PDMS surfaces.

The Young's modulus of the PDMS-based LSR substrates under study ranges from 0.3 to 6.5 MPa (as measured by tensile tests). As a reminder for the reader the modulus values of the LSR substrates under investigation are show in the **Table 3.6** below. Further discussion is presented in terms of Young's moduli.

Table 3.6. *Young's modulus evaluated by tensile tests*

Shore A stiffness	E_{ts}
9	0.3 MPa
34	1.1 MPa
59	3.4 MPa
72	6.5 MPa

Looking at bacterial retention data in the range of Young's modulus close to those reported in the mentioned studies [114,115,119], i.e., the first three data points from **Fig. 3.23a**, some conclusions can be made. In the 0.3 – 3.5 MPa modulus range, the bacterial retention on the flat-like LSR surfaces incubated for 1 hour is inversely correlated to the substrate stiffness ($r = -0.65, p < 0.05$, Pearson correlation analysis). This is in good agreement with the literature. However, this dependence of bacterial retention on Young's modulus values in the given range is difficult to interpret.

As determined earlier, the LSR formulations of varied stiffness were prepared by adjusting at least two parameters: cross-linking degree and silica filler content (see Chapter II). The last one seemingly alters surface thermodynamical properties of the LSR substrates. Based on the analysis of the surface free energy of LSR, we observed that the elevated content of silica fillers enhances the interactions of polar type at the LSR surfaces.

Because both surface energy and substrate stiffness of the investigated LSR samples commonly alter bacterial retention, it was decided to turn to a model surface with a similar chemical composition whose surface characteristics can be controlled. In Chapter V, the effects of stiffness on the initial retention of the *E. coli* bacterium were investigated using model PDMS surfaces of various substrate stiffness. The other parameters that can impact bacterial retention, such as surface chemistry and topography, were kept constant.

b. Effects of texturing

As outlined in Chapter I, the antibacterial effect of superhydrophobic surfaces is mainly based on lowering the liquid – solid contact area restricted to the summits of the textured surface. However, the number of bacteria retained on the textured LSR surfaces increased substantially, compared to the number of bacteria on the flat-like LSR surfaces.

During bacterial retention assays, we observed that after 3 hours of incubation, the textured surfaces emerged from the bacterial suspension no longer repel water and lose

their Cassie-Baxter wetting state. The tilting angle of a representative surface of Shore A stiffness 34, prior and subsequent to 3 hours of incubation was measured using a tilting stage to physically rotate the substrate with a droplet on its surface. The angle at which droplets deposited on the textured substrate started to move from the surface increased from 5 – 10 deg. to 40 – 70 deg. following 3 hours of incubation.

Such a change in the tilting angle strongly indicates the transition from the Cassie-Baxter wetting state to the Wenzel state. The wetting state of the textured surface is determined by a balance between the energy barrier of the wetting state transition and the external forces, such as Laplace pressure, temperature, etc. [94] The energy barrier magnitude depends on the geometry of textured surface (height-to-width aspect ratio of topographic features, spacing between neighboring hills) and the total interfacial energy [94–96].

As mentioned in Chapter I (part 1.2.1), the surface conditioning by molecules originating from the surrounding medium and from cell lysis necessarily alter the physicochemical properties of surfaces. According to a recent study performed by Moreira *et al*. [40], the conditioning of polystyrene (PS) surface with cellular extracts from the *E. coli* bacterium resulted in significantly reduced hydrophobicity. Gomes *et al*. [67] also reported a slight decrease in hydrophobicity of the PS surfaces conditioned with *E. coli* cell wall components. As suggested in the study by Fried *et al*., the transition from Cassie–Baxter to Wenzel state on textured PDMS substrates (for details see Chapter I, part 1.3.2.c) is mainly caused by surface conditioning by bacteria. Moreover, filamentous-like appendages extending from the cell wall surface of *E. coli* allow the bacterial cell to attach within the submicron trenches, thereby contributing to the wetting transition.

According to the mentioned literature, the surface conditioning leads to increased surface energy, thereby diminishing the solid – liquid interface energy and as a result, the energy barrier of the wetting state transition. In this study, the textured surfaces exhibit the rms roughness ranging between 22 μm and 26 μm, which is at least 10 times larger than the bacterium cell size (~2 μm in length). Also, the texturing increased the surface area by about 200 %. The real contact area available to the cell body is therefore greatly increased following the texturing, which may explain an increase in the number of bacteria retained on the textured LSR surfaces by a factor ranging between 3 to 28, compared to the flat-like LSR surfaces. It should also be noted that valleys from the textured surfaces can allow the bacteria to overcome hydrodynamic shear forces. The

similar trend was observed by Hou *et al*. [91], they reported that the *E. coli* preferentially settled in valleys of 5 – 20 μm in width, between protruding features.

Chapter IV

Network mesh nanostructures in cross-linked poly(dimethylsiloxane) visualized by AFM[1]

[1] The contents of this chapter have been published as: Viktoriia Drebezghova, Hubert Gojzewski, Ahmed Allal, Mark A. Hempenius, Corinne Nardin, and G. Julius Vancso, Network Mesh Nanostructures in Cross-Linked Poly(Dimethylsiloxane) Visualized by AFM, *Macromolecular Chemistry and Physics*, **2020**, 2000170.

1. Introduction

Due to the presence of silicon in the main chain and the resulting unusual, and useful properties, silicon containing polymers, including polysiloxanes, polysilanes, and polyferrocenylsilanes have been the subject of intensive research and have found applications in a broad range of technological fields [128,168,169]. Polysiloxanes, in particular poly(dimethylsiloxane)s (PDMS) have been the most researched class of Si containing polymers and have found also the most widespread commercial use [168,170–172]. As is well known, molecular structures of elastomers consist of polymer network chains cross-linked chemically using, e.g., chemical agents. A three-dimensional molecular network forms in cross-linking provided that conditions for gelation are fulfilled [173].

PDMS can form regular molecular networks when, e.g., siloxane chains with end-functions (such as vinyl terminated PDMS) and methylhydrosilane-dimethylsiloxane copolymer cross-linkers are reacted in Pt catalyzed hydrosilylation reactions, e.g., for use as dynamic cell culture substrata [134]. Commercial PDMS materials that belong to different grades of products with the generic name “Sylgard” (such as the grade Sylgard 184 investigated in this study) of Dow-Corning are often used as substrates, e.g., in microcontact printing as stamps, in adhesion studies, or as components of microfluidic devices [174–177]. Commercial PDMS Sylgard 184 “kits” contain nanosilica fillers (see **Annex IV**), so it is also of importance to extract these and explore possible structural differences that may exist between “pristine” and “extracted” materials.

Cross-link density and average molar mass of the network chains between covalent network junctions are fundamental structural parameters to characterize molecular networks. Their values can be determined by various methods, such as equilibrium swelling, mechanical modulus, or measuring solvent thermodynamic activity by applying the Flory–Rehner equation [178]. “Voids” at the nanometer length scale between network polymer chains are usually referred to as “mesh,” while the mesh size (correlation length) is usually considered as an average distance between cross-linking junctions (see **Fig. 4.1**). The typical size range for meshes varies from a few nm to tens of nm [179]. Molecular networks containing these meshes usually exhibit structural heterogeneity displaying inhomogeneous network junction density, dangling chain ends, loops, and network junction shortcuts (**Fig. 4.1**). Polymer network heterogeneities have been studied by various scattering techniques [180]. Results unveiled that depending on

the cross-linking chemistry, molecular networks usually display complex and heterogeneous structures at the molecular scale [181].[151]

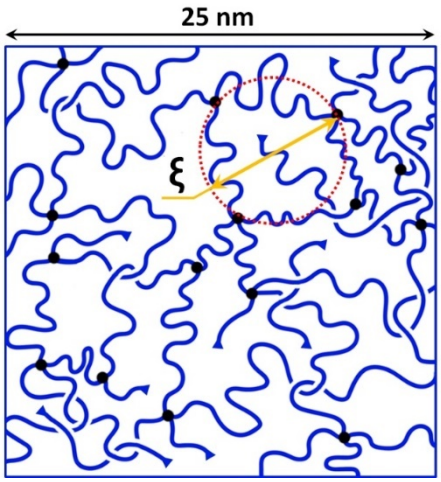

Figure 4.1. Illustration of a mesh structure of cross-linked PDMS. The mesh size (ξ) defined here as the average length between cross-links is on the order of 10 nm. Dangling chains and free chains are also shown.

PDMS networks often serve as models in fundamental physical studies of elastomer molecular network theories due to their rather regular and controlled molecular structure [151]. As PDMS has a low glass transition temperature, the starting chains prior to cross-linking maintain their high flexibility between the cross-link junctions. PDMS is chemically inert, is biocompatible, and is of relatively low cost, thus it has also been intensively used in biomedical applications and soft lithography (microcontact printing) [170]. While the surface of PDMS is hydrophobic, and features chains with significant surface dynamics at RT, various treatments like UV-ozone exposure can render it hydrophilic [151], with a gradual hydrophobic recovery [176,182], depending on the treatment dose.

Albeit PDMS surfaces have been characterized in numerous studies across the length scales, until now real space images showing the expected mesh structure, to our knowledge, have not been reported. We believe that if continuing progress is to be made in the science of polymer networks, direct nanoscale observations of molecular mesh structures in PDMS (and other) elastomers, as a function of molecular composition are needed. Direct visualization of mesh deformation if the elastomer is put under mechanical stress would also be useful, as it can help analyze network deformation models (e.g., affine deformation) and their applicability. Additionally, mesh size distributions and their possible heterogeneities within the bulk of elastomers, in comparison with characteristics

of the cross-linked surface in direct contact with air, would complement the analysis of structure and properties of PDMS for surface related applications.

To tackle these challenges, we embarked upon systematic studies using high resolution atomic force microscopy (AFM) in the peak force quantitative nanomechanical mapping (PF-QNM) mode to directly obtain quantitative information of the elastomer mesh morphology at the nanometer length scale. It has been shown that this imaging mode can provide superior resolution when compared with traditional tapping mode AFM imaging and can yield nanographs with molecular scale details [183]. In this article we discuss the first results of our AFM network research aiming at PDMS network morphology observed with mesh resolution. Additionally, we demonstrate mesh deformation by direct imaging, using PDMS networks under uniaxial mechanical stress.

A few AFM working modes have been used and discussed in the literature to visualize neat Sylgard 184 PDMS surfaces at length scales covering the micrometer and nanometer domains [176,184–192]. In all references free surfaces of Sylgard were observed to be smooth and featureless, and no resolution of the postulated mesh molecular structure has been reported. Similar featureless surfaces were observed in studies providing images of other PDMS elastomers [193,194].

2. Results and discussion

First, we examined the nanometer scale morphology of the PDMS surfaces with different cross-linker concentrations (2.5, 5, 20, and 25 wt.%) by AFM. AFM measurements were performed on free PDMS surfaces that were cross-linked in direct contact with air. Four representative height images for each cross-linker concentration are shown in **Fig. 4.2**. For each image a quantitative height profile is also displayed, scaled to the same height value, to allow for a comparison. For the lowest cross-linker concentration (2.5 wt.%) images lacked sharp contrast and showed some surface roughness with a hint to the presence of some porous microstructure. For 5 wt% cross-linker the apparent surface roughness increased, and the contrast of the surface features captured became sharper. For the two highest cross-linker concentrations, sharp contrast and a morphology showing a nanoporous appearance were observed. For the quantitative analysis of the surface structures, average pore size and pore size distribution, porosity (surface coverage), and roughness values were estimated from AFM images taken at five different spots for each sample. These data are presented in **Fig. 4.3** and **Tables 4.1** and **4.2**.

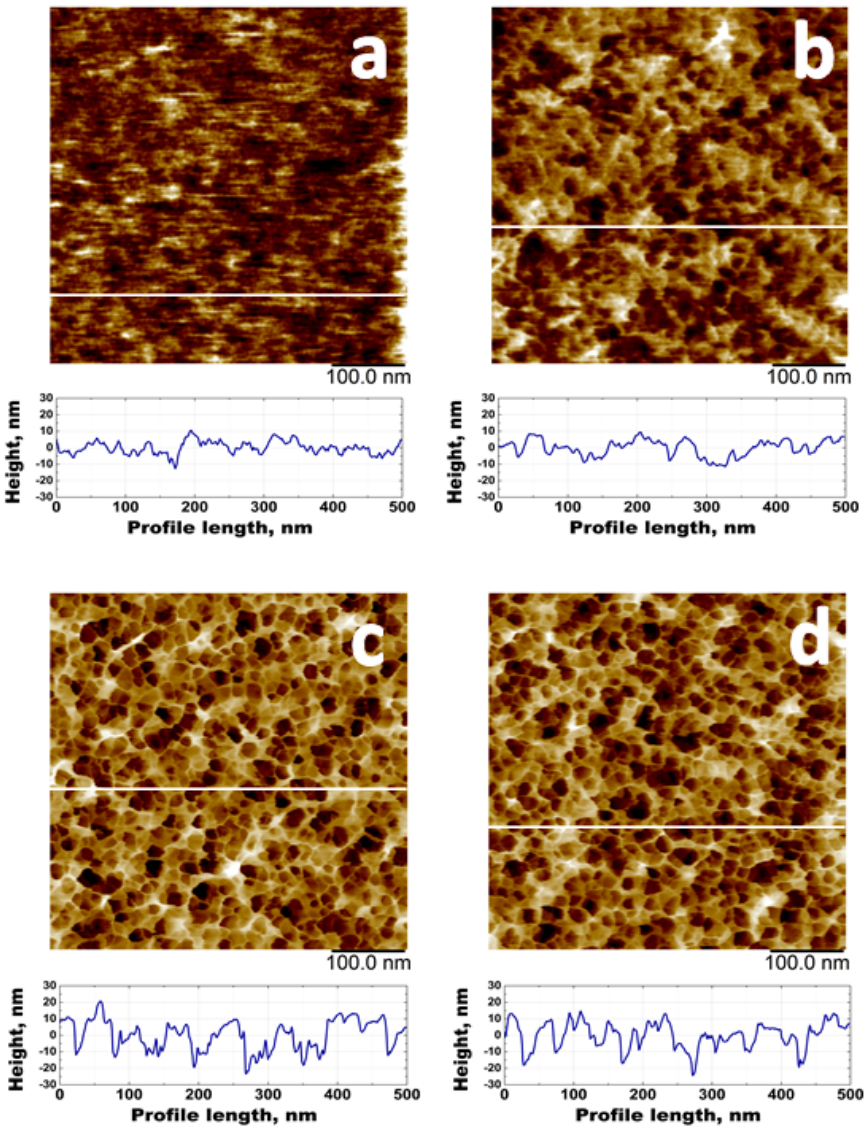

Figure 4.2. AFM height images of the free PDMS surfaces prepared at varied cross-linker concentrations: (a) 2.5, (b) 5, (c) 20, and (d) 25 wt.%. The scan area is 500 × 500 nm^2 for all images. The height-profiles are represented below the nanographs; the profiles were taken along the white lines. μMasch cantilevers as specified in the Experimental Section were used.

Mesh size distributions were estimated using the ImageJ image processing software (version 1.50b). Each distribution presented in **Fig. 4.3** was determined from 200 pores analyzed. The distribution histograms were smoothed using 3-point moving averages. Size distributions on free (in the first raw) and cryofractured (in the second raw) PDMS surfaces were fitted with unimodal and bimodal Gaussian distribution functions, respectively. The surface porosity was determined as the ratio of the area occupied by pores determined from AFM images to the total area of the image.

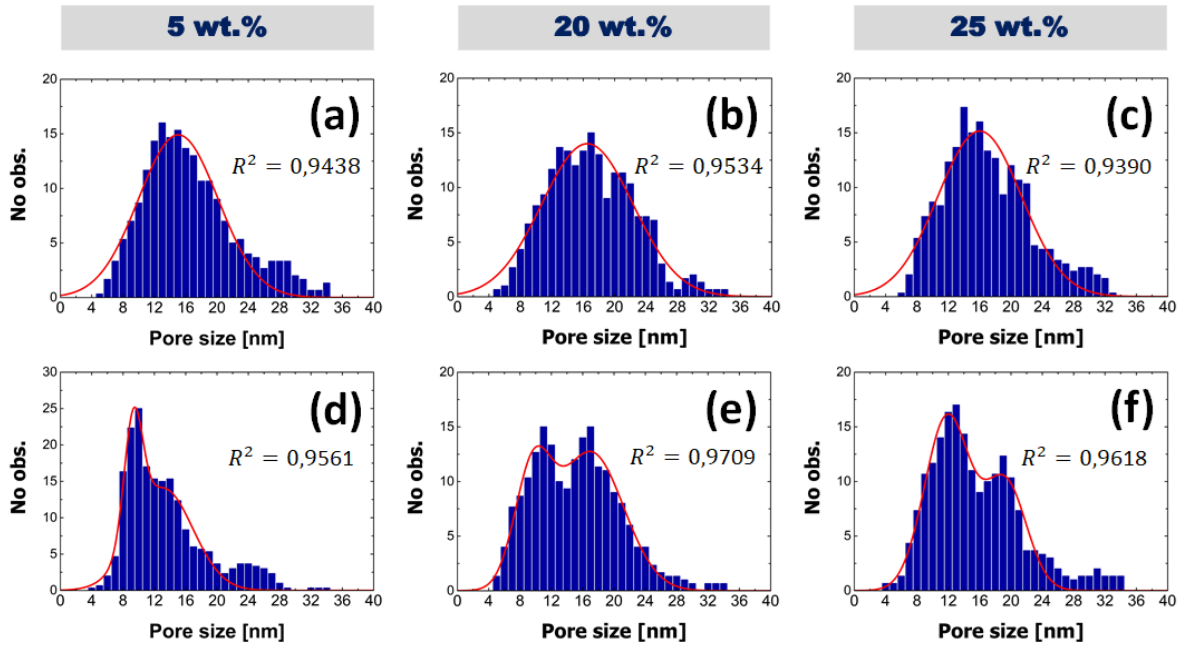

Figure 4.3. (a-c) Pore size distribution on the free and (d-f) cryofractured PDMS surfaces with cross-linker concentration as histograms. The distributions were fitted with Gaussians (red curves). The coefficient of determination for the fitting, R^2, is shown as well.

The mean pore size (diameter) values observed were in the range of 15–16 nm, with an increasing surface coverage (**Table 4.1**) and RMS surface roughness (**Table 4.2**) as a function of the increasing cross-linker concentration. We identify the porous morphology as images of the heterogeneous mesh-like network structure. As the cross-linker concentration increases, network chain mobility decreases, which contributes to sharpening of the contrast of the mesh features captured on the images. We propose that within the mesh interior dangling chains and chemically uncross-linked chains provide a mechanically softer environment, allowing for a somewhat higher penetration of the AFM tip that is scanned at constant applied normal force (peak force). This presumption is supported by quantitative AFM PF-QNM imaging (see **Fig. S2**, **Annex IV**). We must note at this juncture that mesh structures could not be visualized when using standard tapping mode for imaging (see **Fig. S3**, **Annex IV**).

Table 4.1. *Mean size and surface coverage of pores on free and cryofractured PDMS surfaces. Mean standard deviation is shown as well*

Cross-linker concentration, wt.%	*Free PDMS surface*		*Cryofractured PDMS surface*		
	Mean pore size, nm	*Surface coverage, %*	*Mean pore size, nm*		*Surface coverage, %*
			1st peak	*2nd peak*	
5	15.1 ± 5.1	11 ± 1	9.3 ± 1.2	13.1 ± 3.8	7 ± 1
20	16.5 ± 5.8	22 ± 4	9.6 ± 2.3	17.0 ± 4.2	34 ± 4
25	16.0 ± 5.3	33 ± 3	11.9 ± 2.9	19.3 ± 2.7	40 ± 3

Table 4.2. *RMS surface roughness (R_q) values of free and cryofractured PDMS surfaces. Mean standard deviation is shown as well*

Cross-linker concentration, wt.%	*RMS Roughness R_q, nm*	
	Free PDMS surface	*Cryofractured PDMS surface*
2.5	4.4 ± 0.4	–
5	4.8 ± 0.4	11.8 ± 0.7
20	8.6 ± 0.1	8.4 ± 0.8
25	8.9 ± 0.3	8.1 ± 0.4

The question, however, arises: to what extent can one assume that the entire bulk volume of the elastomer exhibits a nanoporous morphology? In order to tackle this issue, we cryofractured (liquid N_2 bath) PDMS specimens obtained at three different cross-linker concentrations in the directions perpendicular to the surface. Optical microscopy (OM) images of the cryofractured specimens are displayed in **Fig. 4.4a-c**. The OM micrographs were obtained by the AFM's OM, showing also the silhouette of the AFM cantilever located above the surface. The AFM scanned areas here represent planes that are perpendicular to the original surface that was cross-linked in contact with air. The sample containing 2.5 wt.% of the cross-linker was too adhesive to be successfully imaged, although we used cantilevers with a higher spring constant (Olympus).

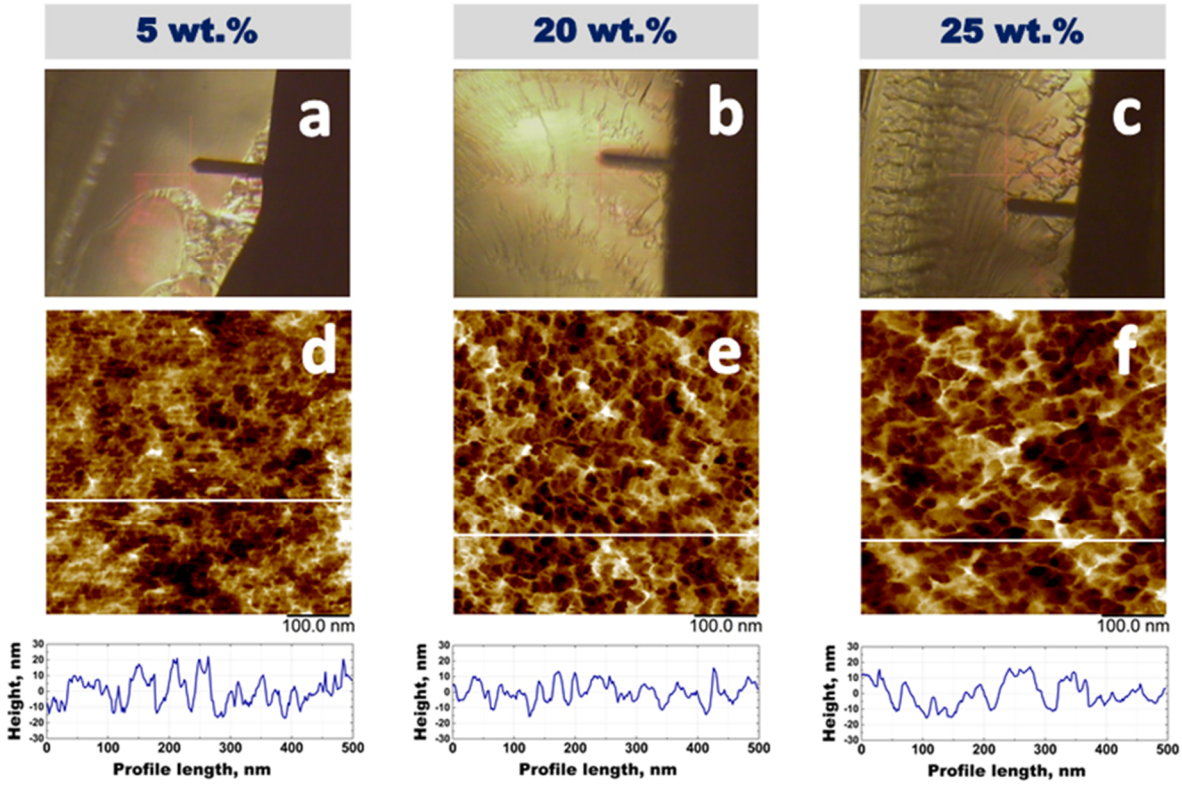

Figure 4.4. Optical images of the cryofractured PDMS surfaces with different cross-linker concentrations: (a) 5, (b) 20, and (c) 25 wt.%. (d–f) AFM height images were taken at scan areas of 500 × 500 nm^2. The height-profiles are represented below the AFM scans; the profiles were taken along the white lines. Olympus cantilevers as specified in the Experimental Section were used.

The appearance of the nanoporous morphology observed is similar to the images captured at the top free surface of the sample, which was cross-linked in contact with air. Again, we attribute the presence of the nanopores to network meshes of softer interior, surrounded by cross-linked (and less mobile) network chains (or bundles of network chains). Thus, we conclude that cross-linked PDMS exhibits nanoporous morphology throughout the entire material, due to the presence of molecular meshes. We also quantified the mesh size distribution, the surface coverage, and the RMS surface coverage of the cryofractured specimens in the cross-section of the elastomer films (see **Fig. 4.3** and **Tables 4.1** and **4.2**). It is interesting to note that the size distributions for the samples shown in **Fig. 4.3** appeared to be bimodal (in some cases even showing three maxima), with mean values of 9–12 and 13–19 nm, depending on the cross-linker concentration. We attribute the bimodal appearance to inhomogeneous network density, i.e., the local distribution of cross-linking junctions is inhomogeneous due to fluctuation of

concentration during mesh network formation [179]. Large topological inhomogeneity occurs often within a scale of 10–100 nm in polymer networks [195,196].

We then considered the question of mesh deformation captured in situ under uniaxial stress. To this end, specimens were elongated, the stress maintained, and the surface of the material under stress was imaged. We expected that if the pores are indeed related to molecular meshes, they would deform with the bulk deformation. A fundamental question to be tackled can be whether this deformation is affine or not. The schematic of the experiment and AFM images are displayed in **Fig. 4.5**. PDMS with 20 wt.% of cross-linker (5:1 base: cross-linking agent ratio) was stretched to 40 % above its original length and the free sample surface was imaged using a Dimension Icon AFM. The sample was elongated before being fixed under stress and placed on the solid sample support without air gap between specimen and sample support.

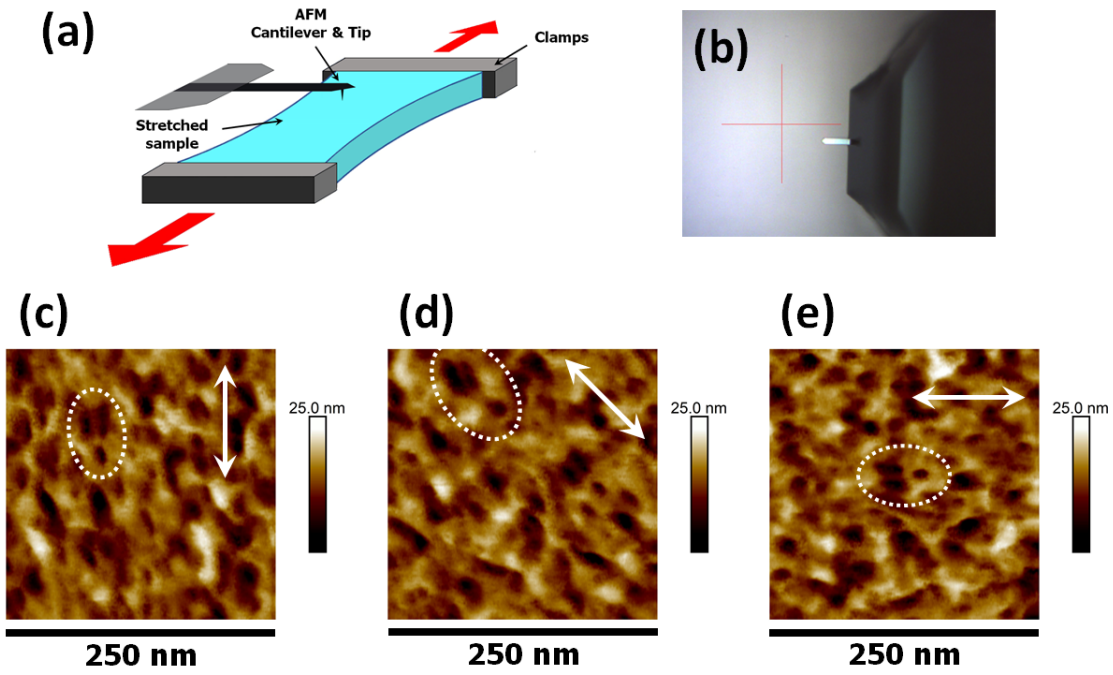

Figure 4.5. (a) Schematic of stretching for imaging of PDMS under mechanical stress, (b) OM micrograph of the top of an AFM cantilever (µMasch) in close proximity (about 20 µm) above the stretched PDMS surface, (c–e) AFM images of free sample surface taken at exactly the same location at different scanning angles, i.e., 0°, 45°, and 90°. The scanning area is 250 × 250 nm^2. White arrows indicate the direction of sample elongation, white dashed circles show the same spot in all the images.

As is obvious in **Fig. 4.5**, the nanopores, attributed to network meshes, were deformed in the direction of the applied stress. The mean aspect ratio of ellipsoid shaped

nanopores was determined by measurements of the length of the major and minor axes by calculating their ratio, for 10 individual pores in the AFM images, captured at 90° scan angle (**Fig. 4.5e**). The average aspect ratio obtained in this way had a value of 1.8 ± 0.3. This value is somewhat higher than the overall macroscopic stretch ratio of the sample (which was 1.4). The deformation was not homogeneous across the specimen due to clamping effects. The difference between mesh aspect ratio following deformation and overall stretch ratio is rationalized by noting that the scanned area was in the specimen section, which experienced higher deformation, away from the clamps. There is however a visible relationship between macroscopic elongation of the sample and mesh deformation at the nanometer length scale. In order to rule out the possibility that the mesh deformations captured were related to AFM scanning artifacts, the scanning angle was also varied. We found that by varying the scan angle (0°, 45°, and 90°), the elongated nanopores were rotating with the rotation of the scan direction, indicating the absence of a possible scan direction related imaging artifact.

Finally, we tackled the question of possible morphology changes prior to, and following removal of free PDMS chains and silica fillers using Soxhlet extraction. A PDMS sample with 20 wt.% of cross-linker was extracted in acetone/*n*-hexane (1:1 mixing ratio) for 48 h at 6 cycles/h (over 250 wash cycles). The swollen sample was then dried in a vacuum oven at 80 °C for 24 h. The mass of the PDMS sample was measured using a high precision scale before the extraction and following the drying step. The mass of the extracted residue was 5 % of the total mass of the cross-linked specimen. We then imaged the surface morphology of the extracted PDMS surface and compared with the unextracted PDMS surface with the same cross-linker concentration. Two representative AFM height images prior to, and following extraction are shown in **Fig. 4.6**. The appearance of the samples and the mesh-like morphology remain unaffected by extraction. The surfaces of the extracted samples appear somewhat smoother, while the apparent mesh size decreases during the extraction. The mesh size decreased following extraction from an average value of (16.5 ± 5.8) nm, for the pristine PDMS surface, to (13.5 ± 4.0) nm. We interpret the mesh size reduction by the leaching out of PDMS chains that were not covalently bound to the network, thus causing a mesh relaxation.

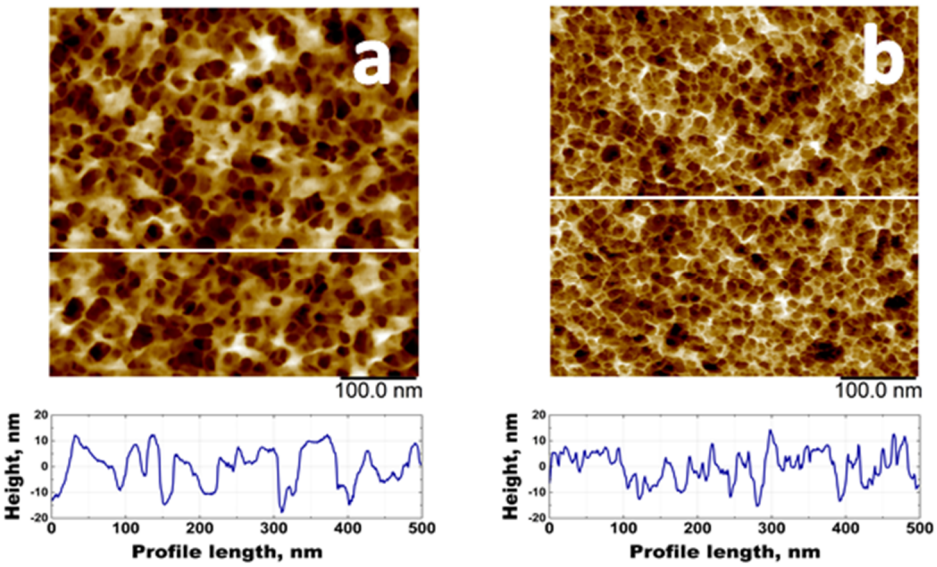

Figure 4.6. AFM height images of (a) pristine and (b) PDMS surfaces after extraction with 20 wt.% cross-linker (512 × 512 lines, scan area: 500 × 500 nm^2). The height-profiles are represented below; the profiles were taken along the white lines. μMasch cantilevers were used.

3. Summary

PF-QNM imaging of cross-linked (PDMS Sylgard 184) networks at the nanometer length scale provided high resolution scanning images that directly capture network mesh structures with mesh size (diameter) values, ranging from 10 to 16 nm obtained at the free surface of PDMS. Perpendicular to the free surface, in cross-sectional areas exposed by cryofracturing, similar mesh structures were observed. When exposed to uniaxial stress, the circular mesh features became elongated, showing network deformation at the nanoscale, as a result of mechanical stress. Our results provided direct evidence that new AFM imaging modes, such as peak force tapping, allow one to systematically study the nanoscale structures and deformation of elastomer networks as a function of molecular parameters (molar mass, cross-link density, and cross-linking chemistry) by direct space nanoscale observations.

4. Experimental section

PDMS elastomer samples investigated here were obtained using standard Sylgard 184 silicone elastomer kits by the Dow Chemical Company, prepared at different composition ratios to yield elastomers with varying cross-link density. For each given ratio, elastomer base and curing agent were thoroughly mixed and degassed under vacuum for 30 min. Then, the mixture was poured into a Petri dish, cured at 60 °C for 24

h, and subsequently incubated at room temperature for another 24 h to achieve complete cross-linking. After curing, PDMS samples (1 mm thick) were removed from the Petri dish and specimens were punched out with a 5 mm circular hole punch. The samples were then cleaned by soaking them in 70 % ethanol for 20 min, followed by a rinsing in Milli-Q water prior to mounting on to an AFM sample holder.

In this study, we used two AFM setups, including a MultiMode 8 AFM instrument (Bruker) supplied by a JV vertical engage scanner and a Dimension Icon microscope (used only to image mechanically stretched samples under tension), both retrofitted with a NanoScope V controller (Bruker). Imaging was performed in the PF-QNM mode to allow to capture topography images at controlled normal forces. The AFM data were collected following a sine-wave sample-tip trajectory with a frequency of 2 kHz and utilizing a peak-force amplitude value of 150 nm. The ScanAsyst optimization in the user interface was set to "on" to acquire high-resolution images at low applied normal forces and to automatically adjust the feedback loop control. Images were captured at constant applied normal forces, employing the "best" scan parameters found by the ScanAsyst for a specific scan area. Two types of soft, rectangular, silicon-made cantilevers were used, i.e., OMCL-AC240TS (Olympus) and HQ:NSC19/Al BS (μMasch) with a nominal tip radius of 7 and 8 nm, respectively. Image processing and data analysis were conducted with the NanoScope (version 8.15—MultiMode 8 AFM, version 9.4—Dimension Icon AFM) and the NanoScope Analysis software (version 1.9), respectively. Measurements were performed in air and at room temperature (≈21 °C). Since the AFM measurements are highly sensitive to tip shape, new AFM tips were used in each consecutive experiment. For examples of tip profiles captured with a high-resolution scanning electron microscope (SEM), see **Fig. S1** (**Annex IV**).

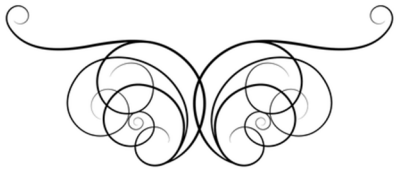

Chapter V

Initial bacterial retention on Polydimethylsiloxane of various stiffnesses: the relevance of modulus (mis)match[2]

[2] The contents of this chapter have been submitted as: Viktoriia Drebezghova, Florence Hakil, Régis Grimaud, Hubert Gojzewski, G. Julius Vancso, Corinne Nardin, Initial bacterial retention on Polydimethylsiloxane of various stiffnesses: the relevance of modulus (mis)match.

1. Introduction

Controlling the colonization of materials by microorganisms is crucial in a wide range of industrial and clinical settings. Biofilms are surface associated bacterial communities embedded in a hydrogel-like matrix, in which high cell density, reduced diffusion and physicochemical heterogeneity play a protective role and induce adaptive cell behaviors. However, the underlying mechanisms that govern the interactions of bacteria with material surfaces remain poorly understood, limiting the *ab initio* design and engineering of biomaterials to control bacterial attachment and further biofilms growth [197]. Preventing biofilm formation thus necessitates enhanced understanding to hinder the initial stage of bacterial adhesion.

The materials properties, often intricately entangled, which alter bacterial attachment include chemistry, hydration, surface charges, the topography, and the mechanical properties [198]. Numerous experimental issues and misinterpretations regarding the cell membrane rigidity and adhesion forces on superhydrophobic surfaces surround the current studies of antibacterial nanostructured surfaces [74].

Owing to continuous advances in polymer chemistry, polymer-based devices have become increasingly used to reduce chronic infection and medical device failure [199,200]. Various antimicrobial polymers, polymer-based hydrogels and polymer coated surfaces are being developed for various applications such as wound healing [201], stem cell encapsulation [202] and bone tissue engineering [203] just to cite few examples. In all cases, the surface material properties, such as wettability, roughness and morphology are shown to affect bacterial adhesion. However, to date, the research conducted in the field of antimicrobial polymers has focused mostly on their chemical and structural aspects [165, 184–186] and the outcomes evidence the difficulty to disentangle the role of surface chemistry, hydration state and charge from the intrinsic material mechanical properties.

Although it is clear that the mechanical interactions between bacterial cells and the extracellular polymeric substance are essential in determining the biofilm assembly and disassembly, as well the mechanical characteristics of the biofilm, the physics of these mechanical interactions remains poorly understood [207,208]. As examples for the complex interplay, poly(ethylene glycol) (PEG) hydrogels of various thicknesses, resistant to protein adsorption, were immobilized on glass slides. The thinner the hydrogel the

higher the number of adherent bacteria. As concluded by the authors, the underlying stiff substrate may however influence the perceived mechanical properties of the hydrogel by the adherent bacteria [209]. These outcomes also raise the question of the role of the hydration state of the hydrogel on the bacterial response. As another example, it is shown that both PEG hydrogels and hydrated brushes evidence that the mechanical properties, the molecular architectures and the thicknesses of PEG-based coatings influence the flow-driven surface motion of *Staphylococcus aureus* MS2 cells [210]. These investigations further highlight the difficulty to assess which of the parameters, the moduli and/or the local polymer concentration plays the critical role. To rule out the role of hydration and surface charges on bacterial adhesion, elastomers that are solvent-free, polymeric materials are of particular interest, especially poly(dimethylsiloxane) (PDMS). PDMS is a material used in various biomedical applications. The first systematic study on the effect of the stiffness of PDMS on bacterial adhesion was conducted by Song *et al*. [114,115]. The authors reported that the stiffness of PDMS of Young's moduli ranging between 0.1 and 2.6 MPa affects the attachment of bacteria, the morphology and the antibiotic susceptibility of the attached cells [114,115]. The authors claimed that the effects of the surface chemistry and roughness were negligible. They suggested that the degree of deformation of the bacterial cell membrane upon contact with the PDMS surfaces of differing stiffness does affect bacterial mechanosensing. This conclusion was based on the observation that the level of the intracellular second messenger, cyclic diguanylate monophosphate decreased with PDMS stiffness [116].

Epoxy-modified silicone was also used to address the issue of enhancing the mechanical properties and adhesion of silicone antifouling coatings [211]. As the content of epoxy increased, the bacteria removal rate decreased, being bacterial adhesion however not only affected by the material elastic modulus and free energy but also by the roughness and hardness of the coating. With increasing hardness and roughness, the number of attached bacteria increased. Allain and coworkers [120] systematically tuned the substrate topography and stiffness while keeping the surface free energy of PDMS substrates constant. The authors indeed used low energy singly charged inert ions to irradiate PDMS to achieve substrates of variable stiffness but exhibiting comparable surface free energy. However, this process resulted in the formation of a wavy (wrinkled) topography at the PDMS surface. The changing topography could limit bacterial surface attachment even in very compliant PDMS (Young's moduli of 0.02 and 0.2 MPa). The intrinsic physicochemical properties associated with PDMS substrates of different stiffnesses were shown to strongly influence bacterial adhesion [117]. Through the use of

polystyrene beads (PS), these authors did show that bacterial adhesion on PDMS samples with Young's moduli ranging from 0.06 to 4.52 MPa is a physical process, which is not mediated by bacterial surface appendages. Subsequently, they used PDMS surfaces of different stiffness coated with a 2 nm highly cross-linked PDMS to confer comparable surface chemistry, while retaining similar mechanical properties for coated and uncoated samples [119]. The authors came to the conclusion that uncoated PDMS of low Young's modulus contained free polymer chains and longer chain ends at the surface lead to higher bacterial adhesion. They concluded also that their work provides the first evidence that bacterial adhesion on the PDMS substrates could largely be attributed to the available free PDMS polymer chains and PDMS polymer chain ends indicated by interfacial adhesion force for molecular bridging on the sample surfaces.

In order to shed further light on the complex issue of cell-substrate adhesion and the impact on it by surface elasticity, we performed systematic research described here. We varied the surface stiffness of PDMS and monitored initial retention while keeping the other surface characteristics unaltered. Bulk and advanced surface characterization techniques, in particular Atomic Force Microscopy (AFM) and X-ray photoelectron spectroscopy (XPS) were used to show that the material surface chemistry and topography do not depend on the degree of cross-linking of the elastomer. Solely materials of varying stiffnesses are exposed to bacteria. To exclude the role of PDMS, not cross-linked, free chains on bacterial retention without affecting the material surface chemistry, we resorted to their Soxhlet extraction. We provide evidence for the role of modulus mismatch between bacteria and substrate surface on initial bacterial retention.

2. Results and discussion

Controlling the colonization of materials by microorganisms is crucial in a wide range of industrial and clinical settings. Biofilms are surface associated bacterial communities embedded in a hydrogel-like matrix, in which high cell density, reduced diffusion and physicochemical heterogeneity play

We first show the results related to preparing the PDMS substrates, and their characterization. PDMS substrates were prepared using the Sylgard-184 silicone kit. This kit was chosen owing to its widespread use for microfluidics and biomedical applications. We produced samples of differing stiffness by varying the cross-linker concentration (2.5, 5, 10, 20, and 25 wt.%) according to conventional methods as described in the section "Materials and Methods". To exclude the role of free PDMS chains on initial bacterial

retention, we performed bacterial retention assays on PDMS surfaces at different cross-linking concentrations prior to, and following the removal of free PDMS chains using Soxhlet's extraction. Successful removal of not cross-linked, free chains by Soxhlet extraction was first assessed by mass loss (**Annex V**, **Table S1**). The mass of the extracted residue was 5 wt.% of the total mass of the cross-linked specimens at 10, 20, and 25 wt.% of cross-linker and 10 wt.% of the total mass at 5 wt.% of cross-linker. Material properties prior and subsequent to Soxhlet extraction were then characterized as described in the following parts. Both bulk and surface properties were characterized prior to analyzing initial bacterial retention.

We first performed TGA analyses of each component (base and cross-linker) since the silica fillers used to reinforce the cross-linked elastomer matrix might alter the physicochemical properties of the material. The filler content determined from the degradation curves of each Sylgard 184 components are reported in **Annex V** (**Fig. S1**). According to TGA, the pre-polymer contains about 23 wt.% of remaining residue whereas the cross-linker residue at 900 °C approaches 5 wt.% although the supplier claims that the pre-polymer (base) and cross-linker contain 30-60 wt.% and 10-30 wt.% of silica filler, respectively [212,213]. The cross-linked PDMS sample contains 54 % of residue that is considerably higher than the residue found in the pre-polymer. Delebecq *et al*. [141] performed a very detailed TGA study of silica-filled PDMS blends and showed that the platinum catalyst can increase the extra residue up to 40 % for vinyl-functionalized silica. In the presence of platinum, PDMS chains generate cross-link points with the silica surface forming a layer of immobilized PDMS chains at the interface. Such immobilization leads to the ceramization of the chain fragments during degradation at high temperatures, and consequently to a final additional residue. From these TGA analyses we can conclude that the components contain far fewer silica fillers than claimed by the suppliers.

Contact angle measurements with solvents of different surface tensions were further performed to determine the surface energy and reveal no significant difference prior and subsequent to Soxhlet extraction (**Fig. 5.1** and **Table 5.1**). The water contact angle value increases with increasing cross-linker concentration between (88 ± 3)° and (104 ± 1)°. The surface energy decreases slightly prior and subsequent to extraction from (28 ± 2) to (25 ± 2) mN/m and (23 ± 3) to (22.3 ± 0.2) mN/m, respectively, with increasing cross-linker concentration.

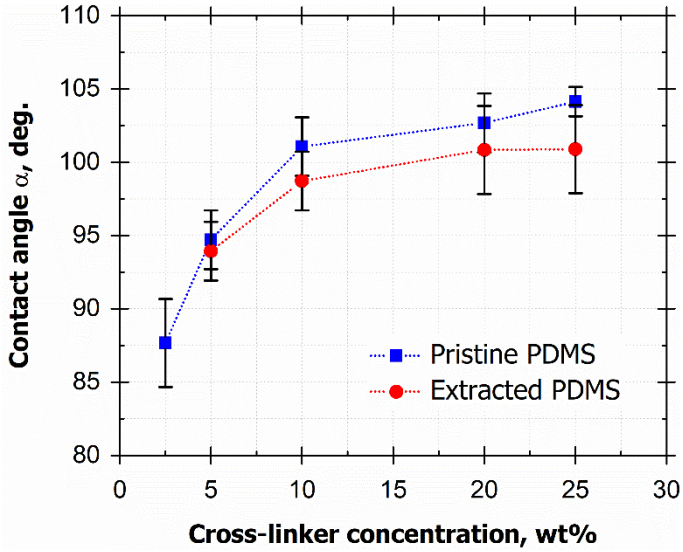

Figure 5.1. Water contact angle of pristine (filled square) and extracted (filled circles) PDMS specimens as a function of cross-linker concentration. Error bars represent standard deviation values obtained from 10 measurements at each data point. Lines are only guides for the eye.

Table 5.1. *Water static contact angle and surface energy of pristine and extracted PDMS specimens as a function of cross-linker concentration*

Sample		*Water contact angle, °*	*Surface energy γ_s, mN/m*
2.5 wt.%	Pristine	(88 ± 3)	(28 ± 2)
	Extracted	*Destroyed*	–
5 wt.%	Pristine	(95 ± 3)	(25.7 ± 0.8)
	Extracted	(95 ± 2)	(23 ± 3)
10 wt.%	Pristine	(101 ± 2)	(25 ± 2)
	Extracted	(99 ± 2)	(22 ± 3)
20 wt.%	Pristine	(103 ± 2)	(25 ± 2)
	Extracted	(101 ± 2)	(21 ± 3)
25 wt.%	Pristine	(104 ± 1)	(25 ± 2)
	Extracted	(101 ± 2)	(23 ± 3)

To characterize the surface chemistry, which defines the above surface energies, we carried out at first FTIR spectroscopy on each component (base and cross-linker). **Fig. S2** (**Annex V**) provides the absorption spectra of each component measured in the transmission mode. The two Sylgard components exhibit a number of common IR bands. Among the most intense are those originating from asymmetrical CH_3 stretching in ≡Si–CH_3 (2960 cm^{-1}), symmetrical CH_3 stretching in ≡Si–CH_3 (1410 cm^{-1}), symmetrical CH_3 deformation in ≡Si–CH_3 (1260 cm^{-1}), asymmetrical Si-O-Si stretching (≈ 1020–1090 cm^{-}

[1]). A broad absorption band at ≈790 – 850 cm^{-1} is common to both components. Aside from the similarities, the spectrum of the Sylgard cross-linker exhibits a peak at 2160 cm^{-1} resulting from the Si-H bond and the small peak at 910 cm^{-1} associated with the vinyl functional group $C=CH_2$. The Si-H and vinyl absorption peaks confirm the presence of the reactive functions in the cross-linker. All the absorption bands are listed in **Annex V** (**Table S2**).

FTIR spectroscopy was also performed on "pristine" cross-linked PDMS samples of differing cross-linker concentrations (2.5, 5, 20, and 25 wt.%) in the ATR mode. The spectra are remarkably similar (**Fig. S3**, **Annex V**), except a minute increase of the low intensity peak at 910 cm^{-1} with increasing cross-linker concentration. This peak, as mentioned above, arises from the vinyl functional group $C=CH_2$. As expected, the absorption band at 2160 cm^{-1} associated with the Si-H cross-linking agent completely vanished.

In a second stage, the elemental composition of the surface was characterized by XPS analysis prior and subsequent to Soxhlet extraction (**Fig. 5.2**). The spectra are provided in **Annex V** (**Fig. S4** to **S6** for the cross-link densities 5, 10 and 20 wt.%, respectively) whereas **Fig. 5.2** and **Table S3** (**Annex V**) give the elemental composition.

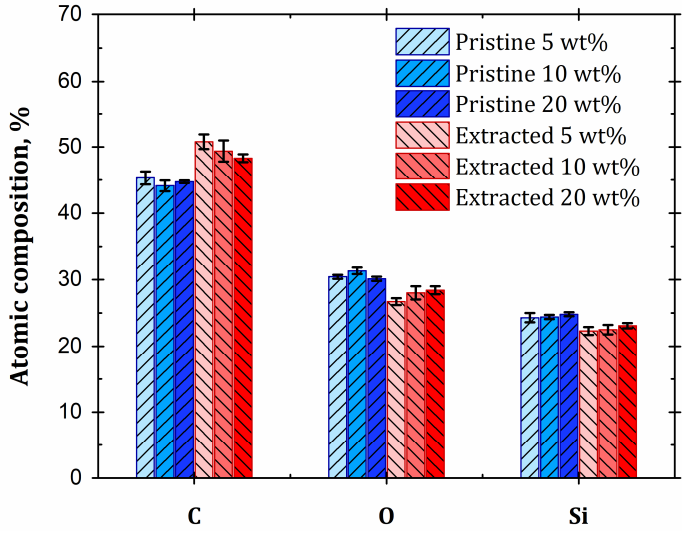

Figure 5.2. XPS analysis of pristine and extracted PDMS specimens (atomic compositions for C, O and Si, respectively) as a function of cross-linker concentration. Error bars represent standard deviations of 3 measured values at each data point.

As can be observed in **Fig. 5.2** and in **Table S3**, the elemental analysis evidences that, within the experimental error, there is no difference in the composition of the PDMS specimens as a function of the cross-linker concentration neither prior to, nor following

Soxhlet extraction. Subsequent to Soxhlet extraction, the C content increases slightly whereas the O and Si content decreases at all cross-linker concentration, which can be explained not only by the removal of free, non-cross-linked PDMS chains but also of some silica fillers. This hypothesis is strengthened by the fact that the C content increase subsequent to Soxhlet extraction is higher at the lower cross-linker concentration, at which lower number of cross-link points between the silica fillers surface and the PDMS chains are generated (as monitored by TGA analysis). Overall, the elemental composition prior and subsequent to extraction can be expected also from the slight decrease of the surface energy as monitored by static contact angle measurements.

Bulk Young's moduli values of PDMS samples were estimated using the theoretical relation (in ideal cases) between the Young's modulus and the shear modulus measured in the parallel-plate geometry, i. e. $E = 3G$. **Fig. 5.3** shows the Young's modulus evolution versus cross-linking concentration of both extracted and un-extracted PDMS samples. When increasing the cross-linker concentration to 10 wt.%, the Young's modulus of the PDMS samples drastically increases. However, when the cross-linker concentration was higher than 10 wt.%, the Young's modulus stabilized at about 1.8 MPa and even decreased to 1.2 MPa at 25 wt.% cross-linker for the un-extracted PDMS.

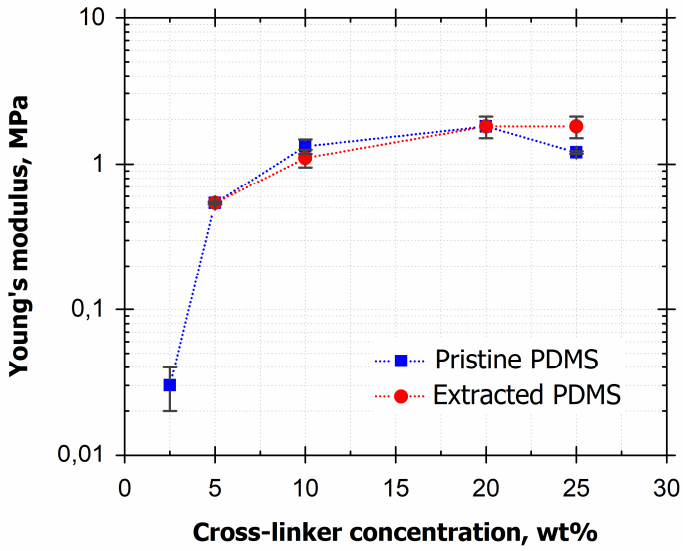

Figure 5.3. Young's modulus of pristine (filled square) and extracted (filled circles) PDMS specimens as a function of cross-linker concentration. Error bars represent SD of 3 measured values at each data point. Lines are only guides for the eye

The extraction of un-cross-linked free chains from the PDMS network did not noticeably affect the bulk Young's modulus. The Young's moduli of the tested PDMS samples are listed in **Table 5.2**.

Table 5.2. *Comparison between Young's modulus values of pristine and extracted PDMS samples*

Cross-linker concentration, wt.%	*Pristine PDMS* ***E****, MPa*	*Extracted PDMS,* ***E****, MPa*	*"No-slip" control test,* ***E****, MPa*
2.5	(0.03 ± 0.01)	*Destroyed*	(0.06)
5	(0.54 ± 0.01)	(0.54 ± 0.01)	(0.63)
10	(1.32 ± 0.15)	(1.11 ± 0.15)	(1.83)
20	(1.8 ± 0.3)	(1.8 ± 0.3)	(1.68)
25	(1.20 ± 0.03)	(1.8 ± 0.3)	(1.26)

By comparing the modulus values of the pristine PDMS measured by the standard method at 10 N applied normal force to those measured using *in situ* curing, one can conclude that the values are similar. Moreover, the Young's modulus values also decrease at higher cross-linker concentrations. Thus, modulus reducing cannot be explained by slip phenomena at the specimen-plate interface that could potentially lead to systematic deviation of the Young's modulus to lower values. A similar reduction of mechanical properties at cross-linker concentrations higher than 10 wt.% (balanced stoichiometry between the pre-polymer and the cross-linker) has been reported in earlier studies [177,214]. At the higher cross-linker concentrations cross-link sites are saturated and the excess of cross-linker leads to dilution of the network, thus reducing the modulus. Between 20 and 25 wt.% all cross-linking sites are expected to become saturated.

Surface topography of soft matter can be efficiently imaged and surface properties studied by various modes of AFM. Surface mechanical properties, like dynamic surface modulus, can also be mapped at the nanoscale by Quantitative Dynamic Nanomechanical Analysis [215,216] (QNM). Regarding the cross-linked PDMS used in this research, we have already reported on surface morphology and stiffness in a detailed QNM study of the PDMS substrates utilized here. We successfully visualized the mesh network structures at the nanometer length scale and reported our findings in this earlier article [135]. The mesh diameter values were found to vary from 10 to 16 nm at the free surface of PDMS. Following Soxhlet solvent extraction the mesh-like appearance remains unchanged, but mesh diameter values decreased somewhat, which was attributed to the removal of non-cross-linked chains and silica filler.

Regarding the PDMS specimens used here, we first display a larger scan-size height AFM image to capture the rather homogeneous PDMS surfaces. As representative examples, we show in **Fig. 5.4** height scans of PDMS at 5 and 25 wt.% cross-linker concentrations, respectively. The surface root mean square roughness, R_{rms}, values were

also determined for these and others (larger scan areas) images (for this data see **Table S4** in **Annex V**). As one can see, the surface microstructure remains essentially unchanged throughout the cross-link densities employed. For instance, the surface roughness values at the 5 μm × 5 μm scale have small values, and change very little becoming a bit lower at higher cross-link densities. The approximately 30 % decrease is attributed to the increased stiffness of the specimens with the highest cross-link density.

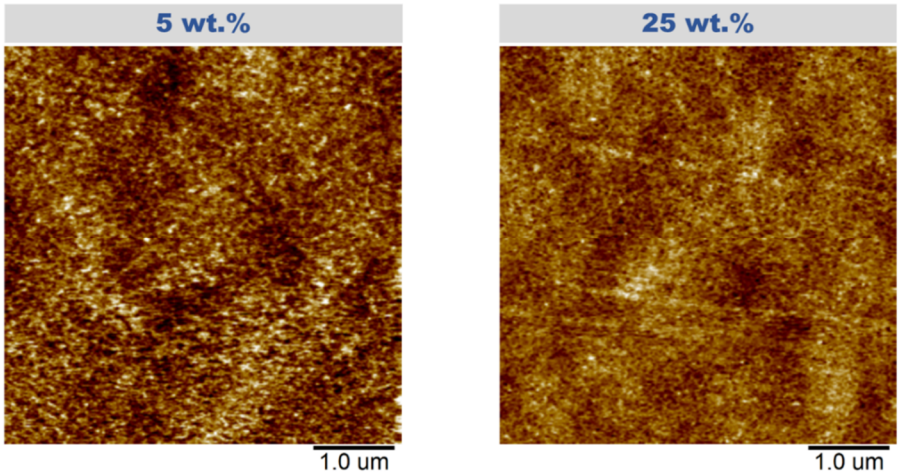

Figure 5.4. AFM height images of the pristine PDMS surface with cross-linker content as indicated. The vertical scale (image height contrast) varies from 0 to 30 nm (dark brown).

We then display higher resolution images for each substrate types used in this work, prior to and following extraction (see **Fig. 5.5**). The PDMS mesh structure can clearly be seen here, as well. As can be observed on **Fig. 5.5**, the network mesh size is not significantly affected by extraction. The average values of the mesh size determined from 200 meshes analyzed for each sample were found to be in the range of 13-16 nm prior to extraction and in the range of 12-13 nm subsequent to extraction (see **Table 5.3**).

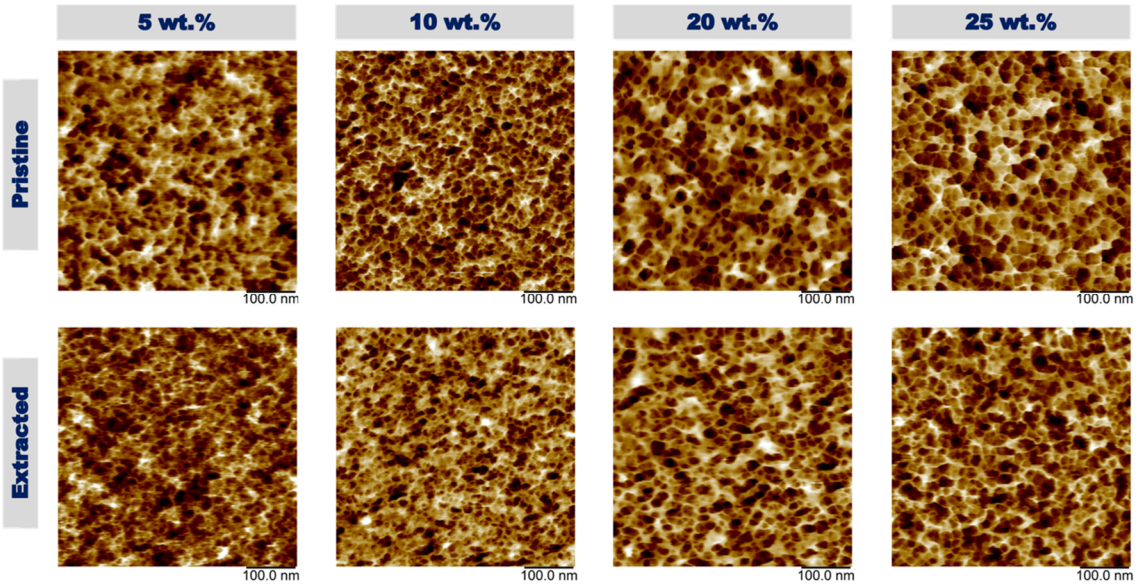

Figure 5.5. AFM height images of the free PDMS surfaces prepared at varied cross-linker concentrations prior to (pristine specimen) and subsequent to (extracted specimen) extraction with cross-linker content as indicated. The scan area is 500 nm × 500 nm for all images.

Table 5.3. *Average values of the network mesh size prior and subsequent to extraction*

Cross-linker concentration, wt.%	*Pristine PDMS surface*	*Extracted PDMS surface*
5	(16 ± 6) nm	(12 ± 3) nm
10	(12 ± 3) nm	(12 ± 3) nm
20	(16 ± 6) nm	(13 ± 4) nm
25	(16 ± 6) nm	(13 ± 4) nm

As here we focus on interface adhesion, of high interest are the measurements of the surface Young's moduli values, as obtained by AFM prior, and subsequent, to Soxhlet extraction. As observed in **Fig. 5.6**, the surface Young's modulus values increase with increasing cross-linker density. However, a significant difference, in contrary to what was observed when measuring the storage modulus, is monitored subsequent to Soxhlet extraction. The surface Young's modulus increased following extraction from 0.7-2.3 MPa, to 2.1-7.8 MPa. Removal of free PDMS chains by extraction should increase the local cross-link density and thus stiffen the elastomer. On the other hand, elimination of stiff silica would weaken the material. We have already shown (see TGA) that extraction removes only very small amounts of silica. As we see a substantial decrease of stiffness with cross-linker concentration (see **Fig. 5.6**), we conclude that the trends observed due to Soxhlet treatment are caused by removal of surface-near chains, as extraction increases the surface stiffness. This observation is very relevant as bacteria sense the surface properties rather than the bulk material, as further evidenced by initial retention studies [198].

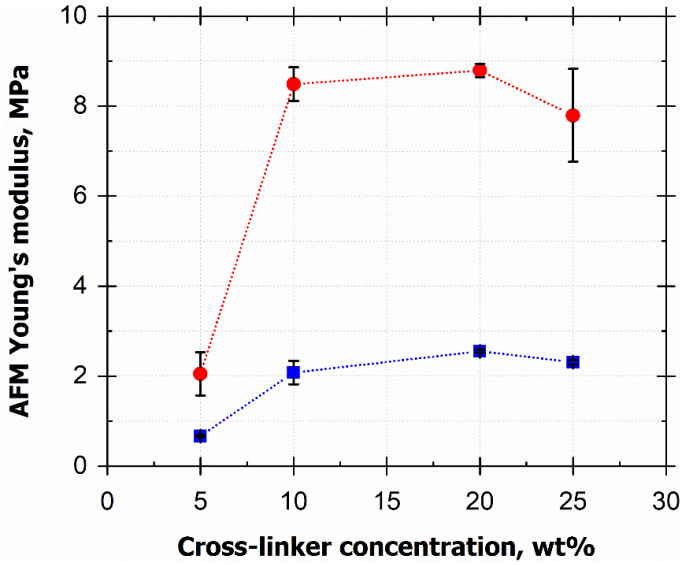

Figure 5.6. AFM surface Young's moduli values as function of the cross-linker content (wt.%) for pristine and extracted PDMS. (Blue squares: prior to extraction; Red circles: following extraction.). Error bars represent standard deviation values of 3 measurements at each data point. Lines are only guides for the eye.

We wish here to recapitulate that the values of the modulus of elasticity for all substrates were determined for their surfaces by AFM, and for the bulk by DMA. For the same PDMS specimens the initial bacterial retention was also studied. Bulk Young's modulus values varied between 0.5 and 1.8 MPa, whereas surface stiffness had values between 2 and 9 MPa. We now briefly discuss the differences observed for the values of stiffness. We first note that the bulk moduli remain essentially unchanged following extraction (see **Table 5.2**). The values of the AFM-measured stiffness for the surface are however strongly dependent on the bulk cross-link density. During AFM tapping the elastic response of the surface depends on the penetration of the stress field into the material, which depends on the contact force and contact area, and the surface modulus. We reason that during extraction free chains are removed from the surface. This causes local stiffening, which reduces the penetration depth of the stress field. However, enhancement of local stress will result in increasing values of the AFM observed "effective" surface modulus, as pointed out by Sokolov *et al*. [217]. Naturally, bacteria experience surface forces and their adherence is determined by their strength. We must keep this in mind for the subsequent discussions.

Fig. 5.7 shows the number of viable bacteria attached to the surface as a function of the bulk storage modulus (**Fig. 5.7a**) and the surface modulus (**Fig. 5.7b**). Experimentally, first the value of the storage modulus, G' was determined by DMA. We

noted that bacterial retention on PDMS samples was inversely proportional to the value of the storage modulus G'. This observation is in good agreement with the literature [114,118]. However, for comparison, we showed in **Fig. 5.7** Young's moduli values, so we needed to convert storage modulus values by DMA to Young's modulus of elasticity. Assuming incompressibility and no frequency dependence, from classical mechanics we know that $E = 3G$. Below we present our discussions in terms of Young's moduli values.

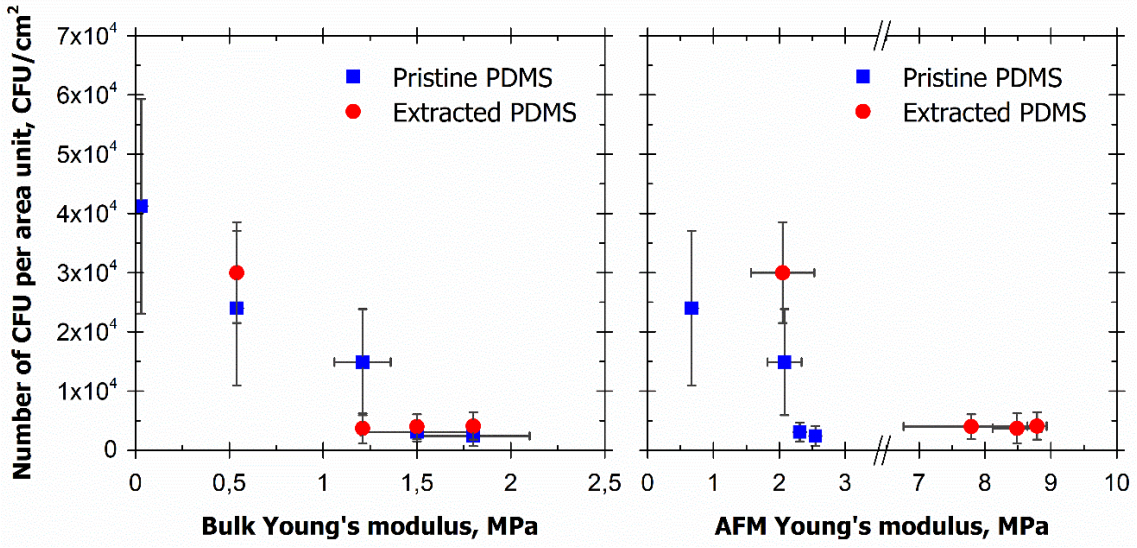

Figure 5.7. The number of colony forming units per surface area as a function of a) the bulk Young's modulus (left) and b) the nanoscale (AFM) Young's modulus (right) of the cross-linked PDMS samples. Each data point represents an average of 9 bacterial retention assays. Error bars represent standard deviations.

As shown in **Fig. 5.7a**, bacterial retention values on the extracted PDMS samples slightly differ from those on the pristine PDMS specimens. **Fig. 5.7a** (data for bulk stiffness) shows that the bacterial retention decreased until a threshold stiffness value at approximately 1.2-1.5 MPa was reached. For higher stiffnesses retention remained low, and unchanged. While these trends were similar when the surface stiffness was considered, the threshold value for surface stiffness was shifted to a significantly higher modulus value of 2.5-2.8 MPa. Remarkably, this value is essentially the same as the surface modulus of the bacteria [218,219].

As the bacterial surface Young's modulus is between 2 to 3 MPa [218,219], the outcome of this work suggests that bacterial adhesion of *Escherichia coli* on PDMS is mechanical as hypothesized earlier by Song *et al.* on PDMS of Young's moduli ranging between 0.1 and 2.6 MPa [114]. Compared to earlier work, here we clearly differentiate between surface and bulk moduli. We identify stiffness threshold values above which

attachment density does not change. These threshold values differ for the surface and the bulk stiffnesses. The crossover between high and changing bacterial retention and low and constant retention can thus be regarded as a contact mechanics effect between soft surfaces and bacteria. We now refer to a study by Ina *et al*. [220] in which adhesion between silica and silicon elastomers were studied to describe adhesion and wetting on elastomers. Without altering the composition of the elastomer, the modulus of PDMS was controlled in the 10^{-3} to 10^{-1} MPa range. The indentation of micrometer-sized silica particles was used to evidence that the transition between adhesion and wetting depends on the particle size. For the smaller particles, indentation is determined by capillary forces and not dependent on the substrate's elastic properties (wetting regime) whereas for larger particles the indentation is determined by both the elastic energy of surface deformation and the work of adhesion in the contact area (adhesion regime). In our investigations, the size and stiffness of the bacterial strain under investigation is constant. Material stiffness dependence of bacterial retention for Young's modulus values lower than that of the bacterial cell surface is tentatively explained by a conformal overlay between the bacterial and elastomer surfaces, respectively. This effect resembles an elasto-capillary phenomenon, where the interface interaction forces for deformable (or fluid) surfaces are balanced also considering the vertical force component in the Young-Dupre equation (substrate deformation) [221].

Due to such elasto-capillary deformations the contact surface between bacteria and substrate are enhanced. Beyond a threshold stiffness (i.e., if surface moduli have similar values, or for stiffer substrates) this effect is losing its impact. If this overlay becomes essentially inefficient for higher substrate stiffnesses beyond a threshold value, the conformal overlay effect is not any more operational. Essential for retention is thus the combination of the elastic energy of surface deformation and the work of adhesion in the contact area as e.g., described by the JKR model.

3. Conclusion

We investigated initial bacterial retention on model (PDMS) surfaces on which, out of the three parameters that determine bacterial retention (chemical composition, stiffness, and surface topography) only one was systematically varied, i.e., the mechanical stiffness, while the two others were unchanged. Substrates were engineered such that the surface modulus values, as measured by AFM ranged between 0.7 and 9 MPa. This was achieved by varying the cross-linking density of PDMS. Following cross-linking, we performed Soxhlet extraction to investigate the effect of non-cross-linked, free chains. The

effect of both bulk and surface moduli on bacterial retention were specifically addressed. We combined bulk and advanced surface characterization techniques to demonstrate that neither the surface chemistry nor the surface topography vary with the substrate preparation. Initial bacterial retention could thus be monitored depending on a single parameter, i.e., materials Young's modulus. We monitored bulk stiffness by DMA and surface stiffness by AFM measurements. The number of bacteria retained, as assessed by initial retention studies, decreases with the increase of both the bulk and the surface mechanical stiffness, and remains essentially unchanged for further stiffening of the substrate beyond a characteristic value that also describes bacterial stiffness. We tentatively explain this observation by considering conformal overlay of bacterial and material surfaces, which might be addressed by considering contact mechanics between bacteria and soft elastomer surfaces.

4. Materials and Methods

4.1. Materials

Cyclohexane (≥99%, GPR RECTAPUR®) and acetone (≥99%) were supplied by VWR Chemicals (Fontenay-sous-Bois, France). Phosphate buffered saline (PBS) (137 mM NaCl, 2.7 mM KCl, 10 mM Na_2HPO_4, 1.76 mM KH_2PO_4, pH = 4.4), chloramphenicol (≥ 98 %) and the nonionic detergent Tween20 were purchased from Sigma-Aldrich (St-Quentin-Fallavier, France). LB and LB agar (for the preparation of plates) were purchased from Difco (Saint-Ferréol, France).

4.2. Bacterial strain and growth medium

The *E. coli* strain used was DH5α carrying the plasmid pSEVA337 which contains the green fluorescent protein (GFP) gene under the control of the constitutive Pem7 promoter. [222] pSEVA337 carrying the resistance to chloramphenicol was obtained from the Standard European Vector Architecture 3.0. The strain was routinely grown at 37 °C in LB and LB agar supplemented with 34 µg/mL chloramphenicol (to maintain the plasmid).

4.3. Preparation of PDMS surfaces

The investigations were carried out with poly(dimethylsiloxane) (PDMS) samples prepared using the Sylgard-184 silicone elastomer kits purchased from the Dow Chemical Company (supplied by Samaro, Lyon, France). The stiffness was adjusted by varying the

cross-linker concentration and thus the cross-linking density. For each given concentration (2.5, 5, 10, 20, and 25 wt.%), the elastomer base and curing agent were thoroughly mixed and degassed under vacuum for 30 min. Then, the mixture was poured into a Petri dish, cured at 60 °C for 24 h, and subsequently incubated at room temperature for another 24 h to achieve complete cross-linking. After curing, the PDMS samples (1 mm thick) were removed from the Petri dish and specimens were punched out with diameters according to the need. The samples were then cleaned by soaking in 70 % ethanol for 20 min, prior to a rinsing step in Milli-Q water.

To extract not cross-linked, free chains, cross-linked PDMS samples prepared at various cross-linker concentration (2.5, 5, 10, 20, and 25 wt.%) were subjected to Soxhlet extraction in acetone/cyclohexane (1:1 mixing ratio) for 48 h at 6 cycles per hour (over 250 wash cycles). The swollen samples were then dried in a vacuum furnace at 80 °C for 24 h. The mass of each PDMS sample was measured using a high precision scale before the extraction and subsequent drying step. The softest specimen at 2.5 wt.% of cross-linker was destroyed and could not be recovered subsequent to extraction.

4.4. Methods

4.4.1. Thermogravimetric analyses (TGA)

Thermogravimetric (TGA) analyses measurements were performed with the not cross-linked material, i.e., on each component (base and cross-linker) separately as well as on the cross-linked PDMS specimen at 20 wt.% of cross-linker. The TGA curves were obtained on a thermogravimetric analyzer Q50 (TA Instruments, New Castle, DE, USA). The experiments were carried out under a nitrogen flow, at a heating rate of 20 °C/min, in a temperature range from 40 to 1000 °C.

4.4.2. Fourier transform infrared (FTIR) spectroscopy

FTIR spectroscopy was performed on both the pre-polymer (base) and the cross-linker components as well as on cured PDMS samples at different cross-linker concentrations (2.5, 5, 20, and 25 wt.%) to evidence the chemical functions exposed to bacteria. The FTIR spectra were measured using a Perkin-Elmer Spectrum One FTIR Spectrometer (Waltham, Massachusetts, USA). The spectra of the pre-polymer and cross-linker components were captured in the transmission mode in the 650-4000 cm^{-1} spectral range, at a 4 cm^{-1} resolution. To this end, a thin layer of each PDMS component (~100 µm) was spread between two polyethylene films (10 µm in thickness) and then mounted into

the sample chamber prior to measurement. The background spectrum of the clean polyethylene films was subtracted from those of the recorded FTIR spectra. The cross-linked PDMS samples were measured in the Attenuated Total Reflection (ATR) mode in the same spectral range.

4.4.3. Dynamic mechanical analysis (DMA)

The dynamic mechanical properties of bulk PDMS before and after extraction were evaluated by measuring the storage modulus (real part of the complex shear modulus, G) in the parallel-plate geometry. The measurements were carried out on both pristine and extracted PDMS specimens at various cross-linker concentrations (2.5, 5, 10, 20, and 25 wt.%), cylindrical in shape (Ø 8 mm, 1 mm thickness) at 25 °C.

First a stress sweep test was performed in the range from 10 to 1000 Pa at a constant frequency of 2 rad/s and at 25 °C. The storage (G') and loss (G'') moduli were found to be independent of the applied shear stress. Frequency sweep tests were done for all the PDMS samples in the range from 80 to 0.045 rad/s at the applied shear stress of 50 Pa and at 25 °C. All the measurements were performed at 10 N applied normal force enabling to avoid slip phenomena at the interface between the plates and the specimens. Experiments were repeated three times to assess the reproducibility of the data.

To ensure the accuracy of the measured data, a series of PDMS samples (2.5, 5, 10, 20, and 25 wt.% cross-linker concentration) was cured within the rheometer (*in situ*) to provide a firm adhesion between the specimen and the plates. The *in situ* cured control specimens of 8 mm in diameter and 1 mm in thickness were characterized in the same measurement conditions: 80 – 0.045 rad/s, 50 Pa applied shear stress, and 25 °C. The applied normal force was fixed at 0.5 N during the frequency sweep measurements.

The bulk Young's moduli of the cross-linked PDMS samples were calculated from the storage modulus measurements using the relation between the Young's modulus, E, and the shear modulus $E = 2G(1 + \nu)$, where ν is Poisson's ratio. Poisson's ratio ν of 0.5 for PDMS was taken from the literature [156,223].

4.4.4. Contact angle measurements

The wetting properties of pristine and extracted PDMS surfaces of various cross-linking density were measured via the static contact angle method using a custom made optical tensiometer. The water droplet volume was of 6-7 µL . A total of 10 droplets were

analyzed using the ImageJ software. All contact angle measurements were conducted at room temperature (21 °C).

For the surface free energy determination, contact angle data of two extra probe liquids, hexadecane and diiodomethane, were measured and analyzed for each sample following the same procedure as with the water droplets. The surface free energy was then determined through the Owens and Wendt equation [159].

4.4.5. X-ray photoelectron spectroscopy (XPS)

XPS spectra were collected on a Quantera SXM (scanning XPS microprobe) from Physical Electronics (aluminium K_α, monochromatic radiation at 1486.6 eV; the base pressure $<3 \times 10^{-8}$ Torr; the detector input angle of 45°) (Feldkirchen, Germany). Compass software for XPS control and Multipak v.9.8.0.19 for data reduction were used. The fitting of the spectra was performed after shifting of the measured spectra with respect to known reference binding energies (aliphatic carbon C1s at 284.8 eV or gold Au4f7/2 at 83.96 eV, silver Ag3d5/2 at 368.21 eV and copper Cu2p3/2 at 932.62 eV).

Five spots (200 μm spot size) for each sample were analyzed, i.e., one for a survey XPS spectra and four for an element spectra and their averaging. Survey XPS spectra were obtained in three cycles with the pass energy of 224 eV.

4.4.6. Atomic Force Microscopy

Pristine and extracted PDMS samples were imaged by AFM using a MultiMode 8 AFM with a NanoScope V controller (Bruker, Santa Barbara, USA), in air and at room temperature (~21 °C). The instrument was operated in the Peak Force Quantitative Nanomechanical Mapping mode (PF-QNM) to record force-distance curves and further processed with the NanoScope Analysis software (version 1.9). An "E" vertical-engagement piezo-scanner was used to acquire data with high resolution. The AFM data was collected following a sine-wave sample-tip trajectory with a frequency of 2 kHz and utilizing a peak-force amplitude value of 150 nm. The ScanAsyst controlled parameters (feedback loop, applied load, etc.) in the user interface of the NanoScope software (version 9.7) were set to "off", in order to apply dedicated scanning settings, particularly low applied normal forces (300 pN – 1 nN) and high feedback loop gain (30 – 70), being both constant for a specific scan. Soft cantilevers were used with a nominal spring constant of 0.5 N/m and silicon-made tip with a nominal radius of 8 nm (μMasch, HQ:NSC19/No Al).

The AFM optical sensitivity (deflection sensitivity) was calculated based on the thermal tune method [224].

The surface Young's modulus obtained by AFM was calculated by fitting the slope of the extended part of force-distance curves with a contact mechanics model based on the Derjaguin, Muller, and Toporov (DMT) theory [225], using the following equation:

$$E = (F_L - F_{adh})\frac{3(1-\nu^2)}{4}R^{-\frac{1}{2}}(z-d)^{-\frac{3}{2}}$$

where: F_L is the applied maximum force (load), F_{adh} is the adhesion force, ν is the Poisson's ratio, R is the AFM tip radius, z is the position of the AFM scanner; d is the cantilever deflection. For the Poisson's ratio a value of 0.49 was used [226]. The nominal spring constant and nominal tip radius values were taken for the calculation.

4.4.7. Bacterial retention on PDMS

DH5α pSEVA337 cells, expressing the GFP, were grown in LB medium under shaking at 37 °C up to the exponential phase of growth at an optical density at 600 nm of 0.6. Cells were harvested by centrifugation at 5000 rpm for 10 min and re-suspended in PBS at an optical density at 600 nm of 0.1 corresponding approximately to 10^7 cells/mL. This bacterial suspension (≈30 mL) was poured in a Petri dish containing clean PDMS samples. After incubation at 37 °C for 1 hour without shaking, the PDMS samples were gently washed by dipping in fresh PBS three times. Then, the adhered cells were detached from the PDMS surfaces by shaking in 10 mL of PBS containing 0.01 vol.% of the Tween20 surfactant. To enumerate colony forming units (CFU) re-suspended in the surfactant-containing PBS we used the counting plate method [166]. Briefly, this procedure consists in spreading 100 µL aliquots from a series of decimal dilutions of the surfactant-containing bacterial suspension on agar plates. The plates are then incubated at 37 °C overnight to count colonies.

To check that the Tween20 did not lyse the cells during the assay, the growth of the strain in LB containing 34 µg/mL of chloramphenicol and LB containing 34 µg/mL of chloramphenicol and 0,01 vol.% Tween20 was monitored by measuring the optical density at 600 nm. (see **Annex V**, **Fig. S7**).

The efficiency of bacterial detaching from PDMS surfaces by rinsing in PBS containing the detergent was also probed by fluorescence microscopy (**Annex V**, **Fig. S8**). To do so, two PDMS samples at 20 wt.% of cross-linker were incubated in the bacterial suspension at 37 °C for 2 hours. One of the samples was gently washed in three PBS

rinsing baths, then a PBS droplet was deposited on the sample and a coverslip was placed on top to immobilize the cells prior to epifluorescence imaging. The second sample also treated through three PBS rinsing baths, followed by shaking in PBS with 0.01 vol.% of the detergent for 20 sec, was subsequently imaged by epifluorescence microscopy.

4.4.8. Epifluorescence microscopy

Samples were mounted between a glass slide and a coverslip, and observed using an Axio Observer Z1 inverted fluorescence microscope (Zeiss, Jena, Germany) equipped with an oil immersion objective 63x NA 1.4. Green fluorescent protein-expressing cells were visualized using a BP 470/40 excitation filter, a FT 495 beam splitter, and a BP 525/50 emission filter. Images were acquired using a Zeiss Axiocam 506 mono camera monitored by the Zeiss Zen 2012 software.

Summary

In **Chapter I** we reviewed the previous studies on the dependence of bacterial adhesion on the physicochemical properties of the substrate (surface energy and wettability, charge, roughness, topography, stiffness). We realized that despite numerous investigations, many contradictory findings are reported in the literature: the bacterial response depends on these intricate properties, often correlated. Concomitantly, the effect of the stiffness on bacterial adhesion has become a topic of interest only in the last few years and was far less considered up to now.

In **Chapter II**, we thus report on analyzes of the bulk properties of commercial LSR grades of various stiffnesses. At first, we determined the silica content and concentration of Si-H groups (cross-link sites) by means of TGA and FTIR, and concluded that the mechanical properties of the LSR grades under investigations were adjusted by varying at least two parameters: cross-link density and silica filler content. Further, we examined the mechanical properties of the cross-linked LSR formulations using two different systems of measurement (in the stretching and in the shear modes).

In the first section of **Chapter III,** we described in detail the topographical properties of both the flat-like LSR and the textured LSR surfaces exhibiting the "lotus leaf effect". The texturing significantly improved the water repellency of the LSR surfaces, and increased their contact angles by 40 – 50°, making them superhydrophobic. In the second section, we discussed the results of the bacterial retention assays on both flat-like and textured LSR surfaces.

Bacterial assays using epifluorescence microscopy revealed numerous disadvantages for this study, since the prolonged exposition of bacteria to the light can cause photobleaching, leading to fading of the fluorescent signal. Bacterial assays using the plate count method revealed that in the 0.3 – 3.5 MPa modulus range (Young's modulus range close to those reported in similar studies), after 1 hour of incubation, the bacterial retention on the flat-like LSR surfaces is inversely correlated to the substrate stiffness. However, this correlation is difficult to interpret, since both surface energy and substrate stiffness of the investigated LSR samples commonly alter bacterial retention.

In contrary to our primary hypothesis, the textured LSR samples exhibiting the "lotus leaf effect" were more favorable to bacterial retention, than the flat-like ones. The conditioning of the textured surfaces exposed to bacterial suspensions can lead to a decrease of the energy barrier of the wetting state transition, resulting in increased liquid

– solid contact area available to the cell body. It is possible that extracellular appendages of bacteria such as flagella are also involved in attachment and enable bacteria to overcome unfavorable anchorage to the surface.

In **Chapter IV**, we discussed the first results of the AFM investigation of the PDMS network morphology observed at the mesh-size resolution. And in **Chapter V** we investigated initial bacterial retention on these model PDMS surfaces on which, out of the three parameters that determine bacterial retention (chemical composition, stiffness, and surface topography) only one was systematically varied, i.e., the mechanical stiffness. The PDMS stiffness was adjusted by varying the cross-linking density of PDMS. We combined bulk and advanced surface characterization techniques to demonstrate that neither the surface chemistry nor the surface topography varies with the substrate preparation. Initial bacterial retention could thus be monitored depending on a single parameter, i.e., materials Young's modulus. The number of bacteria retained, as assessed by initial retention studies, decreases with the increase of both the bulk and the surface mechanical stiffness, and remains essentially unchanged for further stiffening of the substrate beyond a characteristic value that also describes bacterial stiffness. We tentatively explain this observation by considering conformal overlay of bacterial and material surfaces, which might be addressed by considering contact mechanics between bacteria and soft elastomer surfaces.

Going forward, further investigations are foreseen on the basis of the outcomes of this thesis:

- Investigate initial bacterial retention on model PDMS surfaces of various stiffness by direct fluorescent imaging. The issue of photobleaching of fluorescent bacteria could probably be resolved by means of confocal fluorescence microscopy.
- Examine bacterial response on PDMS stiffness using different bacterial strains (e.g., such as Gram-negative *Pseudomonas aeruginosa*, Gram-positive *Staphylococcus epidermidis*).
- Assess bacterial retention on other surfaces of various stiffness (e.g., hydrogels).
- Tackle an approach that consists in surface modification with antimicrobials.

References

[1] A. Sikora, F. Zahra, Nosocomial Infections, in: StatPearls, StatPearls Publishing, Treasure Island (FL), 2021. http://www.ncbi.nlm.nih.gov/books/NBK559312/

[2] R.M. Amin, M.B. Mohamed, M.A. Ramadan, T. Verwanger, B. Krammer, Rapid and sensitive microplate assay for screening the effect of silver and gold nanoparticles on bacteria, *Nanomed.* **4** (2009) 637–643.

[3] I. Mukha, A. Eremenko, G. Korchak, A. Michienkova, Antibacterial Action and Physicochemical Properties of Stabilized Silver and Gold Nanostructures on the Surface of Disperse Silica, *J. Water Resour. Prot*. **2** (2010) 131–136.

[4] S.V. Gudkov, D.E. Burmistrov, D.A. Serov, M.B. Rebezov, A.A. Semenova, A.B. Lisitsyn, A Mini Review of Antibacterial Properties of ZnO Nanoparticles, *Front. Phys.* **9** (2021) 49.

[5] Y.-W. Baek, Y.-J. An, Microbial toxicity of metal oxide nanoparticles (CuO, NiO, ZnO, and Sb2O3) to Escherichia coli, Bacillus subtilis, and Streptococcus aureus, *Sci. Total Environ.* **409** (2011) 1603–1608.

[6] R. Brayner, R. Ferrari-Iliou, N. Brivois, S. Djediat, M.F. Benedetti, F. Fiévet, Toxicological impact studies based on Escherichia coli bacteria in ultrafine ZnO nanoparticles colloidal medium, *Nano Lett.* **6** (2006) 866–870.

[7] R. Dinali, A. Ebrahiminezhad, M. Manley-Harris, Y. Ghasemi, A. Berenjian, Iron oxide nanoparticles in modern microbiology and biotechnology, *Crit. Rev. Microbiol.* **43** (2017) 493–507.

[8] L.M. Armijo, S.J. Wawrzyniec, M. Kopciuch, Y.I. Brandt, A.C. Rivera, N.J. Withers, N.C. Cook, D.L. Huber, T.C. Monson, H.D.C. Smyth, M. Osiński, Antibacterial activity of iron oxide, iron nitride, and tobramycin conjugated nanoparticles against Pseudomonas aeruginosa biofilms, *J. Nanobiotechnology*. **18** (2020) 35.

[9] C. Muñoz-Villagrán, F. Contreras, F. Cornejo, M. Figueroa, D. Valenzuela-Bezanilla, R. Luraschi, C. Reinoso, J. Rivas-Pardo, C. Vásquez, M. Castro, F. Arenas, Understanding gold toxicity in aerobically-grown Escherichia coli, *Biol. Res*. **53** (2020) 26.

[10] K. Zheng, M.I. Setyawati, D.T. Leong, J. Xie, Antimicrobial Gold Nanoclusters, *ACS Nano*. **11** (2017) 6904–6910.

[11] M.J. Hajipour, K.M. Fromm, A. Akbar Ashkarran, D. Jimenez de Aberasturi, I.R. de Larramendi, T. Rojo, V. Serpooshan, W.J. Parak, M. Mahmoudi, Antibacterial properties of nanoparticles, *Trends Biotechnol.* **30** (2012) 499–511.

[12] M. Godoy-Gallardo, U. Eckhard, L.M. Delgado, Y.J.D. de Roo Puente, M. Hoyos-Nogués, F.J. Gil, R.A. Perez, Antibacterial approaches in tissue engineering using metal ions and nanoparticles: From mechanisms to applications, *Bioact. Mater*. **6** (2021) 4470–4490.

[13] L. Wang, C. Hu, L. Shao, The antimicrobial activity of nanoparticles: present situation and prospects for the future, *Int. J. Nanomedicine*. **12** (2017) 1227–1249.

[14] P. Kingshott, J. Wei, D. Bagge-Ravn, N. Gadegaard, L. Gram, Covalent Attachment of Poly(ethylene glycol) to Surfaces, Critical for Reducing Bacterial Adhesion, *Langmuir*. **19** (2003) 6912–6921.

[15] A. Roosjen, H.C. van der Mei, H.J. Busscher, W. Norde, Microbial adhesion to poly(ethylene oxide) brushes: influence of polymer chain length and temperature, *Langmuir ACS J. Surf. Colloids*. **20** (2004) 10949–10955.

[16] E. Ostuni, R.G. Chapman, M.N. Liang, G. Meluleni, G. Pier, D.E. Ingber, G.M. Whitesides, Self-Assembled Monolayers That Resist the Adsorption of Proteins and the Adhesion of Bacterial and Mammalian Cells, *Langmuir*. **17** (2001) 6336–6343.

[17] X. Zhang, D. Brodus, V. Hollimon, H. Hu, A brief review of recent developments in the designs that prevent bio-fouling on silicon and silicon-based materials, *Chem. Cent. J.* **11** (2017) 18.

[18] T. Fenchel, H. Blackburn, G.M. King, Bacterial Biogeochemistry: The Ecophysiology of Mineral Cycling, Academic Press, 2012.

[19] R.H. McBee, C. Lamanna, O.B. Weeks, Definitions of bacterial oxygen relationships, *Bacteriol. Rev*. **19** (1955) 45–47.

[20] M.R.V. User:Athulvis LadyofHatsTranslated by, English: Average prokaryote cell, 2008. https://commons.wikimedia.org/wiki/File:Average_prokaryote_cell-_ml.svg

[21] Online Textbook of Bacteriology, http://www.textbookofbacteriology.net/ken_todar.html (accessed May 17, 2020).

[22] S. Berezin, Y. Aviv, H. Aviv, E. Goldberg, Y.R. Tischler, Replacing a Century Old Technique – Modern Spectroscopy Can Supplant Gram Staining, *Sci. Rep*. **7** (2017) 3810.

[23] C. Berne, C.K. Ellison, A. Ducret, Y.V. Brun, Bacterial adhesion at the single-cell level, *Nat. Rev. Microbiol.* **16** (2018) 616–627.

[24] J.D. Buynak, Cutting and Stitching: The Cross-Linking of Peptidoglycan in the Assembly of the Bacterial Cell Wall, *ACS Chem. Biol*. **2** (2007) 602–605.

[25] W. Rawicz, K.C. Olbrich, T. McIntosh, D. Needham, E. Evans, Effect of Chain Length and Unsaturation on Elasticity of Lipid Bilayers, *Biophys. J*. **79** (2000) 328–339.

[26] G. Francius, P. Polyakov, J. Merlin, Y. Abe, J.-M. Ghigo, C. Merlin, C. Beloin, J.F.L. Duval, Bacterial Surface Appendages Strongly Impact Nanomechanical and Electrokinetic

Properties of Escherichia coli Cells Subjected to Osmotic Stress, *PLoS ONE*. **6** (2011) e20066.

[27] C. Berne, A. Ducret, G.G. Hardy, Y.V. Brun, Adhesins Involved in Attachment to Abiotic Surfaces by Gram-Negative Bacteria, *Microbiol Spectr*. **3** (2017) 27.

[28] T. Schweinitzer, C. Josenhans, Bacterial energy taxis: a global strategy?, *Arch. Microbiol*. **192** (2010) 507–520.

[29] J. Palmer, S. Flint, J. Brooks, Bacterial cell attachment, the beginning of a biofilm, J. Ind. *Microbiol. Biotechnol*. **34** (2007) 577–588.

[30] R.S. Friedlander, H. Vlamakis, P. Kim, M. Khan, R. Kolter, J. Aizenberg, Bacterial flagella explore microscale hummocks and hollows to increase adhesion, *Proc. Natl. Acad. Sci*. **110** (2013) 5624–5629.

[31] Z.D. Blount, The unexhausted potential of E. coli, *ELife*. **4** (2015) e05826.

[32] Infections nosocomiales | Inserm - La science pour la santé, https://www.inserm.fr/information-en-sante/dossiers-information/infections-nosocomiales (accessed May 18, 2020).

[33] B. Carpentier, O. Cerf, Biofilms and their consequences, with particular reference to hygiene in the food industry, *J. Appl. Bacteriol.* **75** (1993) 499–511.

[34] J.W. Costerton, Z. Lewandowski, D.E. Caldwell, D.R. Korber, H.M. Lappin-Scott, Microbial Biofilms, *Annu. Rev. Microbiol.* **49** (1995) 711–745.

[35] Book: Microbiology (Kaiser), Biol. Libr. (2013). https://bio.libretexts.org/Bookshelves/Microbiology/Book%3A_Microbiology_(Kaiser) (accessed October 4, 2020).

[36] F. Ahmad, D. Zhu, J. Sun, Bacterial chemotaxis: a way forward to aromatic compounds biodegradation, *Environ. Sci. Eur.* **32** (2020) 52.

[37] A.J. Slate, D. Wickens, J. Wilson-Nieuwenhuis, N. Dempsey-Hibbert, G. West, P. Kelly, J. Verran, C.E. Banks, K.A. Whitehead, The effects of blood conditioning films on the antimicrobial and retention properties of zirconium-nitride silver surfaces, *Colloids Surf. B Biointerfaces*. **173** (2019) 303–311.

[38] M. Santin, A. Motta, S.P. Denyer, M. Cannas, Effect of the urine conditioning on ureteral stent encrustation and characterization of its protein composition, *Biomaterials*. **20** (1999) 7.

[39] H. Yuan, B. Qian, H. Chen, M. Lan, The influence of conditioning film on antifouling properties of the polyurethane film modified by chondroitin sulfate in urine, *Appl. Surf. Sci.* **426** (2017) 587–596.

[40] J.M.R. Moreira, L.C. Gomes, K.A. Whitehead, S. Lynch, L.A. Tetlow, F.J. Mergulhão, Effect of surface conditioning with cellular extracts on Escherichia coli adhesion and initial biofilm formation, *Food Bioprod. Process.* **104** (2017) 1–12.

[41] S.N.L. Talluri, R.M. Winter, D.R. Salem, Conditioning film formation and its influence on the initial adhesion and biofilm formation by a cyanobacterium on photobioreactor materials, *Biofouling.* **36** (2020) 183–199.

[42] F. Song, H. Koo, D. Ren, Effects of Material Properties on Bacterial Adhesion and Biofilm Formation*, J. Dent. Res*. **94** (2015) 1027–1034.

[43] W.M. Dunne, Bacterial Adhesion: Seen Any Good Biofilms Lately?, *Clin. Microbiol. Rev*. **15** (2002) 155–166.

[44] K.C. Marshall, R. Stout, R. Mitchell, Mechanism of the Initial Events in the Sorption of Marine Bacteria to Surfaces, *J. Gen. Microbiol*. **68** (1971) 337–348.

[45] C.J. van Oss, Acid—base interfacial interactions in aqueous media, *Colloids and Surfaces A: Physicochemical and Engineering Aspects*. **78** (1993) 1–49.

[46] M. Hermansson, The DLVO theory in microbial adhesion, *Colloids Surf. B Biointerfaces*. **14** (1999) 105–119.

[47] Y. Hong, D.G. Brown, Electrostatic Behavior of the Charge-Regulated Bacterial Cell Surface, *Langmuir*. **24** (2008) 5003–5009.

[48] Y. Cheng, G. Feng, C.I. Moraru, Micro- and Nanotopography Sensitive Bacterial Attachment Mechanisms: A Review, *Front. Microbiol*. **10** (2019) 191.

[49] J.H. Adair, E. Suvaci, J. Sindel, Surface and Colloid Chemistry, in: Surf. Colloid Chem. Encycl. Mater. Sci. Technol., Elsevier Science Ltd, 2001: pp. 8996–9006.

[50] M.-N. Bellon-Fontaine, N. Mozes, H.C. van der Mei, J. Sjollema, O. Cerf, P.G. Rouxhet, H.J. Busscher, A comparison of thermodynamic approaches to predict the adhesion of dairy microorganisms to solid substrata, *Cell Biophys*. **17** (1990) 93–106.

[51] J.J. Shephard, D.M. Savory, P.J. Bremer, A.J. McQuillan, Salt Modulates Bacterial Hydrophobicity and Charge Properties Influencing Adhesion of *Pseudomonas aeruginosa* (PA01) in Aqueous Suspensions, *Langmuir*. **26** (2010) 8659–8665.

[52] M.D. Hoffman, L.I. Zucker, P.J.B. Brown, D.T. Kysela, Y.V. Brun, S.C. Jacobson, Timescales and Frequencies of Reversible and Irreversible Adhesion Events of Single Bacterial Cells, *Anal. Chem*. **87** (2015) 12032–12039.

[53] L.A. Pratt, R. Kolter, Genetic analysis of *Escherichia coli* biofilm formation: roles of flagella, motility, chemotaxis and type I pili, *Mol. Microbiol*. **30** (1998) 285–293.

[54] V.D. Gordon, L. Wang, Bacterial mechanosensing: the force will be with you, always, *J. Cell Sci*. **132** (2019) jcs227694.

[55] O.E. Petrova, K. Sauer, Sticky Situations: Key Components That Control Bacterial Surface Attachment, *J. Bacteriol*. **194** (2012) 2413–2425.

[56] P. Di Martino, Extracellular polymeric substances, a key element in understanding biofilm phenotype, *AIMS Microbiol*. **4** (2018) 274–288.

[57] J.W. Costerton, Bacterial Biofilms: A Common Cause of Persistent Infections, *Science*. **284** (1999) 1318–1322.

[58] S.C. Dexter, J.D. Sullivan, J. Williams, S.W. Watson, Influence of Substrate Wettability on the Attachment of Marine Bacteria to Various Surfaces, Appl. Microbiol. 30 (1975) 298–308.

[59] S.C. Dexter, Influence of Substratum Critical Surface Tension on Bacterial Adhesion - in Situ Studies I, (1979) 9.

[60] M. Rosenberg, S. Kjelleberg, Hydrophobic Interactions: Role in Bacterial Adhesion, in: K.C. Marshall (Ed.), Adv. Microb. Ecol., Springer US, Boston, MA, 1986: pp. 353–393.

[61] T.A. Stenström, Bacterial hydrophobicity, an overall parameter for the measurement of adhesion potential to soil particles, *Appl. Environ. Microbiol.* **55** (1989) 142–147.

[62] N. Nuraje, W.S. Khan, Y. Lei, M. Ceylan, R. Asmatulu, Superhydrophobic electrospun nanofibers, *J Mater Chem A*. **1** (2013) 1929–1946.

[63] M. Grivet, J.J. Morrier, G. Benay, O. Barsotti, Effect of hydrophobicity on in vitro streptococcal adhesion to dental alloys, *J. Mater. Sci. Mater. Med*. **11** (2000) 637–642.

[64] Y. Liu, Q. Zhao, Influence of surface energy of modified surfaces on bacterial adhesion, *Biophys. Chem*. **117** (2005) 39–45.

[65] C.I. Pereni, Q. Zhao, Y. Liu, E. Abel, Surface free energy effect on bacterial retention, *Colloids Surf. B Biointerfaces*. **48** (2006) 143–147.

[66] X. Zhang, Q. Zhang, T. Yan, Z. Jiang, X. Zhang, Y.Y. Zuo, Quantitatively Predicting Bacterial Adhesion Using Surface Free Energy Determined with a Spectrophotometric Method, *Environ. Sci. Technol*. **49** (2015) 6164–6171.

[67] L. C. Gomes, J. M. R. Moreira, J. D. P. Araújo, F. J. Mergulhão, Surface conditioning with Escherichia coli cell wall components can reduce biofilm formation by decreasing initial adhesion, *AIMS Microbiol*. **3** (2017) 613–628.

[68] S.F. Rose, S. Okere, G.W. Hanlon, A.W. Lloyd, A.L. Lewis, Bacterial adhesion to phosphorylcholine-based polymers with varying cationic charge and the effect of heparin pre-adsorption, J. Mater. Sci. Mater. Med. 16 (2005) 1003–1015.

[69] S.N. Kang, C.M. Jeong, Y.C. Jeon, E.-S. Byon, Y.-S. Jeong, L.-R. Cho, Effects of Mg-ion and Ca-ion implantations on P. gingivalis and F. nucleatum adhesion, *Tissue Eng. Regen. Med*. **11** (2014) 39–46.

[70] M. Katsikogianni, Y. Missirlis, Concise review of mechanisms of bacterial adhesion to biomaterials and of techniques used in estimating bacteria-material interactions, *Eur. Cell. Mater*. 8 (2004) 37–57.

[71] K. Bazaka, R.J. Crawford, E.P. Ivanova, Do bacteria differentiate between degrees of nanoscale surface roughness?, *Biotechnol. J*. **6** (2011) 1103–1114.

[72] X. Zhang, L. Wang, E. Levänen, Superhydrophobic surfaces for the reduction of bacterial adhesion, *RSC Adv*. **3** (2013) 12003.

[73] S. Wu, B. Zhang, Y. Liu, X. Suo, H. Li, Influence of surface topography on bacterial adhesion: A review (Review), *Biointerphases*. **13** (2018) 060801.

[74] A. Elbourne, J. Chapman, A. Gelmi, D. Cozzolino, R.J. Crawford, V.K. Truong, Bacterial-nanostructure interactions: The role of cell elasticity and adhesion forces, *J. Colloid Interface Sci*. **546** (2019) 192–210.

[75] S.H. Flint, P.J. Bremer, J.D. Brooks, Biofilms in dairy manufacturing plant-description, current concerns and methods of control, *Biofouling*. **11** (1997) 81–97.

[76] R.L. Taylor, J. Verran, G.C. Lees, A.J.P. Ward, The influence of substratum topography on bacterial adhesion to polymethyl methacrylate, *J. Mater. Sci. Mater. Med*. **9** (1998) 6.

[77] M. Quirynen, C.M. Bollen, W. Papaioannou, J. Van Eldere, D. van Steenberghe, The influence of titanium abutment surface roughness on plaque accumulation and gingivitis: short-term observations, *Int. J. Oral Maxillofac. Implants*. **11** (1996) 169–178.

[78] N. Mitik-Dineva, J. Wang, V.K. Truong, P. Stoddart, F. Malherbe, R.J. Crawford, E.P. Ivanova, Escherichia coli, Pseudomonas aeruginosa, and Staphylococcus aureus Attachment Patterns on Glass Surfaces with Nanoscale Roughness, *Curr. Microbiol*. **58** (2009) 268–273.

[79] N. Mitik-Dineva, J. Wang, R.C. Mocanasu, P.R. Stoddart, R.J. Crawford, E.P. Ivanova, Impact of nano-topography on bacterial attachment, *Biotechnol. J*. **3** (2008) 536–544.

[80] N. Mitik-Dineva, J. Wang, V.K. Truong, P.R. Stoddart, F. Malherbe, R.J. Crawford, E.P. Ivanova, Differences in colonisation of five marine bacteria on two types of glass surfaces, *Biofouling*. **25** (2009) 621–631.

[81] E.P. Ivanova, V.K. Truong, H.K. Webb, V.A. Baulin, J.Y. Wang, N. Mohammodi, F. Wang, C. Fluke, R.J. Crawford, Differential attraction and repulsion of Staphylococcus aureus and Pseudomonas aeruginosa on molecularly smooth titanium films, *Sci. Rep*. **1** (2011) 165.

[82] R.P.U. Karunasiri, R. Bruinsma, J. Rudnick, Thin-Film Growth and the Shadow Instability, *Phys. Rev. Lett*. **62** (1989) 788–791.

[83] S. Svensson, M. Forsberg, M. Hulander, F. Vazirisani, P. Thomsen, M. Trobos, A. Palmquist, J. Lausmaa, Role of nanostructured gold surfaces on monocyte activation and Staphylococcus epidermidis biofilm formation, *Int. J. Nanomedicine*. **9** (2014) 775.

[84] R.J. Crawford, H.K. Webb, V.K. Truong, J. Hasan, E.P. Ivanova, Surface topographical factors influencing bacterial attachment, *Adv. Colloid Interface Sci*. **142** (2012) 179–182.

[85] E. Medilanski, K. Kaufmann, L.Y. Wick, O. Wanner, H. Harms, Influence of the Surface Topography of Stainless Steel on Bacterial Adhesion, *Biofouling.* **18** (2002) 193–203.

[86] K.J. Edwards, A.D. Rutenberg, Microbial response to surface microtopography: the role of metabolism in localized mineral dissolution, *Chem. Geol*. **180** (2001) 19–32.

[87] K.A. Whitehead, J. Colligon, J. Verran, Retention of microbial cells in substratum surface features of micrometer and sub-micrometer dimensions, *Colloids Surf. B Biointerfaces*. **41** (2005) 129–138.

[88] K.A. Whitehead, J. Verran, The Effect of Surface Topography on the Retention of Microorganisms, *Food Bioprod. Process*. **84** (2006) 253–259.

[89] D. Perera-Costa, J.M. Bruque, M.L. González-Martín, A.C. Gómez-García, V. Vadillo-Rodríguez, Studying the Influence of Surface Topography on Bacterial Adhesion using Spatially Organized Microtopographic Surface Patterns, *Langmuir*. **30** (2014) 4633–4641.

[90] S. Perni, P. Prokopovich, Micropatterning with conical features can control bacterial adhesion on silicone, *Soft Matter*. **9** (2013) 1844–1851.

[91] S. Hou, H. Gu, C. Smith, D. Ren, Microtopographic Patterns Affect Escherichia coli Biofilm Formation on Poly(dimethylsiloxane) Surfaces, *Langmuir.* **27** (2011) 2686–2691.

[92] U. Mehmood, F.A. Al-Sulaiman, B.S. Yilbas, B. Salhi, S.H.A. Ahmed, M.K. Hossain, Superhydrophobic surfaces with antireflection properties for solar applications: A critical review, *Sol. Energy Mater. Sol. Cells*. **157** (2016) 604–623.

[93] R.N. Wenzel, Resistance of solid surfaces to wetting by water, *Ind. Eng. Chem*. **28** (1936) 988–994.

[94] D. Murakami, H. Jinnai, A. Takahara, Wetting Transition from the Cassie–Baxter State to the Wenzel State on Textured Polymer Surfaces, *Langmuir*. **30** (2014) 2061–2067.

[95] K.B. Golovin, J.W. Gose, M. Perlin, S.L. Ceccio, A. Tuteja, Bioinspired surfaces for turbulent drag reduction, *Philos. Trans. R. Soc. Math. Phys. Eng. Sci*. **374** (2016) 20160189.

[96] R.A. Bidkar, L. Leblanc, A.J. Kulkarni, V. Bahadur, S.L. Ceccio, M. Perlin, Skin-friction drag reduction in the turbulent regime using random-textured hydrophobic surfaces, *Phys. Fluids*. **26** (2014) 085108.

[97] C.R. Crick, S. Ismail, J. Pratten, I.P. Parkin, An investigation into bacterial attachment to an elastomeric superhydrophobic surface prepared via aerosol assisted deposition, *Thin Solid Films*. **519** (2011) 3722–3727.

[98] B.J. Privett, J. Youn, S.A. Hong, J. Lee, J. Han, J.H. Shin, M.H. Schoenfisch, Antibacterial Fluorinated Silica Colloid Superhydrophobic Surfaces, *Langmuir*. **27** (2011) 9597–9601.

[99] F. Hizal, N. Rungraeng, J. Lee, S. Jun, H.J. Busscher, H.C. van der Mei, C.-H. Choi, Nanoengineered Superhydrophobic Surfaces of Aluminum with Extremely Low Bacterial Adhesivity, *ACS Appl. Mater. Interfaces*. **9** (2017) 12118–12129.

[100] E. Fadeeva, V.K. Truong, M. Stiesch, B.N. Chichkov, R.J. Crawford, J. Wang, E.P. Ivanova, Bacterial Retention on Superhydrophobic Titanium Surfaces Fabricated by Femtosecond Laser Ablation, *Langmuir*. **27** (2011) 3012–3019.

[101] C. Sousa, D. Rodrigues, R. Oliveira, W. Song, J.F. Mano, J. Azeredo, Superhydrophobic poly(L-lactic acid) surface as potential bacterial colonization substrate, *AMB Express*. **1** (2011) 34.

[102] R.S. Friedlander, H. Vlamakis, P. Kim, M. Khan, R. Kolter, J. Aizenberg, Bacterial flagella explore microscale hummocks and hollows to increase adhesion, *Proc. Natl. Acad. Sci*. **110** (2013) 5624–5629.

[103] E.P. Ivanova, J. Hasan, H.K. Webb, V.K. Truong, G.S. Watson, J.A. Watson, V.A. Baulin, S. Pogodin, J.Y. Wang, M.J. Tobin, C. Löbbe, R.J. Crawford, Natural Bactericidal Surfaces: Mechanical Rupture of Pseudomonas aeruginosa Cells by Cicada Wings, *Small*. **8** (2012) 2489–2494.

[104] S. Pogodin, J. Hasan, V.A. Baulin, H.K. Webb, V.K. Truong, T.H. Phong Nguyen, V. Boshkovikj, C.J. Fluke, G.S. Watson, J.A. Watson, R.J. Crawford, E.P. Ivanova, Biophysical Model of Bacterial Cell Interactions with Nanopatterned Cicada Wing Surfaces, *Biophys. J*. **104** (2013) 835–840.

[105] E.P. Ivanova, J. Hasan, H.K. Webb, G. Gervinskas, S. Juodkazis, V.K. Truong, A.H.F. Wu, R.N. Lamb, V.A. Baulin, G.S. Watson, J.A. Watson, D.E. Mainwaring, R.J. Crawford, Bactericidal activity of black silicon, *Nat. Commun*. **4** (2013) 2838.

[106] K. Modaresifar, S. Azizian, M. Ganjian, L.E. Fratila-Apachitei, A.A. Zadpoor, Bactericidal effects of nanopatterns: A systematic review, *Acta Biomater*. **83** (2019) 29–36.

[107] R.G. Wells, The role of matrix stiffness in regulating cell behavior, *Hepatology*. **47** (2008) 1394–1400.

[108] N. Wang, J.D. Tytell, D.E. Ingber, Mechanotransduction at a distance: mechanically coupling the extracellular matrix with the nucleus, *Nat. Rev. Mol. Cell Biol*. **10** (2009) 75–82.

[109] D.E. Discher, Tissue Cells Feel and Respond to the Stiffness of Their Substrate, *Science*. **310** (2005) 1139–1143.

[110] J.A. Lichter, M.T. Thompson, M. Delgadillo, T. Nishikawa, M.F. Rubner, K.J. Van Vliet, Substrata Mechanical Stiffness Can Regulate Adhesion of Viable Bacteria, *Biomacromolecules*. **9** (2008) 1571–1578.

[111] K.W. Kolewe, S.R. Peyton, J.D. Schiffman, Fewer Bacteria Adhere to Softer Hydrogels, *ACS Appl. Mater. Interfaces*. **7** (2015) 19562–19569.

[112] K.W. Kolewe, J. Zhu, N.R. Mako, S.S. Nonnenmann, J.D. Schiffman, Bacterial Adhesion Is Affected by the Thickness and Stiffness of Poly(ethylene glycol) Hydrogels, *ACS Appl. Mater. Interfaces*. **10** (2018) 2275–2281.

[113] N. Saha, C. Monge, V. Dulong, C. Picart, K. Glinel, Influence of Polyelectrolyte Film Stiffness on Bacterial Growth, *Biomacromolecules*. **14** (2013) 520–528.

[114] F. Song, D. Ren, Stiffness of Cross-Linked Poly(Dimethylsiloxane) Affects Bacterial Adhesion and Antibiotic Susceptibility of Attached Cells, *Langmuir*. **30** (2014) 10354–10362.

[115] F. Song, M.E. Brasch, H. Wang, J.H. Henderson, K. Sauer, D. Ren, How Bacteria Respond to Material Stiffness during Attachment: A Role of *Escherichia coli* Flagellar Motility, *ACS Appl. Mater. Interfaces.* **9** (2017) 22176–22184.

[116] F. Song, H. Wang, K. Sauer, D. Ren, Cyclic-di-GMP and oprF Are Involved in the Response of Pseudomonas aeruginosa to Substrate Material Stiffness during Attachment on Polydimethylsiloxane (PDMS), *Front. Microbiol*. **9** (2018) 110.

[117] H. Straub, C.M. Bigger, J. Valentin, D. Abt, X. Qin, L. Eberl, K. Maniura-Weber, Q. Ren, Bacterial Adhesion on Soft Materials: Passive Physicochemical Interactions or Active Bacterial Mechanosensing?, *Adv. Healthc. Mater*. **8** (2019) 1801323.

[118] J.D.P. Valentin, X.-H. Qin, C. Fessele, H. Straub, H.C. van der Mei, M.T. Buhmann, K. Maniura-Weber, Q. Ren, Substrate viscosity plays an important role in bacterial adhesion under fluid flow, *J. Colloid Interface Sci*. **552** (2019) 247–257.

[119] F. Pan, S. Altenried, M. Liu, D. Hegemann, E. Bülbül, J. Moeller, W.W. Schmahl, K. Maniura-Weber, Q. Ren, A nanolayer coating on polydimethylsiloxane surfaces enables a mechanistic study of bacterial adhesion influenced by material surface physicochemistry, *Mater. Horiz*. **7** (2020) 93–103.

[120] S.L. Arias, J. Devorkin, A. Civantos, J.P. Allain, *Escherichia coli* Adhesion and Biofilm Formation on Polydimethylsiloxane are Independent of Substrate Stiffness, *Langmuir*. **37** (2021) 16–25.

[121] C.R. McMillin, Biomedical Applications of Rubbers and Elastomers, *Rubber Chem. Technol*. **79** (2006) 500–519.

[122] S. Madhumanchi, T. Srichana, A.J. Domb, Polymeric Biomaterials, in: Biomed. Mater., Springer International Publishing, 2021: pp. 49–100.

[123] J.E. Mark, Thermoset Elastomers, in: M. Kutz (Ed.), Appl. Plast. Eng. Handb. Second Ed., William Andrew Publishing, 2017: pp. 109–125.

[124] M. Fontanille, Y. Gnanou, Chimie et physico-chimie des polymères, DUNOD, Paris, 2002.

[125] H. Steinfink, B. Post, I. Fankuchen, The crystal structure of octamethyl cyclotetrasiloxane, *Acta Crystallogr*. **8** (1955) 420–424.

[126] K.J. Saunders, Organic Polymer Chemistry, Springer Netherlands, Dordrecht, 1988.

[127] F. Angot, Élastomères siloxanes à liens dynamiques, Université Pierre et Marie Curie - Paris VI, 2016. https://tel.archives-ouvertes.fr/tel-01918184.

[128] M.A. Brook, Silicon in Organic, Organometallic, and Polymer Chemistry, John Wiley&Sons, John Wiley & Sons, New York, 2000.

[129] A. Colas, J. Curtis, Silicone Elastomers: History and Biomaterials, in: Biomater. Sci. - 2nd Ed., Elsevier, 2005.: p. 20.

[130] P. Lucas, J.-J. Robin, Silicone-Based Polymer Blends: An Overview of the Materials and Processes, in: Funct. Mater. Biomater., Springer Berlin Heidelberg, Berlin, Heidelberg, 2007: pp. 111–147.

[131] P. Mazurek, S. Vudayagiri, A.L. Skov, How to tailor flexible silicone elastomers with mechanical integrity: a tutorial review, *Chem. Soc. Rev*. **48** (2019) 1448–1464.

[132] B. Karstedt, Platinum-vinylsiloxanes, US3715334A, 1973. https://patents.google.com/patent/US3715334A/en

[133] L.N. Lewis, J. Stein, Y. Gao, R.E. Colborn, G. Hutchins, Platinum Catalysts Used in the Silicones Industry, *Platin. Met. Rev*. **41** (1997) 66–75.

[134] M. Mayer, R. Rabindranath, J. Börner, E. Hörner, A. Bentz, J. Salgado, H. Han, H. Böse, J. Probst, M. Shamonin, G.J. Monkman, G. Schlunck, Ultra-Soft PDMS-Based Magnetoactive Elastomers as Dynamic Cell Culture Substrata, *PLoS ONE*. **8** (2013) e76196.

[135] V. Drebezghova, H. Gojzewski, A. Allal, M.A. Hempenius, C. Nardin, G.J. Vancso, Network Mesh Nanostructures in Cross-Linked Poly(Dimethylsiloxane) Visualized by AFM, *Macromol. Chem. Phys*. (2020) 2000170.

[136] M. Bont, C. Barry, S. Johnston, A review of liquid silicone rubber injection molding: Process variables and process modeling, *Polym. Eng. Sci*. **61** (2021) 331–347.

[137] E. Delebecq, F. Ganachaud, Looking over Liquid Silicone Rubbers: (1) Network Topology vs Chemical Formulations, *ACS Appl. Mater. Interfaces*. **4** (2012) 3340–3352.

[138] E. Narro Medrano, WACKER Solid and Liquid Silicone Rubber - Materials and Processing GUIDELINES, 2014.

[139] Bluestar Silicones. Healthcare liquid silicone rubber - injection molding guide. http://www.silbione.com/wp-content/uploads/2014/02/LSR-Users-Guide.pdf.

[140] G.L. Flowers, S.T. Switzer, Background material properties of selected silicone potting compounds and raw materials for their substitutes, United States: n. p. (1978).

[141] E. Delebecq, S. Hamdani-Devarennes, J. Raeke, J.-M. Lopez Cuesta, F. Ganachaud, High Residue Contents Indebted by Platinum and Silica Synergistic Action during the Pyrolysis of Silicone Formulations, *ACS Appl. Mater. Interfaces*. **3** (2011) 869–880.

[142] M.E. Jeff LeFan, Liquid Silicone Rubber Injection Molding, St.-Gobain Perform. *Plast. Tech. Pap*. (2011).

[143] MettlerToledo™, The MultiSTAR® DSC Sensor Family Outstanding Resolution and Sensitivity, Technical Paper, 2010, (n.d.).

[144] MettlerToledo™, DSC Measurements at High Heating Rates - Advantages and Limitations, Thermal Analysis Application No. UC 191, (n.d.).

[145] B. Caubet, Caractérisation de Silicone Liquide (LSR) : Essais de traction - Rhéologie - Mesure de l'angle de contact, (2018) 25.

[146] A.J.C.B. de Saint-Venant, Mémoire sur la torsion des prismes, *Mém. Présentés Par Divers Savants À L'Académie Sci*. **14** (1856) 233–560.

[147] TA Instruments, ARES Rheometer: Rheometrics Series User Manual, New Castle, DE, 2003.

[148] C. Dessi, S. Coppola, D. Vlassopoulos, Dynamic mechanical analysis with torsional rectangular geometry: A critical assessment of constrained warping models, *J. Rheol*. **65** (2021) 325.

[149] ASTM-D5279, Standard Test Method for Plastics: Dynamic Mechanical Properties: In Torsion, West Conshohocken, PA, 2013.

[150] A. Harkous, G. Colomines, E. Leroy, P. Mousseau, R. Deterre, The kinetic behavior of Liquid Silicone Rubber: A comparison between thermal and rheological approaches based on gel point determination, *React. Funct. Polym*. **101** (2016) 20–27.

[151] K. Efimenko, W.E. Wallace, J. Genzer, Surface Modification of Sylgard-184 Poly(dimethyl siloxane) Networks by Ultraviolet and Ultraviolet/Ozone Treatment, *J. Colloid Interface Sci*. **254** (2002) 306–315.

[152] A. Karlsson, New Analytical Methods for Silicone Elastomers Used in Drug Delivery Systems, (2003). http://urn.kb.se/resolve?urn=urn:nbn:se:kth:diva-3533.

[153] IR Spectrum Table & Chart, Sigma-Aldrich. (n.d.) https://www.sigmaaldrich.com/technical-documents/articles/biology/ir-spectrum-table.html.

[154] A. Harkous, Analyse du comportement thermo-rhéo-cinétique et de l'adhésion des silicones liquides, These de doctorat, Nantes, 2015. http://www.theses.fr/2015NANT201.

[155] E. Pucci, G. Saccomandi, A Note on the Gent Model for Rubber-Like Materials, *Rubber Chem. Technol.* **75** (2002) 839–852.

[156] J.E. Mark, The Polymer Data Handbook, Second Edition, Oxford University Press, Oxford, New York, 2009.

[157] C. Dessi, G. Tsibidis, D. Vlassopoulos, M. De Corato, M. Trofa, G. D'Avino, P.L. Maffettone, S. Coppola, Analysis of dynamic mechanical response in torsion, *J. Rheol*. **60** (2016) 275.

[158] I.L. Radchenko, E.V. Radchenko, G.V. Vaganov, A.D. Vilesov, Powdered polymer composition for a superhydrophobic coating and method for producing a superhydrophobic coating, US20160200915A1, 2016. https://patents.google.com/patent/US20160200915A1/en.

[159] D.K. Owens, R.C. Wendt, Estimation of the surface free energy of polymers, *J. Appl. Polym. Sci*. **13** (1969) 1741–1747.

[160] L.A. Girifalco, R.J. Good, A Theory for the Estimation of Surface and Interfacial Energies. I. Derivation and Application to Interfacial Tension, *J. Phys. Chem*. **61** (1957) 904–909.

[161] K. Akhtar, S.A. Khan, S.B. Khan, A.M. Asiri, Scanning Electron Microscopy: Principle and Applications in Nanomaterials Characterization, in: S.K. Sharma (Ed.), Handb. Mater. Charact., Springer International Publishing, Cham, 2018: pp. 113–145.

[162] A. Devillez, S. Lesko, W. Mozer, Cutting tool crater wear measurement with white light interferometry, *Wear*. **256** (2004) 56–65.

[163] J. Peltonen, M. Järn, S. Areva, M. Linden, J.B. Rosenholm, Topographical Parameters for Specifying a Three-Dimensional Surface, *Langmuir*. **20** (2004) 9428–9431.

[164] D. Hanahan, Studies on transformation of Escherichia coli with plasmids, *J. Mol. Biol*. **166** (1983) 557–580.

[165] M. Wagner, R. Amann, H. Lemmer, K.H. Schleifer, Probing activated sludge with oligonucleotides specific for proteobacteria: inadequacy of culture-dependent methods for describing microbial community structure, *Appl. Environ. Microbiol*. **59** (1993) 1520–1525.

[166] S. Josset, N. Keller, M.-C. Lett, M.J. Ledoux, V. Keller, Numeration methods for targeting photoactive materials in the UV-A photocatalytic removal of microorganisms, *Chem. Soc. Rev*. **37** (2008) 744.

[167] L.M. Harwood, C.J. Moody, Experimental organic chemistry : principles and practice, Oxford : Blackwell Scientific, 1989.

[168] J.E. Mark, H.R. Allcock, R. West, Inorganic Polymers, Second Edition, Oxford University Press, Oxford, New York, 2005.

[169] R.L.N. Hailes, A.M. Oliver, J. Gwyther, G.R. Whittell, I. Manners, Polyferrocenylsilanes: synthesis, properties, and applications, *Chem. Soc. Rev*. **45** (2016) 5358–5407.

[170] J.C. McDonald, D.C. Duffy, J.R. Anderson, D.T. Chiu, H. Wu, O.J.A. Schueller, G.M. Whitesides, Fabrication of Microfluidic Systems in Poly(dimethylsiloxane), *Electrophoresis*. **21** (2000) 27–40.

[171] M.P. Wolf, G.B. Salieb-Beugelaar, P. Hunziker, PDMS with designer functionalities—Properties, modifications strategies, and applications, *Prog. Polym. Sci*. **83** (2018) 97–134.

[172] S.J. Benight, C. Wang, J.B.H. Tok, Z. Bao, Stretchable and self-healing polymers and devices for electronic skin, *Prog. Polym. Sci*. **38** (2013) 1961–1977.

[173] P.J. Flory, Molecular Size Distribution in Three Dimensional Polymers. I. Gelation1, *J. Am. Chem. Soc*. **63** (1941) 3083–3090.

[174] I.D. Johnston, D.K. McCluskey, C.K.L. Tan, M.C. Tracey, Mechanical characterization of bulk Sylgard 184 for microfluidics and microengineering, *J. Micromech. Microeng*. **24** (2014) 035017.

[175] R.N. Palchesko, L. Zhang, Y. Sun, A.W. Feinberg, Development of polydimethylsiloxane substrates with tunable elastic modulus to study cell mechanobiology in muscle and nerve, *PloS One*. **7** (2012) e51499.

[176] A. Oláh, H. Hillborg, G.J. Vancso, Hydrophobic recovery of UV/ozone treated poly(dimethylsiloxane): adhesion studies by contact mechanics and mechanism of surface modification, *Appl. Surf. Sci*. **239** (2005) 410–423.

[177] A. Mata, A.J. Fleischman, S. Roy, Characterization of Polydimethylsiloxane (PDMS) Properties for Biomedical Micro/Nanosystems, *Biomed. Microdevices*. **7** (2005) 281–293.

[178] Z. Tan, R. Jaeger, G.J. Vancso, Crosslinking studies of poly(dimethylsiloxane) networks: a comparison of inverse gas chromatography, swelling experiments and mechanical analysis, *Polymer*. **35** (1994) 3230–3236.

[179] K. Saalwächter, S. Seiffert, Dynamics-based assessment of nanoscopic polymer-network mesh structures and their defects, *Soft Matter*. **14** (2018) 1976–1991.

[180] S. Seiffert, Origin of nanostructural inhomogeneity in polymer-network gels, *Polym. Chem*. **8** (2017) 4472–4487.

[181] F.D. Lorenzo, S. Seiffert, Nanostructural heterogeneity in polymer networks and gels, *Polym. Chem*. **6** (2015) 5515–5528.

[182] H. Hillborg, N. Tomczak, A. Olàh, H. Schönherr, G.J. Vancso, Nanoscale Hydrophobic Recovery: A Chemical Force Microscopy Study of UV/Ozone-Treated Cross-Linked Poly(dimethylsiloxane), *Langmuir*. **20** (2004) 785–794.

[183] A. Bahrami, C. Bailly, B. Nysten, Spatial resolution and property contrast in local mechanical mapping of polymer blends using AFM dynamic force spectroscopy, *Polymer*. **165** (2019) 180–190.

[184] G.A. Diaz-Quijada, D.D.M. Wayner, A Simple Approach to Micropatterning and Surface Modification of Poly(dimethylsiloxane), *Langmuir*. **20** (2004) 9607–9611.

[185] D.J. Guo, H.M. Han, W. Jing, S.J. Xiao, Z.D. Dai, Surface-hydrophilic and protein-resistant silicone elastomers prepared by hydrosilylation of vinyl poly (ethylene glycol) on hydrosilanes-poly (dimethylsiloxane) surfaces, *Colloids Surf A*. **308** (2007) 129–135.

[186] C. de Menezes Atayde, I. Doi, Highly stable hydrophilic surfaces of PDMS thin layer obtained by UV radiation and oxygen plasma treatments, *Phys. Status Solidi C*. **7** (2010) 189–192.

[187] R. Jellali, J.-L. Duval, E. Leclerc, Analysis of the biocompatibility of perfluoropolyether dimethacrylate network using an organotypic method, *Mater. Sci. Eng. C*. **65** (2016) 295–302.

[188] Z. Qian, D. Ross, W. Jia, Q. Xing, F. Zhao, Bioactive polydimethylsiloxane surface for optimal human mesenchymal stem cell sheet culture, *Bioact. Mater*. **3** (2018) 167–173.

[189] S. Pinto, P. Alves, C.M. Matos, A.C. Santos, L.R. Rodrigues, J.A. Teixeira, M.H. Gil, Poly(dimethyl siloxane) surface modification by low pressure plasma to improve its characteristics towards biomedical applications, *Colloids Surf. B Biointerfaces*. **81** (2010) 20–26.

[190] M. Dirany, L. Dies, F. Restagno, L. Léger, C. Poulard, G. Miquelard-Garnier, Chemical modification of PDMS surface without impacting the viscoelasticity: Model systems for a better understanding of elastomer/elastomer adhesion and friction, *Colloids Surf. Physicochem. Eng. Asp.* **468** (2015) 174–183.

[191] H. Huang, I. Dobryden, P.A. Thorén, L. Ejenstam, J. Pan, M.L. Fielden, D.B. Haviland, P.M. Claesson, Local surface mechanical properties of PDMS-silica nanocomposite probed with Intermodulation AFM, *Compos Sci Technol*. **150** (2017) 111–119.

[192] T. Li, Y. Zhuo, V. Håkonsen, S. Rønneberg, J. He, Z. Zhang, Epidermal Gland Inspired Self-Repairing Slippery Lubricant-Infused Porous Coatings with Durable Low Ice Adhesion, *Coatings*. **9** (2019) 602.

[193] I. Keranov, T.G. Vladkova, M. Minchev, A. Kostadinova, G. Altankov, P. Dineff, Topography characterization and initial cellular interaction of plasma-based Ar+ beam-treated PDMS surfaces, *J. Appl. Polym. Sci*. **111** (2009) 2637–2646.

[194] G. Liu, W.-S. Hung, J. Shen, Q. Li, Y.-H. Huang, W. Jin, K.-R. Lee, J.-Y. Lai, Mixed matrix membranes with molecular-interaction-driven tunable free volumes for efficient bio-fuel recovery, *J. Mater. Chem. A*. **3** (2015) 4510–4521.

[195] Y. Gu, J. Zhao, J.A. Johnson, A (Macro)Molecular-Level Understanding of Polymer Network Topology, *Trends Chem*. **1** (2019) 318–334.

[196] Y. Gu, J. Zhao, J.A. Johnson, Polymer Networks: From Plastics and Gels to Porous Frameworks, *Angew. Chem. Int. Ed*. **59** (2020) 5022–5049.

[197] E.P. Magennis, A.L. Hook, M.C. Davies, C. Alexander, P. Williams, M.R. Alexander, Engineering serendipity: High-throughput discovery of materials that resist bacterial attachment, *Acta Biomater*. **34** (2016) 84–92.

[198] L. Ploux, A. Ponche, K. Anselme, Bacteria/Material Interfaces: Role of the Material and Cell Wall Properties, *J. Adhes. Sci. Technol*. **24** (2010) 2165–2201.

[199] L. Tallet, V. Gribova, L. Ploux, N.E. Vrana, P. Lavalle, New Smart Antimicrobial Hydrogels, Nanomaterials, and Coatings: Earlier Action, More Specific, Better Dosing?, *Adv. Healthc. Mater*. **10** (2021) 2001199.

[200] N. Gour, K.X. Ngo, C. Vebert-Nardin, Anti-Infectious Surfaces Achieved by Polymer Modification: Anti-Infectious Surfaces Achieved, *Macromol. Mater. Eng*. **299** (2014) 648–668.

[201] R. Wang, B. Zhou, D. Xu, H. Xu, L. Liang, X. Feng, P. Ouyang, B. Chi, Antimicrobial and biocompatible ε-polylysine–γ-poly(glutamic acid)–based hydrogel system for wound healing, *J. Bioact. Compat. Polym*. **31** (2016) 242–259.

[202] P. Kühn, R. Rozenbaum, E. Perrels, P. Sharma, P. van Rijn, Anti-Microbial Biopolymer Hydrogel Scaffolds for Stem Cell Encapsulation, *Polymers*. **9** (2017) 149.

[203] S. Sánchez-Salcedo, M. Colilla, I. Izquierdo-Barba, M. Vallet-Regí, Preventing bacterial adhesion on scaffolds for bone tissue engineering, *Int. J. Bioprinting*. **2** (2016).

[204] M.M. Konai, B. Bhattacharjee, S. Ghosh, J. Haldar, Recent Progress in Polymer Research to Tackle Infections and Antimicrobial Resistance, *Biomacromolecules*. **19** (2018) 1888–1917.

[205] A. Gallardo, E. Martínez-Campos, C. García, A.L. Cortajarena, J. Rodríguez-Hernández, Hydrogels with Modulated Ionic Load for Mammalian Cell Harvesting with Reduced Bacterial Adhesion, *Biomacromolecules*. **18** (2017) 1521–1531.

[206] Q. Cao, S. Wu, L. Wang, X. Shi, G. Li, Effects of the morphology of sulfobetaine zwitterionic layers grafted onto a silicone surface on improving the hydrophilic stability, anti-bacterial adhesion properties, and biocompatibility, *J. Appl. Polym. Sci*. **135** (2018) 46860.

[207] Y. Ren, C. Wang, Z. Chen, E. Allan, H.C. van der Mei, H.J. Busscher, Emergent heterogeneous microenvironments in biofilms: substratum surface heterogeneity and bacterial adhesion force-sensing, *FEMS Microbiol. Rev*. **42** (2018) 259–272.

[208] S. Moorthy, J. Keklak, E. Klein, Perspective: Adhesion Mediated Signal Transduction in Bacterial Pathogens, *Pathogens*. **5** (2016) 23.

[209] A.S. Mijailovic, S. Galarza, S. Raayai-Ardakani, N.P. Birch, J.D. Schiffman, A.J. Crosby, T. Cohen, S.R. Peyton, K.J. Van Vliet, Localized characterization of brain tissue mechanical properties by needle induced cavitation rheology and volume-controlled cavity expansion, *J. Mech. Behav. Biomed. Mater*. **114** (2021) 104168.

[210] K.W. Kolewe, S. Kalasin, M. Shave, J.D. Schiffman, M.M. Santore, Mechanical Properties and Concentrations of Poly(ethylene glycol) in Hydrogels and Brushes Direct the Surface Transport of *Staphylococcus aureus*, *ACS Appl. Mater. Interfaces*. **11** (2019) 320–330.

[211] R. Zhao, Z. Zhang, Y. Qi, Influence of Epoxy Content on the Properties and Marine Bacterial Adhesion of Epoxy Modified Silicone Coatings, *Coatings*. **10** (2020) 126.

[212] Corporation DC (2010/05/03) SYLGARD(R) 184 SILICONE ELASTOMER KIT (BASE). MSDS No: 01064291, (n.d.).

[213] Corporation DC (2011/03/15) SYLGARD(R) 184 SILICONE ELASTOMER KIT (CURING AGENT). MSDS No: 01064291, (n.d.).

[214] J.-H. Seo, K. Sakai, N. Yui, Adsorption state of fibronectin on poly(dimethylsiloxane) surfaces with varied stiffness can dominate adhesion density of fibroblasts, *Acta Biomater*. **9** (2013) 5493–5501.

[215] B. Pittenger, S. Osechinskiy, D. Yablon, T. Mueller, Nanoscale DMA with the Atomic Force Microscope: A New Method for Measuring Viscoelastic Properties of Nanostructured Polymer Materials, *JOM*. **71** (2019) 3390–3398.

[216] R. Garcia, Nanomechanical mapping of soft materials with the atomic force microscope: methods, theory and applications, *Chem. Soc. Rev*. **49** (2020) 5850–5884.

[217] M.E. Dokukin, I. Sokolov, Quantitative Mapping of the Elastic Modulus of Soft Materials with HarmoniX and PeakForce QNM AFM Modes, *Langmuir*. **28** (2012) 16060–16071.

[218] A. Cerf, J.-C. Cau, C. Vieu, E. Dague, Nanomechanical Properties of Dead or Alive Single-Patterned Bacteria, Langmuir. 25 (2009) 5731–5736. https://doi.org/10.1021/la9004642.

[219] H.H. Tuson, G.K. Auer, L.D. Renner, M. Hasebe, C. Tropini, M. Salick, W.C. Crone, A. Gopinathan, K.C. Huang, D.B. Weibel, Measuring the stiffness of bacterial cells from growth rates in hydrogels of tunable elasticity: Measuring cellular mechanical properties with hydrogels, *Mol. Microbiol*. **84** (2012) 874–891.

[220] M. Ina, Z. Cao, M. Vatankhah-Varnoosfaderani, M.H. Everhart, W.F.M. Daniel, A.V. Dobrynin, S.S. Sheiko, From Adhesion to Wetting: Contact Mechanics at the Surfaces of Super-Soft Brush-Like Elastomers, *ACS Macro Lett*. **6** (2017) 854–858.

[221] R.W. Style, R. Boltyanskiy, Y. Che, J.S. Wettlaufer, L.A. Wilen, E.R. Dufresne, Universal Deformation of Soft Substrates Near a Contact Line and the Direct Measurement of Solid Surface Stresses, *Phys. Rev. Lett*. **110** (2013) 066103.

[222] D. Hanahan, Studies on transformation of Escherichia coli with plasmids, *J. Mol. Biol*. **166** (1983) 557–580.

[223] R.H. Pritchard, P. Lava, D. Debruyne, E.M. Terentjev, Precise determination of the Poisson ratio in soft materials with 2D digital image correlation, *Soft Matter*. **9** (2013) 6037.

[224] J.L. Hutter, J. Bechhoefer, Calibration of atomic-force microscope tips, *Rev. Sci. Instrum*. **64** (1993) 1868–1873.

[225] B.V. Derjaguin, V.M. Muller, YU.O. Toporov, Effect of contact deformations on the adhesion of particles, *J. Colloid Interface Sci*. **53** (1975) 314–326.

[226] A. Müller, M.C. Wapler, U. Wallrabe, A quick and accurate method to determine the Poisson's ratio and the coefficient of thermal expansion of PDMS, *Soft Matter*. **15** (2019) 779–784.

Annex I. Bulk properties of LSRs

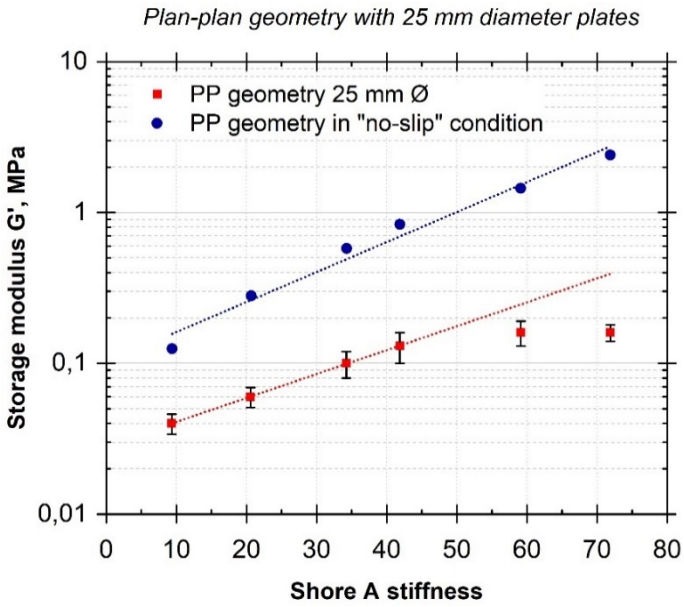

Figure S1. Storage modulus as a function of Shore A stiffness of Elastosil LSR formulations. Shear measurements performed in parallel-plate geometry using *ex situ* (squares) and *in situ* (circles) prepared LSR specimens

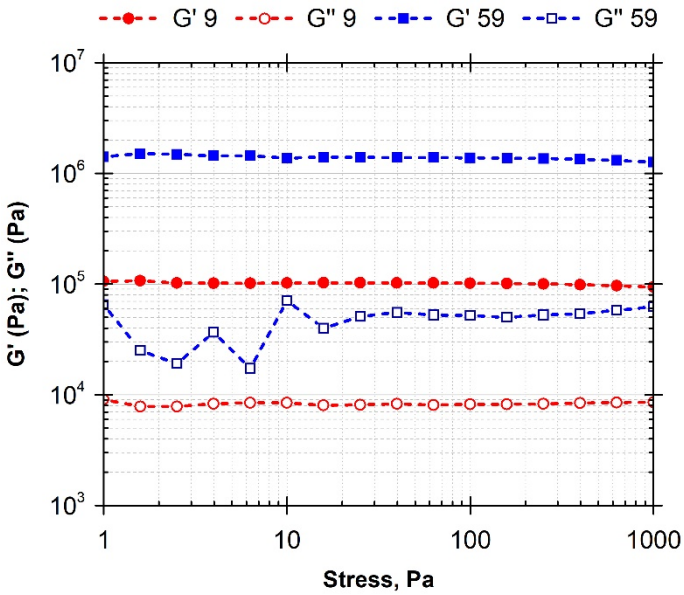

Figure S2. Stress sweep test made on two representative *ex-situ* cured LSR specimens with Shore A stiffness 9 (circles) and 59 (squares) in the parallel-plates geometry at a frequency 10 rad/s (8 mm in diameter, 1 mm in thickness). Storage and loss moduli are represented in logarithmic scale.

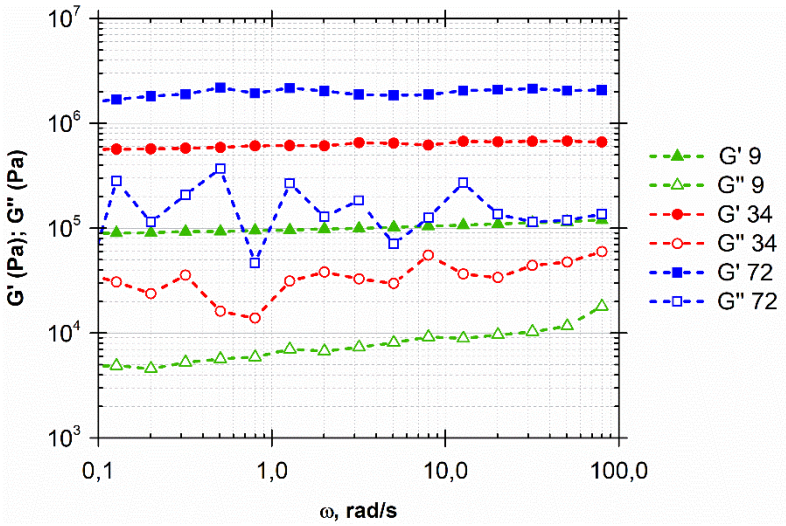

Figure S3. Deformation sweep test of three representative *ex-situ* cured LSR specimens of Shore A stiffness 9, 34, and 72 in the rectangular torsion geometry at a frequency 2 rad/s (thin-wall rectangular bars of 40 mm in length, 10 mm in width, and 2 mm in thickness). Storage and loss moduli are represented in logarithmic scale.

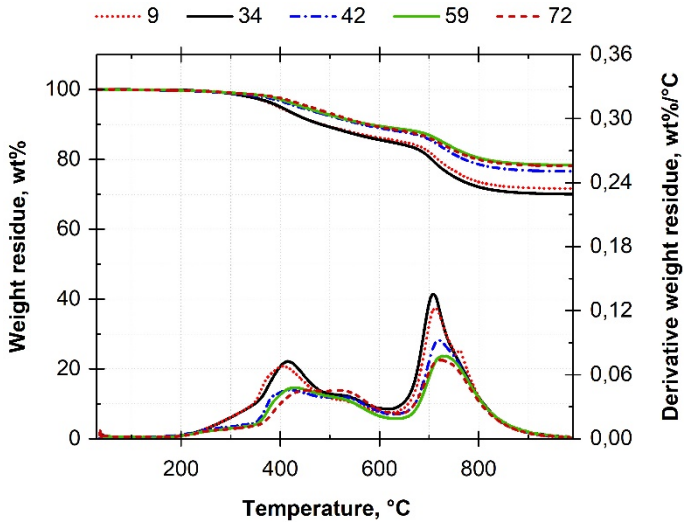

Figure S4. TGA thermograms and corresponding DTG profiles of precured LSR formulations with varied Shore A stiffness (9, 34, 42, 59, and 72).

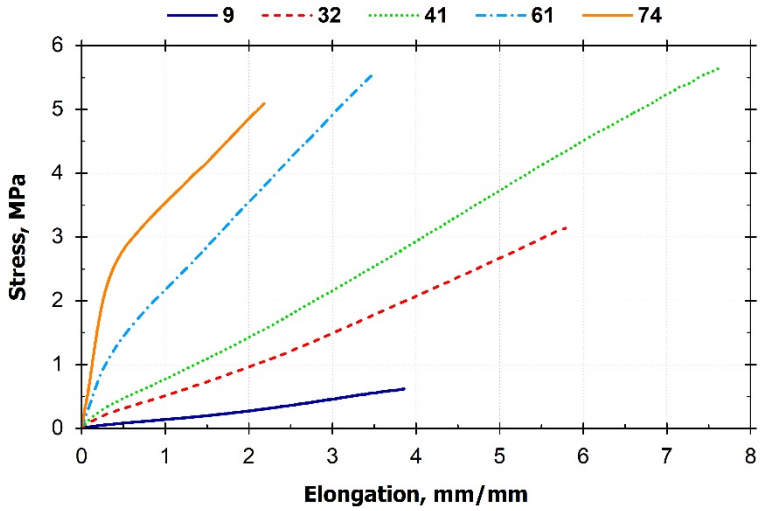

Figure S5. Stress-strain curves obtained from the post-cured LSR samples of varied Shore A stiffness

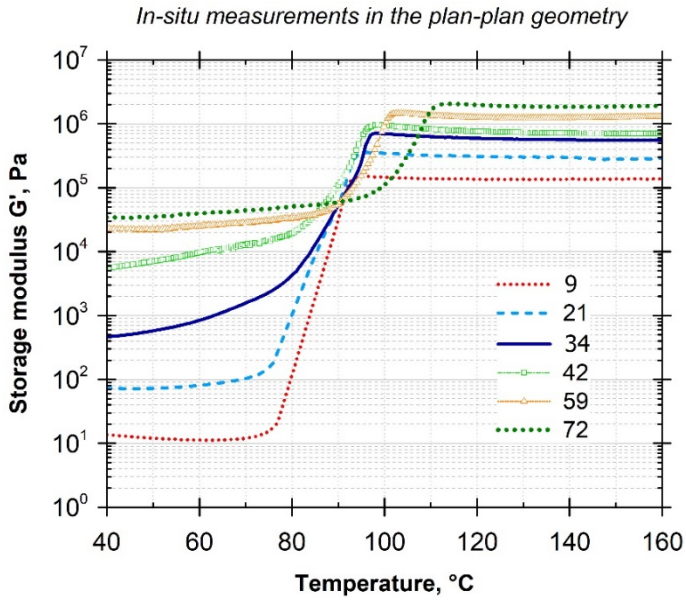

Figure S6. Storage G' modulus evolution with temperature during the curing of LSR formulations with varied Shore A stiffness (9; 21; 34; 42; 59; 72). Thermomechanical measurements performed in the parallel-plate geometry with plates of 25 mm in diameter

Annex II. Surface characterization of the LSR

a. Error estimation of the surface tension γ_s

The variance of y is calculated as:

$$S_y^2 = \frac{\sum_{i=1}^{n}(y_i - a - bx_i)}{n-2}$$

To clarify the denominator $n-2$ appearing in this expression, the degree of freedom is equal to $n-2$ because parameters a and b are both calculated from the same data set.

$$S_a^2 = S_y^2 \cdot \frac{\sum_{i=1}^{n} x_i^2}{D}$$

$$S_b^2 = S_y^2 \cdot \frac{n}{D}$$

where

$$D = n\sum_{i=1}^{n} x_i^2 - \left(\sum_{i=1}^{n} x_i\right)^2$$

The standard deviations of components a and b:

$$S_a = S_y \cdot \sqrt{\frac{\sum_{i=1}^{n} x_i^2}{D}}$$

$$S_b = S_y \cdot \sqrt{\frac{n}{D}}$$

The standard deviations of polar and dispersive components, $S_{\gamma_s^p}$ and $S_{\gamma_s^d}$, respectively are calculated as:

$$S_{\gamma_s^p} = \frac{\partial \gamma_s^p}{\partial a} \cdot S_a = 2a \cdot S_a$$

$$S_{\gamma_s^d} = \frac{\partial \gamma_s^d}{\partial b} \cdot S_b = 2b \cdot S_b$$

$$S_{\gamma_s} = S_{\gamma_s^p} + S_{\gamma_s^d}$$

At 80% confidence a true surface tension value is lying within the interval:

$$\left[\gamma_s - t_{0.8}^1 \cdot \frac{S_{\gamma_s}}{\sqrt{n}};\ \gamma_s + t_{0.8}^1 \cdot \frac{S_{\gamma_s}}{\sqrt{n}}\right]$$

For 80% confidence with one degree of freedom, the two-sided t-value is 3.078. The surface tension values are finally represented as $\gamma_s \pm 1.777 \cdot S_{\gamma_s}$.

b. SEM images of the textured LSR

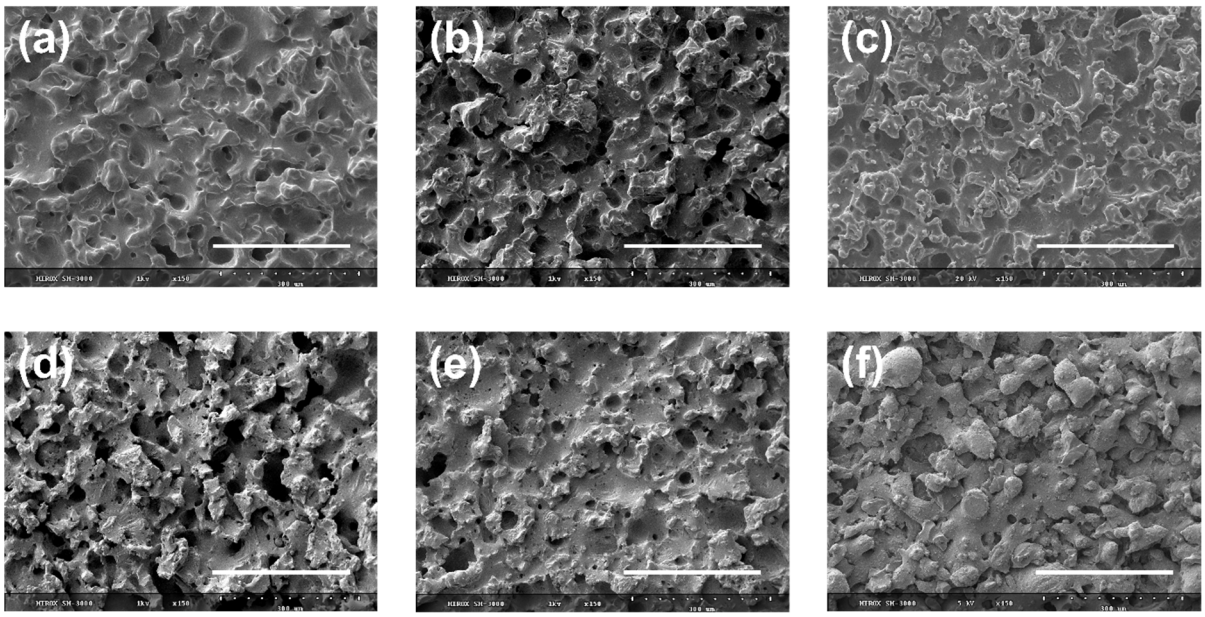

Figure S6. SEM images of the textured LSR samples of varied Shore A stiffness: (a) 9, (b) 21, (c) 34, (d) 59, (e) 72. (f) SEM image of the superhydrophobic foil used as print surface. The scale bars represent 300 µm.

c. Surface roughness parameters of the flat-like LSR

Table S1. *Surface topography parameters of the flat-like LSR samples of varied stiffness*

Shore A stiffness	S_a, µm	S_q, µm
9	0.3	0.4
21	0.3	0.4
34	0.3	0.4
59	0.3	0.4
72	0.3	0.4

Annex III. Bacterial retention assays

a. Protocol:

All the manipulations with the bacterial inoculum were performed under sterile conditions in Class II biosafety cabinet (IPREM, Pau, France).

Overnight culture:

To obtain the bacterial pre-culture, a frozen aliquot of bacteria *Escherichia Coli DH5α λ-pir pSEVA337 GFP pem-7 Cm^R* was inoculated into a flask containing 5 ml of lysogeny broth (LB) medium and 34 µg·mL^{-1} of chloramphenicol. The flask was then kept overnight in a rotational incubator at 200 rpm at the optimal growing temperature 37°. The optical density of the overnight culture measured using a UV/vis spectrophotometer reached a value of about 4.

Bacterial culture growth:

- The overnight culture was re-suspended in a sterile Erlenmeyer flask containing 50 ml of LB and 34 µg·mL^{-1} of chloramphenicol to 0.02 optical density.
- The flask with inoculum was then mounted to a rotating turntable of incubator and kept at 200 rpm and 37° for about 3-4 hours to 0.6 optical density.
- Then, the bacterial culture in the exponential phase of growth was poured into a sterile flacon, securely closed, and subsequently centrifuged at 5000 rpm for 10 min at ambient temperature.
- The supernatant was removed, and bacteria were re-suspended in PBS to 0.1 optical density.

Annex IV. Mesh nanostructures in cross-linked poly(dimethylsiloxane) visualized by AFM

1. SEM imaging of AFM tips

High resolution AFM tip imaging by SEM was performed using a JEOL JSM-7610F at 2 kV operating voltage. Examples are presented in **Fig. S1**.

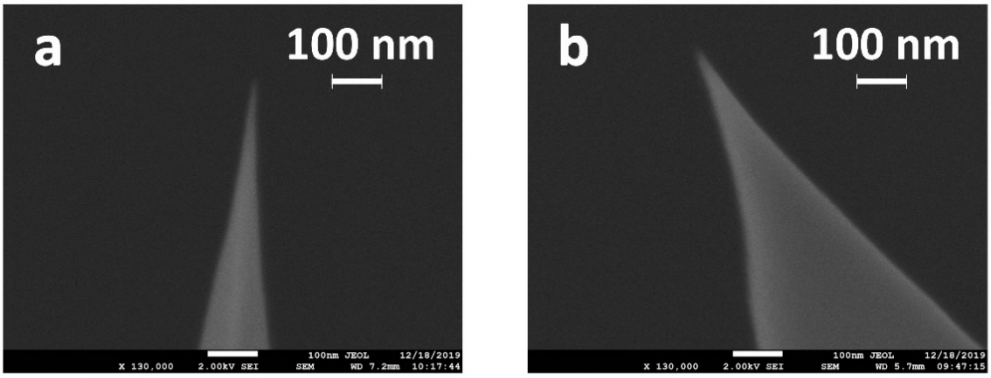

Figure S1. SEM micrographs: (a) OMCL-AC240TS (Olympus) and (b) HQ:NSC19/Al BS (µMasch) AFM tips

2. Quantitative PF-QNM imaging of the mesh-like network structure

The adhesion force and Young's modulus images were quantified by determining the sensitivity of the AFM optical system on a bare silicon wafer (as a rigid reference) and the cantilever spring constant by the thermal tune method, as well as employing the "relative modulus determination method" with the PDMS elastic reference (3.5 MPa; Bruker) [1]. An example is presented in **Fig. S2**.

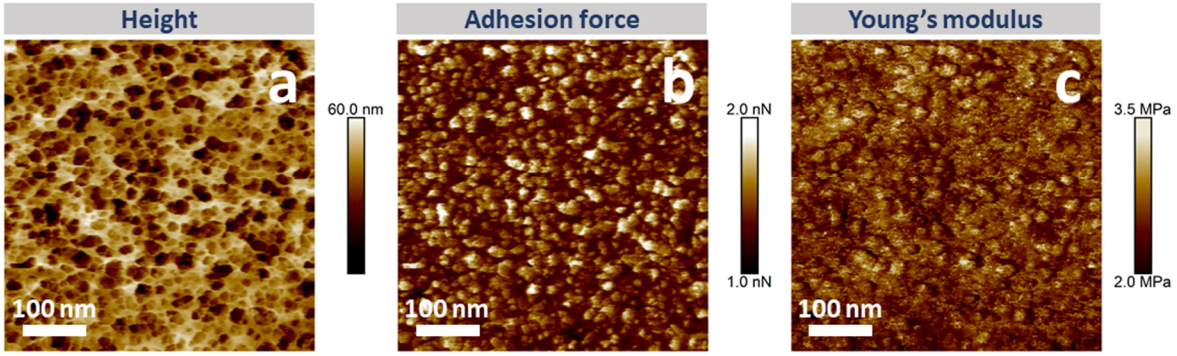

Figure S2. PF-QNM AFM images of the free PDMS surfaces with 20 wt.% cross-linker concentration: (a) height, (b) adhesion force, and (c) Young's modulus. The scan area is 500 x 500 nm^2 for all the images. Olympus cantilever was used

3. Free PDMS surface AFM imaging in standard tapping mode. A comparison with PF-QNM mode

Tapping mode images were obtained at set point amplitude values of 350 mV, while the free oscillation amplitude of the (free) vibrating cantilever was 500 mV. We found these parameters as the optimum to unveil topography and phase contrast for the specimens with a minimum of artifacts, e.g, streaking. A representative example of free PDMS (with 20 wt.% cross-linker concentration) surface is shown in **Fig. S3**.

Note that the images shown in **Fig. S2** (PF-QNM mode) and **S3** were collected at (exactly) the same spot and by using (physically) the same Olympus cantilever, thus the height images are directly comparable. Matching only the scale bars in height images (60 nm vs. 6 nm) one can see a tremendous difference between these two imaging modes when the PDMS surface profile was tracked.

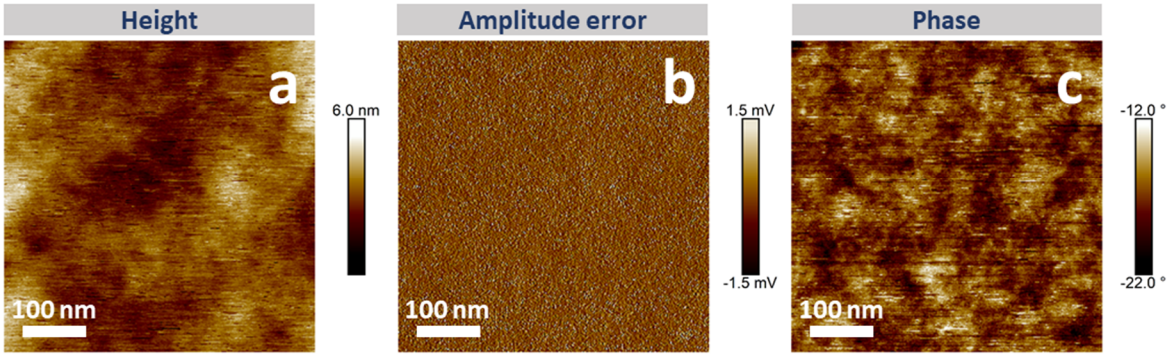

Figure S3. Tapping mode AFM images of the free PDMS surfaces with 20 wt.% cross-linker concentration: (a) height, (b) amplitude error, and (c) phase. The scan area is 500 x 500 nm^2 for all the images. Olympus cantilever was used

4. Composition of PDMS Sylgard 184

Sylgard 184 (Dow Corning) used in this study is a two-components based silicone elastomer kit containing a base and a curing agent. The composition of both the chemicals is provided by the supplier [2,3] (see Table S1). Sylgard 184, mainly consisting of siloxane chains (> 60.0 wt.% for two components), contains a reinforcing silica in both the base and the curing agent.

Table S1. *Composition of PDMS Sylgard 184 (as specified by the supplier DOW Chemical)*

Components	Content, wt.%
Sylgard 184 Base	
Dimethyl siloxane, dimethylvinyl-terminated	> 60.0
Dimethylvinylated and trimethylated silica	30.0 – 60.0
Tetra(trimethylsiloxy) silane	1.0 – 5.0
Ethylbenzene	< 1.0
Sylgard 184 Curing Agent	
Dimethyl, methylhydrogen siloxane	75.0
Dimethyl siloxane, dimethylvinyl-terminated	15.0 – 35.0
Dimethylvinylated and trimethylated silica	10.0 – 30.0
Tetramethyl tetravinyl cyclotetrasiloxane	1.0 – 5.0

References

[1] H. Gojzewski, B. Imre, C. Check, R. Chartoff and G. J. Vancso, *J. Polym. Sci. B*, 2016, **54**, 2298-2310.

[2] Corporation DC (2010/05/03) SYLGARD(R) 184 SILICONE ELASTOMER KIT (BASE). MSDS No: 01064291.

[3] Corporation DC (2011/03/15) SYLGARD(R) 184 SILICONE ELASTOMER KIT (CURING AGENT). MSDS No: 01064291.

Annex V. Initial bacterial retention on Polydimethylsiloxane of various stiffnesses: the relevance of modulus (mis)match

Table S1. *Mass loss subsequent to Soxhlet extraction*

Cross-linker concentration, wt.%	*Mass loss, wt.%*
2.5	*Destroyed*
5	10
10	4
20	5
25	5

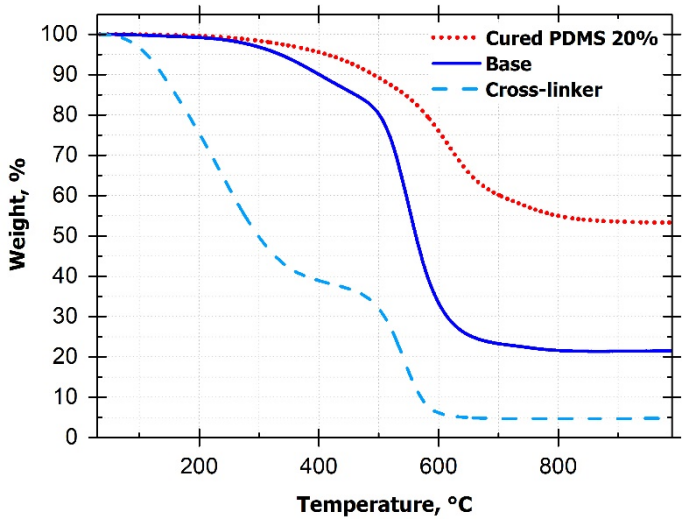

Figure S1. TGA curves of Sylgard 184 base (solid line), Sylgard 184 cross-linker (dashed line), and cured sample at 20 wt.% cross-linking (dotted line).

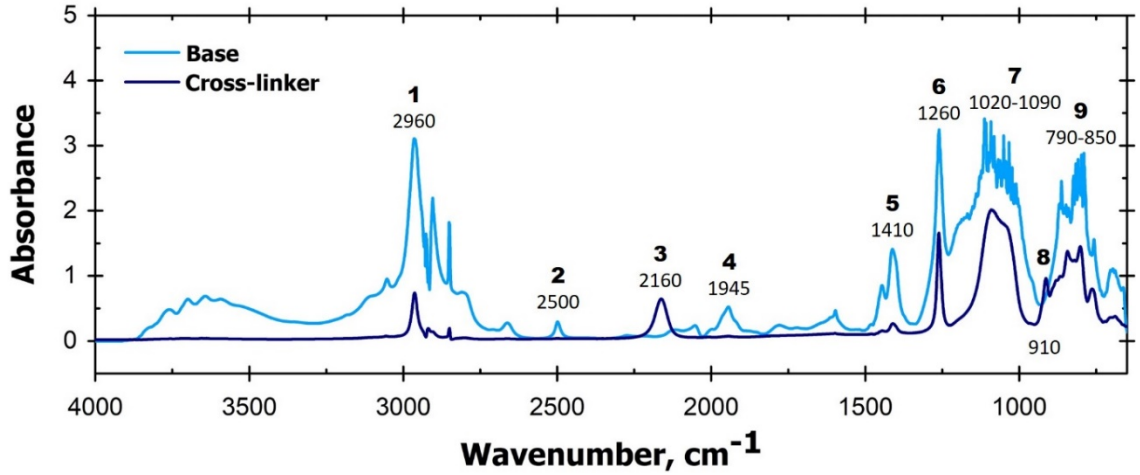

Figure S2. FTIR-Transmission spectra of Sylgard 184 base (light blue) and Sylgard 184 cross-linker (dark blue)

Table S2. *IR absorption bands of Sylgard 184 base, and Sylgard 184 cross-linker*

Peak n° (Fig. 3)	*Wavenumber, cm^{-1}*	*Description*	*Ref.*
1	2960	Asymmetrical CH_3 stretching in ≡Si–CH_3	[1]
2	2500	Overtone band of CH_3 deformation 1260 cm^{-1}	[2]
3	2160	Si-H group stretching	[2]
4	1945	Siloxane backbone stretching	[2]
5	1410	Symmetrical CH_3 stretching in ≡Si–CH_3	[1]
6	1260	Symmetrical CH_3 deformation in ≡Si–CH_3	[1]
7	1020–1090	Asymmetrical Si-O-Si stretching	[1,2]
8	910	Vinyl functional group C=CH_2	[3]
9	790 – 850	CH_3 rocking and Si–C stretching in ≡Si–CH_3, Si-O stretching in ≡Si–OH	[1]

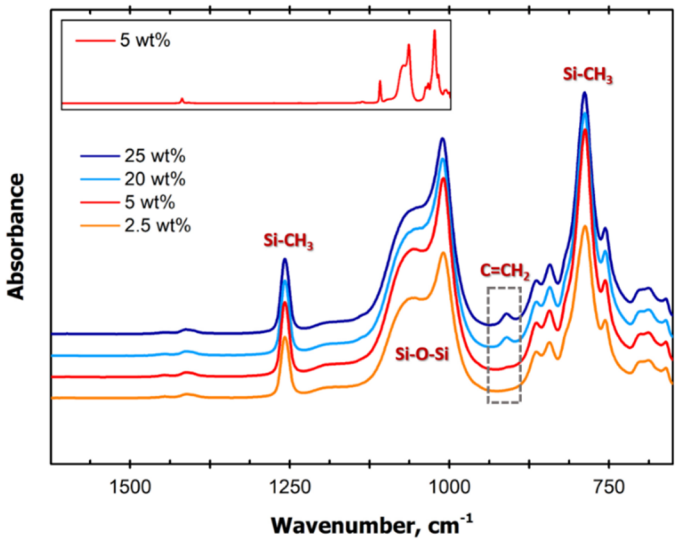

Figure S3. FTIR-ATR spectra of cured PDMS samples with different cross-linker concentration (2.5, 5, 20, and 25 wt.%).

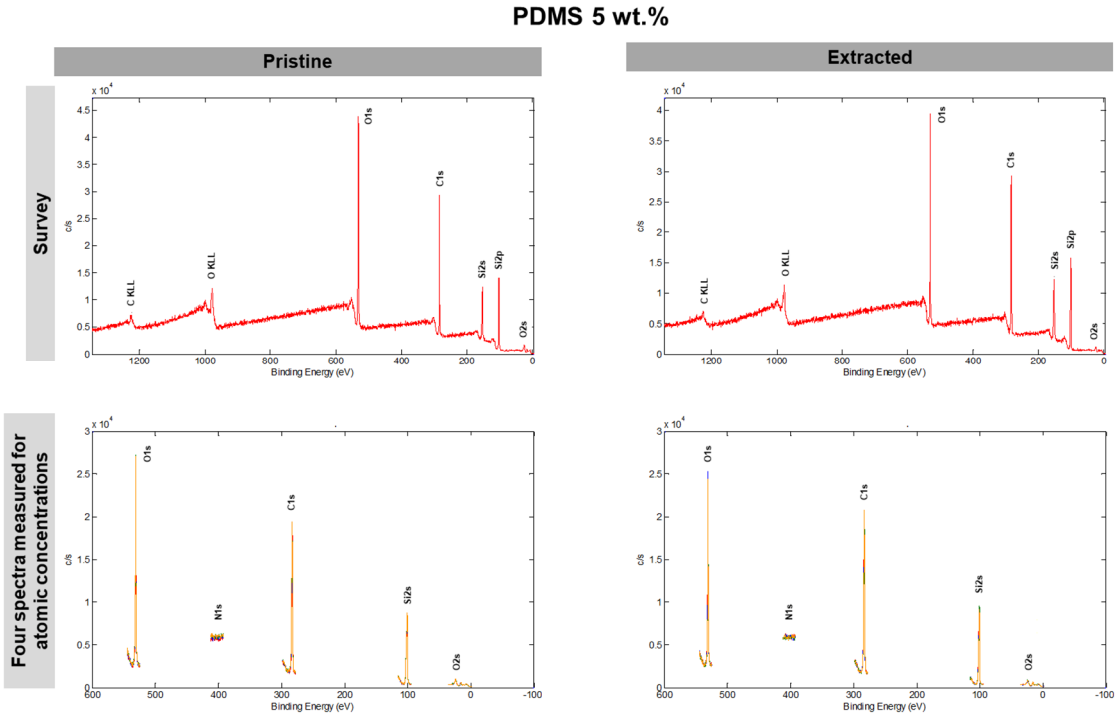

Figure S4. XPS survey spectra and four element spectra of O1s, N1s, C1s, Si2p and O2s regions for pristine and extracted PDSM with 5 wt.% of the cross-linker

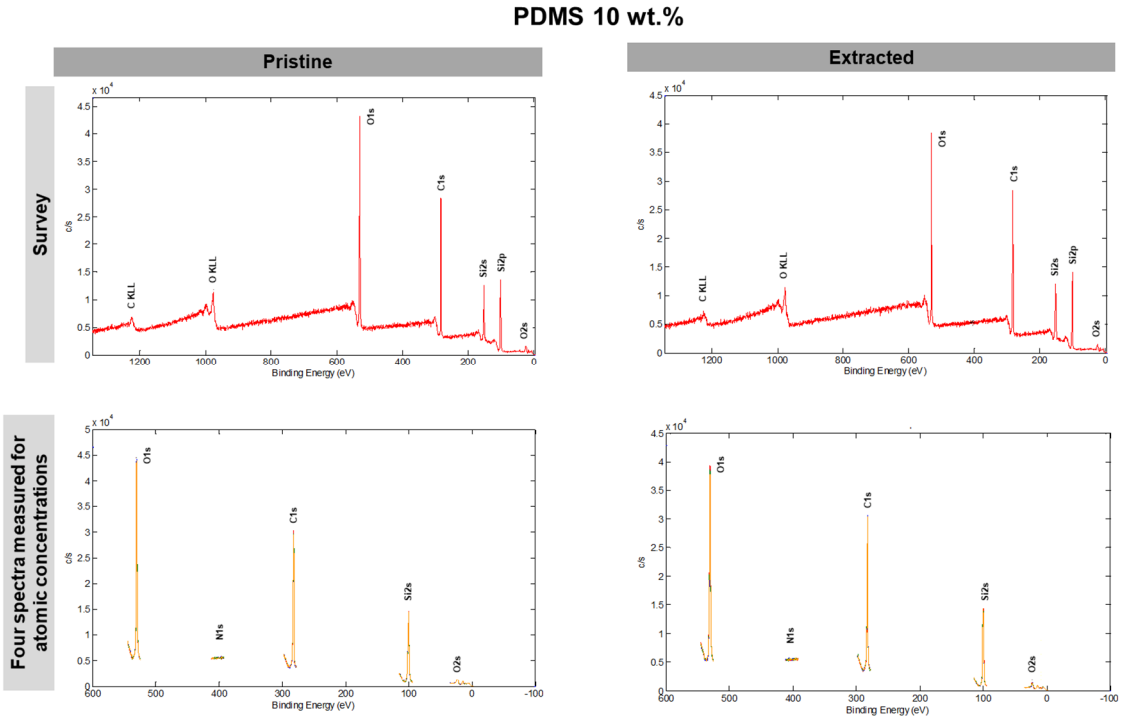

Figure S5. XPS survey spectra and four element spectra of O1s, N1s, C1s, Si2p, O2s regions for pristine and extracted PDSM with 10 wt.% of the cross-linker

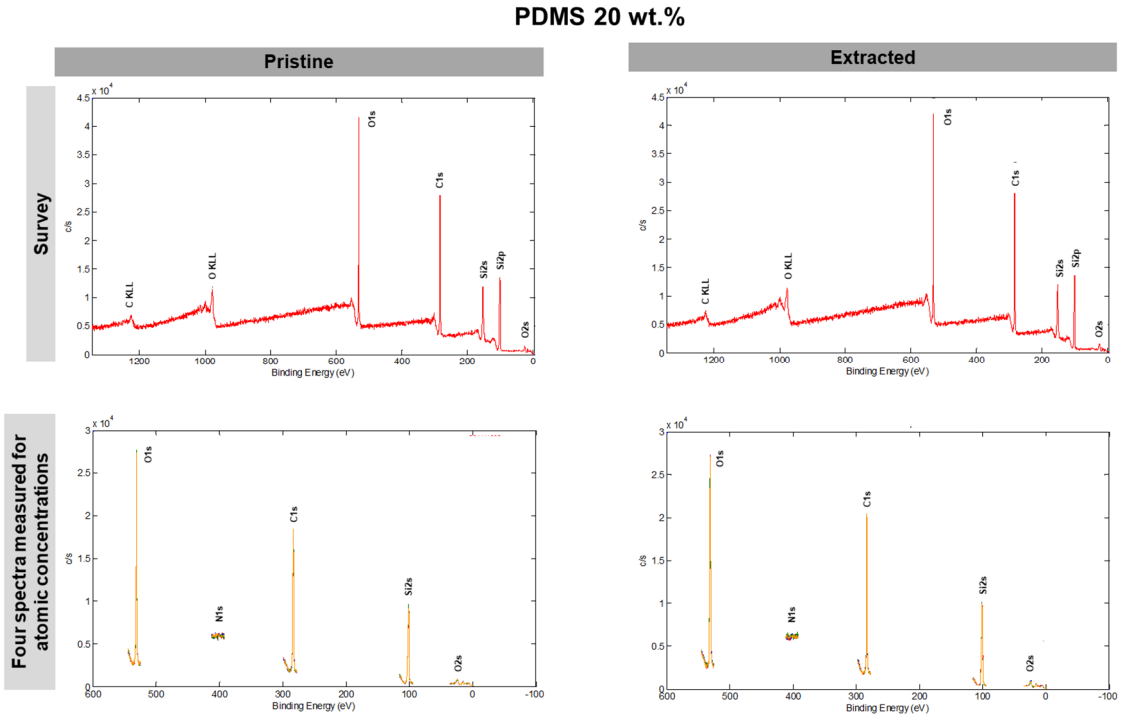

Figure S6. XPS survey spectra and four element spectra of O1s, N1s, C1s, Si2p, O2s regions for pristine and extracted PDSM with 20 wt.% of the cross-linker

Table S3. *Elemental composition of the PDMS surface prior and subsequent to Soxhlet extraction*

Sample		**C, %**	**O, %**	**Si, %**
5 wt.%	Pristine	(45.3 ± 1)	(30.4 ± 0.3)	(24.3 ± 0.7)
	Extracted	(50.8 ± 1.1)	(26.7 ± 0.5)	(22.3 ± 0.6)
10 wt.%	Pristine	(44.1 ± 1)	(31.3 ± 0.5)	(24.4 ± 0.3)
	Extracted	(49.4 ± 1.6)	(28 ± 1)	(22.5 ± 0.7)
20 wt.%	Pristine	(44.7 ± 0.2)	(30.1 ± 0.3)	(24.8 ± 0.3)
	Extracted	(48.3 ± 0.6)	(28.4 ± 0.6)	(23.1 ± 0.4)

Table S4. *RMS surface roughness, R_{rms}, values of the PDMS surfaces at large scan areas*

Scan size	**5 wt.%**	**10 wt.%**	**20 wt.%**	**25 wt.%**
5 × 5 μm²	3.95 nm	*No data*	3.12 nm	2.81 nm
10 × 10 μm²	5.18 nm	*No data*	3.24 nm	3.43 nm
30 × 30 μm²	5.31 nm	*No data*	4.30 nm	4.49 nm

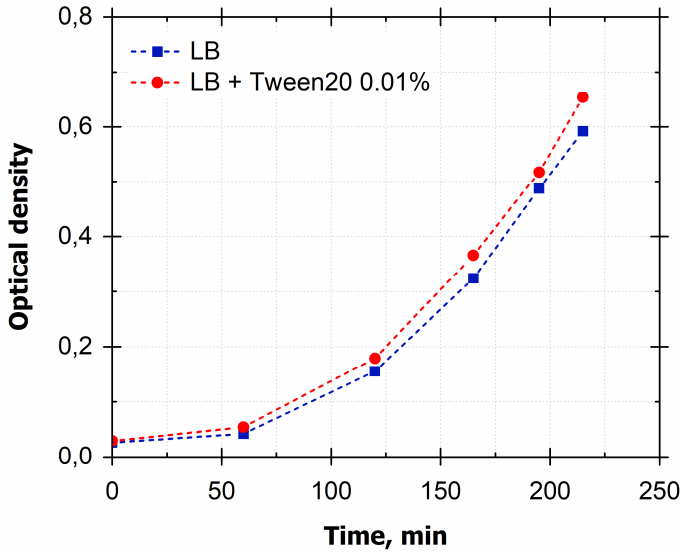

Figure S7. Growth of DH5α pSEVA337 in LB with 34 μg/mL of chloramphenicol (filled squares) and in LB with 34 μg/mL of chloramphenicol plus 0.01 % Tween 20 (filled circles). Lines are only guides for the eye.

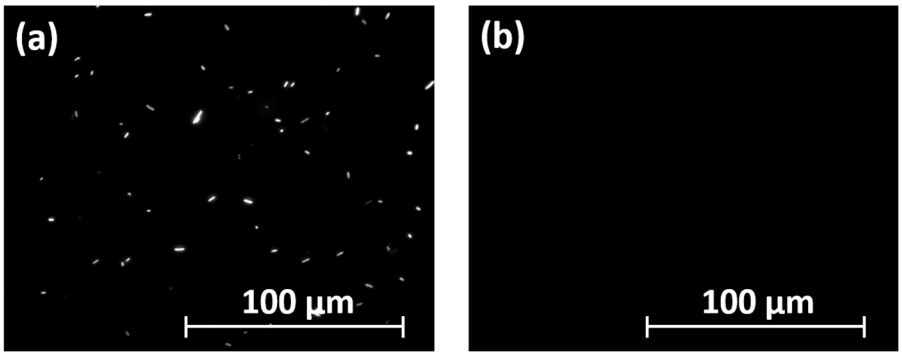

Figure S8. Epifluorescence images of the PDMS surfaces at 5 wt.% cross-linker (a) only rinsed in three PBS baths and (b) rinsed in three PBS baths and shaken in PBS containing 0.01 % Tween 20 for 20 sec

References

[1] K. Efimenko, W.E. Wallace, J. Genzer, Surface Modification of Sylgard-184 Poly(dimethyl siloxane) Networks by Ultraviolet and Ultraviolet/Ozone Treatment, *J. Colloid Interface Sci.* 254 (2002) 306–315. https://doi.org/10.1006/jcis.2002.8594.

[2] A. Karlsson, New Analytical Methods for Silicone Elastomers Used in Drug Delivery Systems (2003).

[3] IR Spectrum Table & Chart, Sigma-Aldrich. https://www.sigmaaldrich.com/technical-documents/articles/biology/ir-spectrum-table.html (accessed October 19, 2020)